THE STRUCTURE OF ANNUAL AND INTERANNUAL WIND VARIABILITY IN THE TROPICS

by

DAVID SCOTT GUTZLER

B.S. University of California (Berkeley)
(1977)

M.S. University of Washington
(1980)

Submitted to the Department of
Earth, Atmospheric, and Planetary Sciences
in Partial Fulfillment of the Requirements
for the Degree of

DOCTOR OF PHILOSOPHY

at the

MASSACHUSETTS INSTITUTE OF TECHNOLOGY

January 1986

© Massachusetts Institute of Technology 1986

Signature of Author_____
Department of Earth, Atmospheric, and
Planetary Sciences, October 31, 1985

Certified by_____
D. E. Harrison
Thesis Supervisor

Accepted by_____
Theodore Madden
Chairman, Department Committee on Graduate Students

WITHDRAWN FROM MASSACHUSETTS INSTITUTE OF TECHNOLOGY
APR 09 1986
MIT LIBRARIES

THE STRUCTURE OF ANNUAL AND INTERANNUAL WIND VARIABILITY IN THE TROPICS

by

DAVID SCOTT GUTZLER

Submitted to the Department of
Earth, Atmospheric, and Planetary Sciences
in Partial Fulfillment of the Requirements for the Degree of
Doctor of Philosophy in Meteorology
October, 1985

ABSTRACT

Multi-year time series of monthly mean wind observations from a network of rawinsonde stations are examined in order to document the three-dimensional structure of wind variability in the tropical troposphere on seasonal time scales. The geographical and vertical structure of the annual mean, annual variability, and interannual variability of the zonal and meridional wind components are described in turn. The inclusion of the vertical structure of variability allows the direct interpretation of wind fluctuations in terms of diabatic heating and convection.

All major features in the seasonal wind climatologies derived from this data set are consistent with earlier studies, confirming the significance of the seasonal cycle. The annual mean, annual cycle, and semiannual cycle of the zonal wind have appreciable magnitude throughout the troposphere; significant meridional winds near the equator are confined to layers near the top and bottom of the troposphere.

A transition in the vertical structure of zonal wind interannual variability occurs at about 12° latitude in each hemisphere. Poleward of 12°, the standard deviation of seasonal anomalies increases rapidly with height, and anomalies are positively correlated in the vertical (an "equivalent-barotropic" structure). Equatorward of 12°, the vertical gradient of variability is much smaller, and anomalies in the upper and lower troposphere are negatively correlated, with a node in mid-troposphere (a "baroclinic" structure). Time series of the fluctuations of empirical orthogonal function modes with these vertical structures are strongly correlated with the Southern Oscillation. The vertical structure of interannual zonal wind fluctuations near the equator resembles the large-scale forced response to a vertical profile of anomalous latent heating with a broad maximum in mid-troposphere.

Zonal wind anomalies composited with respect to the phases of El Niño events reveal a distinct pattern over the near-equatorial eastern Indian and western Pacific Oceans which seems to be related to the onset of El Niño. One season prior to the ocean surface warming in the eastern

Pacific which defines El Niño, anomalous low-level convergence and upper level divergence are observed in the vicinity of Indonesia. The pattern subsequently propagates eastward as the warm sea surface temperature anomaly moves westward. The fully developed phase of El Niño incorporates both anomalies over the central Pacific one year after the initial appearance of the atmospheric anomaly pattern. The wind anomalies are "phase-locked" to the annual cycle; that is, the evolution of the anomalies with respect to the seasonal cycle is nearly the same for each El Niño event. The anomaly pattern has spatial and temporal scales corresponding to zonal wave number two and a period of two years. This space-time structure is not consistent with the dynamics of atmospheric equatorial Kelvin waves. Therefore, the wind anomalies must be part of an air-sea interactive system.

Thesis supervisor: D. E. Harrison
Title: Assistant Professor of Meteorology

TABLE OF CONTENTS

Page

ABSTRACT 2

ACKNOWLEDGEMENTS 5

CHAPTER 1: INTRODUCTION
1.1 Objectives 6
1.2 Data 10

CHAPTER 2: THE ANNUAL VARIABILITY OF TROPICAL WINDS
2.1 Introduction 18
2.2 Annual mean winds 24
2.3 Annual and semiannual cycles 31
2.4 Annual variability over the Equatorial Western Pacific . 49
2.5 Discussion 60

CHAPTER 3: SPATIAL STRUCTURE OF SEASONAL WIND ANOMALIES
3.1 Introduction 63
3.2 Geographical distribution of interannual variance . . 73
3.3 Vertical structure of seasonal anomalies 84
3.4 Horizontal structure of seasonal anomalies 104
a. Correlations between wind anomalies and the SOI . . 105
b. Spatial EOFs over the equatorial western Pacific . . 119
3.5 Discussion 125

CHAPTER 4: TEMPORAL EVOLUTION OF SEASONAL WIND ANOMALIES OVER THE WESTERN PACIFIC OCEAN
4.1 Introduction 128
4.2 Spatial structure of composite El Niño event phases . 132
4.3 Complex EOF analysis of zonal wind anomalies 140
4.4 Comparison of individual El Niño events 158
4.5 Discussion 174

CHAPTER 5: CONCLUSION 187

APPENDIX A: SEASONAL MEAN WIND PLOTS 193

APPENDIX B: EMPIRICAL ORTHOGONAL FUNCTIONS
B.1 Introduction 202
B.2 EOFs of scalar wind components 203
B.3 EOFs of vector winds 206
B.4 Generalization of EOFs for propagating waves 207

APPENDIX C: SIGNIFICANCE TESTS
C.1 Correlation coefficients 209
C.2 Eigenvalues and eigenvectors 210

APPENDIX D: LIST OF FIGURES 214

REFERENCES 218

ACKNOWLEDGEMENTS

To my thesis advisor, Ed Harrison, my gratitude for his encouragement, advice, and advocacy (not to mention financial support). Our discussions were always both productive and pleasurable, a combination whose rarity among advisor-student relationships I fully appreciate. Doing science with Ed has been fun, and how many graduate students finish up with that attitude?

To my colleagues in the Center for Meteorology and Physical Oceanography at MIT, my thanks for maintaining an environment conducive to intellectual growth, where everyone is simultaneously a teacher and a student. The members of my thesis committee, Ed Lorenz, Reginald Newell, and Peter Stone, were inquisitive and supportive. I have benefited tremendously from discussions with Randy Dole, Steve Ghan, Bill Gutowski, Richard Lindzen, Ron Miller, Sumant Nigam, Rick Rosen, Rennie Selkirk, and Steve Zebiak, among many others. I received crucial computing assistance along the way from Diana Spiegel and Steve Garner.

To all my friends in and around Cambridge, special thanks for defending my sanity against the assault of the 'Tute. Between softball games, hikes in the White Mountains, gluttonous dinners, and beer hour, I've been much too busy to notice how miserable and broke I'm supposed to have been for three years.

To my wife, Jane, my love and a question: now that I'm finished too, why don't we both quit and buy that nice cabin in the woods?

Chapter 1

INTRODUCTION

1.1 Objectives

Studies of global atmospheric variability on interannual time scales have underscored the importance of the tropics. The clearest interannual signal in the troposphere is a tropical coupled ocean/atmosphere phenomenon known as El Niño / Southern Oscillation (or ENSO). The ENSO signal shows up as the dominant mode of interannual variability in studies of tropical surface variables (Kidson, 1975); Pacific Ocean sea surface temperature (Weare et al., 1976), and tropical upper tropospheric winds (Arkin, 1982). The ENSO signal has also been shown to be correlated with interannual variability in middle latitudes (Horel and Wallace, 1981).

Observational studies of interannual variability and ENSO generally fall into one of two categories: studies of near-surface variables (wind, temperature, pressure, and rainfall), or studies of upper tropospheric variables. Early studies of ENSO, beginning with the original identification of the Southern Oscillation by Walker (1924), were restricted to the former category. As interest grew and data sets became more comprehensive, a fairly complete and detailed picture has emerged of the evolution and structure of ENSO-associated anomalies near the surface (Rasmusson and Carpenter, 1982).

Documentation of the upper tropospheric component came later. Horel and Wallace (1981) presented evidence for global-scale correlations of the geopotential height field at 200 mb with the Southern Oscillation. In the tropics, most studies have been restricted to the 200 mb level

(e.g. Arkin, 1982, and Selkirk, 1984), where analyzed wind fields are most reliable.

Modeling studies pertaining to ENSO and interannual variability may also be divided into two groups: ocean models (with parameterized atmospheric forcing), and atmosphere models (with parameterized ocean forcing). Early models describing the anomalous ocean circulation associated with ENSO (e.g. McCreary, 1976) were driven by a prescribed surface wind stress. More sophisticated coupled models, such as that developed by Zebiak (1984), allowed anomalies of the surface wind field and oceanic mixed layer to feed back upon each other. However, the atmosphere above the surface in this model was heavily parameterized by assuming a fixed vertical structure for atmospheric wind anomalies.

Models of the atmosphere's response to oceanic El Niño conditions have concentrated on the stationary response in the upper troposphere. This emphasis has been due in large part to the interest in the distant atmospheric mid-latitude response, which is most evident in the upper troposphere on long time scales. The coupling between the surface and upper troposphere can be specified in several ways. The simplest models merely fixed the vertical structure (e.g. the barotropic model of Hoskins et al., 1977). Models with more vertical resolution (e.g. the five-layer baroclinic model of Hoskins and Karoly, 1981) were forced by a prescribed tropical heating anomaly of fixed vertical structure. Alternatively, the sensitivity of the response of a model with fixed vertical structure could be tested by changing that vertical structure arbitrarily (Lim and Chang, 1983). A more complicated primitive equation model was used by Geisler (1981) to examine vertical structure variability, but it was again necessary to assume a prescribed vertical

heating profile. Finally, sophisticated atmospheric models could allow the atmosphere to respond directly to prescribed sea surface temperature anomalies via interactive precipitation and three-dimensional wind fields (e.g. the general circulation model simulation of Shukla and Wallace, 1983). The vertical structure of the equilibrium response then depended on the model's treatment of clouds, convection, and the planetary boundary layer.

Verification of the validity of these models is made complicated by the uncertainty in choosing an appropriate vertical structure for large-scale heating. Yanai et al. (1973) derived a heating profile with a broad maximum near 400 mb based on synoptic data from the western Pacific. Hantel and Baader (1978) derived a similar profile from zonally averaged data. Schneider and Lindzen (1977) proposed a profile with a maximum near 300 mb. Houze (1982) derived a profile with a sharper maximum near 300 mb, with no net heating below 500 mb.

The vertical structure of the variability of the tropical atmosphere represents a major uncertainty - an uncertainty largely unaddressed by the observational studies to date. This thesis describes an observational study of the three-dimensional structure of tropical wind fluctuations on seasonal time scales, using data from a network of radiosonde stations in low latitudes.

Chapter 2 describes the climatological structure of the wind field, examining in turn the annual mean, the annual cycle, and the semiannual cycle. Comparison of the vertical structure of seasonal and interannual wind fluctuations is of interest because near the equator both are thought to be primarily responses to the geographical distribution of latent heat release (Ramage, 1968; Webster, 1972). Furthermore, the

annual cycle appears to be coupled to interannual variability, since a notable feature of ENSO is its tendency to be 'phase-locked' to the annual cycle (Rasmusson and Carpenter, 1982).

The climatology of the near-equatorial band from Trivandrum [located at 8°N 77°E] eastward to Atuona [10°S 139°W] is examined in detail. This region encompasses the 'Walker Circulation' (Bjerknes, 1969), a zonally oriented mass circulation cell whose fluctuations are closely associated with the Southern Oscillation (Julian and Chervin, 1978).

Interannual variability is considered in Chapter 3. First, the magnitude of interannual variance is documented for zonal and meridional wind components throughout the tropical troposphere, and compared to the variance contained in the annual and semiannual cycles. Characteristic vertical structures of interannual variability are found through one-dimensional empirical orthogonal function (1dEOF) analyses carried out separately for each station and season.

The three-dimensional structure of interannual variability is considered in Section 3.4. We show that the ENSO signal is correlated with time series of the dominant vertical modes of seasonal wind variability, and conversely that the vertical structure of ENSO-related interannual tropical wind variability is concisely described by the 1dEOF modes.

A separate empirical orthogonal function analysis is carried out for seasonal zonal wind anomalies at the network of near-equatorial stations between Trivandrum and Atuona. This 2dEOF analysis describes fluctuations of the Walker Circulation in terms of standing oscillations in the longitude-height plane. The time series of principal components associated with the first two modes of the analysis are correlated with each other at lag, and both are correlated with the Southern Oscillation, in-

dicating that the seasonal zonal wind fluctuations over this network are best described as a propagating anomaly which is associated with the Southern Oscillation.

Seasonal wind anomalies over the Trivandrum-Atuona network during El Niño events are examined in detail in Chapter 4. The results of the 2dEOF analysis are confirmed and extended by a complex empirical orthogonal function (CEOF) analysis, which explicitly includes both standing and propagating oscillations. In addition, wind anomalies composited from five El Niño events show an eastward-propagating feature which is clearly evident in the season prior to the onset of the oceanic El Niño.

Chapter 5 presents a summary of the results and principal conclusions. Separate brief discussions of the theory of empirical orthogonal functions, and statistical significance considerations, are contained in appendices.

1.2 Data

The monthly mean observations used in this study were obtained from Monthly Climatic Data for the World, archived on tape at the National Center for Atmospheric Research (Jenne and Crutcher, 1976). Station data were chosen for this study rather than an analysis product to maximize data reliability and increase the length of the time series. Analysis products have been used to study surface winds (e.g. Rasmusson and Carpenter, 1982; Barnett, 1983), where the number of observations is much greater than at upper levels, and 200 mb winds (Arkin, 1982; Selkirk, 1984), where cloud top movement and aircraft data can be used to enhance the analysis. At other levels, however, the tropics present

special problems that make interpolation schemes difficult, and their output questionable. First, the density of the data network is much lower than in midlatitudes. Furthermore, the condition of quasi-geostrophy which is used to constrain the wind field in mid-latitude objective analysis schemes is not satisfied in the tropics; the divergent component of the flow is typically quite important. Hence, although gridded data offer obvious advantages of computational ease and spatial resolution (spurious though it may be), we prefer to base this study on station data directly.

A list of the stations used, with a summary of each station's record, is presented in Table 1.1. A map labelling the stations is shown in Fig. 1.1. These 34 stations each had a record at least seven years long. Data at six levels (850, 700, 500, 300, 200, and 150 mb) were considered. The data record extends through the end of 1980.

Data quality was checked carefully. For each station, the following steps were taken in the course of calculating seasonal means. First, duplicate records, and records with one or more of the six levels of interest missing, were removed from the time series. Then, the mean and variance at each level for each calendar month were computed. These statistics were used to calculate time series of monthly anomalies, and anomalies normalized by standard deviation. The time series were examined for suspicious data, with special attention paid to observations departing from the calendar monthly mean by more than three standard deviations. A similar technique was employed by Trenberth and Paolino (1980) to identify suspicious values in time series of monthly mean sea level pressure.

Attempts were made to check suspicious data against two independent

TABLE 1.1

Stations used and period of record for each wind time series.

Station name	WMO #	latitude	longitude	period of record
Abidjan	65578	5.3°N	3.9°W	Jan 64 - Oct 80
Antofagasta	85442	23.5°S	70.4°W	Aug 57 - Dec 80
Atuona	91925	9.8°S	139.0°W	Apr 69 - Jan 80
Bangkok	48455	13.7°N	100.5°E	Jan 57 - May 80
Belem	82193	1.4°S	48.5°W	Aug 68 - Jun 75
Bogota	80222	4.6°N	74.1°W	Sep 60 - Dec 79
Calcutta	42809	22.5°N	88.4°E	Apr 64 - Dec 80
Canton	91700	2.8°S	171.7°W	Jan 57 - Aug 67
Cocos	96996	12.1°S	96.9°E	Jul 64 - Nov 80
Dakar	61642	14.7°N	17.5°W	Jan 64 - Dec 80
Dar es Salaam	63894	6.9°S	39.2°E	Jun 61 - Dec 77
Darwin	94120	12.4°S	130.9°E	Jul 64 - Nov 80
Fort Lamy	64700	12.1°N	15.0°E	Jun 64 - Dec 78
Hilo	91285	19.7°N	155.1°W	Jan 57 - Dec 80
Johnston	91275	17.0°N	169.5°W	Jan 59 - Dec 80
Khartoum	62721	15.6°N	32.6°E	Jan 64 - Dec 80
Koror	91400	7.3°N	134.5°E	Sep 57 - Dec 80
Kota Kinabalu	96471	6.0°N	116.1°E	Mar 68 - Dec 80
Lae	94027	6.7°S	147.0°E	Sep 64 - Dec 73
Lima	84628	12.0°S	77.1°W	May 67 - Dec 80
Majuro	91376	7.1°N	171.4°E	Jan 59 - Dec 80
Miami	72202	25.8°N	80.3°W	Jan 57 - Oct 77
Nairobi	63741	1.3°S	36.8°E	Feb 58 - Dec 80
Natal	82599	5.9°S	35.3°W	Jan 68 - Dec 80
Noumea	91592	22.3°S	166.5°E	Jul 64 - Dec 80
Pago Pago	91765	14.3°S	170.6°E	Apr 66 - Dec 80
Port Sudan	62641	19.6°N	37.2°E	Jan 64 - Dec 75
San Andres	80001	12.8°N	81.7°E	Jun 57 - Feb 80
Singapore	48694	1.3°N	103.9°E	Mar 60 - Dec 80
Tahiti	91938	17.6°S	149.6°E	Jan 64 - Dec 80
Trinidad	78970	10.7°N	61.5°E	Aug 67 - Dec 80
Trivandrum	43371	8.5°N	77.0°E	Jan 63 - Dec 80
Truk	91334	7.5°N	151.9°E	Sep 57 - Dec 80
Veracruz	76692	19.2°N	96.1°W	Feb 64 - Dec 80

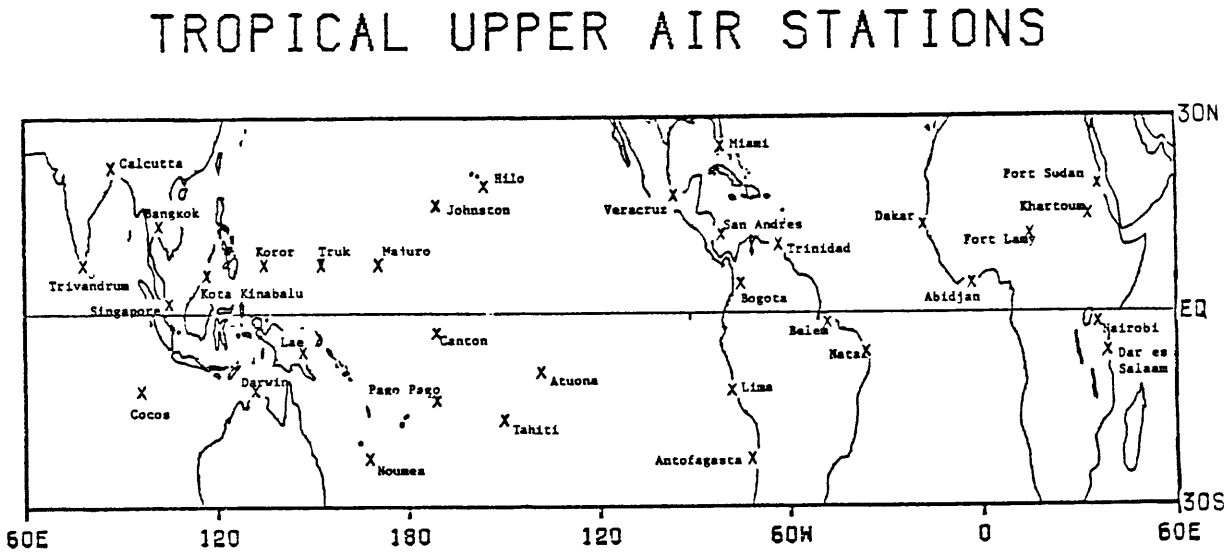


Figure 1.1 - Station network, with names and locations of the 34 stations used in this study.

sources: the monthly-averaged National Meteorological Center (NMC) Tropical Analysis of 200 mb winds for the period 1968-1974 (obtained from the NMC Climate Analysis Center by R. Newell and H. Selkirk) and an atlas of monthly-averaged 200 mb and 850 mb streamfunction fields for the period 1965-1974 (Krishnamurti et al., 1983). Contemporaneous reports from nearby stations were also considered in some cases.

A conservative approach to data rejection was maintained. Only values which appeared to be extremely outlandish were eliminated from the time series. In some cases, the source of error was obvious (e.g., units digit dropped from the reported wind direction) and corrected values substituted into the time series. Erroneous records without readily identifiable corrections were eliminated from the time series without substitution.

This process of error identification and removal or correction was subjective, but it has produced reliable time series of maximum duration. Some of the errors encountered did not represent anomalies of greater than three standard deviations, but were clearly incorrect nevertheless. For example, the 3σ criterion did not satisfactorily flag anomalous data for cases in which two anomalous reports existed in the series for a single level and calendar month, which simply caused the variance to be so large that all data represented "acceptable" normalized anomalies. The corrected time series probably still contain some errors. However, we firmly believe that the results presented here are statistically reliable and represent real signals.

The corrected time series of monthly means were used to calculate seasonal means, which form the basis for most of the statistics of interannual variability presented in the thesis. Months were grouped

into seasons in standard fashion: December-January-February (generally referred to as DJF), March-April-May (MAM), June-July-August (JJA), and September-October-November (SON). If one month was missing from a season, the seasonal mean refers to an average over the two available monthly means with climatology assumed for the missing month; if two or three months were missing, no seasonal mean was calculated. The number of seasonal average values obtained at each station are plotted in Fig. 1.2 for each calendar season. For most stations and seasons, more than 15 years of data are present, encompassing three or more El Niño events.

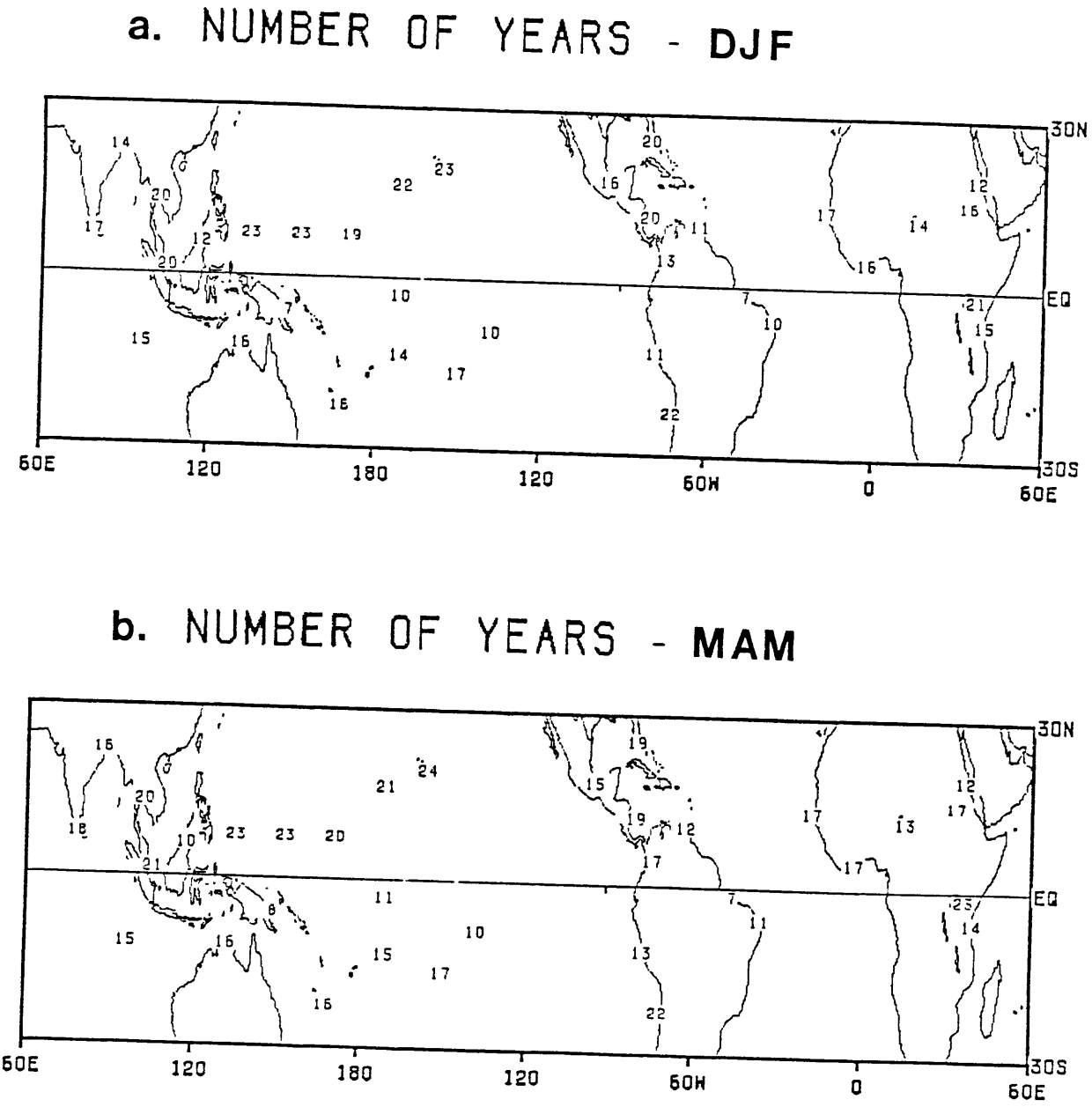
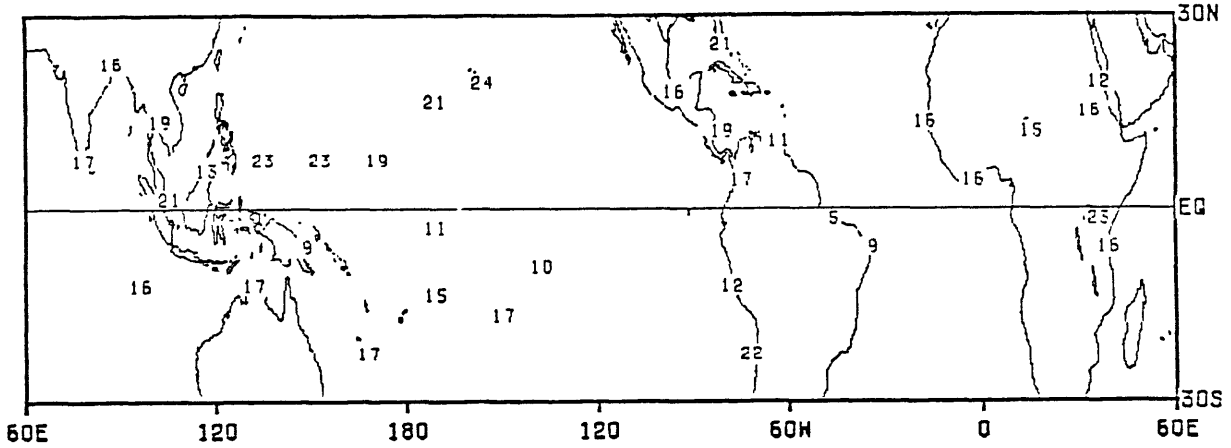


Figure 1.2 - Number of mean observations available at each station for each season. (a) DJF season. (b) MAM season.

c. NUMBER OF YEARS - **JJA**



d. NUMBER OF YEARS - **SON**

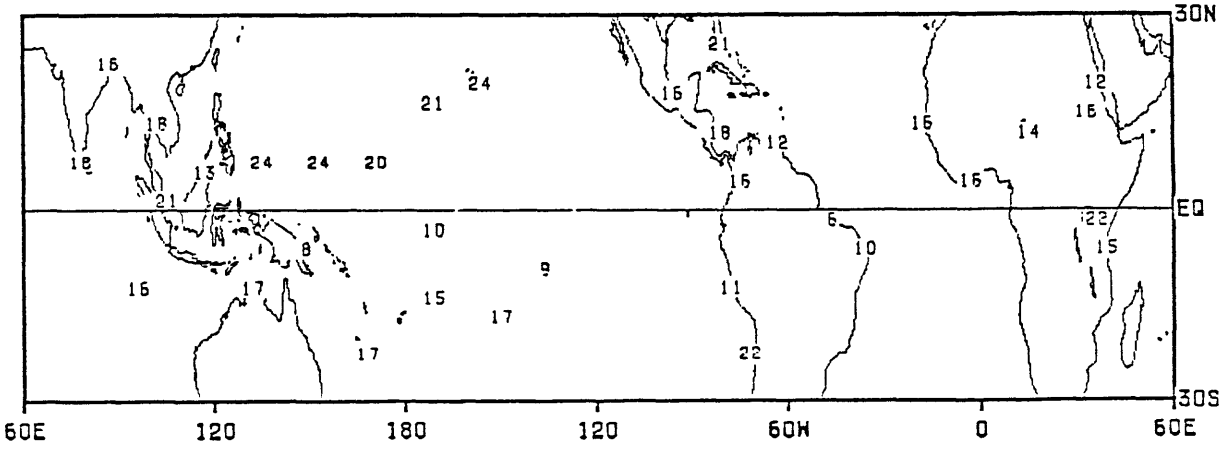


Figure 1.2 (continued) - Number of seasonal mean observations available at each station for each season. (c) JJA season. (d) SON season.

Chapter 2

THE ANNUAL VARIABILITY OF TROPICAL WINDS

2.1 Introduction

In this chapter, the annual variability of climatological monthly-averaged winds is examined. Knowledge of the annual variability is prerequisite to a study of anomalous conditions. This is particularly true in the tropics, for several reasons.

First, nonlinearity is crucially important in air-sea coupling. The zonal asymmetries in both the mean and anomalous wind fields are thought to be determined primarily by the geographical distribution of latent heating. Webster (1972) reproduced many of the observed features of the mean flow in a two-level model with a zonally symmetric basic state taken from observations, and idealized steady forcing designed to simulate the observed tropical latent heat distribution. He then studied the response of the model to additional imposed forcing from middle latitudes by fixing the longitudinal distribution of meridional wind at 40° latitude to agree with climatological values, and found improved reproduction of the observed standing eddies in the subtropics (Webster, 1973). Webster concluded that near the equator, the asymmetries in the mean winds are forced primarily by near-equatorial latent heating, while remote forcing predominated closer to the lateral boundaries of his model. A subsequent study of interannual variability using a coupled ocean/atmosphere model (Zebiak, 1984) required the surface convergence associated with both the mean and anomalous wind fields in order to obtain adequate El Niño simulations. Although Zebiak's model explicitly

calculated only the anomalous circulation, prior prescription of a realistic annual variability was necessary in order to obtain a realistic forced response.

Second, the tropical circulation (unlike middle latitudes) exhibits considerable persistence from season to season, so that much of the anomalous variability occurs on time scales similar to the annual variability.

Third, a striking feature of interannual variability associated with El Niño / Southern Oscillation is its "phase-locking" to the annual cycle (Rasmusson and Carpenter, 1982), directly suggesting the coupling between annual and interannual variability.

The annual variability of surface parameters in the tropics has been extensively documented, particularly over the Pacific Ocean region. Atlases of ship observations of surface variables and satellite-observed cloudiness for the tropical Atlantic and Pacific Oceans have been compiled by Hastenrath and Lamb (1978) and Weare et al. (1980), respectively. Horel (1982b) reviewed and updated the observed annual cycles of surface wind, sea level pressure, sea surface temperature, and rainfall over the Pacific. He demonstrated the important modulating role of the ocean on the annual cycle of atmospheric surface variables.

Paucity of data has limited the scope of studies of variability above the surface. Several investigators, including Newell et al. (1972), Gray et al. (1976), and Oort (1983), have plotted seasonal mean wind fields at standard levels for each season, from which the gross features of the annual variability could be surmised. Newell et al. (1972) and Oort (1983) used station data similar to the network used

here, interpolating across large data-void areas to create maps. Gray et al. (1976) used the National Meteorological Center's tropical strip analysis to define climatology.

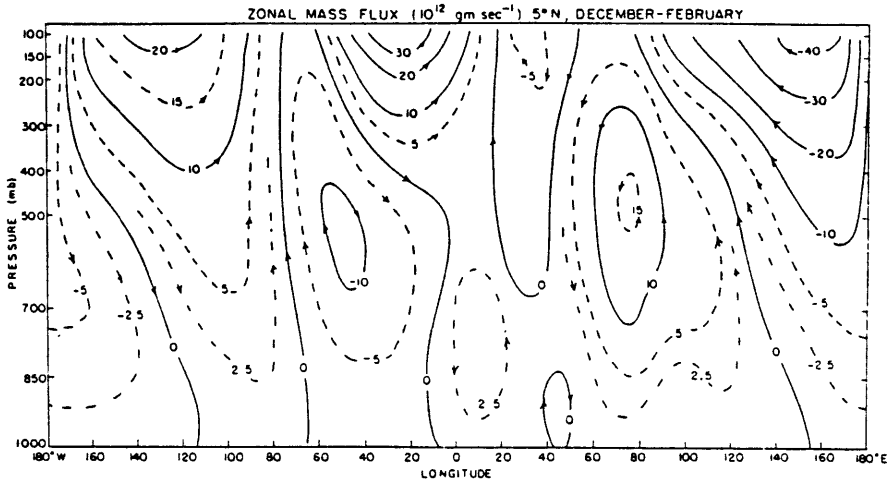
The flux of mass associated with zonal convergence and divergence over the western equatorial Pacific is known as the Walker Circulation. It was named by Bjerknes (1969) after Sir Gilbert Walker, who first documented the associated zonally oriented surface pressure oscillation over the Pacific (Walker, 1924). Newell et al. (1974) defined the Walker Circulation using a diagnostic quantity called the zonal mass flux, calculated from

$$M_z^*(p) = \int_{p_0}^{p} u^* \left(\frac{a\delta\phi}{g}\right) dp \qquad [2.1]$$

where u^* is the zonal wind with the zonal mean zonal wind subtracted out, a is the earth's radius, g represents gravitational acceleration, and $\delta\phi$ is the latitudinal width of the domain. The zonal mean wind was removed in order to separate the zonally symmetric motions (which Newell et al. defined as the Hadley circulation) from the zonally asymmetric motion (defined as the Walker circulation).

The climatological zonal mass fluxes calculated from [2.1] for a latitudinal strip of width 10° centered on 5°N for the DJF and JJA seasons, taken from Newell et al. (1974), are shown in Fig. 2.1. Since M_z^* approximates a stream function (to the extent that v is negligible), the contours of M_z^* in the longitude-height plane delineate zonal and vertical motions. Hartmann et al. (1984) noted the westward tilt with height of the DJF mass flux between 100°E and 160°E (Fig. 2.1a), and argued that this tilt was evidence for an elevated vertical profile of heating (Houze, 1982). Notice that no such tilt is evident in the JJA

a.



b.

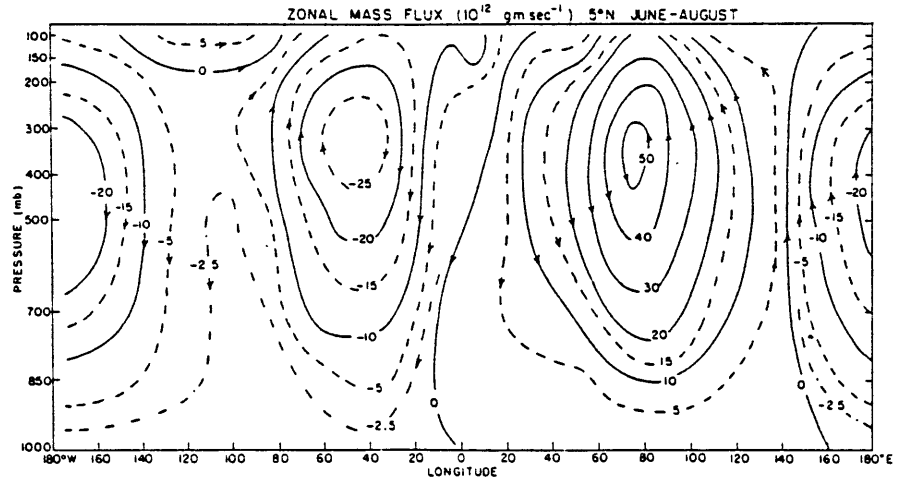


Figure 2.1 - Eastward zonal mass flux for a 10° latitudinal strip centered on 5°N, based on departures from the zonal mean zonal wind (taken from Newell et al., 1974).

(a) DJF season.
(b) JJA season.

zonal mass flux (Fig. 2.1b).

Subtraction of the zonal mean is convenient mathematically, but is not necessarily the best way to define the Walker Circulation over the Pacific. Studies of interannual variability are complicated by using zonal wind departures because the zonal mean itself has considerable interannual variability. A more fundamental physical problem derives from recent work by Zebiak (1984), who modeled ENSO variability as a local Pacific Ocean phenomenon. If Zebiak is correct, there is no basis for defining the Walker Circulation using departures from a zonal average. Therefore, the Walker Circulation is defined in this thesis by calculating the zonal mass flux using the zonal wind with the zonal mean included, that is

$$M_z(p) = \int_{p_0}^{p} -u \left(\frac{a\delta\phi}{g}\right) dp \approx \sum_{l=1}^{L} -u_l \, p_l \left(\frac{a\delta\phi}{g}\right) \qquad [2.2]$$

where p_l is the pressure thickness of the layer associated with each pressure level (given in Table 1 of Appendix B). The sign of M_z is reversed in [2.2] relative to [2.1] so that the westward mass flux of the Walker Circulation will appear as a positive M_z cell.

The semiannual cycle of zonal winds in the tropics was examined by van Loon and Jenne (1969, 1970). They noted that the semiannual cycle accounted for most of the annual variability in the tropical upper troposphere. The phase of this harmonic varied only slightly with longitude, having westerly wind maxima at 200 mb in May and November in the tropics and throughout the Southern Hemisphere. A phase reversal was observed near the equatorial tropopause, so that westerly wind maxima in the lower stratosphere occurred in February and August. Similar semiannual cycles were found in the temperature field of the troposphere

near the equator (with May-November maxima) and subtropical Southern Hemsiphere over Australia (with February-August maxima), and in the latitude of the axis of the Southern Hemisphere subtropical jet stream (positioned furthest equatorward in May and November). Van Loon and Jenne concluded that these semiannual cycles were related manifestations of the back-and-forth seasonal movement of the Hadley circulation.

The first principal aim of this chapter is to reproduce and synthesize previous results, presenting a unified, three-dimensional description of the annual variability of tropical winds. The questions to be addressed are very basic: How large is the magnitude of the annual mean wind compared with the amplitudes of the annual and semiannual cycles (i.e. how much seasonality exists in the tropics)? Are the results of surface wind studies applicable to higher levels? What are the vertical structures of the important periodic fluctuations in the tropical wind field, the semiannual cycle in the zonal component and the annual cycle in the meridional component?

Secondly, the documentation of annual variability in this chapter is developed in order to answer important questions concerning interannual variability in subsequent chapters. Without adequate resolution of the seasonal cycle, the interannual variability calculations to follow cannot be properly interpreted.

The annual variability of the wind at different stations and levels will be treated here in terms of annual and semiannual cycles, and also in terms of the month-by-month march of climatology without regard to Fourier decomposition. For clarity, the word 'cycle' will be reserved for Fourier harmonics. Hence, the annual cycle and semiannual cycle refer strictly to Fourier harmonics with periods of twelve and six

months, respectively. Cycles have well-defined amplitudes and phases. The word "variability" is used more generally here. In middle latitudes, the annual variability is almost completely described by the annual mean and annual cycle. In the tropics, however, the semiannual cycle has substantial amplitude as well.

Section 2 of this chapter discusses the annual mean wind field in the tropics by examining maps of the vector wind at each pressure level over the entire tropical network. The annual mean Walker Circulation is then considered separately in terms of the zonal mass flux, calculated from [2.2], over a near-equatorial zonal cross-section extending from Trivandrum at the southern tip of India to Atuona in the mid-Pacific. Section 3 then considers the annual and semiannual cycles of the wind field at each level. The vertical structure and geographical distribution of these cycles are documented. Section 4 discusses the annual variability of the wind field over the western Pacific in detail, showing the transition from a monsoonal climatological regime near Asia to a trade wind regime over the mid-Pacific, and the climatological seasonal migration of the Walker Circulation. A summary of the results in Section 5 concludes the chapter.

2.2 Annual mean winds

Vector plots of the annually averaged wind at each station are shown in Fig. 2.2 for each of the six pressure levels. The length of each vector represents the speed of the wind, with each vector centered on the station location. The length scale is the same for each plot to facilitate comparison. No smoothing, contouring, or interpolation has been implemented.

Figure 2.2

(a) Annual mean wind at 850 mb, with the wind speed represented by the length of each vector. The mid-point of each vector corresponds to the station location.

(b) As in (a), but for 700 mb.

(c) As in (a), but for 500 mb.

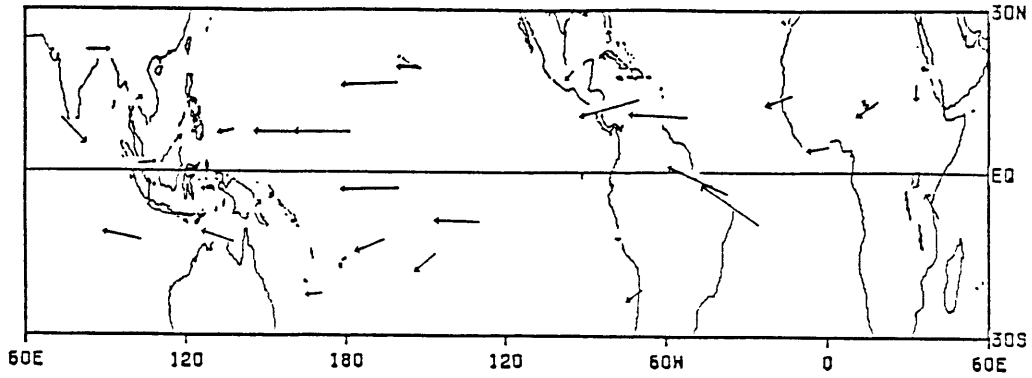
(d) As in (a), but for 300 mb.

(e) As in (a), but for 200 mb.

(f) As in (a), but for 150 mb.

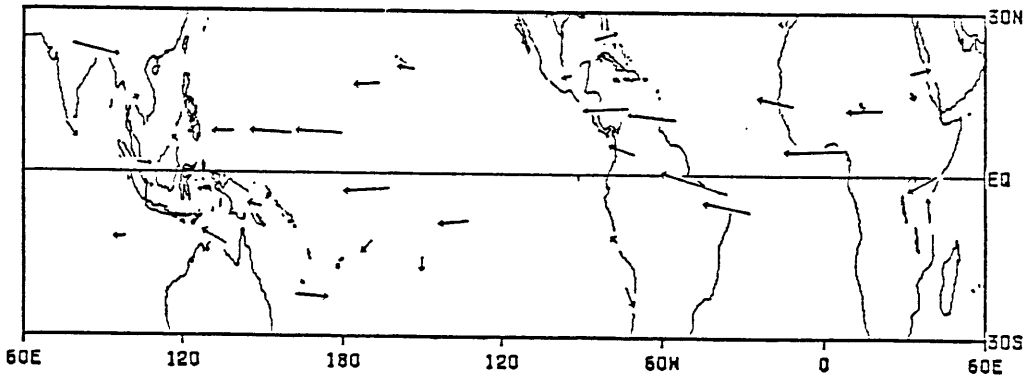
a. ANNUAL MEAN 850 MB

SCALE: ——— = 10 M/S



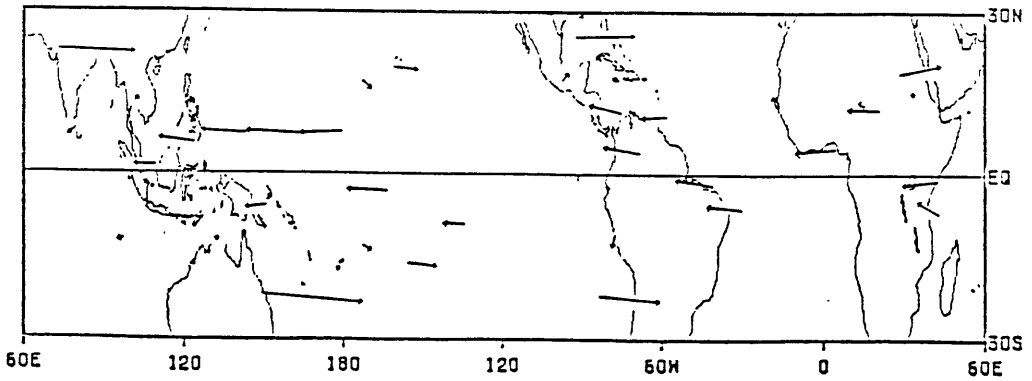
b. ANNUAL MEAN 700 MB

SCALE: ——— = 10 M/S



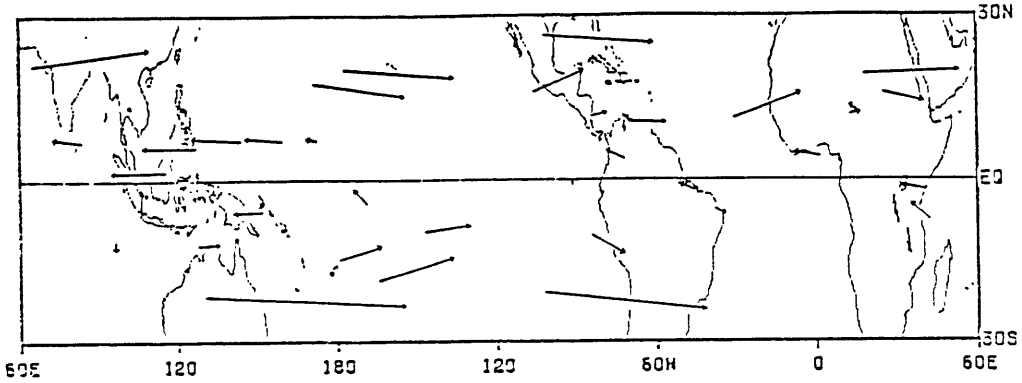
c. ANNUAL MEAN 500 MB

SCALE: ——— = 10 M/S



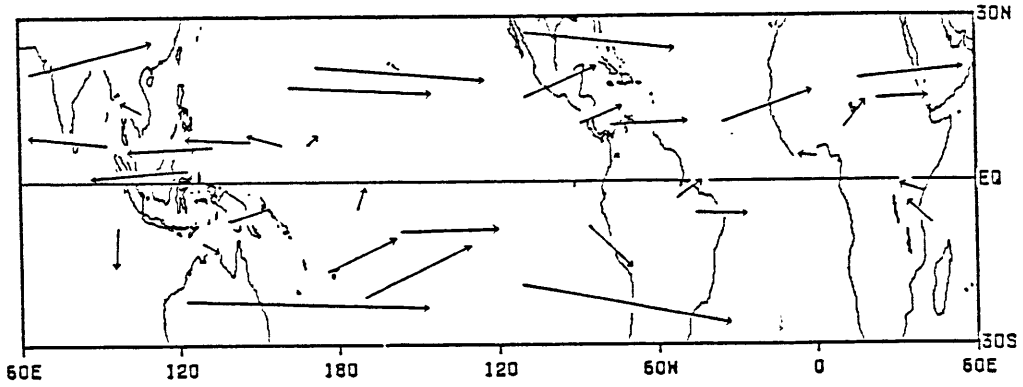
d. ANNUAL MEAN 300 MB

SCALE: ——— = 10 M/S



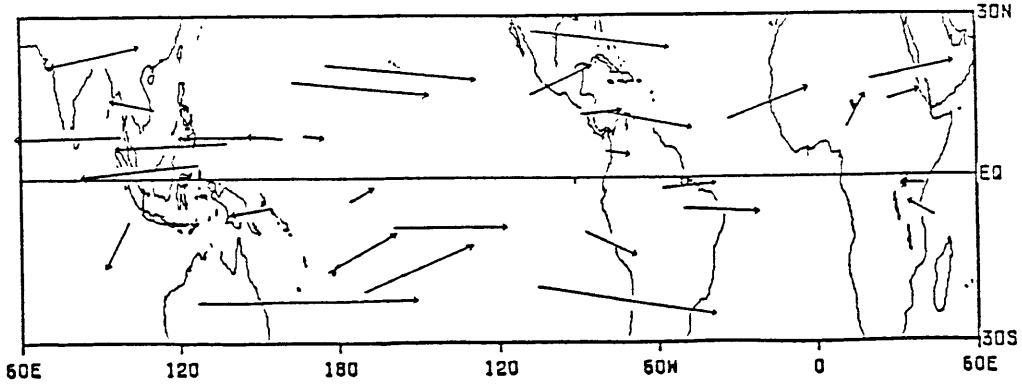
e. ANNUAL MEAN 200 MB

SCALE: ——— = 10 M/S



f. ANNUAL MEAN 150 MB

SCALE: ——— = 10 M/S



At 850 mb , the winds have an easterly component everywhere except over Southeast Asia. The tropical Pacific easterlies all have speeds between 5 and 10 m/s, showing the uniformity of the trade winds near the top of the marine boundary layer. Over most of the Pacific, the annual mean of the 850 mb zonal wind component has much greater magnitude than the total variability of monthly means, a feature also noted by Horel (1982b) in the Pacific surface wind field.

However, great caution must be exercised in extrapolating from the 850 mb level to the surface or vice versa. Harrison and Gutzler (1985) compared monthly wind climatologies at 850 mb and the surface for five western Pacific islands, and found significant climatological wind shears which varied widely with location and (to a lesser extent) with season. In particular, the magnitude of the meridional wind component was found to be much smaller at 850 mb compared with the surface.

At higher levels, the subtropics in both hemispheres are marked by strong westerly shear with height up to 300 mb (as, for example, at Noumea [22°S 166°E] and Hilo [20°N 155°W]). Equatorial regions, where the annually averaged meridional temperature gradients are slight, show little vertical wind shear.

The meridional component of the annual mean wind is small. Over the South Central Pacific at Tahiti [18°S 150°W] and Pago Pago [14°S 171°W], southerly winds at 850 mb occur coincident with a strong annual mean sea surface temperature gradient separating warm western Pacific waters from the cooler eastern Pacific (Horel, 1982b).

In the upper three levels (between 300 and 150 mb), the wind field has almost no directional vertical shear at all. Easterly winds prevail over the western Pacific and equatorial Africa, with westerlies

elsewhere. Troughs over the subtropical eastern Pacific in both hemispheres are clearly discernable. Strong westerlies occur poleward of 200 latitude in both hemispheres, where the annual mean mid-tropospheric meridional temperature gradient is strongest (Oort, 1983).

From Africa westward into the eastern Pacific, the meridional wind field at 850 mb (and to a lesser degree at 700 mb) converges into the annual mean Intertropical Convergence Zone, located approximately at 5°N. Dividing the bands of annual mean westerlies and easterlies in equatorial latitudes at 850 mb are regions of convergence and divergence of the zonal wind. The winds converge in the vicinity of 120°E, over the maritime continent, and diverge around Africa, in a data-sparse area. The wind reversal at upper levels over the Pacific is shifted longitudinally about 60° to the east, so that the center of equatorial Pacific divergence is located near the dateline. Therefore, the longitudinal extent of westerlies along the equator is 60° greater in the upper troposphere than near the surface.

Fig. 2.3a shows the annual mean vector wind at stations in the Trivandrum-Atuona cross-section, plotted as a function of longitude and height. The station names (abbreviated) are shown along the top of the plot, and the six pressure levels included in the mean soundings appear on the right side. It is apparent that $|v| << |u|$ throughout the cross-section, with the exception of the near-surface layer at Trivandrum and the upper troposphere at Atuona. In the interior of the cross-section, the neglect of v seems justified.

The annual mean zonal mass flux, computed from [2.2], is shown in Fig. 2.3b. The curves were drawn using a bilinear interpolation scheme. Westward mass transport is associated with positive values of $\partial M/\partial z$.

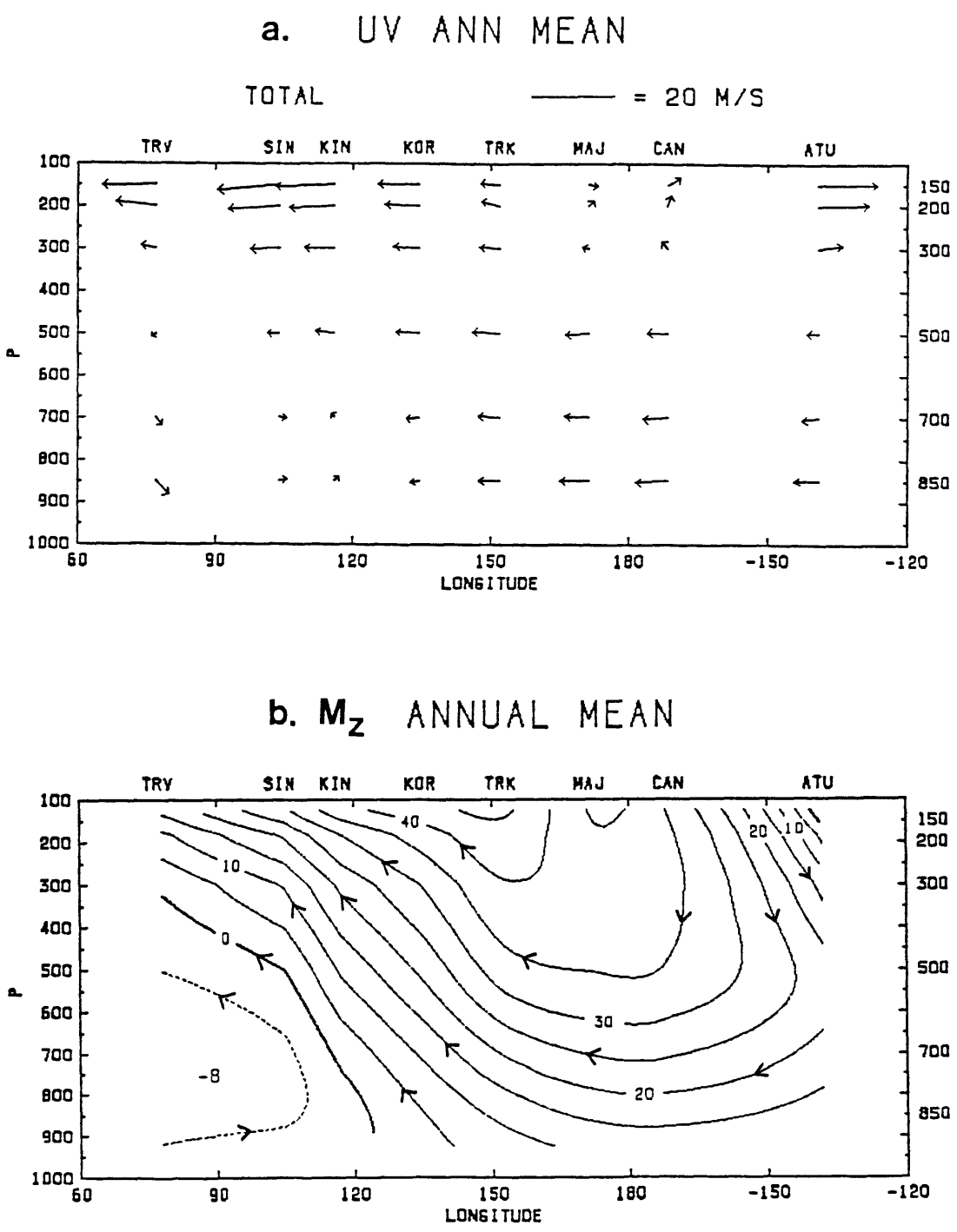


Figure 2.3 - (a) Annual mean vector wind at eight stations near the equator over the eastern Indian and western Pacific Oceans. (b) Westward zonal mass flux based on the zonal winds shown in (a). Contour interval 5×10^9 kg/sec, with negative contours dashed.

Invoking continuity of mass, upward mass transport must be associated with positive values of $\partial M/\partial x$. Hence, the annual mean Walker Circulation shown in Fig. 2.3b transports mass downward between Canton and Atuona, then westward in the lower half of the troposphere across the date line, and upward over the western Pacific. The zero lines in Fig. 2.3b are located where the zonal wind on a constant pressure surface changes sign. Therefore, the shifts with height of the position of large-scale convergence and divergence noted in Fig 2.3a appear as tilts in the zonal mass flux. The annual mean Walker Circulation has a pronounced westward tilt with height between 90°E and 180°, and has the same magnitude and vertical structure as the Newell et al. (1974) M_z^* field for DJF (Fig. 2.1a).

2.3 Annual and semiannual cycles

The annual and semiannual cycles of zonal and meridional winds were calculated from the monthly mean climatology at each station. The cycles were defined as the Fourier harmonics with period 12 months (annual cycle) and 6 months (semiannual cycle), defined from the 12-point time series of climatological winds. The statistics are summarized in Table 2.1. For each station and pressure level, separate statistics are tabulated for zonal (u) and meridional (v) wind components. For each component, the leftmost column contains the annual mean wind (units m/s, westerly/southerly winds positive). The next four columns contain the amplitude and phase of the annual (M_1) and semiannual (M_2) cycles, where the amplitudes have units m/s, and the phase refers to the month of maximum westerly/southerly wind. The next column, labelled VAR12, is the total variance contained in M_1 and M_2, that is

$$VAR12 = (R_1^2 + R_2^2) / 2$$

where R_1 and R_2 are the amplitudes of M_1 and M_2, respectively. Table 2.1 is included here for completeness. In order to describe the variability, vector plots of M_1 and M_2 are presented for each wind component and pressure level.

Vector plots of the annual cycle of the zonal wind component $M_1(u)$ at each station are shown in Fig. 2.4 for each of the six pressure levels. An analogous set of plots for $M_1(v)$ appears in Fig. 2.5. The length of each vector represents the magnitude of the harmonic, and the phase is indicated by the vector orientation. A vector directed southward indicates a maximum in the annual cycle (i.e. maximum westerlies) centered on the January monthly mean. The phase progression proceeds clockwise, so that a vector directed westward indicates a maximum in the annual cycle centered on the April monthly mean, etc. (i.e. vectors directed southward, westward, northward, and eastward correspond to annual cycle maxima on January 15, April 15, July 15, and October 15, respectively).

Consider first the annual cycle of the zonal wind at 850 mb (Fig. 2.4a). The magnitude of the annual cycle is greatest in the vicinity of Southeast Asia and Indonesia, where it exceeds 5 m/s. The annual cycle here is larger than the annual mean, so that the climatological winds reverse with season, being westerly during JJA and easterly during DJF. Moving eastward into the Pacific, the magnitude of the annual cycle decreases and the time of weakest easterlies is later in the year. Since the magnitude of the annual mean increases between Southeast Asia and the mid-Pacific (Fig. 2.2a), the western Pacific is a transition zone where the monsoonal regime near the Asian continent gradually

TABLE 2.1

Annual mean and variability of zonal and meridional wind components for each station and pressure level. AVG = Annual mean; M1 = Annual cycle; M2 = Semiannual cycle; VAR12 = variance associated with the annual + semiannual cycles. Units: AVG, AMP = m/s; VAR12 = m^2/s^2; PHASE = month of year.

ANNUAL VARIABILITY ALL YEARS

		U						V					
		AVG	M1		M2		VAR12	AVG	M1		M2		VAR12
			AMP	PHASE	AMP	PHASE			AMP	PHASE	AMP	PHASE	
ABIDJAN	850	-2.5	2.4	7.1	1.8	1.9	4.5	-0.5	1.6	6.0	0.6	4.8	1.4
	700	-7.5	2.8	8.3	2.6	1.7	7.3	-0.3	0.9	8.0	0.1	0.6	0.4
	500	-5.0	0.6	7.7	1.2	2.0	0.9	-0.3	0.7	1.9	0.5	5.1	0.4
	300	-3.3	7.6	1.4	1.1	6.0	27.0	0.5	1.9	0.9	0.7	5.5	2.0
	200	-2.3	12.4	1.2	2.4	5.6	79.4	0.2	2.2	1.7	0.4	2.8	2.6
	150	0.0	11.5	0.8	2.6	5.6	69.8	1.3	2.6	1.7	1.1	2.1	4.0
ANTOFAGA	850	-1.9	0.1	2.2	0.1	1.9	0.0	-1.4	1.0	7.3	0.1	1.0	0.5
	700	1.1	1.4	7.6	0.1	1.8	1.0	-2.5	0.9	1.3	0.2	0.6	0.4
	500	7.7	5.4	7.6	0.6	4.2	14.5	-0.7	1.6	1.3	0.3	5.6	1.3
	300	20.1	8.2	7.8	1.8	4.3	35.4	-2.2	1.5	5.9	0.3	2.7	1.2
	200	26.0	8.8	7.7	3.5	4.4	45.1	-4.7	5.7	6.7	1.1	1.8	16.9
	150	22.3	8.0	7.5	3.5	4.6	38.5	-3.4	4.6	6.6	0.4	1.8	10.6
ATUONA	850	-5.5	0.1	11.9	0.5	4.4	0.1	0.2	0.7	6.3	0.5	3.4	0.3
	700	-3.7	0.9	8.1	1.0	4.3	1.0	-0.4	0.3	8.0	0.2	3.7	0.1
	500	-2.7	1.5	11.7	0.9	4.0	1.6	0.1	0.5	7.7	0.4	0.6	0.2
	300	5.5	1.1	10.7	0.8	3.8	0.9	0.7	1.5	11.9	1.2	1.1	1.9
	200	11.9	1.5	12.1	1.1	2.8	1.7	0.2	2.1	12.1	2.0	0.9	4.2
	150	14.0	4.1	1.2	1.4	2.2	9.5	0.0	1.1	11.6	1.3	1.0	1.4
BANGKOK	850	0.9	6.2	6.4	2.4	1.5	21.9	0.7	1.7	4.3	0.4	2.3	1.5
	700	0.6	4.3	6.6	3.1	1.2	14.1	0.5	0.8	5.0	0.3	6.2	0.4
	500	0.3	2.5	4.8	2.2	1.6	5.6	0.5	0.8	4.7	0.4	4.5	0.4
	300	-0.5	6.2	2.2	1.5	2.0	20.4	0.4	2.6	1.7	0.2	3.5	3.4
	200	-2.6	11.1	1.8	1.6	3.5	62.8	1.3	6.5	1.3	0.3	3.9	21.2
	150	-5.7	14.2	1.6	2.6	4.0	103.5	1.4	8.4	1.3	0.5	3.1	35.8
BELEM	850	-7.5	1.0	6.5	0.2	3.2	0.6	3.4	2.4	6.9	1.0	0.9	3.4
	700	-8.1	0.7	2.1	0.6	4.2	0.5	2.6	0.5	7.9	0.3	1.3	0.2
	500	-4.7	4.3	0.6	0.7	0.6	9.5	0.7	0.6	5.6	0.2	4.0	0.2
	300	-1.6	4.0	12.4	0.7	0.6	8.4	0.7	0.5	2.9	0.2	4.6	0.2
	200	3.1	1.4	9.9	2.1	1.4	3.1	2.2	3.3	0.6	0.8	5.2	5.7
	150	6.6	0.8	8.9	2.0	1.1	2.4	0.5	1.5	10.8	1.7	4.9	2.5
BOGOTA	850	0.0	0.0	1.0	0.0	1.0	0.0	0.0	0.0	1.0	0.0	1.0	0.0
	700	-3.1	0.8	0.8	0.5	4.1	0.4	1.1	0.7	6.7	0.4	1.8	0.4
	500	-4.6	2.5	0.9	1.8	4.5	4.8	0.7	1.3	6.7	0.3	2.1	0.9
	300	-2.5	4.2	1.1	1.3	5.0	9.5	1.1	1.8	2.4	0.3	6.2	1.7
	200	-0.4	4.0	1.6	1.6	5.8	9.1	0.4	5.7	1.6	0.8	4.3	16.8
	150	3.1	4.4	2.0	1.8	5.7	11.5	-0.4	3.0	1.3	1.1	4.4	5.2
CALCUTTA	850	2.6	2.7	2.8	0.3	0.5	3.8	0.0	3.2	6.8	0.7	2.7	5.3
	700	5.6	6.1	2.2	0.4	5.6	18.6	-1.4	3.1	8.5	0.9	2.1	5.3
	500	9.2	12.2	1.6	0.7	6.1	74.6	-0.3	1.9	8.9	0.9	1.7	2.2
	300	14.9	23.2	1.6	1.4	4.9	269.7	1.9	1.1	12.3	0.1	1.1	0.6
	200	15.5	27.8	1.5	3.3	4.6	391.3	3.8	5.3	1.1	1.2	5.4	14.7
	150	11.7	26.4	1.5	3.8	4.6	355.5	2.5	5.7	1.2	1.7	5.0	17.7

ANNUAL VARIABILITY ALL YEARS

		U						V					
		AVG	M1		M2		VAR12	AVG	M1		M2		VAR12
			AMP	PHASE	AMP	PHASE			AMP	PHASE	AMP	PHASE	
CANTON	850	-7.2	1.9	11.8	1.3	5.6	2.6	-0.2	1.0	7.8	0.3	4.1	0.5
	700	-5.6	3.4	0.7	0.9	6.2	6.1	-0.3	0.2	7.1	0.1	5.9	0.0
	500	-4.9	3.9	1.4	0.7	5.0	7.9	0.1	0.3	3.3	0.3	2.8	0.1
	300	-1.3	2.3	1.7	0.9	5.0	3.4	1.7	1.3	2.7	0.3	4.5	0.9
	200	0.9	1.9	2.4	1.3	4.7	2.6	2.7	3.8	1.8	0.4	5.5	7.2
	150	3.1	2.1	3.5	1.7	4.3	3.6	1.7	1.9	1.5	0.6	5.1	2.0
COCOS	850	-4.6	2.9	1.5	0.7	1.7	4.4	1.0	0.4	9.2	0.2	1.9	0.1
	700	-1.4	0.2	12.0	0.4	2.8	0.1	-0.1	0.2	3.3	0.5	1.5	0.1
	500	-0.8	1.0	7.2	0.7	4.8	0.7	-0.3	0.6	0.6	0.2	2.8	0.2
	300	0.1	1.0	7.3	3.3	4.7	5.9	-1.1	1.1	0.7	0.4	4.8	0.7
	200	-0.2	1.1	7.2	4.7	4.7	11.9	-4.9	2.7	1.8	0.3	2.2	3.6
	150	-2.8	1.5	7.0	6.1	4.7	19.6	-5.5	2.1	2.8	0.4	6.3	2.3
DAKAR	850	-3.2	1.6	2.8	0.5	1.8	1.4	-1.2	1.0	9.8	1.0	1.6	1.0
	700	-4.2	6.4	1.8	0.4	4.5	20.8	0.9	1.7	1.8	0.9	3.7	1.9
	500	-0.4	9.3	1.5	1.4	4.4	44.0	1.3	1.6	1.3	0.4	5.3	1.3
	300	8.2	13.7	1.6	2.5	4.7	96.6	3.0	2.8	1.3	0.5	5.8	4.1
	200	11.4	17.9	1.5	4.1	4.7	168.4	3.8	1.6	2.5	0.9	4.3	1.7
	150	10.1	17.5	1.4	6.7	4.8	176.4	3.8	1.9	3.7	0.8	4.5	2.1
DARWIN	850	-4.1	4.3	1.3	2.2	1.3	11.6	1.3	1.1	5.9	0.4	3.2	0.7
	700	-3.1	2.8	4.7	2.0	1.4	5.9	1.7	1.3	11.6	0.7	3.9	1.1
	500	0.4	1.1	6.2	0.1	6.3	0.6	-0.1	0.5	1.0	0.4	5.0	0.2
	300	2.5	2.8	7.3	3.3	4.9	9.4	0.2	0.2	10.2	0.3	4.8	0.1
	200	2.1	4.1	7.4	5.0	4.8	20.8	-1.1	1.3	1.1	0.3	1.0	0.9
	150	0.3	5.6	7.3	6.1	4.9	34.3	-0.5	1.0	2.8	1.3	1.0	1.3
DESALAAM	850	-1.7	1.2	3.3	1.1	1.2	1.3	2.9	5.4	7.0	1.4	4.1	15.7
	700	-0.5	1.0	5.8	2.4	1.6	3.5	2.2	2.9	7.5	0.6	4.3	4.2
	500	-2.5	0.9	5.8	1.1	1.4	1.0	1.5	0.6	7.6	0.1	1.7	0.2
	300	-2.4	2.3	7.4	2.3	4.6	5.2	2.1	0.5	7.2	0.5	1.3	0.3
	200	-2.9	3.1	8.6	5.7	4.3	21.0	2.7	1.9	0.9	0.5	1.2	1.9
	150	-3.2	1.6	9.9	7.0	4.4	25.4	1.7	2.4	1.4	0.4	3.9	3.0
FORTLAMY	850	-2.6	1.6	6.8	1.2	0.8	2.0	-1.7	1.8	7.3	0.7	6.4	1.9
	700	-4.4	3.8	1.4	0.9	1.0	7.7	-0.3	1.8	1.0	0.5	2.1	1.7
	500	-4.0	4.7	1.3	1.4	1.7	11.8	0.0	0.9	0.9	0.2	3.2	0.4
	300	1.3	10.2	1.5	0.5	0.6	51.9	0.3	1.0	11.1	0.5	1.3	0.7
	200	2.8	12.7	1.4	3.1	4.7	85.6	3.2	3.9	0.8	1.3	1.2	8.4
	150	2.3	14.5	1.4	4.3	4.8	114.6	4.1	3.4	1.0	1.4	1.1	7.0
HILO	850	-3.0	0.8	1.1	0.3	1.3	0.4	0.1	0.8	1.5	0.1	5.4	0.3
	700	-2.1	2.1	1.7	0.5	2.6	2.3	0.3	0.2	1.4	0.1	0.7	0.0
	500	3.0	3.8	2.2	0.9	1.9	7.8	-0.3	0.9	6.7	0.1	3.1	0.5
	300	13.5	5.9	2.5	0.9	2.4	17.9	-1.1	3.4	7.2	0.8	3.8	6.0
	200	21.0	7.3	2.9	1.5	3.8	28.2	-1.6	4.8	7.5	0.9	3.9	12.0
	150	18.6	7.1	3.1	1.8	4.3	26.4	-1.8	5.5	7.6	0.6	3.1	15.5
JOHNSTON	850	-7.2	1.4	1.0	0.2	2.4	1.0	-0.3	0.2	10.2	0.1	4.4	0.0
	700	-3.2	1.5	2.4	0.1	2.7	1.2	-0.3	0.4	7.9	0.2	4.2	0.1
	500	1.1	3.4	2.8	0.5	2.3	5.9	-1.0	1.7	7.5	0.5	4.2	1.5
	300	11.4	5.3	3.2	1.4	3.6	15.1	-1.6	3.7	7.6	1.4	4.6	7.9
	200	17.8	5.8	3.9	3.3	4.3	22.0	-0.8	4.7	7.6	1.7	4.6	12.6
	150	17.0	6.1	4.2	3.0	4.4	22.9	-1.6	4.9	7.6	0.8	4.8	12.2
KHARTOUM	850	0.0	1.6	7.1	1.2	0.8	2.0	-2.0	3.4	7.7	0.8	1.1	6.1
	700	0.3	4.8	1.8	0.8	6.3	11.8	-0.8	0.9	11.4	0.5	6.1	0.5
	500	0.3	6.7	1.8	0.2	1.2	22.4	0.1	0.4	8.8	1.0	1.4	0.5
	300	5.0	14.6	1.7	1.3	4.5	106.8	-1.1	1.4	8.8	0.6	1.4	1.2
	200	6.3	20.5	1.6	4.5	4.7	219.4	0.3	1.0	9.9	2.4	1.1	3.5
	150	4.1	22.4	1.5	6.2	4.6	269.0	1.2	2.1	7.4	1.7	1.2	3.7

ANNUAL VARIABILITY ALL YEARS

		U						V					
		AVG	M1		M2		VAR12	AVG	M1		M2		VAR12
			AMP	PHASE	AMP	PHASE			AMP	PHASE	AMP	PHASE	
KINABALU	850	1 0	3 1	8 1	0.3	6.0	4.7	1.0	1.4	8.2	0 2	5.4	1.0
	700	-0 6	3 6	8.0	0.3	1 0	6 4	0.6	0.5	8 4	0 1	2.1	0.1
	500	-4 5	2 1	8 1	0.8	5 4	2.6	0 5	0.3	8.4	0.2	1.3	0.1
	300	-7.1	1 0	1.6	2.2	4 7	2.9	0 0	1.5	2.0	0 2	0.9	1.2
	200	-10.8	3 2	2 1	4.0	4 6	13.0	-0 5	6 8	1 8	0.5	2.5	23.2
	150	-14.4	3.6	2.5	4.4	4 6	16.2	-0.6	8.3	1.6	1.6	2.0	36.0
KOROR	850	-2 4	4.8	8 2	0.7	3 5	11.7	-0 4	1.5	7.9	0.2	5.8	1.1
	700	-2 9	2.9	8.1	0.9	3.4	4.7	0 0	0.7	7.7	0.1	6.4	0.2
	500	-5 4	2.6	7 7	1.4	4 2	4.3	0.5	0.3	9.5	0.5	1.1	0.2
	300	-6 0	0 9	6 2	2.4	4 7	3.3	0.1	1.1	2.4	0.3	5.4	0 7
	200	-7 8	1.3	4.7	3.2	4.8	5.9	0.1	5 2	2.2	0.3	4.7	13.5
	150	-9.3	2.4	5.2	4.2	4.9	11.7	-0.4	6.2	1.9	0.6	2.1	19.1
LAE	850	0 6	3 4	1.7	0.7	2.0	5 9	0.7	1.7	7 6	0.2	4.5	1.4
	700	-1 6	4 6	1.4	0 3	2 0	10 7	0 4	0.4	8 5	0.2	1.7	0.1
	500	-2 6	3 0	1.4	0 9	5 2	4.8	-0.3	0 0	3.6	0.3	4.7	0.0
	300	-3 6	1.7	1 1	2.7	3.3	5.0	-0 2	0.4	3.9	0.3	2.3	0.1
	200	-5 0	0 4	10 2	3.7	5.3	7.0	-1.6	2.1	2.4	0.2	1.8	2.3
	150	-5 8	2.4	7.6	4.0	5.2	11.1	-0.9	1.6	2.6	0.4	2.3	1.4
LIMA	850	0 2	0 1	1.3	0.3	3.8	0.0	-0.3	0.6	8.4	0.3	0.8	0.2
	700	-0.6	0.8	1.4	0.2	2 9	0 4	0.6	1.4	7 4	0.2	6.4	1.0
	500	-0 4	0.5	6.6	0.3	6 3	0 2	-1.4	2.3	1.0	0.3	4.3	2.7
	300	4 0	6 6	7.3	2.0	5.3	24.1	-2.3	0.8	6 7	0 4	2.2	0.4
	200	5 4	10.7	7.2	2.8	5.2	61.3	-5.0	3.0	6.7	0.9	1.5	5.0
	150	6.4	9.6	7.1	3.3	5.2	51.6	-2.9	3.4	6.7	0.7	1.5	6.1
MAJURO	850	-6.8	1.7	9.3	0.7	3 2	1.8	0.0	1.0	7.5	0.2	4.0	0.6
	700	-5.5	0.6	0.9	1.0	3 6	0.7	0.3	0.4	6.2	0.1	3.4	0.1
	500	-5 1	1.4	5.5	2.7	4 4	4.6	-0.2	0.8	6.7	0.3	3.6	0.4
	300	-0.7	1.7	3.8	3.2	4 6	6.6	0.2	0.9	6.0	0.7	4.9	0.6
	200	2 0	1.9	4.7	4.4	4.7	11.2	1.1	1.8	3.1	0.7	5.8	1.8
	150	2.8	3 3	6.3	4.8	4.7	16.8	-0.1	0.6	3.7	0.7	6.2	0.4
MIAMI	850	-0 4	2.1	2.1	0 6	1.6	2.3	1.4	0.8	6.3	0.8	1.5	0.6
	700	2 7	4.5	1.7	0.5	1 8	10.2	0.8	0 5	7 8	0 9	1.4	0.5
	500	7 3	9.0	1.7	0.4	3.2	40 3	0.1	0.6	11 6	1.4	1.3	1.2
	300	13 7	15 6	1.7	2.3	4.3	123.9	-1 0	1.3	0 5	1.4	0.9	1.9
	200	18 6	19.9	1.8	4 6	4 4	209 1	-2.0	2 9	0.8	1.4	0.8	5.2
	150	17.3	19.2	1.8	4.5	4.5	195 4	-2 2	3 7	1.0	1.1	1.1	7.4
NAIROBI	850	0 0	0 0	1.0	0.0	1.0	0.0	0 0	0 0	1 0	0 0	1.0	0.0
	700	-3.1	3.0	7.3	1.8	1 3	6 1	-1.6	2.9	7 5	0.3	5.0	4.2
	500	-4.3	2.3	7.1	1.3	1.0	3 5	-0 6	0 6	2 2	0 2	5.2	0.2
	300	-3 0	2 0	8 0	1 2	4.8	2.7	0 5	0 6	12.2	0.4	1.4	0.3
	200	-3 0	1 9	10 0	4 7	4.2	13 1	0.8	2 7	0.9	1.2	1.5	4.5
	150	-3 2	4 3	12.0	5.9	4 3	26 8	0.1	2.5	0.9	0.9	1.8	3.5
NATAL	850	-7 2	0.6	2 9	0.6	3.4	0.4	4.9	2.0	7.6	0.6	1.7	2.1
	700	-5.5	0.4	7.7	1.1	3 4	0.7	1.2	0.3	5.7	0.3	5.7	0.1
	500	-4 7	1.4	0 7	0.3	4.7	1.1	0.4	0.4	6 9	0.1	2.2	0.1
	300	1.4	2.4	1.1	1.1	1.3	3 6	-0 7	1.5	1.7	0.4	3.3	1.2
	200	6 3	0 8	1.3	2 0	1 6	2.4	-0.2	2 3	1 0	0.3	4 4	2.8
	150	9.3	0.4	4.8	2.3	1.4	2.8	-0.5	1 2	1.2	0.6	4.6	1.0
NOUMEA	850	-2 0	2.1	7.9	0 4	6 2	2.3	-0 3	0 6	6.2	0 3	3.7	0.2
	700	3 8	4.7	7 4	0.7	6.4	11.5	-0.3	0 4	9 1	0 4	3 7	0.2
	500	12 6	9 2	7 5	0 9	5.9	42 9	-1 0	0 7	12 4	0 7	3 5	0.5
	300	25 0	12 3	7 6	2.8	5 1	79 8	-1.3	0 8	11 8	1.0	2 8	0.9
	200	30.4	12.0	7 7	5.6	5.0	88 2	-0 8	1 1	11 3	1.7	2.7	2.0
	150	27 5	10.4	7.6	5.5	5.0	69.1	0.3	0 5	9.7	1.3	2.8	0.9

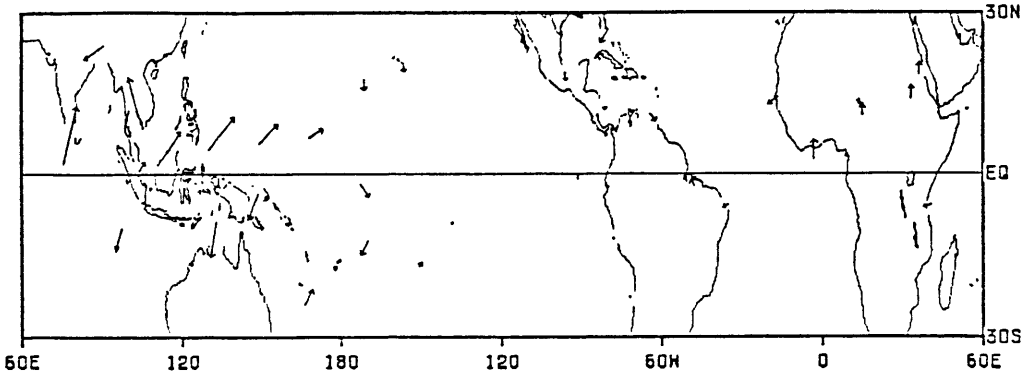
ANNUAL VARIABILITY ALL YEARS

		U						V					
		AVG	M1		M2		VAR12	AVG	M1		M2		VAR12
			AMP	PHASE	AMP	PHASE			AMP	PHASE	AMP	PHASE	
PAGOPAGO	850	-3.5	1.9	1.9	0.1	5.3	1.8	-1.5	1.0	7.5	0.2	5.2	0.5
	700	-1.2	0.3	1.1	0.3	5.1	0.1	-1.4	0.5	7.2	0.2	6.4	0.1
	500	0.9	1.4	9.0	0.8	4.8	1.3	-0.6	0.3	3.0	0.2	6.3	0.1
	300	5.4	4.3	8.6	1.4	5.0	10.1	1.7	0.6	4.6	0.1	5.8	0.2
	200	8.6	5.3	8.6	2.3	5.0	16.7	4.0	1.2	3.0	0.7	4.0	1.0
	150	8.6	4.7	8.5	2.6	5.0	14.4	4.7	2.2	2.0	0.6	4.1	2.7
PTSUDAN	850	-0.6	1.5	6.8	2.8	1.2	5.1	0.3	1.9	0.8	1.3	5.0	2.7
	700	2.3	3.6	2.3	2.2	0.9	9.1	0.6	1.6	1.1	1.8	4.6	2.8
	500	5.1	9.7	1.8	0.8	1.2	47.0	1.1	0.2	5.7	0.5	6.1	0.1
	300	11.5	20.6	1.7	2.0	4.3	214.8	0.5	1.3	8.3	0.6	0.8	1.0
	200	12.9	25.4	1.6	5.2	4.5	336.7	1.3	2.6	7.9	2.0	1.2	5.3
	150	10.2	23.6	1.6	6.3	4.5	348.0	2.2	2.8	7.6	1.6	0.9	5.1
SANANDRE	850	-7.5	0.2	12.2	2.0	4.0	1.9	-2.1	1.4	7.2	0.3	3.2	1.0
	700	-5.8	1.0	2.6	1.7	4.0	2.0	-0.3	1.2	7.1	0.3	2.9	0.8
	500	-4.0	1.5	2.9	1.3	4.5	2.1	1.0	1.2	7.3	0.6	1.3	1.0
	300	1.9	5.3	2.3	1.1	1.3	14.9	0.5	1.7	0.9	1.2	0.9	2.2
	200	5.1	6.7	2.3	1.6	1.0	23.7	2.0	4.8	1.2	1.4	0.6	12.6
	150	5.0	6.5	2.3	1.4	6.4	22.3	0.5	4.1	1.1	0.6	0.5	8.4
SINGPORE	850	2.1	1.3	8.4	0.6	5.6	1.1	0.1	3.3	7.5	0.5	4.2	5.7
	700	1.9	1.0	8.5	0.9	6.3	0.9	-0.2	0.7	7.4	0.4	3.9	0.4
	500	-2.4	1.0	12.3	0.5	5.4	0.6	0.0	0.5	7.4	0.0	6.5	0.1
	300	-6.8	2.4	1.6	1.3	4.3	3.7	-0.2	2.1	1.7	0.3	3.2	2.2
	200	-12.0	3.5	2.2	3.2	4.4	11.1	-0.9	6.3	1.7	0.9	2.5	20.3
	150	-14.8	4.0	2.7	3.6	4.5	14.5	-1.5	5.9	1.7	1.0	1.9	18.1
TAHITI	850	-2.6	0.5	8.0	0.2	5.1	0.2	-2.1	0.6	7.3	0.5	4.0	0.3
	700	-0.2	1.9	8.1	0.8	5.6	2.2	-1.6	0.8	6.9	0.2	3.7	0.3
	500	3.5	4.3	8.2	1.2	5.2	10.0	-0.4	0.5	8.9	0.4	1.6	0.2
	300	9.3	8.0	8.3	1.6	5.3	33.4	2.7	0.3	10.2	1.4	1.8	1.0
	200	13.2	9.0	8.3	2.3	5.3	43.1	6.2	1.5	0.9	0.7	1.5	1.3
	150	13.6	8.6	8.3	2.7	5.3	40.7	5.6	3.4	1.0	1.0	1.5	6.2
TRINIDAD	850	-7.4	1.1	11.6	1.2	3.3	1.3	0.4	1.2	7.7	0.7	4.3	0.9
	700	-5.4	2.7	1.5	1.5	3.7	4.8	0.5	0.6	7.6	0.2	4.6	0.2
	500	-3.4	3.0	2.1	1.5	4.1	5.7	-0.3	0.9	6.7	0.4	4.3	0.5
	300	4.6	7.4	1.8	0.6	5.9	27.2	0.0	1.8	5.7	0.1	3.2	1.7
	200	9.8	6.7	1.7	1.6	5.5	23.6	0.4	2.1	2.8	0.1	4.8	2.1
	150	10.7	5.3	1.6	2.6	5.2	17.6	-1.9	0.2	6.5	0.8	4.2	0.4
TRVNDRUM	850	3.2	8.0	7.4	2.0	0.8	33.7	-3.0	1.6	1.2	1.1	4.6	2.0
	700	1.5	7.2	7.8	3.2	0.9	30.9	-1.8	1.0	11.2	0.5	0.5	0.6
	500	-0.8	3.9	7.2	0.8	1.0	7.8	-0.7	0.4	7.5	0.2	2.9	0.1
	300	-3.6	4.5	2.6	0.9	4.1	10.5	0.4	1.1	1.2	0.7	3.2	0.9
	200	-9.6	12.5	2.0	3.2	4.0	83.3	0.7	4.8	1.4	0.7	4.5	11.8
	150	-13.2	17.4	1.8	4.3	4.1	160.4	-0.8	6.0	1.3	1.8	4.5	19.6
TRUK	850	-4.9	2.8	8.4	1.1	3.2	4.6	-0.1	1.3	7.9	0.4	4.1	0.9
	700	-5.0	1.0	7.7	1.3	3.5	1.4	0.2	0.5	7.3	0.2	3.0	0.2
	500	-6.4	2.5	6.8	2.0	4.3	5.1	0.1	0.3	8.0	0.2	1.9	0.1
	300	-4.3	1.7	6.3	2.4	4.7	4.4	0.2	0.6	4.1	0.2	4.7	0.2
	200	-3.7	2.2	6.2	3.2	4.9	7.6	1.1	3.6	2.6	0.2	4.8	6.5
	150	-3.8	3.7	6.6	4.0	4.8	14.7	-0.1	3.2	2.3	0.9	1.5	5.4
VERACRUZ	850	-1.0	1.0	0.7	0.6	4.3	0.7	-1.2	1.5	3.5	0.5	1.0	1.2
	700	-1.2	2.3	1.8	0.7	4.2	2.8	-0.3	1.3	2.6	1.0	1.5	1.4
	500	0.7	5.6	2.0	0.4	3.4	15.5	0.9	2.3	1.5	0.9	1.6	3.0
	300	6.3	8.0	2.2	0.7	3.9	32.2	2.6	4.7	1.5	0.3	1.6	11.1
	200	9.0	9.2	2.3	1.4	4.5	42.9	3.7	5.8	1.5	0.4	5.0	17.0
	150	7.6	9.0	2.2	1.7	4.7	42.1	3.5	6.4	1.6	0.7	5.1	21.0

Figure 2.4 - Vector plots of the annual cycle in the zonal wind component. The length of each vector represents the magnitude of the annual cycle, and the orientation of each vector represents the phase: southward-oriented vectors represent annual cycle maxima in mid-January, with the phase progressing clockwise, so that westward-oriented vectors represent annual cycle maxima in mid-April, and so forth.

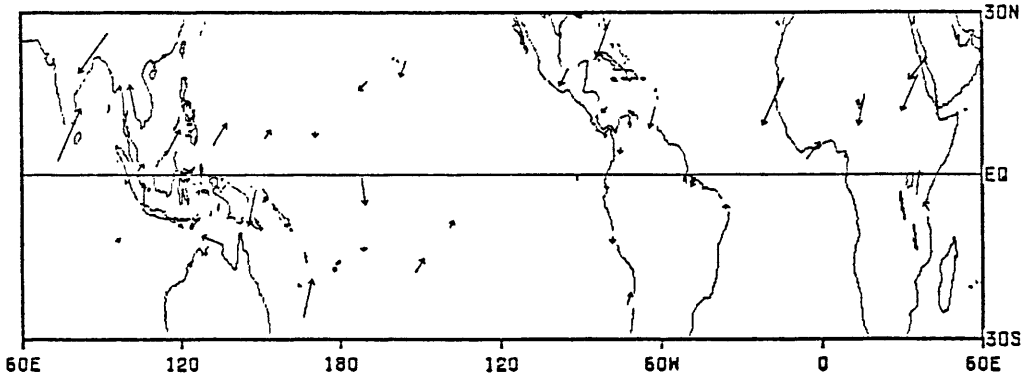
a. ANNUAL CYCLE U 850 MB

SCALE: ——— = 10 M/S



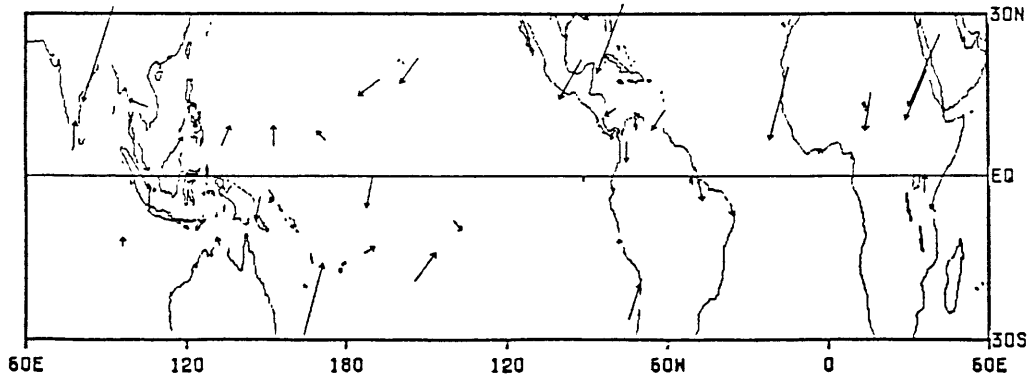
b. ANNUAL CYCLE U 700 MB

SCALE: ——— = 10 M/S

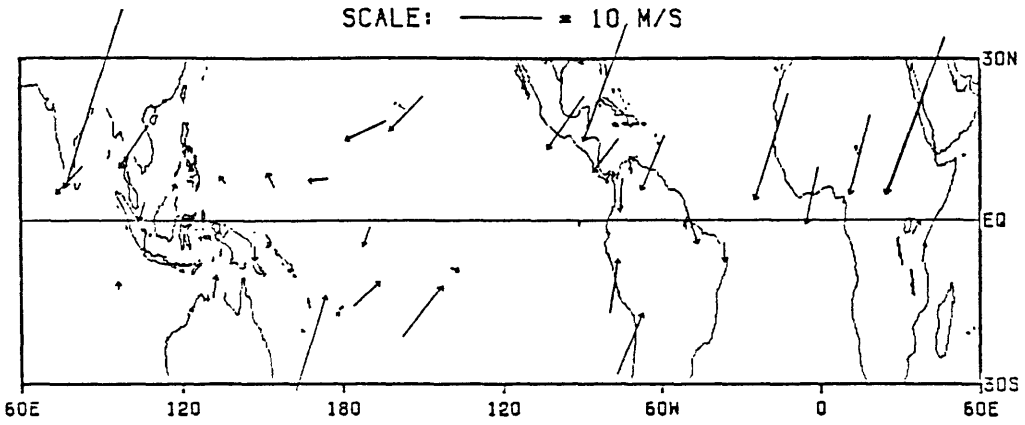


c. ANNUAL CYCLE U 500 MB

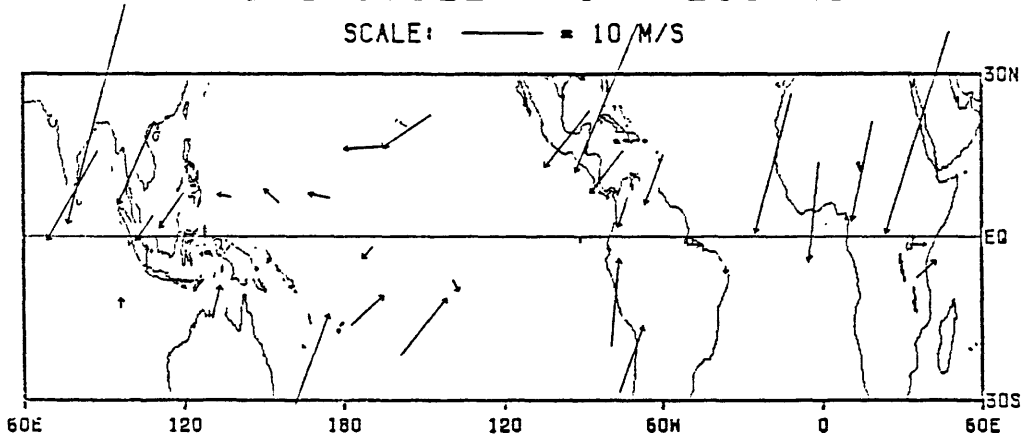
SCALE: ——— = 10 M/S



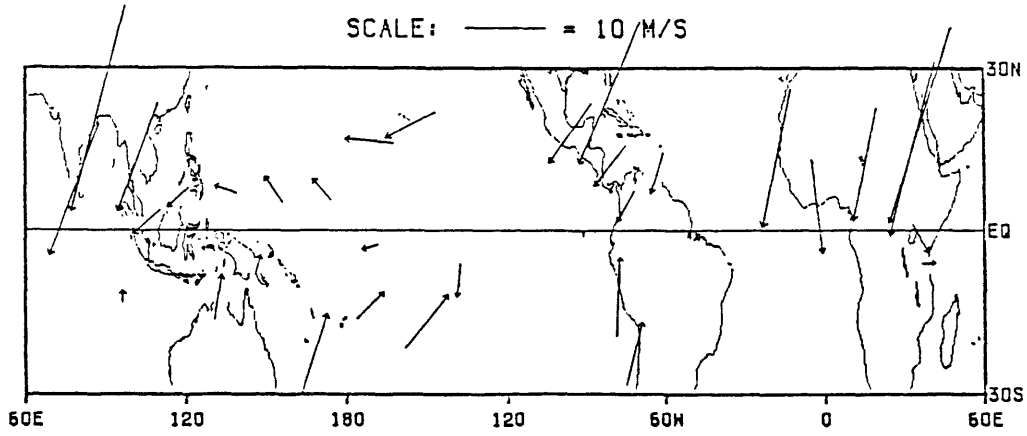
d. ANNUAL CYCLE U 300 MB



e. ANNUAL CYCLE U 200 MB



f. ANNUAL CYCLE U 150 MB



shifts to a steady trade regime in mid-ocean. The phases over the Pacific agree closely with the annual cycle phases of surface wind speed (with the sign reversed, because the annual mean wind is easterly) and surface zonal wind component shown by Horel (1982b).

South of the equator over the far western Pacific and eastern Indian Ocean, the phase of the annual cycle reverses so that the maximum westerly wind occurs in late summer in the Southern Hemisphere. Over the western Pacific and eastward to the Atlantic Ocean in the trade wind regime, the annual cycle has very small amplitude.

At higher levels (Figs. 2.4b-2.4f), annual cycle maxima occur late in the local winter at all subtropical stations in both hemispheres, and amplitudes increase with height up to 200 mb. Near the equator, however, the amplitude remains nearly constant with height and very small (typically less than 5 m/s). A phase shift occurs over the western Pacific, where maximum westerlies in the upper troposphere occur in late spring.

$M_1(v)$ at each level is plotted in Fig. 2.5. The scale of the vectors in Fig. 2.5 has been expanded by a factor of two relative to Fig. 2.4. At 850 mb, $R_1(u)$ and $R_1(v)$ are comparable over the east coast of Africa, where a strong low level southerly jet occurs from May through September, and over Southeast Asia. Elsewhere, $M_1(v)$ is small (on the order of 1 m/s), with maximum southerlies in July. Physically, the phase in both hemispheres represents the alternation in the strength of the Hadley circulations, the strongest low-level equatorward flow occurring late during each hemisphere's winter season. This signature decays very rapidly with height. At the surface, $R_1(v) > R_1(u)$ throughout the Pacific (Horel, 1982b). At 850 mb, the inequality is reversed over the ocean, and at 700 mb $R_1(v)$ is negligible.

At 300 mb and above, $R_1(v)$ increases rapidly with height, with a February maximum over the western Pacific and Southeast Asia, and similar phase but smaller amplitude south of the equator. At upper levels, the annual cycle in v has greater amplitude than the annual mean, but less amplitude than the annual cycle in u. Moving eastward into the Pacific at 200 and 150 mb, the amplitude decreases as the phase shifts to a springtime maximum. This pattern is the same as the annual cycle in u (cf. Fig. 2.4e-f) with the phase of $M_1(v)$ leading the phase of $M_1(u)$ locally by one season.

To the northeast, the phase of $M_1(v)$ at Johnston [17°N 170°W] and Hilo [20°N 155°W] is opposite that observed over the western Pacific at stations south of the trade wind maximum. Hence, the annual cycle phase reversal in surface wind at the latitude of the trade wind maximum, which was noted by Horel (1982b) and observed at 850 mb in Figs. 2.4a and 2.5a, is mirrored in the upper troposphere only in the meridional wind field.

Plots of the amplitude and phase of the semiannual cycle M_2 in u and v are shown in Figs. 2.6 and 2.7, respectively. Significant amplitudes are found only for the zonal component. At low levels, winter-summer maxima in the semiannual cycle of u (represented by north-south oriented vectors) are found over Southeast Asia, Africa, and northern Australia, with weak spring-autumn maxima elsewhere in the tropics.

The latitudinal dependence of $R_1(u)$ and $R_2(u)$ in the upper troposphere contrast sharply. The annual cycle decreases near the equator to the extent that the annual variability of the zonal wind at 200 mb at stations within a narrow equatorial strip is primarily contained in the semiannual cycle (Fig. 2.8).

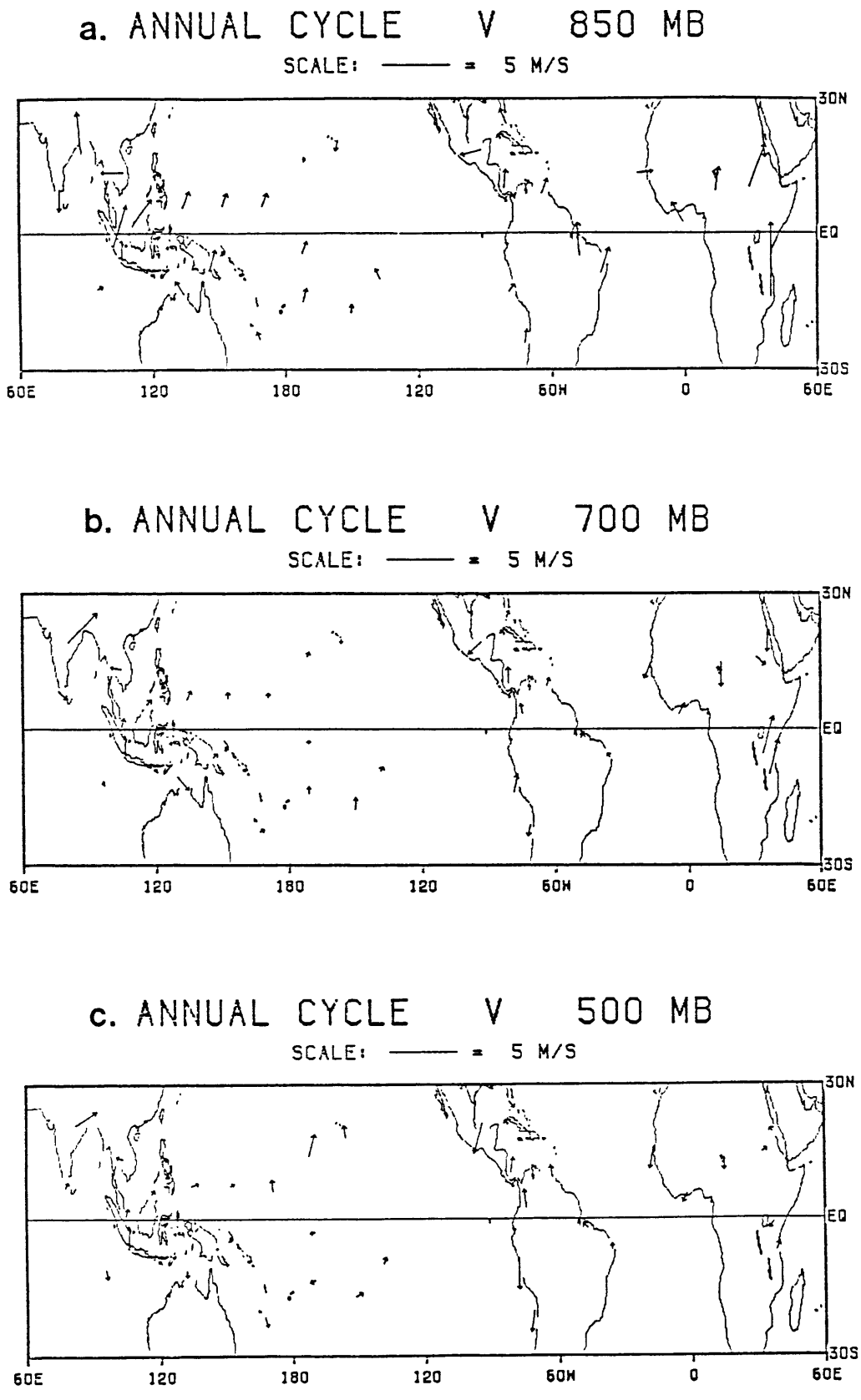
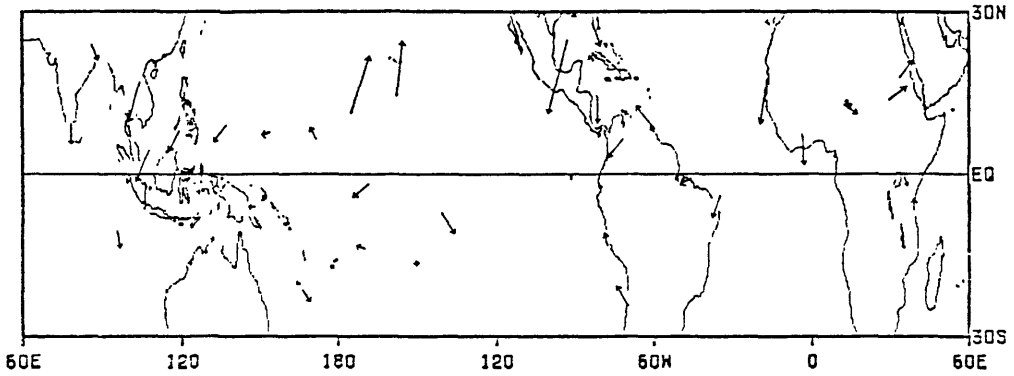


Figure 2.5 - As in Fig. 2,4, but for the annual cycle in the meridional wind component.

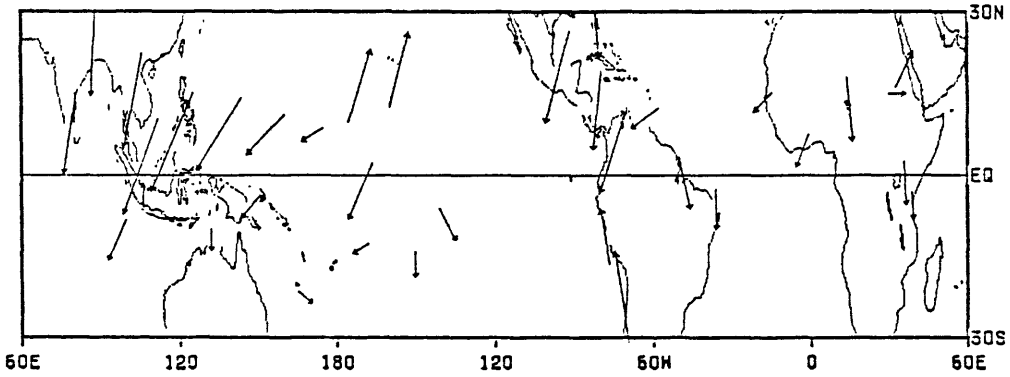
d. ANNUAL CYCLE V 300 MB

SCALE: —— = 5 M/S



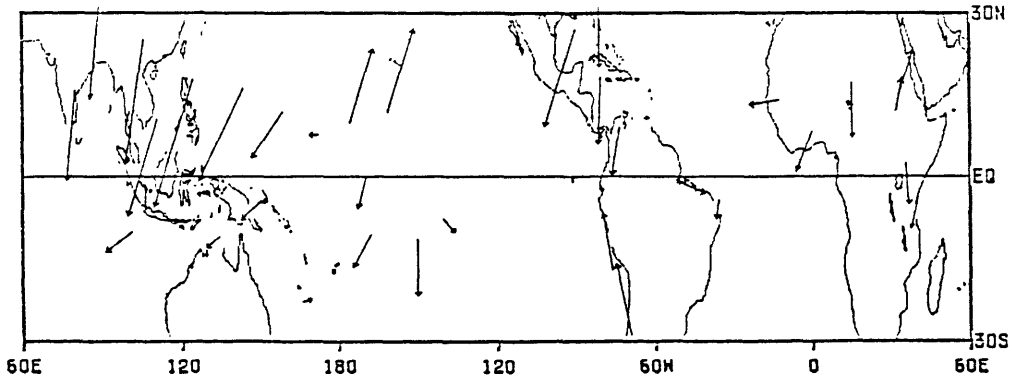
e. ANNUAL CYCLE V 200 MB

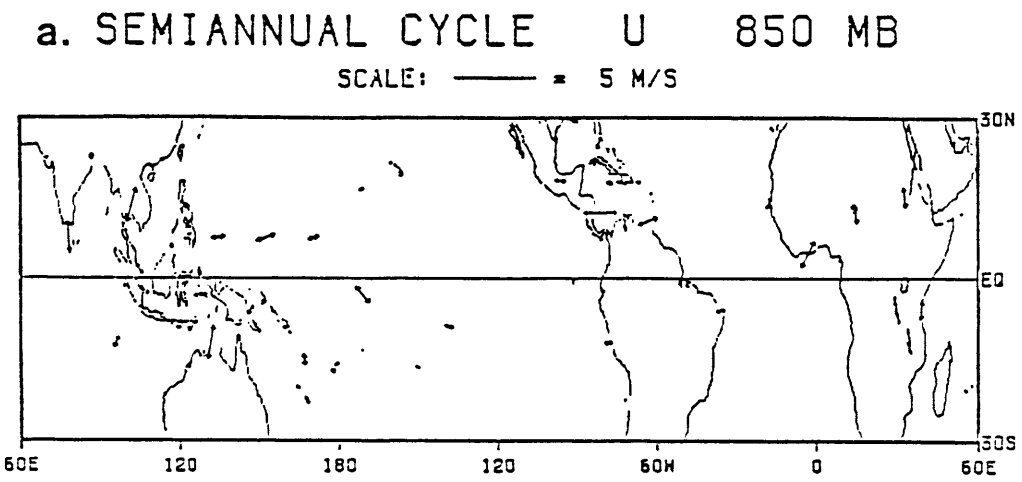
SCALE: —— = 5 M/S

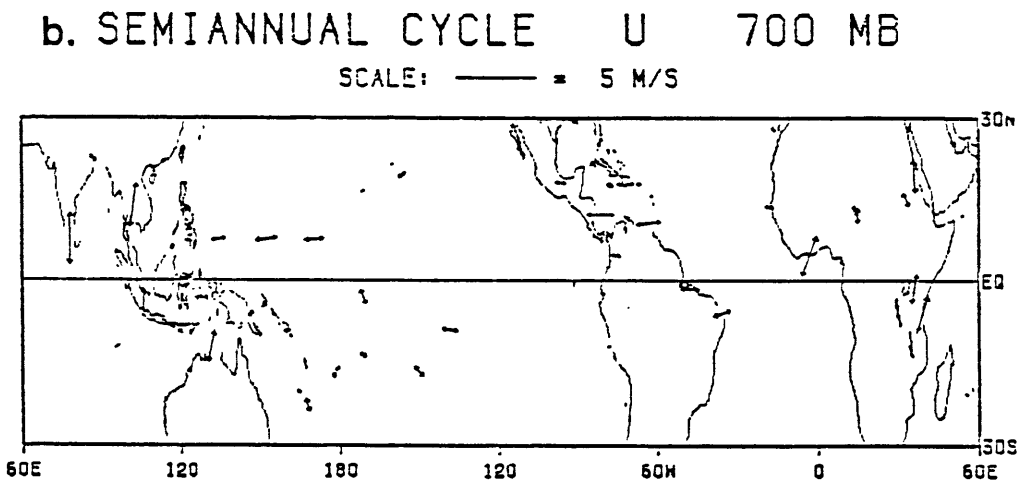


f. ANNUAL CYCLE V 150 MB

SCALE: —— = 5 M/S







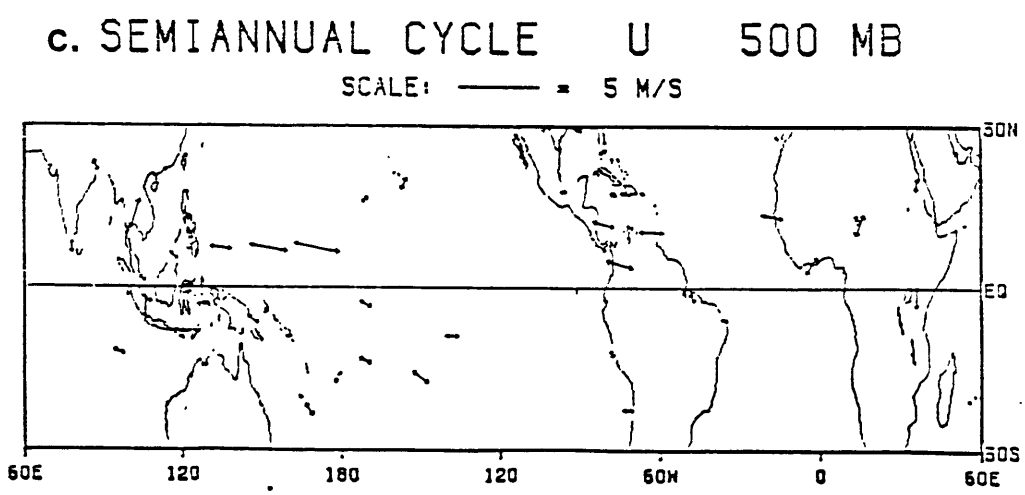
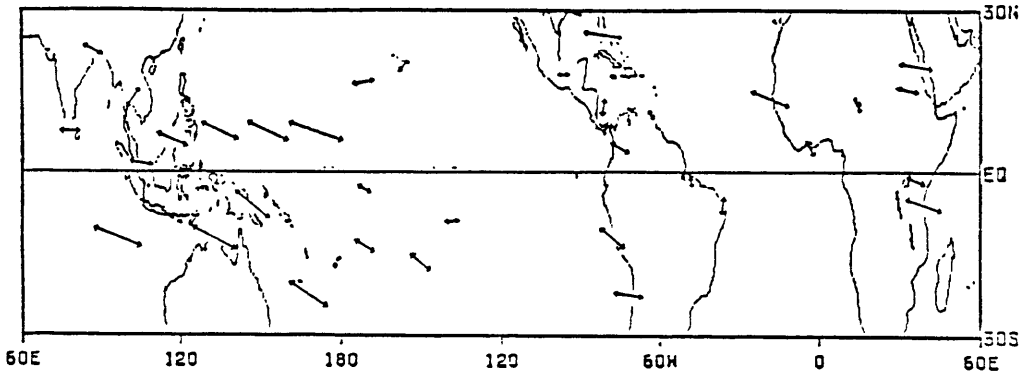


Figure 2.6 - As in Fig. 2.4, but for the semiannual cycle in the zonal wind component. Arrowheads on each vector indicate the maxima in the semiannual cycle using the same phase convention as in Fig. 2.4.

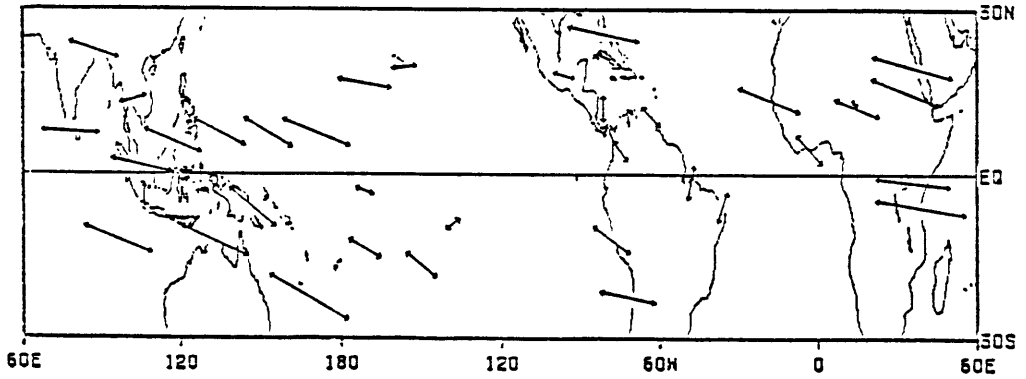
d. SEMIANNUAL CYCLE U 300 MB

SCALE: —— = 5 M/S



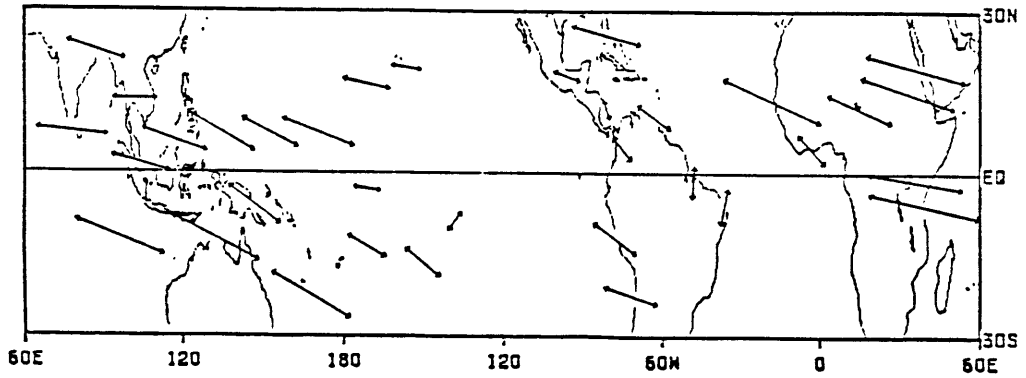
e. SEMIANNUAL CYCLE U 200 MB

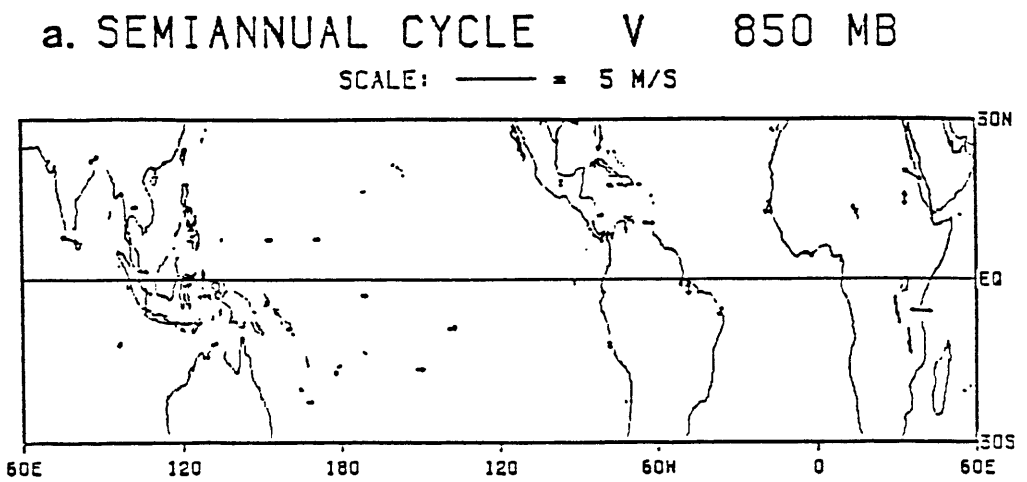
SCALE: —— = 5 M/S

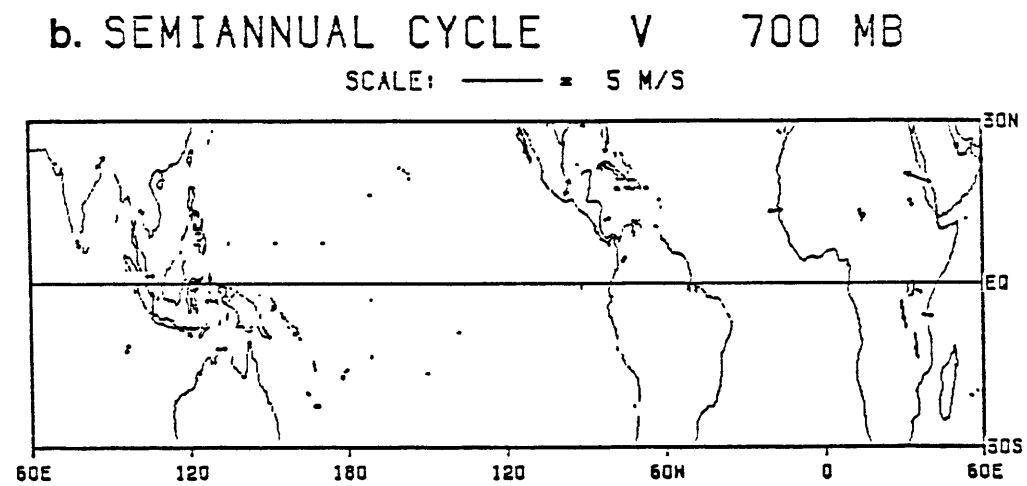


f. SEMIANNUAL CYCLE U 150 MB

SCALE: —— = 5 M/S







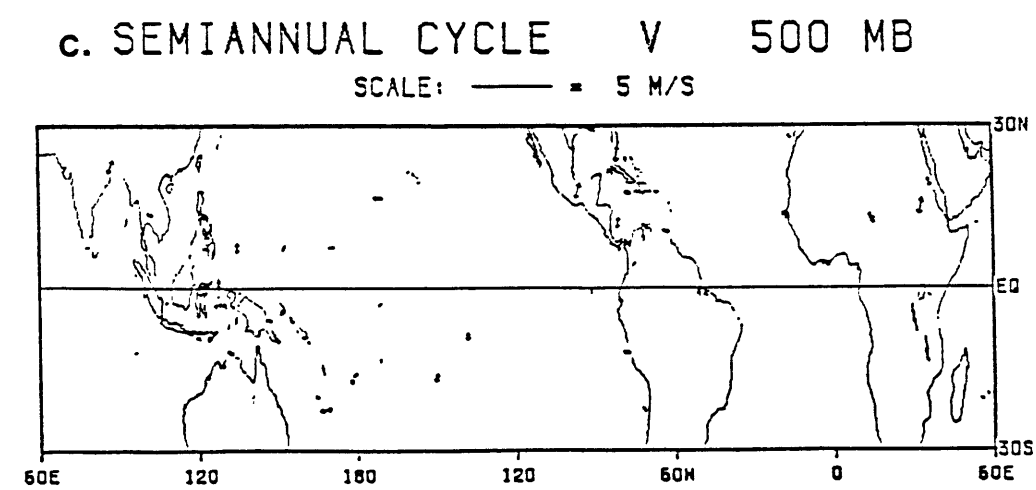
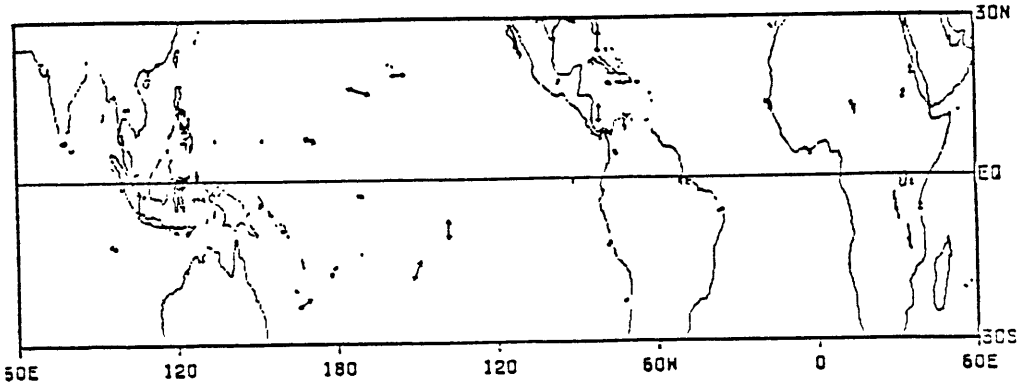


Figure 2.7 - As in Fig. 2.6, but for the semiannual cycle in the meridional wind component.

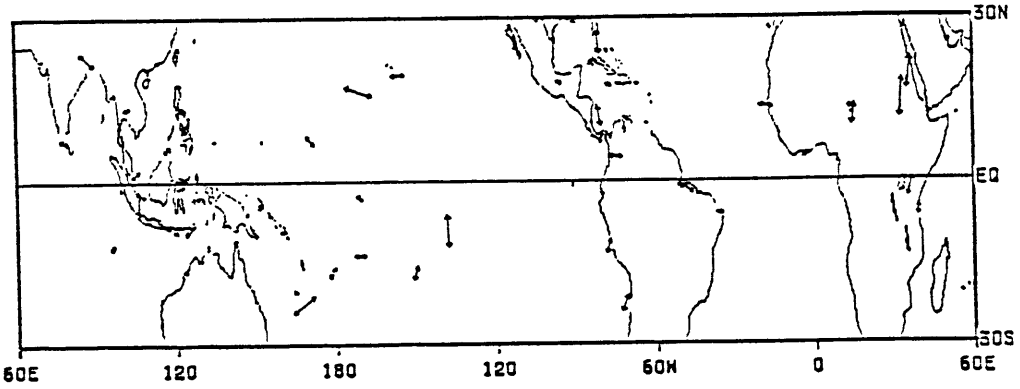
d. SEMIANNUAL CYCLE V 300 MB

SCALE: —— = 5 M/S



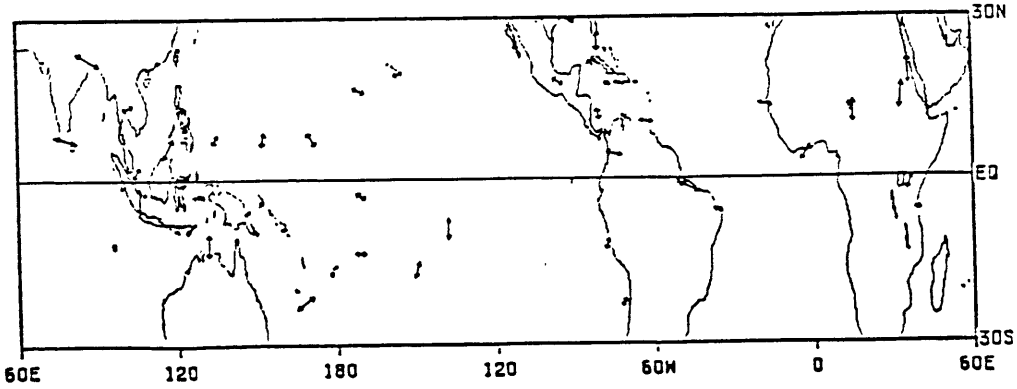
e. SEMIANNUAL CYCLE V 200 MB

SCALE: —— = 5 M/S



f. SEMIANNUAL CYCLE V 150 MB

SCALE: —— = 5 M/S



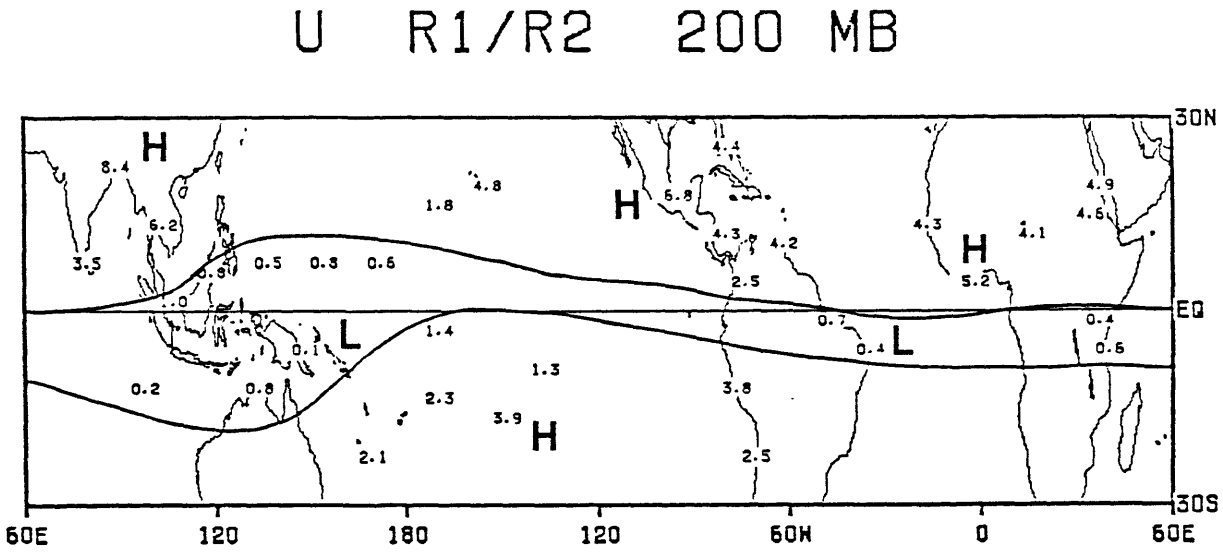


Figure 2.8 - Ratio of the amplitude of the annual cycle to the amplitude of the semiannual cycle, for the 200 mb level zonal wind at each station.

At all locations, the phase of $M_2(u)$ shifts to maxima during late spring and late autumn and the amplitude increases steadily with height. At 200 and 150 mb, both the amplitude and phase of $M_2(u)$ are nearly uniform throughout the tropics. Hence, although there is a general consistency between the annual cycle in v and the semiannual cycle in u as suggested by van Loon and Jenne (1969, 1970), the vertical structures of the cycles differ. The phases of $M_1(v)$ and $M_2(u)$ are in quadrature, as expected. However, $R_1(v)$ is large only in thin layers at the bottom and top of the troposphere, whereas the vertical structure of $R_2(u)$ is a monotonic increase with height.

To test the reliability of these statistics, the annual mean and annual and semiannual cycles were calculated for separate decades 1961-70 and 1971-80 for all stations whose data records were sufficiently long. Amplitudes and phases of the cycles all proved extremely reproducible: amplitudes agreed to within 1 m/s for the two decades, and phases agreed to within one month for all cycles with amplitudes greater than 1 m/s. This result confirms the reliability of the harmonic statistics (and therefore, indicates that the presence of a spectral peak at period 40-50 days does not significantly impact the estimates of the climatological monthly means from which the harmonics were calculated), and also indicates the lack of any recent discernable trends in the annual cycle on decadal time scales.

2.4 Annual variability over the equatorial western Pacific

An alternative framework for illustration of the annual variability is the presentation of the various monthly or seasonal mean winds

themselves, without Fourier decomposition. In this section, the annual variability is presented in a format which includes the annual mean and monthly departures from the annual mean for both u and v components in one plot for a single station. This format will be used to review the annual variability, plotted as a function of pressure, at eight stations near the equator - Trivandrum , Singapore, Kota Kinabalu, Koror, Truk, Majuro, Canton, and Atuona. The western Pacific region is shown here to be a transition zone between the monsoonal circulation near the Asian continent and the trade wind circulation over the mid-ocean.

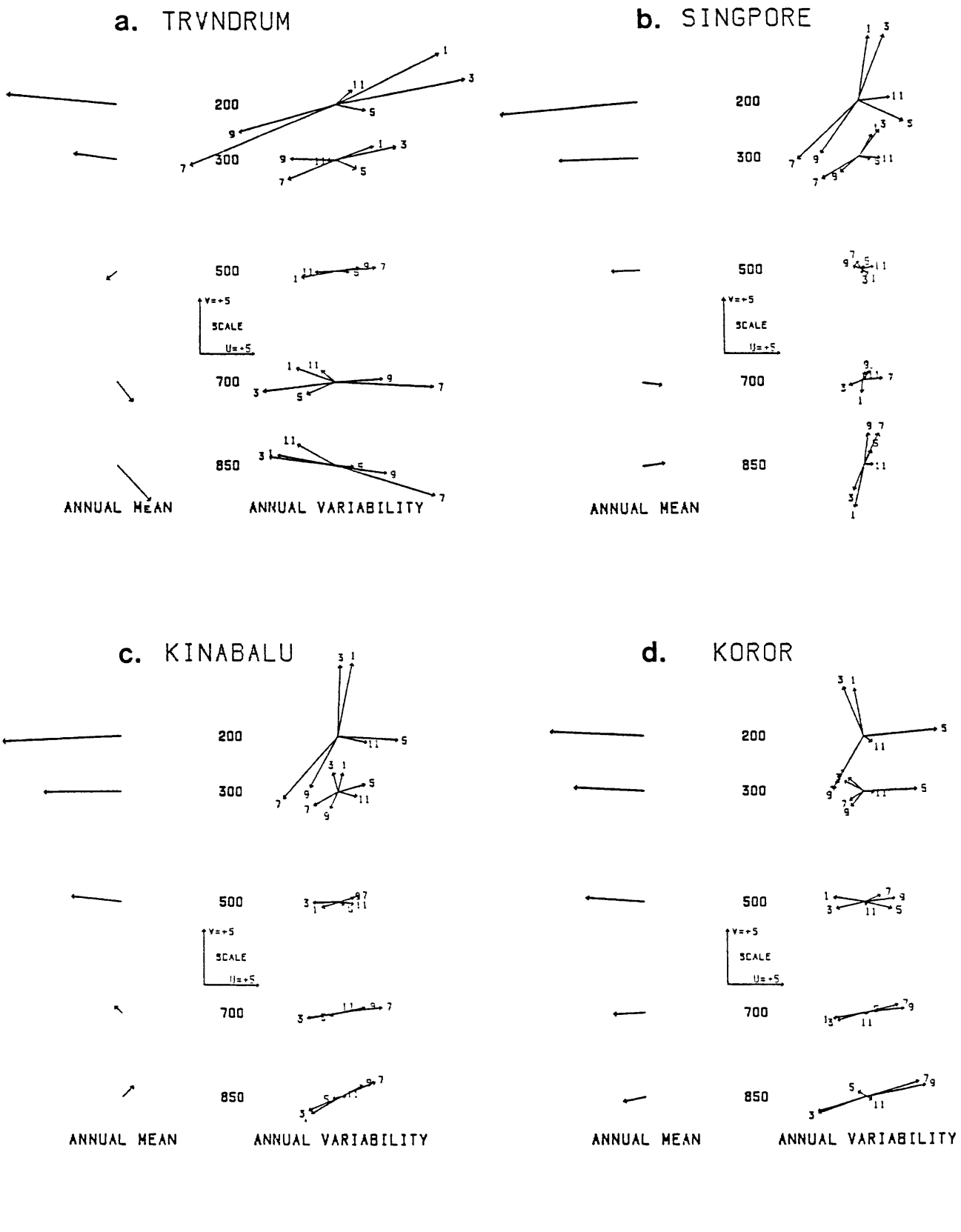
The same network of stations was used to create the annual mean zonal mass flux cross-section in Section 2.2. The seasonal variability of the zonal mass flux along this cross-section is presented in this section.

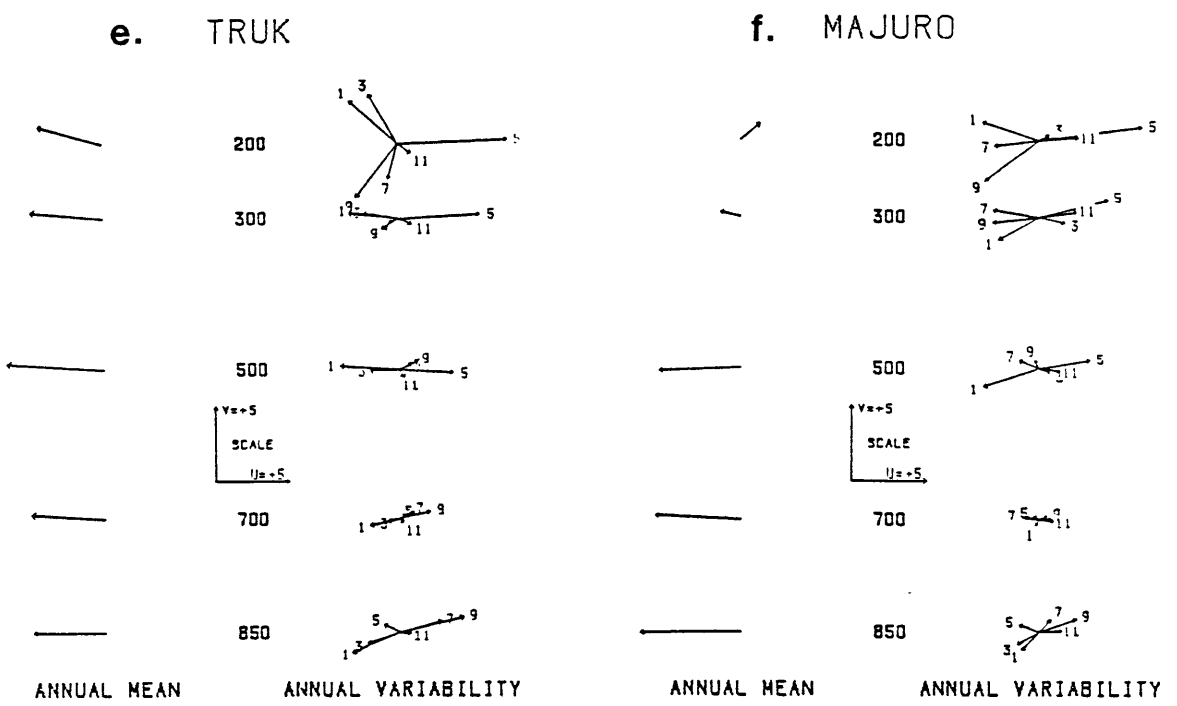
The annual mean and annual variability of the wind from 850 mb to 200 mb at Trivandrum are shown in Fig. 2.9a. The annual mean wind is plotted on the left as a function of pressure, and the monthly climatological means for six months (January, March, May, July, September, and November, labelled 1,3,5,7,9, and 11 respectively) on the right. The annual mean has been subtracted from each monthly mean wind vector. Many of the features described in Sections 2.2 and 2.3 can be seen in this plot. The near-surface annual mean wind is westerly and northerly, with strongest westerlies in the Northern Hemisphere summer. The meridional component vanishes at 500 mb and increases again in the upper troposphere, with meridional variability comparable at 200 and 850 mb. The reversal of the phase of the annual cycle in mid-troposphere is clearly evident.

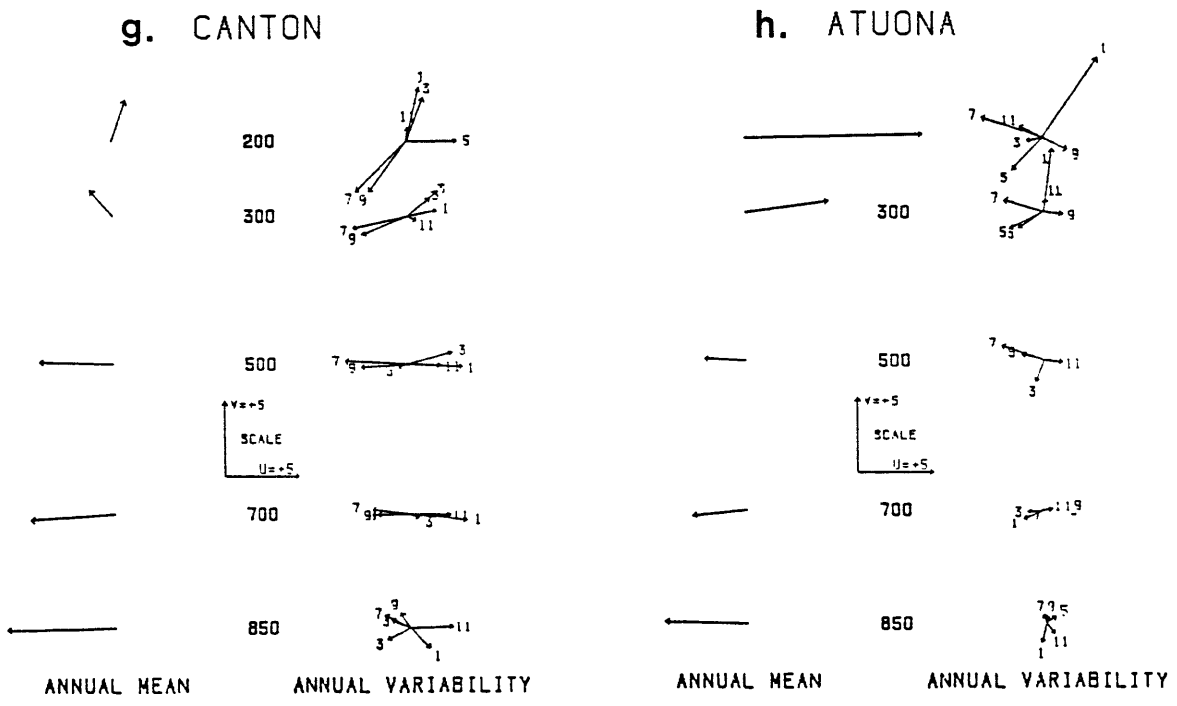
By comparison, the annual mean meridional wind at Singapore, shown

Figure 2.9 - Annual mean wind and annual variability at stations near the equator along a longitudinal band extending from the southern tip of India eastward to the mid-Pacific (see cross section A in Fig. 3.18). For each station, the annual mean is plotted as a function of height on the left, with the departures from the annual mean for six months (January, March, May, July, September, and November, denoted 1, 3, 5, 7, 9, 11, respectively) on the right. All vectors are plotted using the same scale.

(a) Trivandrum [8°N 77°E]
(b) Singapore [1°N 104°E]
(c) Kota Kinabalu [6°N 116°E]
(d) Koror [7°N 134°E]
(e) Truk [7°N 151°E]
(f) Majuro [7°N 171°W]
(g) Canton [2°S 171°W]
(h) Atuona [10°S 139°W]


a. TRVNDRUM
b. SINGPORE
c. KINABALU
d. KOROR
200
300
500
700
850
V=+5
SCALE
U=+5
ANNUAL MEAN
ANNUAL VARIABILITY


e. TRUK
f. MAJURO
200
300
500
700
850
V=+5
SCALE
U=+5
ANNUAL MEAN
ANNUAL VARIABILITY
ANNUAL MEAN
ANNUAL VARIABILITY


g. CANTON
h. ATUONA
200
300
500
700
850
V=+5
SCALE
U=+5
ANNUAL MEAN
ANNUAL VARIABILITY
ANNUAL MEAN
ANNUAL VARIABILITY

in Fig. 2.9b, is smaller than at Trivandrum, but the annual variability of v is greater, and the meridional departures from the annual mean are reversed in sign. The zonal variability at Singapore leads that at Trivandrum by several months.

Kota Kinabalu (Fig. 2.9c) is near the center of annual mean low level zonal wind convergence. The center of annual mean upper level divergence remains far to the east, indicative of the tilt of the Walker Circulation. The meridional variability at low levels is greatly reduced compared to Singapore, and the zonal variability is larger by about the same proportion.

Further east at Koror (Fig. 2.9d), the annual mean zonal wind at 850 mb and 700 mb has switched to easterly. In the upper troposphere, the annual cycle, which is so sharply defined at Trivandrum, has been reduced in amplitude so that it is comparable to the semiannual cycle. The result is a minimal shift in summer departures from the annual mean, but a rotation of the late winter climatology from southwesterly departures at Trivandrum to southeasterly departures at Koror.

Truk (Fig. 2.9e) represents nearly the midpoint between monsoonal and trade wind regimes. The annual mean wind is easterly at all levels with very little vertical shear. The annual mean wind speed is about the same as the magnitude of annual variability. In the lower troposphere, the annual variability dominates the annual mean at stations west of Truk, and the reverse is true east of Truk.

At Majuro (Fig. 2.9f), the low-level climatology is dominated by the easterly annual mean, the speed of which is about twice as great as the amplitude of the annual variability. In contrast, the annual mean above 500 mb is small, Majuro being in a region of upper level divergence.

Meridional variability is small at all levels, with the annual cycle predominant at low levels and the semiannual cycle predominant aloft. The winds at Canton (shown in Fig. 2.9g), 17° east of Majuro and nearer the equator, are similar.

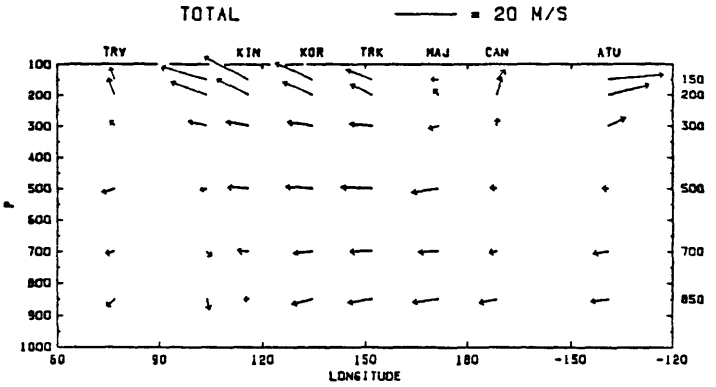
As the final plot in this sequence, Fig. 2.9h presents the annual mean and variability at Atuona, located in the mid-Pacific 10° south of the equator. Westerlies prevail in the upper troposphere. The annual variability of the zonal component is small at all levels, and the phase of the variability is the opposite of the Northern Hemisphere stations.

The annual variability of the Walker Circulation is shown in plots of the seasonal-average equatorial wind and zonal mass flux for the Trivandrum-Atuona cross-section, shown in Figs. 2.10 and 2.11. The climatological values of u and v for each season (Fig. 2.10) demonstrate that $|u| > |v|$ so that M_z reasonably approximates a mass stream function in the longitude-height plane. The error associated with neglecting v is greater for seasonal averages than for the annual average. In the upper troposphere between 100°E and 130°E, where the annual variability in the meridional wind is greatest, the meridional wind has nearly half the amplitude of the zonal wind in the DJF and JJA seasons, so that the neglect of v introduces an error of nearly one-third in the stream function approximation M_z.

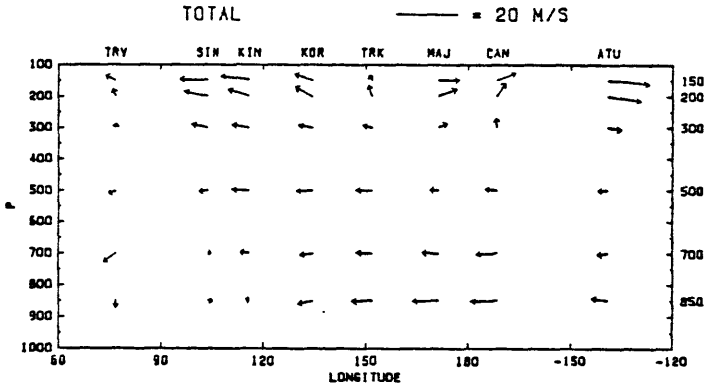
The seasonal variability of the zonal mass flux is shown in Fig. 2.11. The Walker Circulation is most intense in the DJF season, when the maximum westward mass flux is 80×10^9 kg/sec at 150°E, about twice the annual mean (and twice the intensity of the M_z^* cell in Fig 2.1a). The westward tilt with height of the rising branch in DJF is less than the annual mean, and less than the M_z^* cell. In MAM, the Walker Circulation

Figure 2.10 - As in Fig. 2.3a, but for individual seasons: (a) DJF; (b) MAM; (c) JJA; (d) SON.

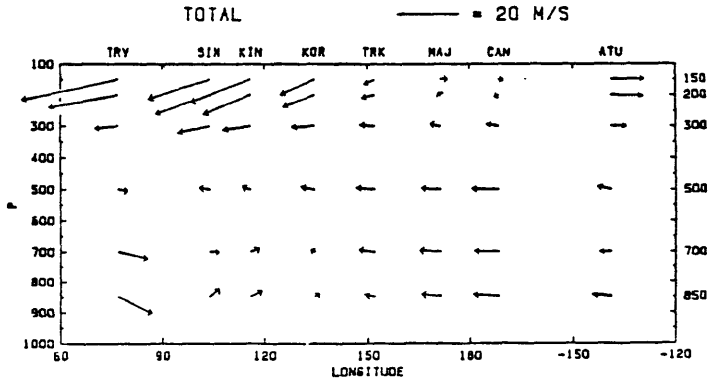
a. UV DJF MEAN



b. UV MAM MEAN



c. UV JJA MEAN



d. UV SON MEAN

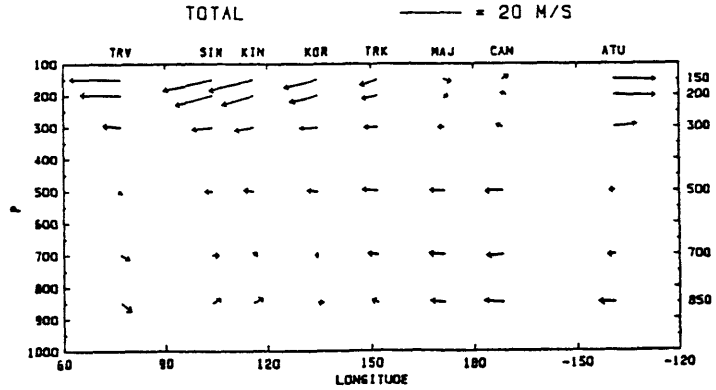
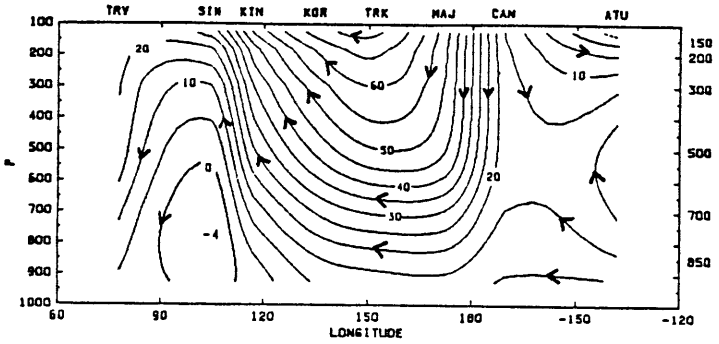
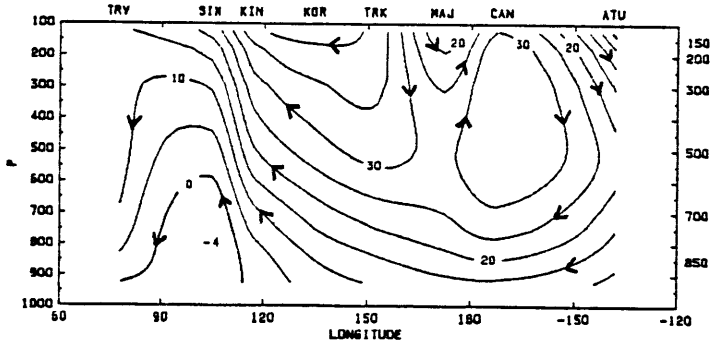


Figure 2.11 - As in Fig. 2.3b, but for individual seasons: (a) DJF; (b) MAM; (c) JJA; (d) SON.

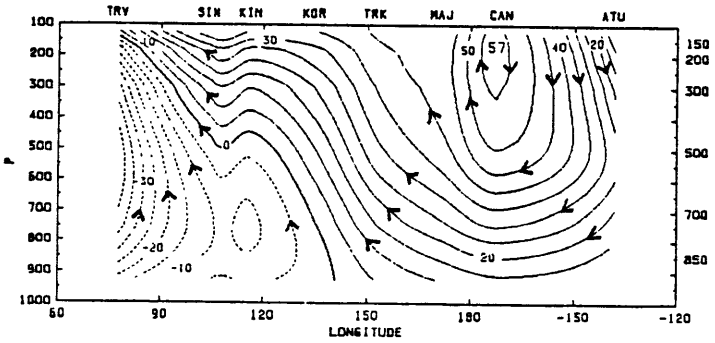
a. M_Z - DJF



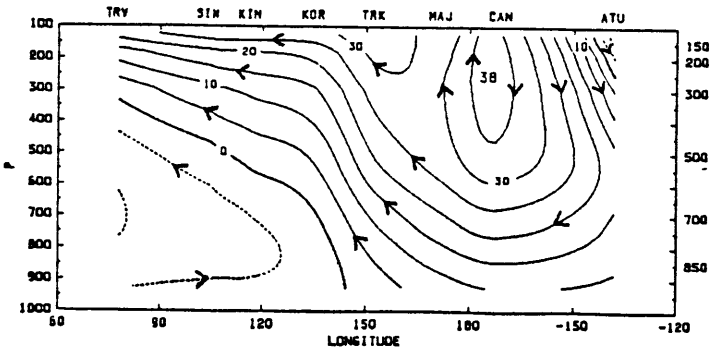
b. M_Z - MAM



c. M_Z - JJA



d. M_Z - SON



weakens and splits, with one cell zcentered at 130°E and a second centered near the date line. In JJA, the circulation intensifies again. The date line cell in JJA has nearly double the intensity of the MAM cell, the central isopleth of the cell increasing from $30x10^9$ kg/sec in MAM to $55x10^9$ kg/sec in JJA. The position of this cell is consistent with the M_z^* cell for this season (Fig. 2.1b), but its intensity is doubled, and the westward tilt with height of the rising branch is apparent in M_z but absent in M_z^*. The reverse cell to the west is dramatically stronger and shifted westward, so that M_z shows concentrated upward motion over Trivandrum, as it should during the Indian summer monsoon. Both cells weaken in intensity again during SON.

The seasonal cycle of the Walker Circulation can be summarized as follows: (1) a confined, intense Walker cell in DJF; (2) broadening to the east and split, weaker Walker cells in MAM; (3) intensification of the Walker Circulation near the date line and the monsoon circulation over the Indian Ocean in JJA; (4) weakening of the zonal circulation intensity with no shift in position in SON; (5) westward shift of the Walker Circulation and intensification in DJF.

2.5 Discussion

In this chapter, the annual variability of the wind field has been calculated based on climatological monthly means, from which the annual and semiannual cycles can be resolved easily. In subsequent chapters, which deal with interannual variability, we prefer to use seasonal means (in order to minimize aliasing due to 40-50 day oscillations, a point which will be discussed further in Chapter 3). Note that such aliasing does not seriously impact the calculation of climatological monthly

means, as evidenced by the reproducibility of the annual and semiannual cycles in separate decades.

The climatological seasonal averages for each station and pressure level are shown in Appendix A. Seasonally averaged climatological wind fields have been presented previously in atlas form by Newell et al. (1972), Gray et al. (1976), and Oort (1983). A comparison of these three seasonal climatologies with the present data revealed no significant differences, despite the different periods of record available for each set of analyses.

This encouraging result implies that the seasonal cycle in the tropics is well-defined, even in records only a few years in length. Hence, the subtraction of climatology to calculate seasonal departures makes physical sense. Since there are parts of the tropical atmosphere where interannual variability exceeds annual variability, and the Southern Oscillation is the dominant signal of interannual variability (both results to be shown in Chapter 3), the presence of El Niño events in the data records of all of the atlases listed above is probably a necessary element for their similarity.

Above the surface, the magnitude of the zonal wind is greater than the magnitude of the meridional wind. At the surface, other studies indicate that the situation is much different. Horel (1982b) found that meridional variability exceeded zonal variability in the tropical Pacific surface wind field. Harrison and Gutzler (1985) showed that the meridional component of the wind was much smaller at 850 mb compared to the surface. Results presented in this chapter demonstrate that the reduction with height of the meridional wind continues up to the middle troposphere.

The annual variability of the meridional wind at the top of the troposphere has also been shown here to die out with decreasing height over a small pressure interval. The annual cycle in upper tropospheric meridional wind associated with the Hadley circulation is confined to a narrower layer than the semiannual cycle in the zonal wind. Meridional winds of significant amplitude are confined to layers approximately 150 mb thick at the top and bottom of the troposphere.

The observation that $|u| >> |v|$ near the equator allows the neglect of meridional winds in our calculation of zonal mass flux cells, which can be interpreted as approximations to streamlines in the longitude-height plane. The zonal mass flux over the western Pacific was used to examine the annual mean and seasonal variability of the Walker Circulation. The annual mean Walker Circulation was shown to have a pronounced westward tilt with height, consistent with the observed displacement of the center of upper tropospheric divergence in the annual mean zonal wind field relative to the center of lower tropospheric convergence. The Walker Circulation displayed a seasonal cycle featuring a semiannual cycle in intensity, with maximum intensity in the DJF and JJA seasons. The vertical structure of the rising branch of the Walker Circulation derived from M_z has a westward tilt with height in all seasons.

Including the zonal mean zonal wind in the definition of the zonal mass flux emphasizes the strength of the Walker Circulation. Mass flux intensity derived from M_z^* implies that the monsoon dominates the mass circulation field near the equator in JJA, whereas the M_z cells associated with the Walker and monsoon circulations have about the same intensity. We shall return to the zonal mass flux to consider its temporal anomalies in Chapter 4.

Chapter 3

SPATIAL STRUCTURE OF SEASONAL WIND ANOMALIES

3.1 Introduction

Historically, observational studies of tropical seasonal anomalies have described individual climatic phenomena, each of which has a distinct signal. Examples of such phenomena are the monsoons, the Hadley circulation, and the Southern Oscillation.

The monsoon regimes over India and Southeast Asia exhibit pronounced interannual variability, which has been an object of study for many years because of the profound social and economic implications of monsoon rains. Shukla (1984) has recently reviewed the observational record of the Indian summer monsoon. Significant interannual variability is evident in the monsoon system, but its causes or predictability are still poorly understood.

The Hadley cell, describing the mean meridional circulation in the tropics, also varies in intensity from year to year. Bjerknes (1966) viewed the interannual variability of the Hadley circulation as a mechanism for tropical-extratropical interaction.

The Southern Oscillation, a prominent zonally oriented fluctuation in the sea-level pressure field over the tropical South Pacific Ocean, is the surface manifestation of a mass circulation cell called the Walker Circulation (discussed in Chapter 2). The Southern Oscillation is associated with the equatorial Pacific rainfall and sea surface temperature variability which accompany oceanic El Niño events (Bjerknes, 1969; Julian and Chervin, 1978; Rasmusson and Carpenter, 1982).

A number of studies have shown these climatic phenomena to be interrelated. For example, Krishnamurti (1971) and Krishnamurti et al. (1973) showed that fluctuations in the meridional and zonal divergent circulations at 200 mb over the Pacific were coupled to the region of intense convection over the Indonesian region, and Rasmusson and Carpenter (1983) found significant correlations between summer monsoon rainfall over India and the Southern Oscillation.

Within the past decade, the Southern Oscillation has been shown to be the dominant signal in the global tropics on seasonal time scales, and therefore it has become a standard index for observational studies of tropical interannual variability. Kidson (1975) found that time series of the gravest components of empirical orthogonal function analyses of monthly mean tropical sea level pressure, temperature, and rainfall, were each highly correlated with sea level pressure fluctuations at Djakarta [6°S 107°E], an index of the Southern Oscillation. Subsequently, the Southern Oscillation was shown to be correlated with seasonal anomalies in the extratropical circulation (Horel and Wallace, 1981; Arkin, 1984; Mysak, 1984). Troup (1961, 1967) showed that equatorial upper level wind fluctuations over the Indian Ocean and central Pacific are negatively correlated, and suggested that this opposition was associated with the Southern Oscillation. Arkin (1982) and Selkirk (1984) examined the relationship between 200 mb tropical winds and the SOI, using a twelve-year record of the National Meteorological Center tropical analysis.

High correlations were found, particularly for the zonal wind component. A sample of their results are shown in Fig. 3.1, which contains (a) a time series of a Southern Oscillation Index; (b,c) maps of the

correlation coefficient between this index and time series of seasonally averaged zonal and meridional wind components (for the DJF season), taken from Selkirk (1984); (d) the spatial variability associated with the first EOF of combined zonal and meridional 200 mb wind seasonal anomalies, taken from Arkin (1982).

The Southern Oscillation Index used by Arkin and Selkirk, which shall also be used in this thesis, is the difference between normalized anomalies of seasonally-averaged sea level pressure at Tahiti [18°S 150°W] and Darwin [12°S 131°E]. This particular index (which shall be abbreviated SOI hereafter) was recommended by Chen (1982), who determined that it contained a greater fraction of its variance within the 2-7 year period band compared with similar indices. During El Niño events, sea surface temperatures (SSTs) are abnormally warm over the eastern Pacific, meaning that the climatological east-west SST gradient is reduced and the Walker circulation is weakened. Therefore the (Tahiti-Darwin) pressure gradient is reduced and the SOI is negative. Notice that the SOI has much greater amplitude in the decade of the seventies than it does in the sixties. Arkin (1982) and Selkirk (1984) used the same data set, spanning the period 1968-1979, which contained one very weak El Niño and two strong ones.

The most prominent features on Selkirk's DJF zonal wind correlation map (Fig. 3.1b) are the region of positive correlation in the mid-Pacific on the equator, and the regions of negative correlation about 25° poleward in both hemispheres. Additional centers of negative correlation appear over the northeastern Indian Ocean and over the equatorial Atlantic Ocean.

The geographical extent of high correlations in the meridional wind

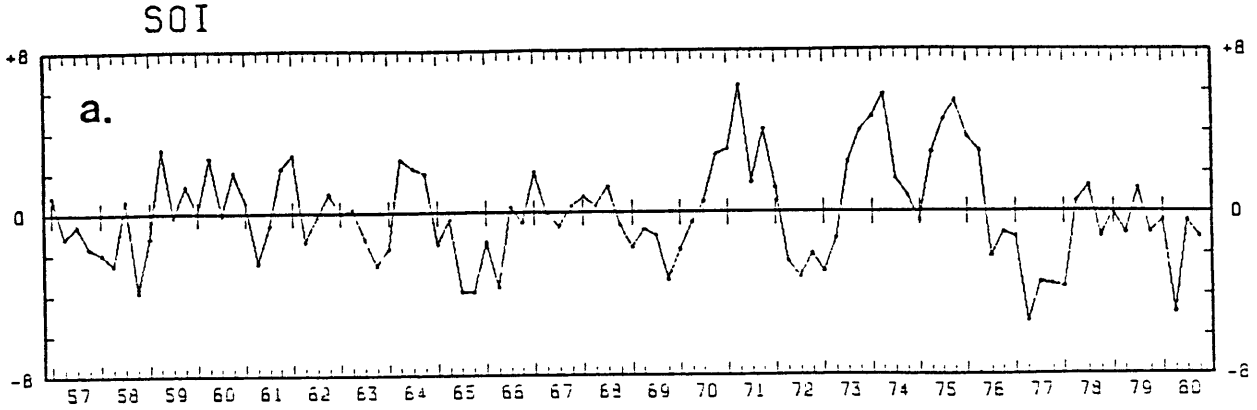
Figure 3.1

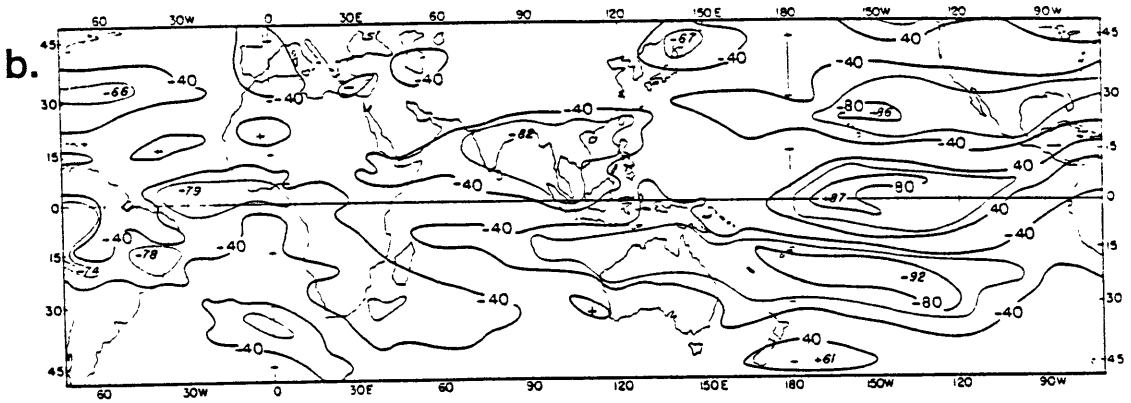
(a) Time series of Southern Oscillation Index (SOI).

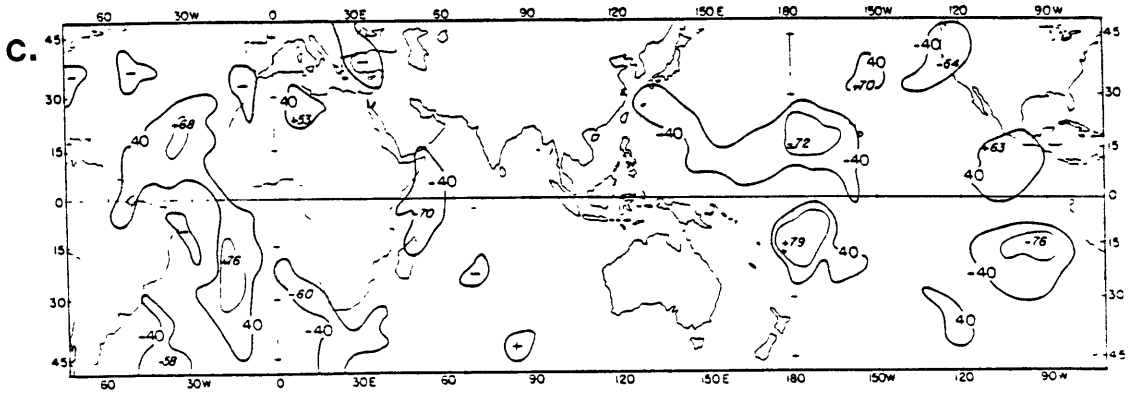
(b) Correlation coefficient between seasonal anomalies of zonal wind at 200 mb and SOI for the DJF season, taken from Selkirk (1984).

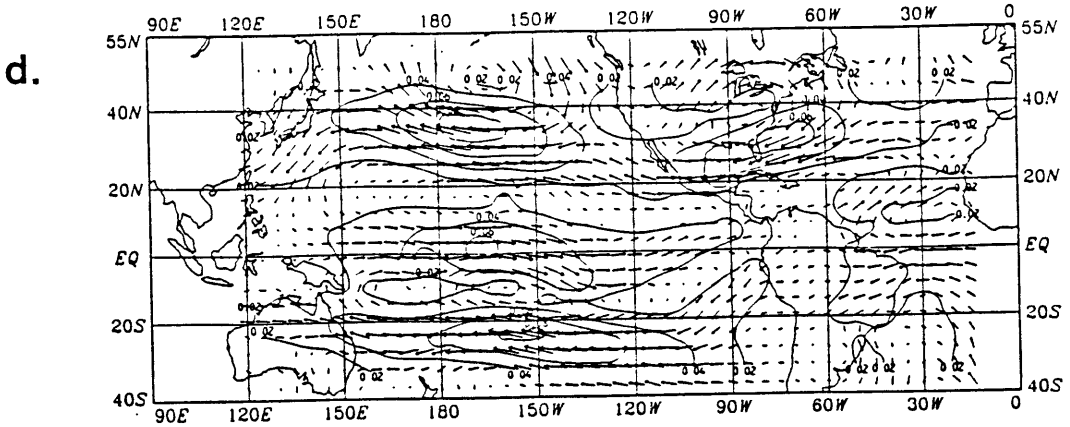
(c) As in (b), but for seasonal anomalies of meridional wind.

(d) Spatial variability associated with gravest mode of an EOF analysis of combined zonal and meridional 200 mb seasonal wind anomalies, taken from Arkin (1982).


SOI
a.
+8
0
-8
57 58 59 60 61 62 63 64 65 66 67 68 69 70 71 72 73 74 75 76 77 78 79 80


b.


c.


d.
90E 120E 150E 180 150W 120W 90W 60W 30W 0
55N
40N
20N
EQ
20S
40S

field is more limited (Fig. 3.1c). Positive SOI is associated with meridional anomalies at 15° latitude in both hemispheres directed toward the equator at the western end of the strip of anomalous equatorial westerlies, with oppositely-directed meridional anomalies at the eastern end.

Together, the anomalous DJF zonal and meridional wind patterns imply the existence of a pair of troughs straddling the equator over the eastern Pacific. This zonal wind pattern was repeated in the statistics for other seasons, but the associated meridional wind anomalies were less reproducible.

The principal features of the correlation maps are reproduced in the gravest EOF mode described by Arkin (1982), shown in Fig. 3.1d. Over the Pacific, the EOF mode includes positive zonal wind anomalies along the equator, negative zonal wind anomalies along latitudes 30°N and 25°S, and cyclonic circulations centered just east of the dateline at 15°N and 10°S. Since the EOF mode is determined independently of the SOI, its close resemblence to the SOI - wind correlation patterns indicates that the El Niño - Southern Oscillation signal, which is defined in terms of surface variables, is prominent in the upper troposphere as well.

Arkin (1984) determined further that the residual 200 mb seasonal wind variance <u>not</u> correlated with the SOI had very little power at interannual time scales, suggesting that the residual was effectively 'noise'. Therefore, the SOI - wind correlation maps and wind EOF calculations are complementary analyses describing the same tropical anomaly patterns.

All of these studies have described exclusively the horizontal structure of variability, either at the surface or at 200 mb. The

observed vertical structure of tropical variability has been investigated only for higher frequency fluctuations. The vertical structure of daily wind fluctuations over the tropical western Pacific was studied by Adams (1971) using one-dimensional empirical orthogonal functions (1dEOFs). He found that the statistically dominant mode of Northern Hemisphere summertime meridional wind fluctuations had a "baroclinic" structure, i.e. wind anomalies of opposite sign in the upper and lower troposphere. In the Northern Hemisphere winter season, however, the dominant mode had an "equivalent barotropic" structure, with anomalies of like sign throughout the troposphere.

The presence of a wide range of frequencies in time series of daily data makes it difficult to interpret Adams' results. Adams sought to explain the vertical structure in terms of tropical easterly waves, which have a time scale of about one week (Wallace, 1971). He interpreted the summer structure as the signature of tropical easterly waves, and attributed the winter structure to the lack of such waves. However, Madden and Julian (1971) documented the existence of a peak in the variance spectrum of the zonal wind at stations near the equator at a period of 40-50 days. Recent work (Madden, personal communication) indicates the presence of the 40-50 day wave in meridional winds as well. The variability in Adams' data may have been associated primarily with the 40-50 day wave.

The 40-50 day signal has also been found in outgoing longwave radiation statistics (Weickmann, 1983), and in time series of atmospheric angular momentum (Anderson and Rosen, 1983). In order to minimize spurious interannual variability due to aliasing of the 40-50 day signal, the monthly mean data taken from Monthly Climatic Data for

the World were averaged into seasonal means for the interannual variability calculations presented in Chapters 3 and 4.

Modeling studies of tropical tropospheric interannual variability have focused on simulating the time-independent circulation response to large-scale stationary heat sources. Gill (1980) investigated the response to prescribed forcing of a shallow water model in which the horizontal and vertical components of motion on an equatorial β-plane are separated, following the procedure formulated by Matsuno (1966). Gill was interested in the horizontal response, so he assumed that the vertical structure was simply the first baroclinic mode,

$$V(z) = V_h \sin(\pi z/D)$$

where z is height and D is the depth of the troposphere. This structure assumes that the heating is distributed sinusoidally in the vertical, with maximum amplitude at height D/2. The equivalent depth h of the shallow water model was then determined by

$$h = c^2/g = (N^2D^2)/(\pi^2 g) \qquad [3.1]$$

where c is the shallow water phase speed and N is the Brunt-Vaisala frequency. Gill assumed values for N and D of .012 s^{-1} and 15 km, so that the equivalent depth of the response was about 350 m and the implicit level of maximum heating was 7.5 km (about 400 mb).

The vertical structure assumption was tested within the context of the shallow water equations by Geisler and Stevens (1983), and Lim and Chang (1983). Geisler and Stevens verified that the sinusoidal wind structure assumed by Gill (1980) represented the correct response when the rigid lid at z=D implicit in Gill's calculation was moved to a much higher level. Lim and Chang (1983) tested the sensitivity of the shallow water model to arbitrary changes in the equivalent depth. They

considered the implications of assuming an equivalent depth so large that the response was effectively equivalent barotropic. An equivalent depth of 1500 m allowed such a response in their model. The larger phase speed of such a mode meant that its meridional extent was greater, making the mode less subject to equatorial trapping. Its westward-propagating Rossby component could propagate entirely around the equator and affect the response to the east of the forcing region. They argued that such behavior was consistent with the observed tendency for tropical upper tropospheric temperatures to fluctuate in phase at all longitudes on an interannual time scale, and also consistent with the apparent tropical forcing of middle latitude teleconnections with an equivalent barotropic structure (Horel and Wallace, 1981).

Geisler (1981) simulated the Walker Circulation using a steady primitive equation model linearized about a motionless basic state with constant static stability. He examined the sensitivity of this model to changes in the vertical structure of the prescribed diabatic heating and dissipation. He obtained realistic amplitudes using the Yanai et al. (1973) profile with damping supplied by cumulus friction. The most serious discrepancy between the model's response, expressed in terms of the zonal mass flux and observations (the Newell et al. (1974) M_z^* field for DJF shown in Fig. 2.1a) was that the model's center of overturning was around 600 mb, whereas the observed M_z^* overturning occurred between 400 and 500 mb.

The validity of many of these modeling studies hinges on the relevance of the heating profile calculated by Yanai et al. (1973). The profile was derived from synoptic data observed over the western Pacific. It was intended to represent the atmospheric heating due to

moisture condensation in towering cumulus clouds. The profile's vertical structure has a broad maximum near 400 mb and decreases to near zero at the bottom and top of the troposphere.

The vertical structure of the Yanai et al. heating profile was questioned by Houze (1982), who included the diabatic effect of stratus clouds in a heating profile based on GATE data from the tropical Atlantic. Houze argued that in the deck surrounding the cumulus clouds, moisture condenses in the upper troposphere and evaporates below cloud level in the lower troposphere. This effect, when added to the heating from the cumuli, yielded a heating profile with a pronounced maximum in the upper troposphere and weak net heating in the lower troposphere. When this profile was used to force a linearized primitive equation model (Hartmann et al., 1984), the effect was to raise the node of the wind response to about 400 mb and tilt the zonal circulation cells so that the upper branch of the cell was located to the west of the lower branch. Hence, compared to the circulation cells forced by a Yanai et al. profile, the circulation cells forced by Houze's elevated heating profile more closely resembled the DJF M_z^* field.

The vertical structure of interannual variability is a major source of uncertainty in modeling studies. However, the observational studies to date have examined only the horizontal structure of variability, either at the surface or at the 200 mb level. In this chapter, the three-dimensional distribution and structure of tropical interannual wind fluctuations based on station rawinsonde data is documented and described.

First, the geographical and vertical distribution of interannual

variability will be examined in Section 3.2. The magnitude and distribution of interannual variance will be compared to the periodic annual variability discussed in the previous chapter. Then, the vertical structure of interannual variability will be examined. The 1dEOF analysis technique will be employed in Section 3.3 to define the characteristic vertical structure of seasonal wind anomalies at each station. Section 3.4 considers the three-dimensional structure of interannual variability. In part (a), correlations between the SOI and the three-dimensional wind field are presented, and the vertical structure of the correlation statistics are compared with the vertical structures derived from the 1dEOF calculations from Section 3.3. In part (b), a separate two-dimensional EOF (2dEOF) calculation is developed to describe the longitude-height structure of seasonal zonal wind variability over the Trivandrum-Atuona cross-section. A summary and discussion in Section 3.5 conclude the chapter.

3.2 Geographical distribution of interannual variance

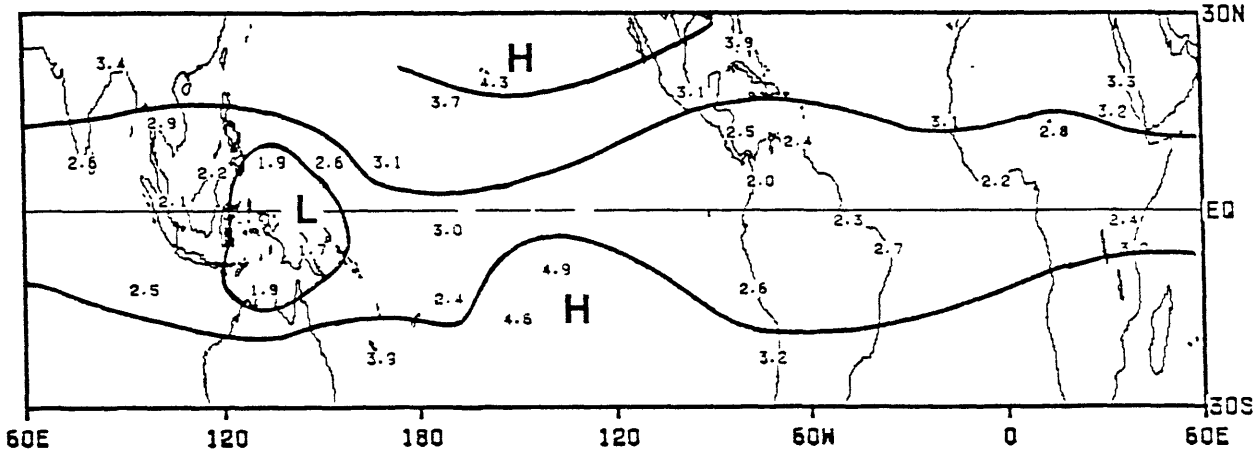
Fig. 3.2 contains plots of the standard deviation of seasonal anomalies of the zonal wind at three levels: 200 mb, 500 mb, and 850 mb. Data from all calendar seasons are included in these statistics, with separate seasonal means (shown in Appendix A) removed for each season.

At 850 mb, the standard deviation of the zonal wind is of order 1 m/s. This number varies from less than 0.5 m/s along the west coast of South America south of the equator, to greater than 1.5 m/s at islands in the equatorial western Pacific. The region of maximum variability corresponds to the location of greatest surface wind anomalies associated with ENSO events (Rasmusson and Carpenter, 1982). During the

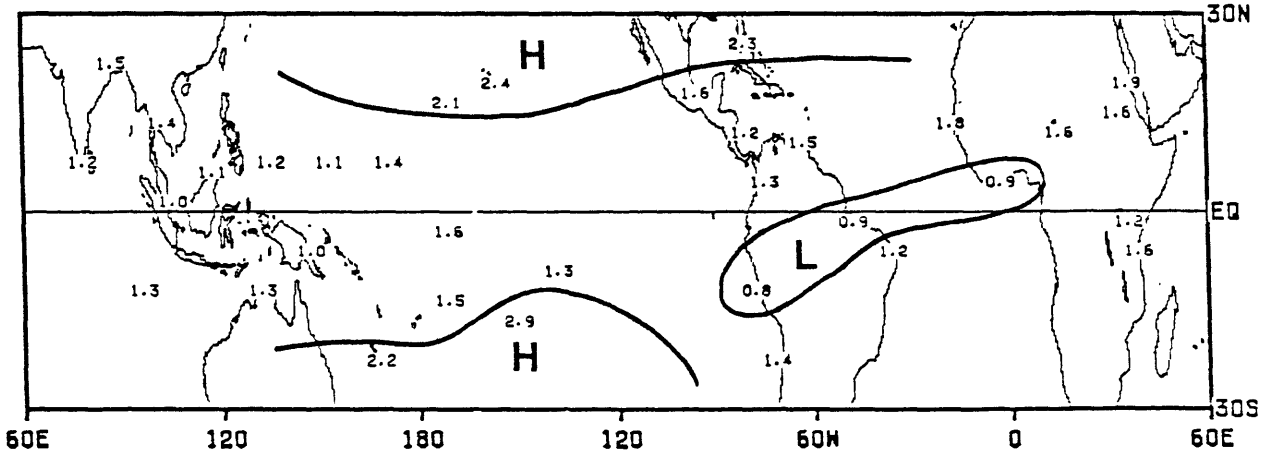
Figure 3.2 - Standard deviation of time series of seasonal anomalies of zonal wind (all seasons included). Units m/s.

(a) 200 mb level, with 2, 3, and 4 m/s contours drawn.
(b) 500 mb level, with 1 and 2 m/s contours drawn.
(c) 850 mb level, with 0.5 and 1.5 m/s contours drawn.

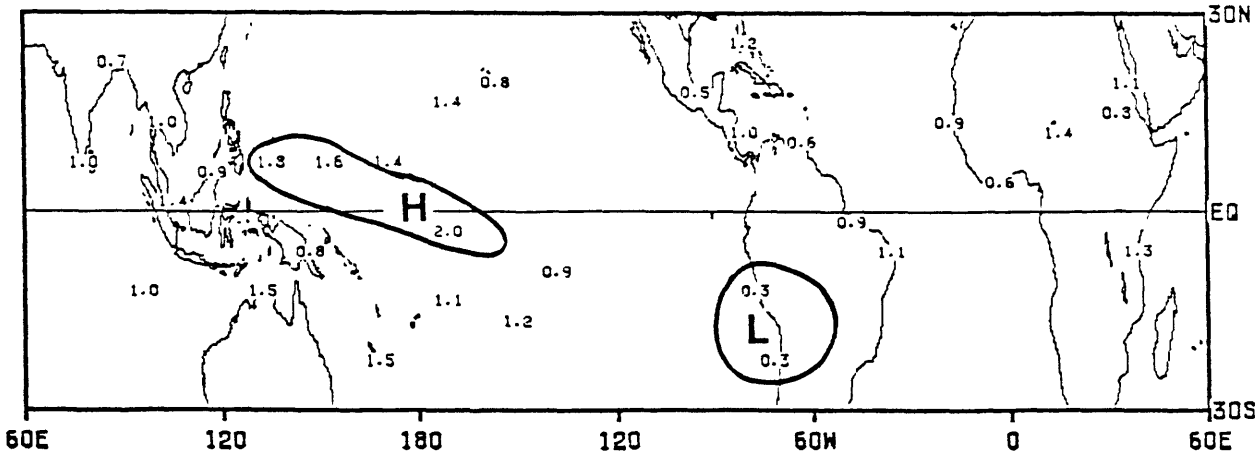
a. SIGMA U 200 MB



b. SIGMA U 500 MB



c. SIGMA U 850 MB



"Transition" phase of the composite event, defined by Rasmusson and Carpenter as the period from August to October following South American coastal sea surface temperature warming, westerly wind anomalies exceed 2.5 m/s near 5°N 160°E.

Harrison and Gutzler (1985) considered the relationship between surface and 850 mb level wind variability at five western Pacific islands, and found that the standard deviation of monthly mean zonal winds increased by a factor of two from the surface to 850 mb. It is apparent from Fig. 3.2, however, that the variability equatorward of 10° does not increase further with height in the lower troposphere.

At 500 mb, horizontal gradients of zonal wind variability are small. A slight minimum, where the standard deviation is less than 1.0 m/s, exists near the equator over South America and western Africa. Maximum variability occurs over the subtropics of the Pacific Ocean in both hemispheres.

A similar pattern is observed at 200 mb, but the variability gradients are larger. The variability increases with height from 500 mb to 200 mb everywhere. The standard deviation is generally less than 3.0 m/s within 12° of the equator except over the eastern Pacific, where the subropical maxima extend equatorward. Minimum variability occurs near the equator around 130°E.

The interannual variability of the zonal wind increases with height everywhere in the tropics except over the equatorial western Pacific, where the variability decreases with height in the lower troposphere and increases with height in the upper troposphere. The difference between the two vertical profiles of variability is illustrated in Fig. 3.3. The interannual standard deviation of seasonally averaged zonal wind for all

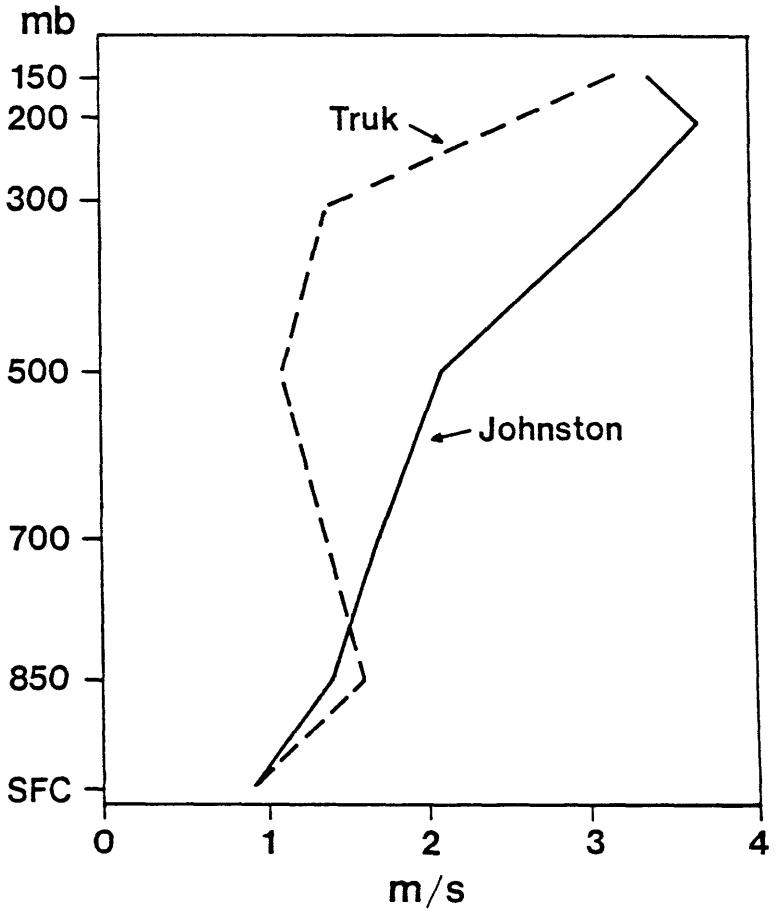


Figure 3.3 - Vertical profile of the standard deviation of seasonal anomalies of zonal wind at Truk (7°N 151°E, dashed line), and Johnston (17°N 170°W, solid line).

six pressure levels at Truk [8°N 152°E] is plotted as a dashed line, and the corresponding profile for Johnston [17°N 170°W] is plotted as a solid line. The two curves have been extended to the surface using the surface wind data of Harrison and Gutzler (1985).

The variability increases monotonically with height at Johnston up to its maximum value at 200 mb. This profile is typical of geopotential height variability (in all frequency ranges) in middle latitudes (Blackmon et al., 1979). Since large scale wind fluctuations in the extratropics are nearly geostrophic, this profile of variability applies to the mid-latitude wind field as well.

The Truk profile, with its mid-tropospheric minimum, is similar to the simple $\cos(\pi z/D)$ profile assumed by Gill (1980) as the stationary response to a near-equatorial latent heat anomaly, but with two important differences. These are at the bottom, where boundary layer dissipation could explain the decrease in variability below 850 mb, and at the top, where the variability increases sharply above 300 mb.

This vertical profile of interannual variability is observed only over the equatorial western Pacific. It is distinctly different from the vertical profile of daily zonal wind variability, which increases monotonically with height (Newell et al., 1972; Oort, 1983).

The standard deviation of seasonal anomalies of the meridional wind is shown in Fig. 3.4. At 850 mb, a broad region of low variability (less than 0.5 m/s) extends across the equatorial Pacific. The variability increases with height everywhere to approximately 1.5 m/s at 200 mb. Above 850 mb, the longitudinal gradients of variability are negligible; at each level, minimum values of the standard deviation are found along the equator and the variability increases poleward in both hemispheres.

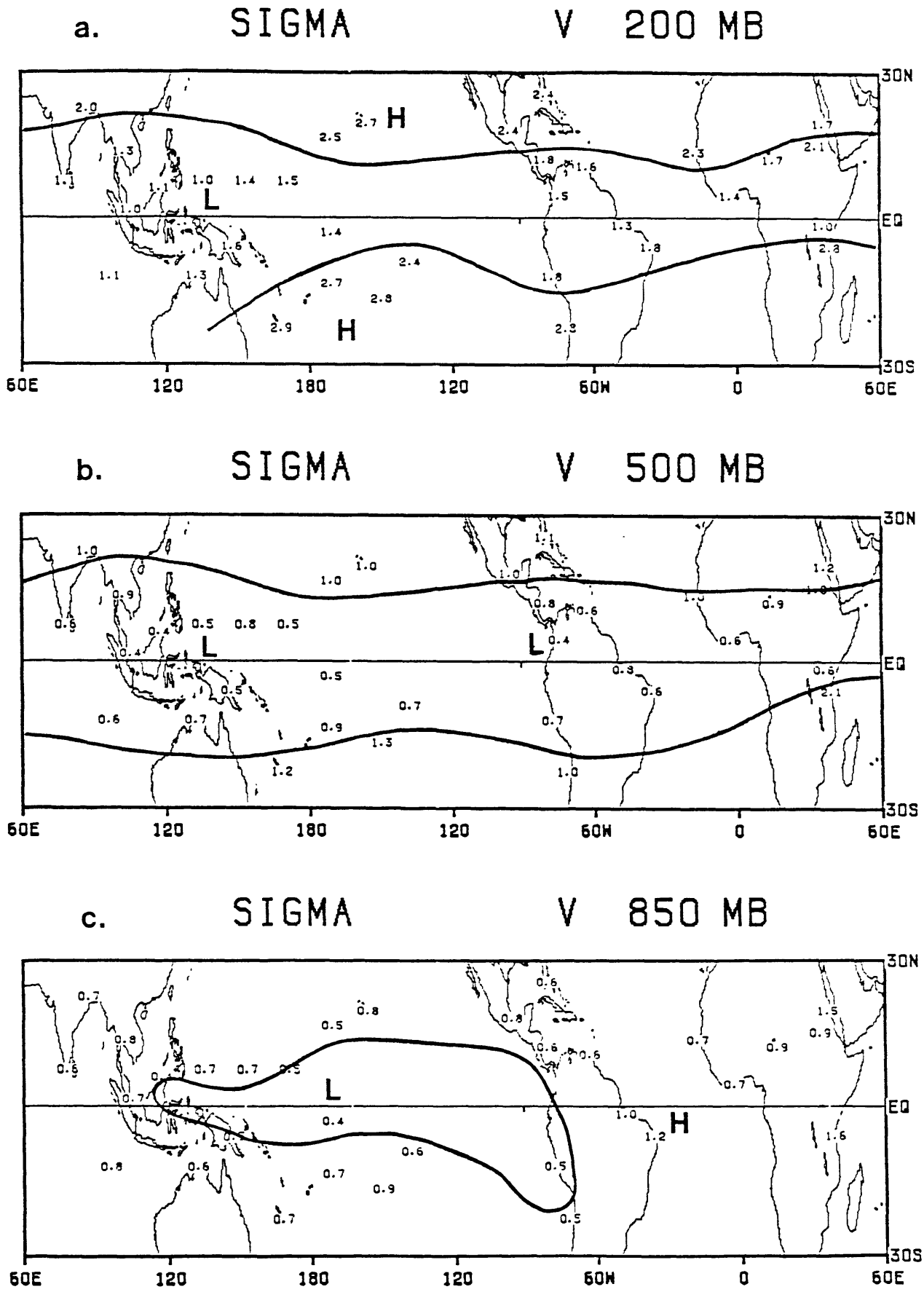
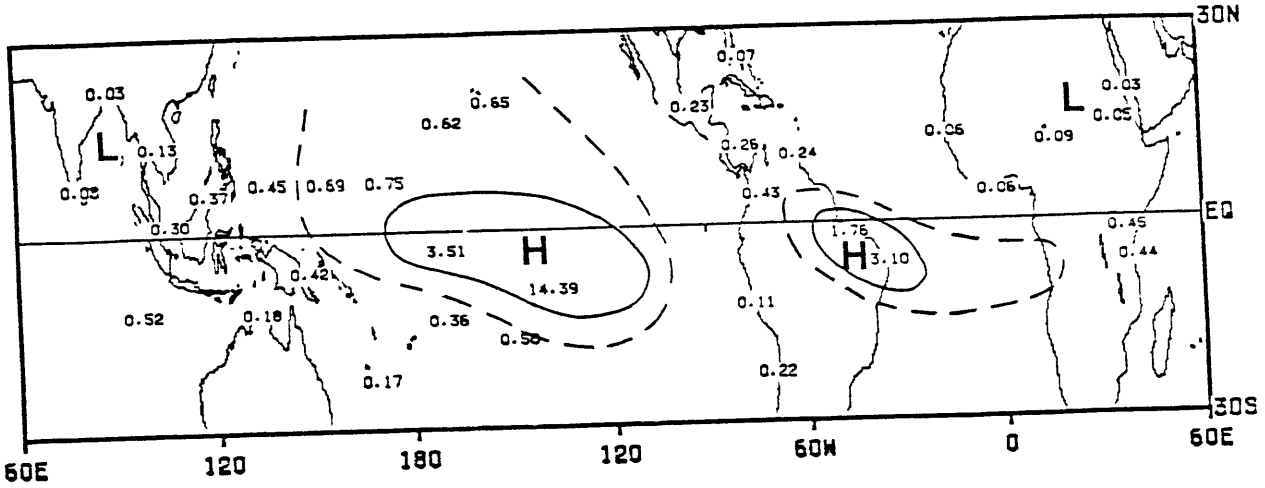


Figure 3.4 - As in Fig. 3.2, but for seasonal anomalies of meridional wind.

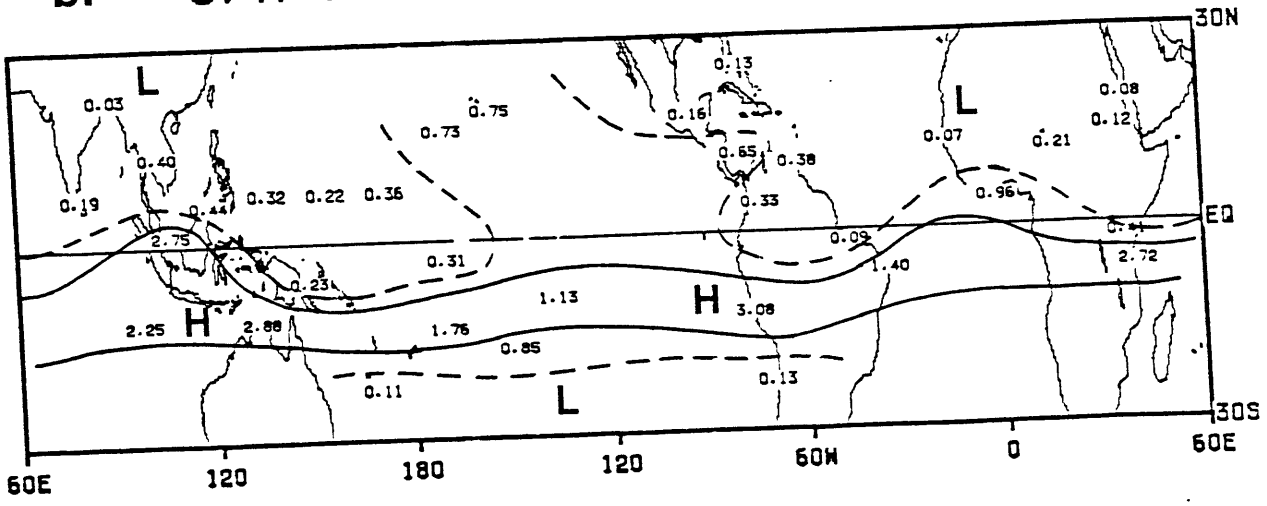
Figure 3.5 - Ratio of interannual variance to periodic variance (annual + semiannual cycles) for zonal wind at:

(a) 200 mb level
(b) 500 mb level
(c) 850 mb level

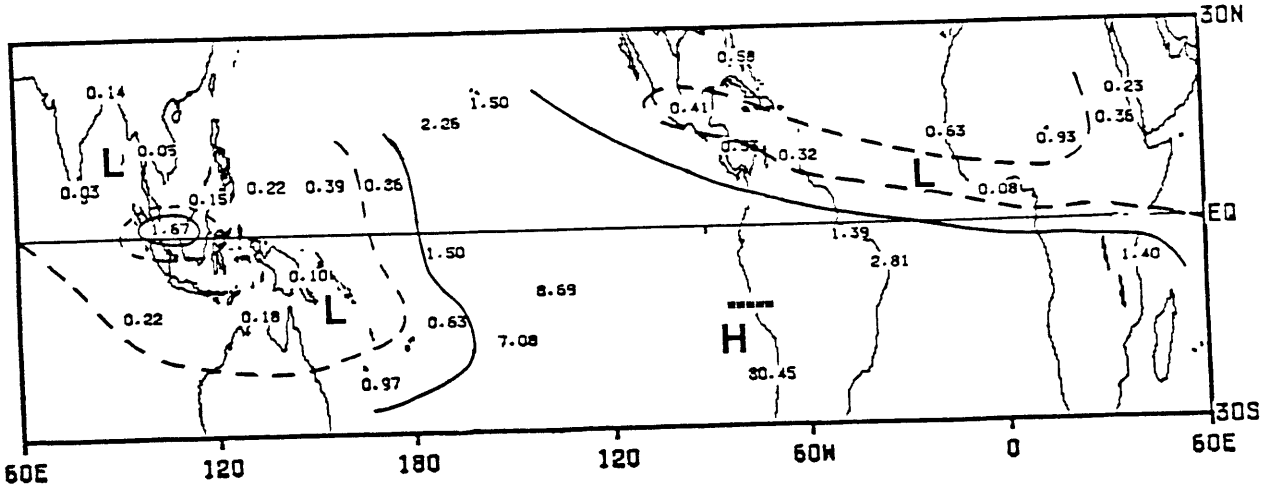
a. S/R RATIO U 200 MB



b. S/R RATIO U 500 MB



c. S/R RATIO U 850 MB



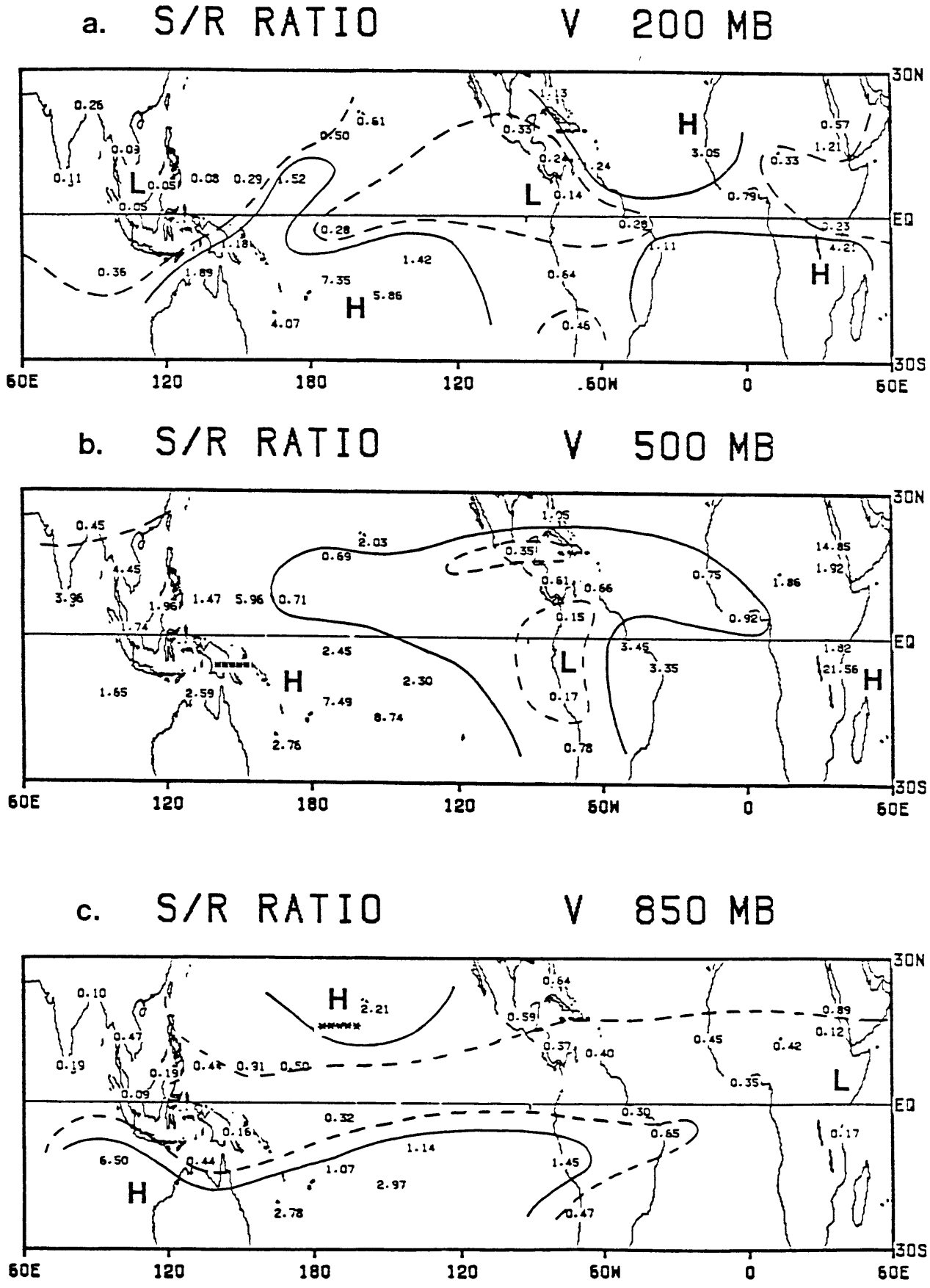


Figure 3.6 - As in Fig. 3.5, but for meridional wind.

Thus, the vertical profile of meridional wind variability is the same everywhere in the tropics. No counterpart to the western Pacific zonal wind vertical profile is found in the meridional wind field.

The magnitude of interannual variability relative to the periodic variability is described by Figs. 3.5 and 3.6, which contain plots of the variance ratio

$$S/R = \frac{\sigma_I^2}{0.5\ (R_1^2 + R_2^2)} \qquad [3.2]$$

where σ_I^2 is the interannual variance (the square of each standard deviation shown in Figs. 3.2 and 3.4), R_1 is the amplitude of the annual cycle, and R_2 is the amplitude of the semiannual cycle. The denominator in [3.2] is the quantity VAR12 shown for each station and pressure level in Table 2.1. If S/R is much less than 1.0, then the annual variability is much greater than interannual fluctuations (for example, this is the case for mid-latitude surface temperatures, since the warmest of winters is still much colder than a very cool summer). If the ratio equals 1.0, then interannual and annual variability are equal. Where there is very little annual variability, S/R can be much greater than one.

At 850 mb, the amplitude of the semiannual cycle is smaller than the amplitude of the annual cycle or the interannual variability for both the zonal and meridional wind components (with the exception of the southeastern Pacific region, where the standard deviation of each component of the variability is less than 1 m/s), and the interannual variance is not strongly dependent on location. Hence, the geographical distribution of S/R is determined primarily by the amplitude of the annual cycle. For the zonal wind at 850 mb, S/R is greater than one over the entire tropical eastern Pacific and south of the equator over South

America and Africa. Over the western Pacific, Southeast Asia, Central America, and North Africa, periodic variability is greater than interannual variability.

At 500 mb, interannual variability of the zonal wind is greatest compared with annual variability in a strip around 10°S latitude, which again corresponds to a region of small annual cycle amplitude. The S/R ratio is less than one throughout the Northern Hemisphere, but remains highest over the subtropical eastern Pacific. At 200 mb, interannual variability is comparable to annual variability only over the eastern Pacific and equatorial South America.

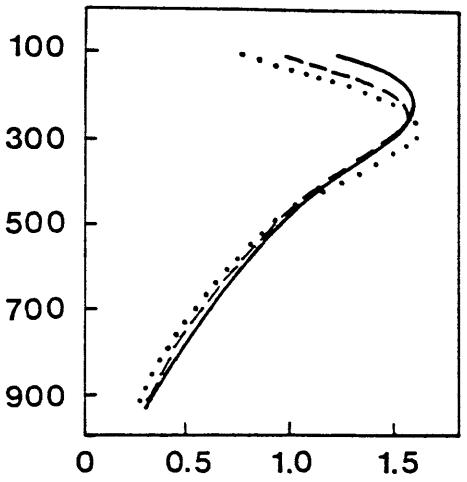
The vertical structure of S/R in the meridional wind field is dominated by the vertical structure of the annual cycle associated with the Hadley circulation. Where the local Hadley circulation is strong, at 850 mb and 200 mb over Africa, the maritime continent, and northern South America, S/R is small. Over the subtropical Pacific, particularly in the Southern Hemisphere, S/R is greater than one and most of the variance is interannual rather than seasonal. At 500 mb, the interannual component dominates the total variability everywhere except western South America and Central America, where the annual cycle in v is appreciable.

3.3 Vertical structure of interannual variability

The local vertical structure of seasonal wind anomalies is examined in this section through the application of one-dimensional empirical orthogonal function (1dEOF) analysis. This technique transforms a set of time series of winds at n points in space into a set of time series of n orthogonal modes which provide an efficient and (one hopes) a physically meaningful framework for discussing variability.

This analysis technique has become widely used in climate studies. Its application to studies of the vertical structure of atmospheric disturbances began with the work of Holmström (1963), who sought to determine the average structure of geopotential height, temperature, and wind components for the Northern Hemisphere extratropics by considering soundings from a large network of radiosonde stations on a single day. Blackmon et al. (1979) used the same technique to examine spatial variations in the vertical structure of geopotential height fluctuations by carrying out separate EOF expansions for the time series associated with each station. Adams (1971) compared vertical EOF expansions of daily time series at several stations in the tropical western Pacific.

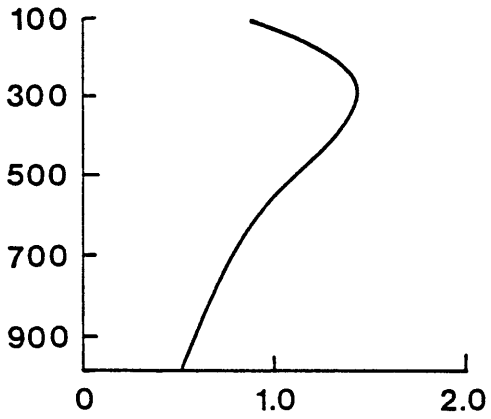
A sample of these results is shown in Fig. 3.7. The gravest modes of Holmström's analysis for geopotential height, and zonal and meridional wind components, are shown in Fig. 3.7a. For each parameter, anomalies from the mean state (which in this case is a spatial average) tend to have the same sign at all levels, with the amplitude of the anomaly increasing with height. Blackmon et al. found that temporal height anomalies had the same vertical structure (Fig. 3.7b). Adams found that the vertical structure of meridional wind anomalies in the tropical western Pacific varied from place to place, and also from season to season. At Truk [8°N 152°E], meridional wind anomalies tended to have a vertical structure similar to extratropical anomalies during his February-May period, but a very different vertical structure, with a node in mid-troposphere, during the July-October season (Fig. 3.7c). He denoted the vertical structure in which anomalies have the same sign at all levels as "equivalent barotropic", and the structure with anomalies of different sign in the upper and lower troposphere as "baroclinic".



a.

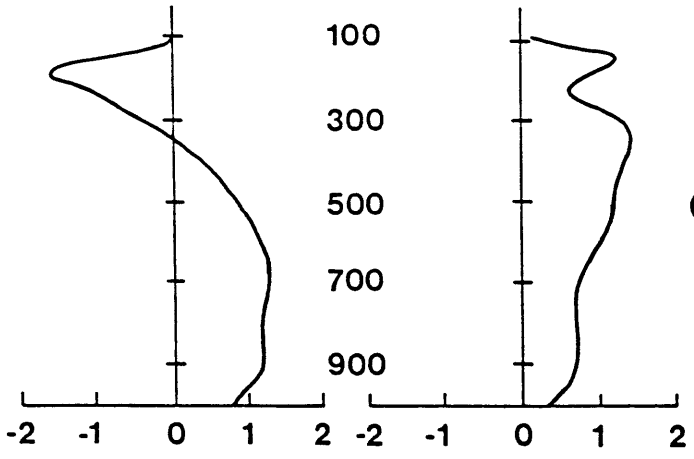
Figure 3.7

(a) Shape of the dominant EOF mode of temperature (solid line), zonal wind (dotted line) and meridional wind (dashed line), taken from Holmstrom (1963).



b.

(b) Shape of the dominant EOF mode of daily wintertime geopotential height fluctuations at [50°N 160°W], taken from Blackmon et al. (1979).



c.

(c) Shape of the dominant EOF mode of daily meridional wind fluctuations at Truk [8°N 152°E] for July-October 1967 (left) and February-May 1967 (right), taken from Adams (1971).

In this section, interannual variability of wind components at each station is examined, following the 1dEOF procedure developed by Blackmon et al. (1979). The analysis technique is discussed in detail in Section 2 of Appendix B. In brief, the procedure is as follows.

First, the time mean is removed from the time series of winds separately for each station, season, and pressure level. 1dEOF analyses are then carried out on the time series of seasonal anomalies, grouping the data in several different ways. The first set of analyses described below treat the zonal and meridional wind components separately for the four calendar seasons. Then, a single analysis for individual stations is made including all seasons together. In each case, the 1dEOFs are the eigenvectors of the mass-weighted covariance matrix of wind fluctuations, i.e. the solutions of

$$\left[\overline{u_l\, u_m}\, w_{lm}\right]\left[E_l^k\right] = \lambda^k E_l^k \qquad k,l,m = 1,..,6$$

where u_l is a scalar wind component at level l, w_{lm} is a mass-weighting factor, λ^k and E_l^k are the eigenvalues and eigenvectors, and the overbar represents a time average. By convention, the eigenvalues are ordered such that $\lambda^1 > \lambda^2 > \ldots > \lambda^6$. The eigenvalues represent the fraction of variance associated with each eigenvector. The eigenvectors form an orthonormal basis set, so that the original time series of winds can be reconstructed by summing together the complete set of eigenvectors multiplied by the associated time series of principal components P^k, which are defined by projecting the eigenvectors E_l^k onto the wind field at each point in time.

In the subtropics of both hemispheres, the vertical structure of interannual wind variations is similar to the equivalent-barotropic

structure documented by Holmström and Blackmon et al. in the extratropics. As an example, Fig. 3.8 shows the gravest mode of zonal wind variability at Johnston [17°N 170°W], for seasonal anomalies for (a) the DJF season only; (b) the JJA season only; and (c) all seasons, along with the percentage of the total mass-weighted variance explained by the mode. The vertical structure of the gravest mode varies little from season to season, so that the mode based on year-round data has the same structure as any of the seasonal modes. This single mode explains about 80% of the total interannual variance.

Near-equatorial wind fluctuations typically exhibit a different vertical structure. Plots of the gravest 1dEOF mode derived from zonal wind anomalies at Canton [3°S 171°W] are shown in Fig. 3.9, for DJF, JJA, and all seasons. Over half the zonal variance is associated with a vertical structurein which wind anomalies have opposite signs in the upper and lower troposphere. Generally, the amplitude of the gravest mode at near-equatorial stations has its maximum amplitude in the upper troposphere, as at Canton. Following Adams (1971), a mode with this shape shall be denoted as exhibiting a "baroclinic" structure. The statistical uncertainty of these eigenvectors is considerably greater than the gravest modes at Johnston, because the data record is so much shorter at Canton. The shape of this mode is closely reproduced at many other near-equatorial stations, however.

The gravest mode at each station for each season always takes on one of these two forms. However, at some locations the shape of the mode is not the same for all seasons. At Majuro [7°N 171°E], the mode describing DJF fluctuations has an equivalent-barotropic structure (Fig. 3.10a), while the mode describing JJA fluctuations has a baroclinic structure

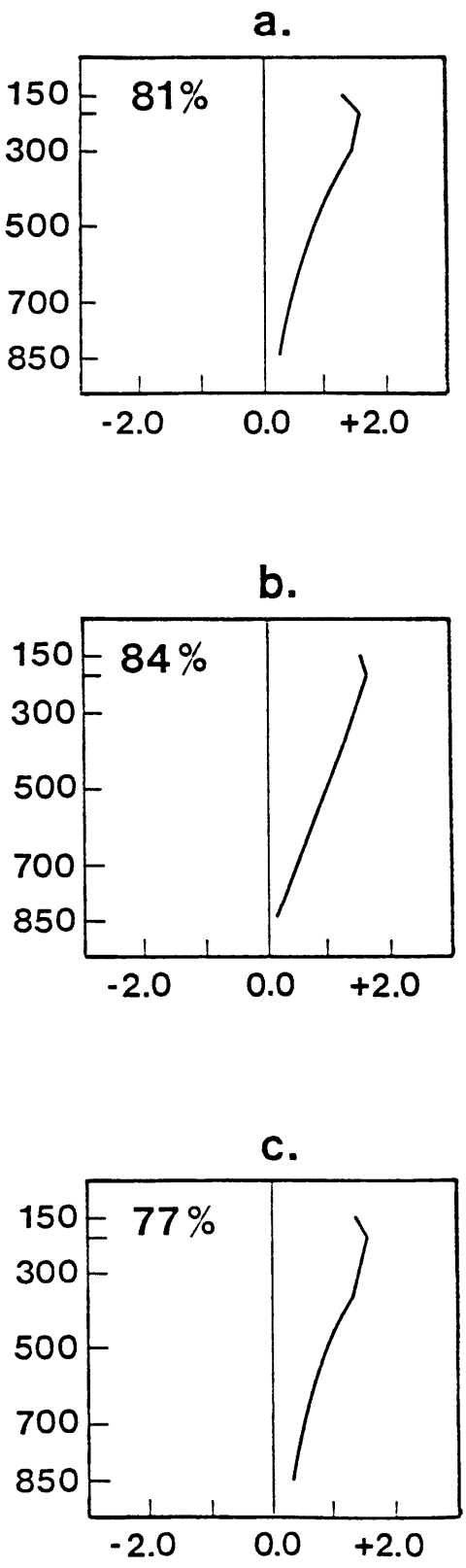


Figure 3.8 - Gravest mode of the EOF expansion of seasonal anomalies of zonal wind at Johnston [17°N 170°W] based on:

(a) DJF data only
(b) JJA data only
(c) all seasons

Percentage of total mass-weighted variance explained by the gravest mode is shown for each mode.

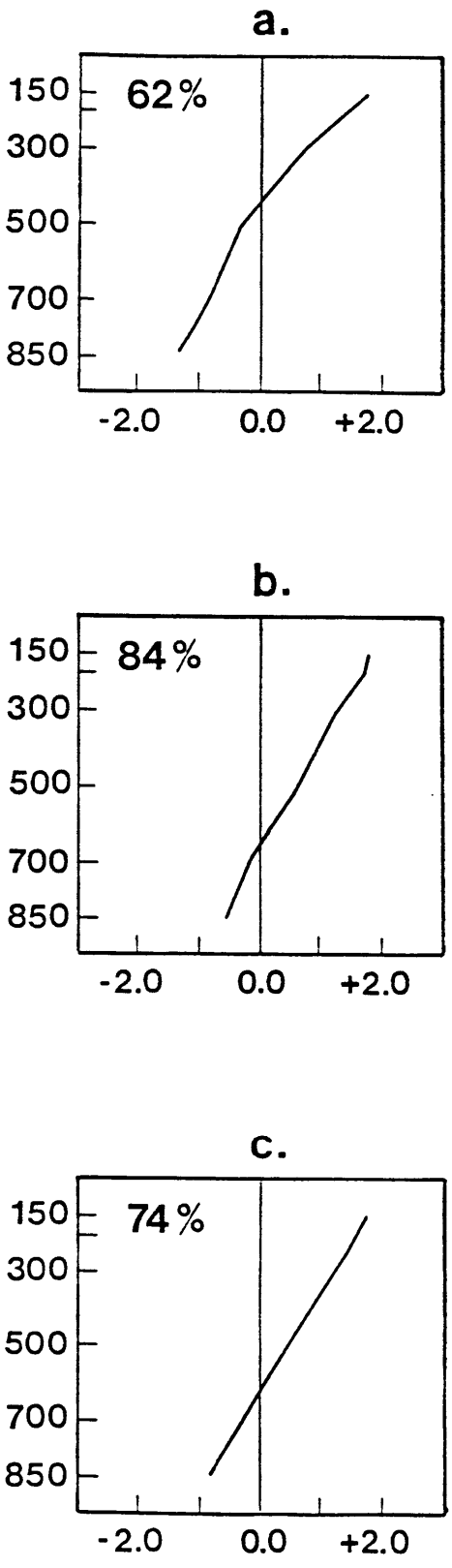


Figure 3.9 - As in Fig. 3.8, but for Canton [3°S 171°W]

(Fig. 3.10b). The mode based on year-round data has a hybrid structure and explained an appreciably smaller fraction of the total variance.

Similarly, the gravest mode based on seasonal anomalies for DJF (local summer) at Darwin [12°S 131°E] is baroclinic in shape (Fig. 3.11a), while the corresponding mode for JJA (local winter, Fig. 3.11b) is equivalent-barotropic. Here, the gravest mode using year-round data (Fig. 3.11c) takes the shape of the summer mode, since the interannual variability of summer anomalies is much greater than the variability during the other three seasons, but only half of the total variance is explained by this mode.

The geographical and seasonal variability of the shape of the gravest mode is shown in Fig. 3.12. In each figure, a "1" is plotted at each station where interannual variability of the zonal wind has an equivalent-barotropic structure, and a "2" is plotted where the gravest mode has a baroclinic structure. Separate plots are shown for each season, and are labelled with reference to Northern Hemisphere seasons. Also shown on each plot are regions of intense convection, as defined by the 240° contour of the climatological outgoing longwave radiation field for each season, taken from Janowiak et al. (1985).

The equivalent-barotropic vertical structure is predominant at stations poleward of 12° latitude in both hemispheres for all seasons. Considering also the results of earlier studies, we conclude that this vertical structure is representative of mid-latitude fluctuations for a broad range of frequencies, and does not seem to vary appreciably with season or longitude.

Equatorward of 12°, the latitudinal range over which the predominant vertical structure of interannual variability is baroclinic corresponds

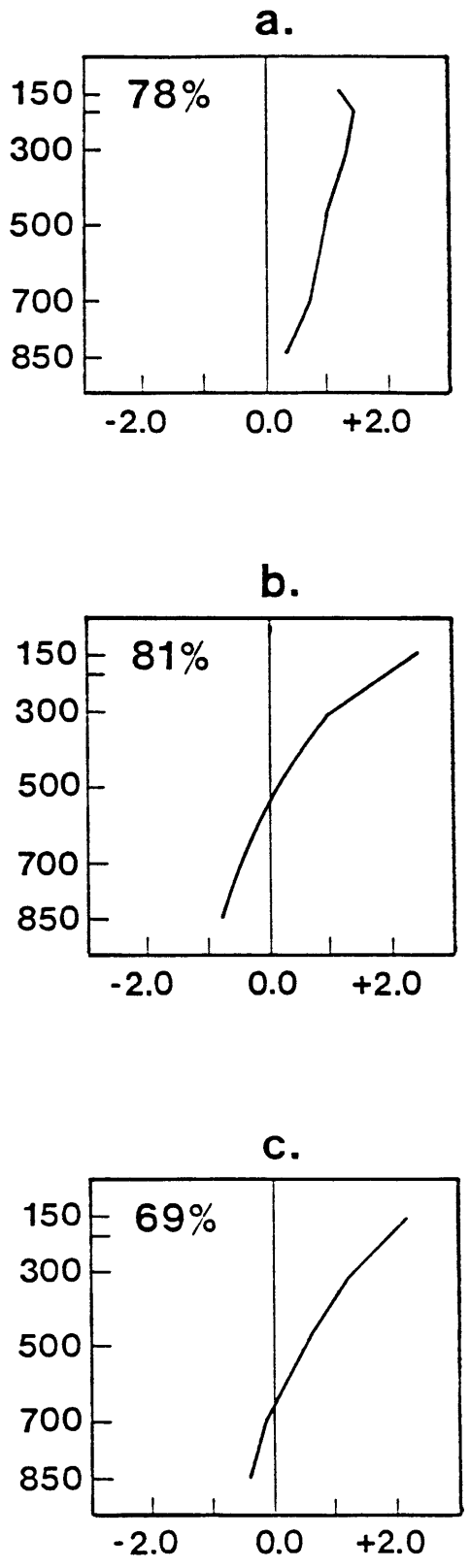


Figure 3.10 - As in Fig. 38 , but for Majuro [7°N 171°E]

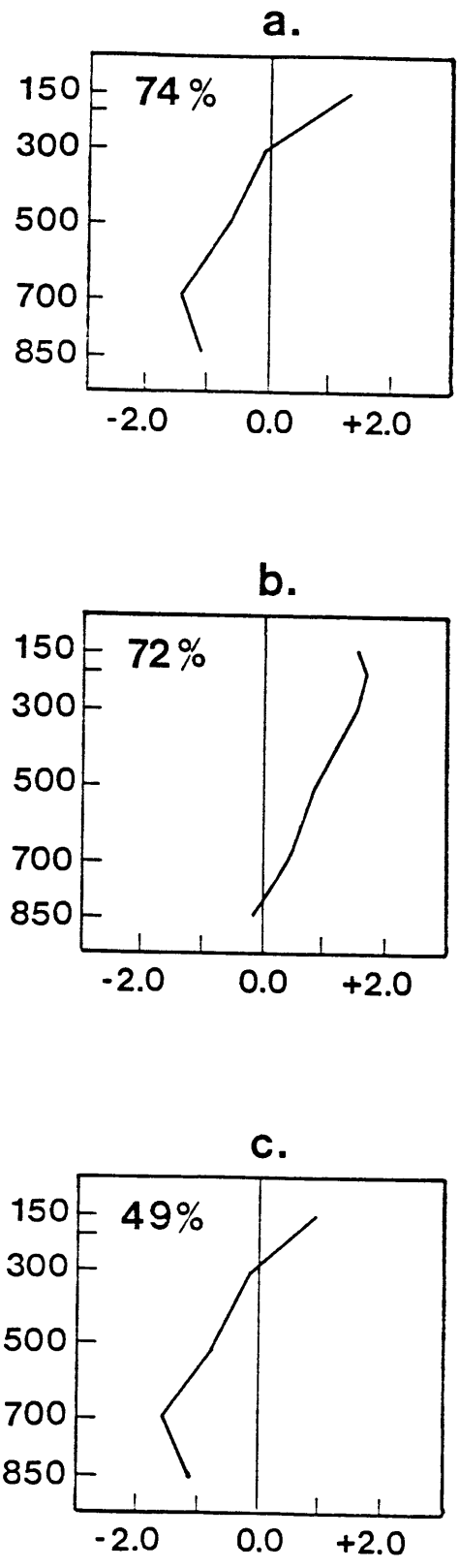
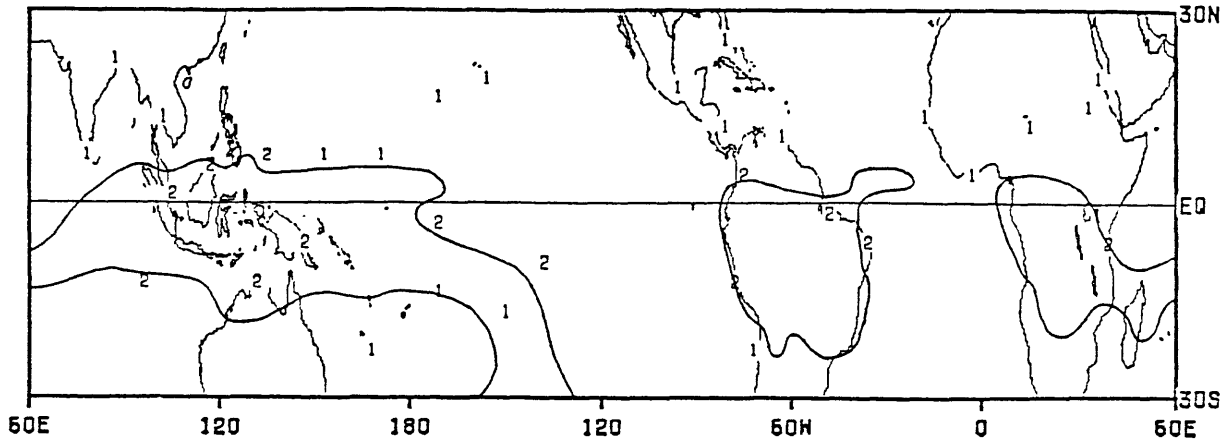


Figure 3.11 - As in Fig. 3.8, but for Darwin [12°S 131°E]

a. DOMINANT MODE U DJF



b. DOMINANT MODE U MAM

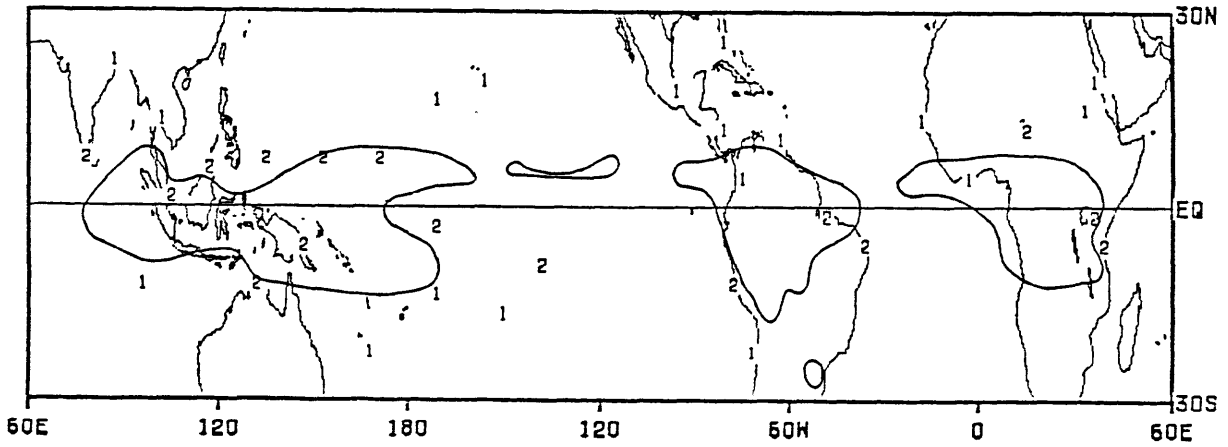
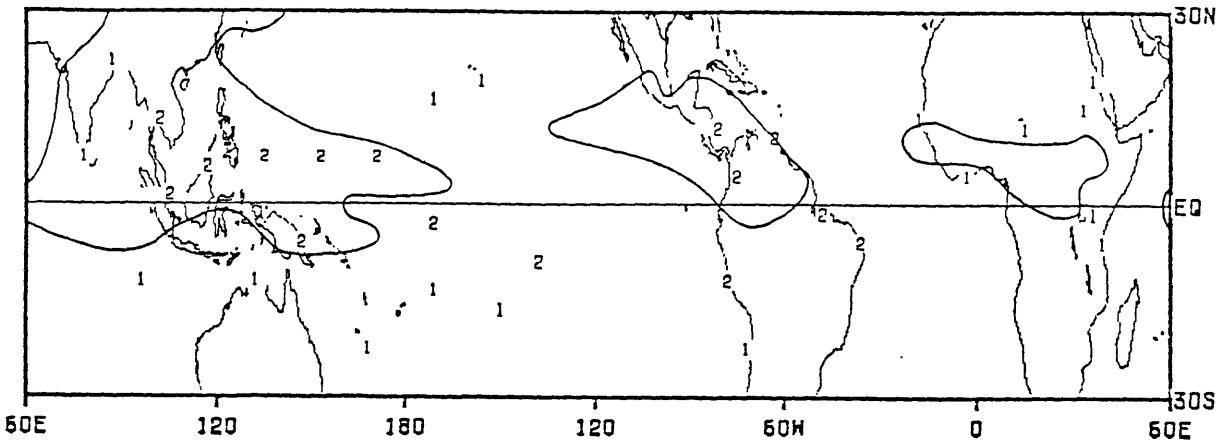


Figure 3.12 - Shape of the gravest vertical mode of zonal wind fluctuations at each station. "1" represents an equivalent-barotropic shape, and "2" represents a baroclinic shape. Contours delineate regions where the climatological outgoing infrared brightness temperature is less than 240° (taken from Janowiak et al., 1985).

(a) DJF season.
(b) MAM season.

c. DOMINANT MODE U JJA



d. DOMINANT MODE U SON

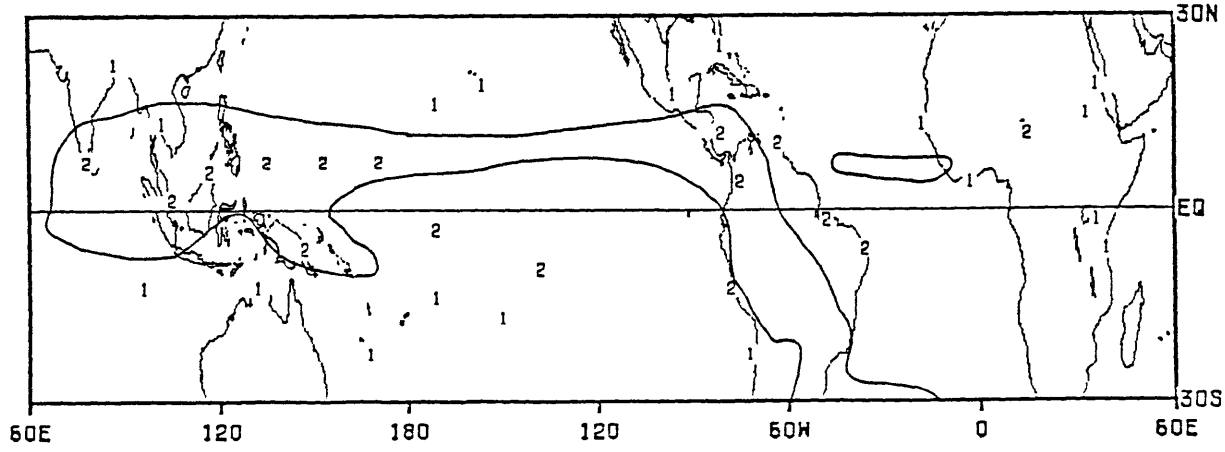


Figure 3.12 (continued)

(c) JJA season.
(d) SON season.

closely to the latitudinal extent of intense near-equatorial convection. For example, the vertical structure at Darwin (on the northern coast of Australia) is baroclinic for interannual fluctuations during Southern summer (cf. Fig. 3.10a) and autumn, when the 240° longwave isotherm reaches its southernmost extent. An equivalent-barotropic structure dominates the variability during Southern winter (cf. Fig. 3.10b) and spring, when the ITCZ retreats northward. The baroclinic mode is predominant for all seasons at stations nearer the equator in the Pacific, which remain within the band of intense convection year-round. This interpretation of the latitudinal half-width of the band of baroclinic mode prodominance agrees well with a study of cloudiness fluctuations by Murakami (1975), who found large interannual changes in longitudinal cloudiness perturbations between 15°N and 15°S.

The climatological longitudinal limits of intense convection do not correspond to changes in the shape of the dominant vertical mode. The interannual variability at Atuona [10°S 139°W] is described by a baroclinic vertical structure for all seasons, despite the station's location in the eastern Pacific dry zone.

These results can be interpreted in terms of the concepts of stationary equatorial heat-forced circulations discussed in Section 3.1. The latitudinal extent of the response to equatorial forcing of the Gill (1980) model is determined by the equatorial Rossby radius y_E, defined as

$$y_E = \sqrt{\frac{c}{2\beta}} = \frac{(gh)^{1/4}}{(2\beta)^{1/2}} \qquad [3.3]$$

which is about 10° of latitude at the equator for h = 350 m. This width agrees well with the latitudinal wigth of baroclinic vertical mode

predominance shown in Fig. 3.12. The extent of equatorial trapping is not very sensitive to the details of the vertical distribution of heating, because the Rossby radius is proportional to the fourth root of h.

The longitudinal extent of the response is much less limited. It is more sensitive to changes in the equivalent depth (Lim and Chang, 1983), because c is proportional to the square root of h in [3.1]. The sensitivity of the longitudinal extent of the response to changes in the linear damping coefficient was examined by Zebiak (1982). For realistic values of equivalent depth, damping, and heating, the response to a patch of anomalous heating over the western Pacific of the shallow water model extends eastward completely across the Pacific and westward to the mid-Indian Ocean. In conjunction with the other major centers of convection over South America and Africa, the domain of the forced response with the baroclinic vertical structure observed here should span all longitudes.

Furthermore, anomalous heating over the Pacific is typically associated with a longitudinal shift in the Indonesian center of convection, so that the forcing region can be located a large distance eastward from its climatological position. Heddinghaus and Krueger (1981) found that the dominant mode of an EOF decomposition of nonseasonal outgoing longwave radiation variability described a fluctuation along the equator between longitudes 120°E and 180°.

The percentage of variance explained by the gravest mode of zonal wind interannual variability is plotted in Fig. 3.13 for each season. The dominance of the gravest mode is most pronounced over the eastern Pacific Ocean, where one mode typically accounts for over 80% of the

variance. A very clear vertical structure transition with latitude takes place across this region, since the dominant mode changes shape near the equator. The gravest mode explains less than 60% of the variance over equatorial Africa and the western Pacific.

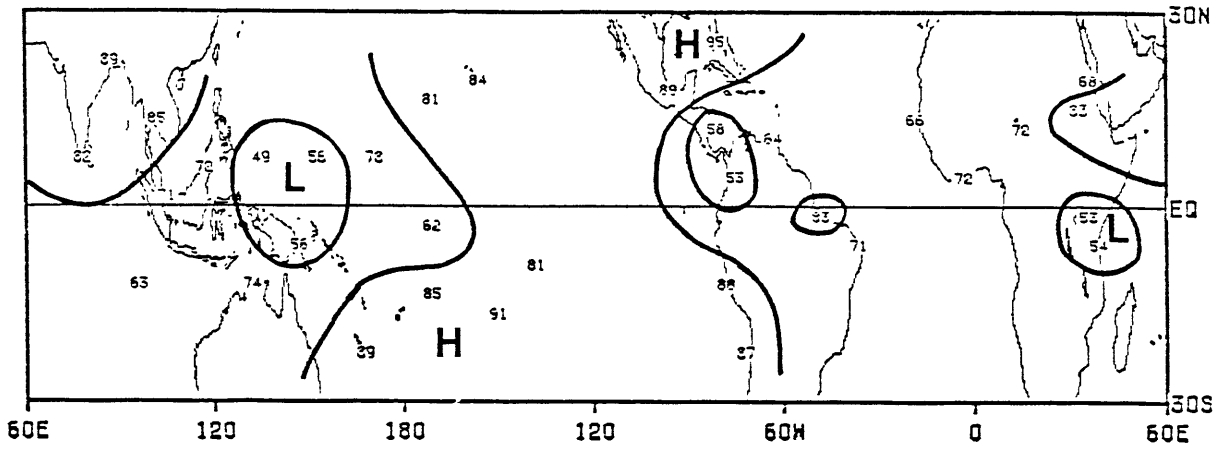
Estimates of the statistical uncertainty of the shape of the gravest mode, and percentage of variance it explains, are developed in Section 2 of Appendix C. For time series with 15-20 degrees of freedom, the uncertainty in the first eigenvalue (or, equivalently, the percentage of variance) is about one-third (Table C.2). One degree of freedom per year is assumed here. The shape of the gravest mode is resolved with confidence when the percentage of variance explained by the mode exceeds about 70% (80%) for time series of length 20 (15) years. This considerable statistical uncertainty is mitigated by the association of the baroclinic modes with regions of intense equatorial convection, lending plausibility to the geographical distribution of mode structures.

The same EOF procedure applied to meridional wind anomalies yielded results which were much less readily interpreted. The eigenvector modes were less distinctly separable and their shapes were not as simple as the modes based on zonal variability. Fig 3.14 shows the percentage of mass-weighted variance explained by the gravest meridional wind modes for each station for DJF and JJA seasons. The percentage of variance exceeds 80% for only a very few stations, so that the difference between eigenvalues 1 and 2 was generally much less for the meridional modes than for the zonal modes. Since the uncertainty in the shape of an eigenvector increases as the separation between neighboring eigenvalues decreases, we generally have less confidence in the meridional wind eigenvectors relative to the zonal wind eigenvectors.

Zonal and meridional wind components were treated together by calculating the EOFs of vector wind anomalies, using the methodology of Hardy and Walton (1978), as outlined in Section 3 of Appendix B. The complex elements of the eigenvectors represent both u and v components. By rotating each eigenvector so that the variance of the imaginary part of the time series of associated principal components is minimized, the phase of each eigenvector assumes its preferred orientation, i.e. the axis along which most of the variability takes place. Near the equator, it was generally found that the preferred orientation of the gravest mode of each complex decomposition was nearly zonal at all levels. For example, the gravest modes describing the vertical structure of vector wind interannual variability at Majuro are shown in Fig. 3.15. The horizontal (zonal) component dominates the element of the eigenvector at each level. The vertical structures of the horizontal components for both the DJF and JJA seasons are nearly identical to the structures derived from the zonal wind anomalies alone (Fig. 3.10).

The lack of coherent vertical structures in meridional wind fluctuations is consistent with the structure of the forced, stationary circulation responses in simple models (Gill, 1980; Geisler, 1981), which have a meridional component only very near the forcing region. However, it is also possible that whatever coherent structures are present in the meridional wind field are simply lost in the climate "noise". The interannual variance is smaller for v than for u (Figs. 3.2 and 3.4), but the high-frequency variability associated with tropical waves is distributed almost equally between zonal and meridional wind components (Wallace, 1971). Hence, Luther and Harrison (1984) found that aliasing due to sampling errors in estimates of time-averaged tropical

a. % VARIANCE EOF1 U **DJF**



b. % VARIANCE EOF1 U **MAM**

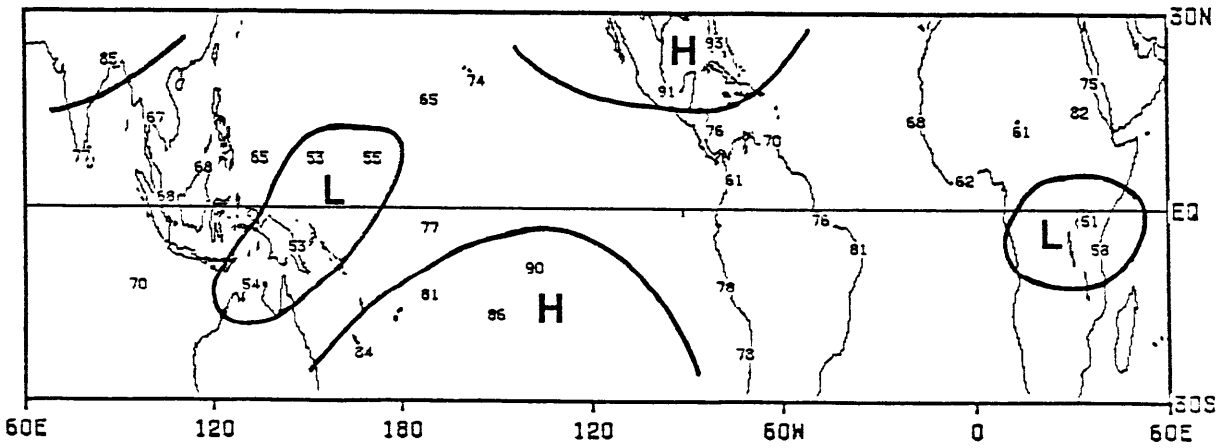
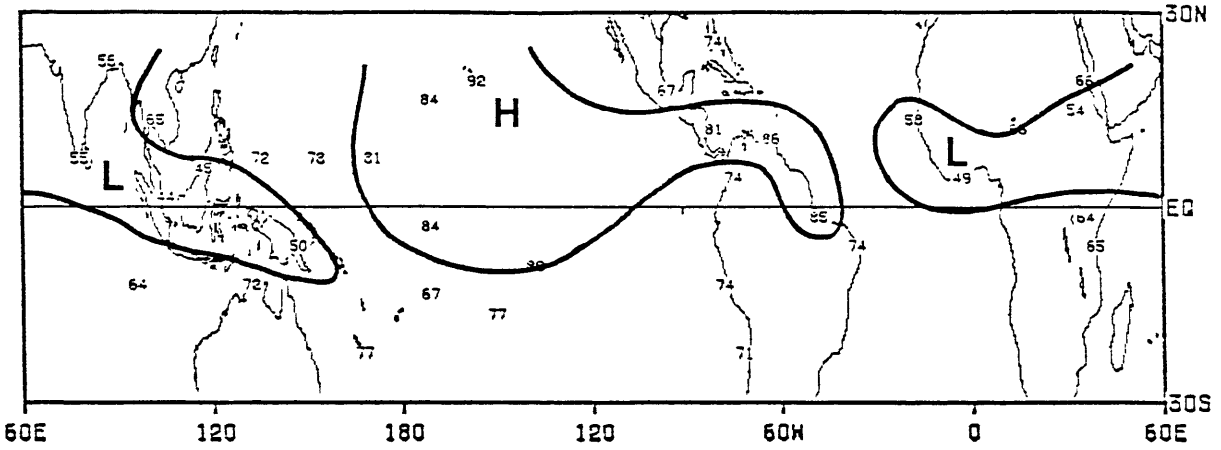


Figure 3.13 - Percentage of variance explained by the gravest vertical mode of zonal wind fluctuations at each station.
(a) DJF season.
(b) MAM season.

c. % VARIANCE EOF1 U JJA



d. % VARIANCE EOF1 U SON

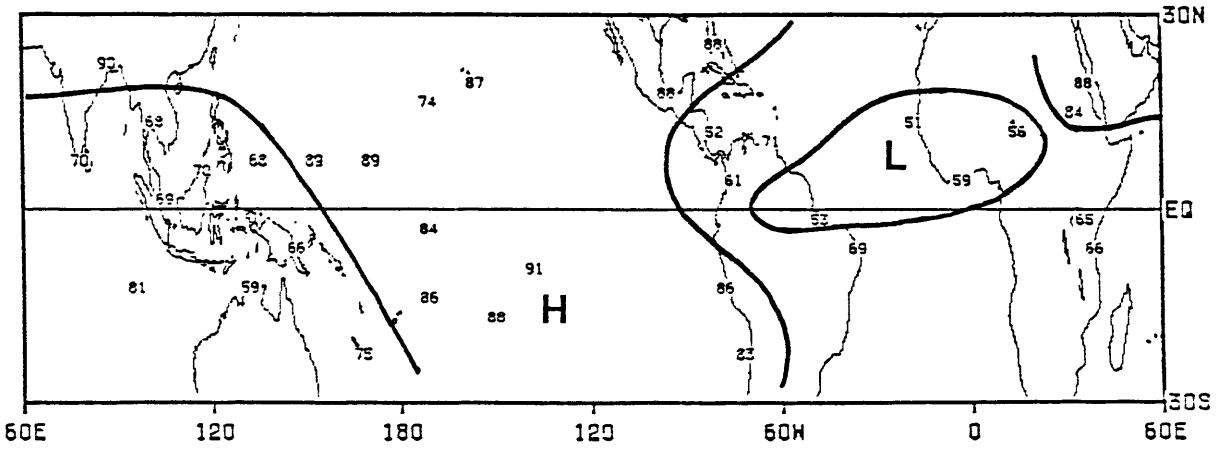
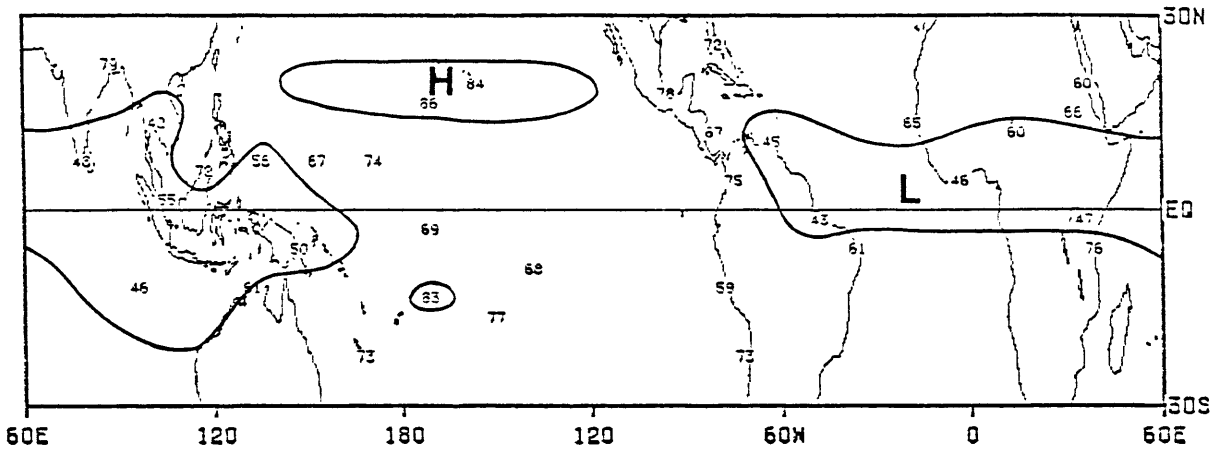


Figure 3.13 (continued) - Percentage of variance explained by the gravest vertical mode of zonal wind fluctuations at each station.
(c) JJA season.
(d) SON season.

a. % VARIANCE EOF1 V DJF



b. % VARIANCE EOF1 V JJA

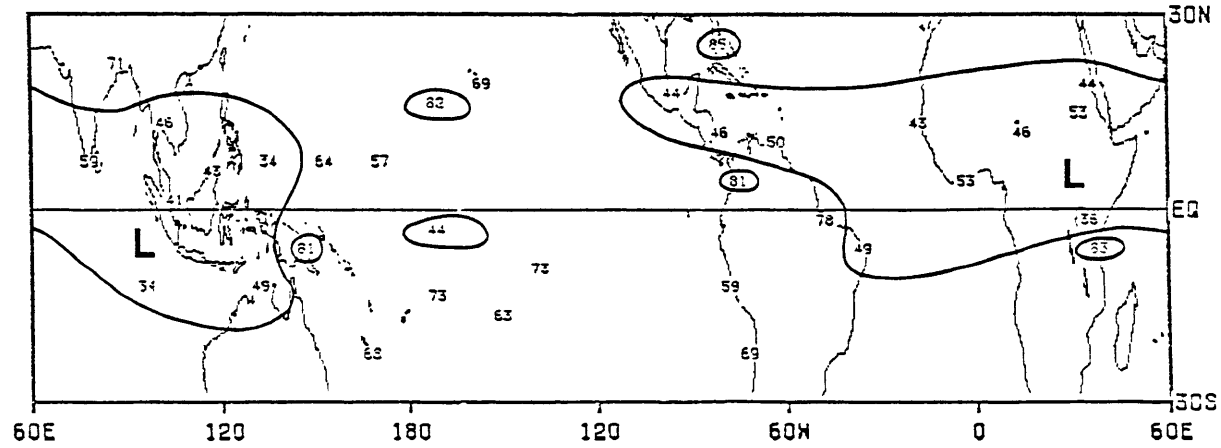


Figure 3.14 - As in Fig. 3.13, but for meridional wind fluctuations.
(a) DJF season.
(b) JJA season.

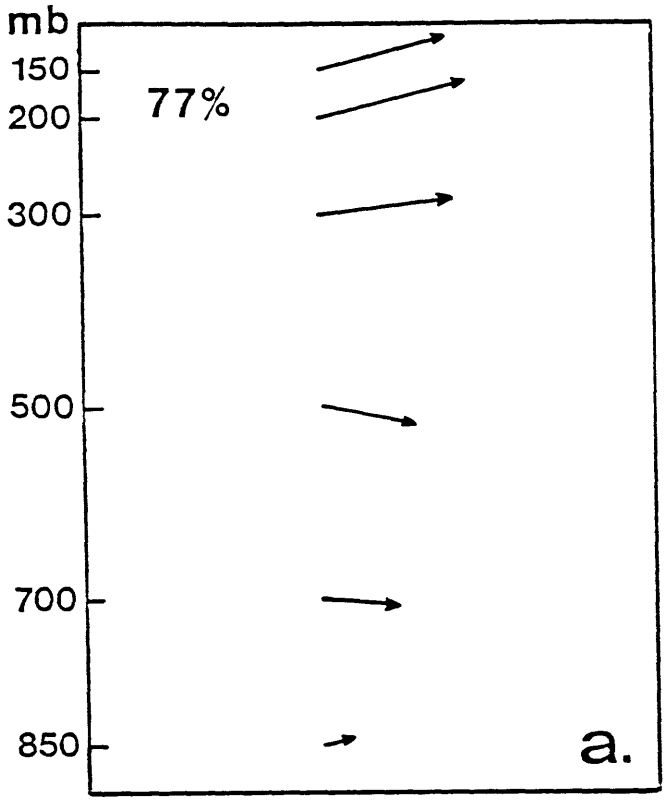
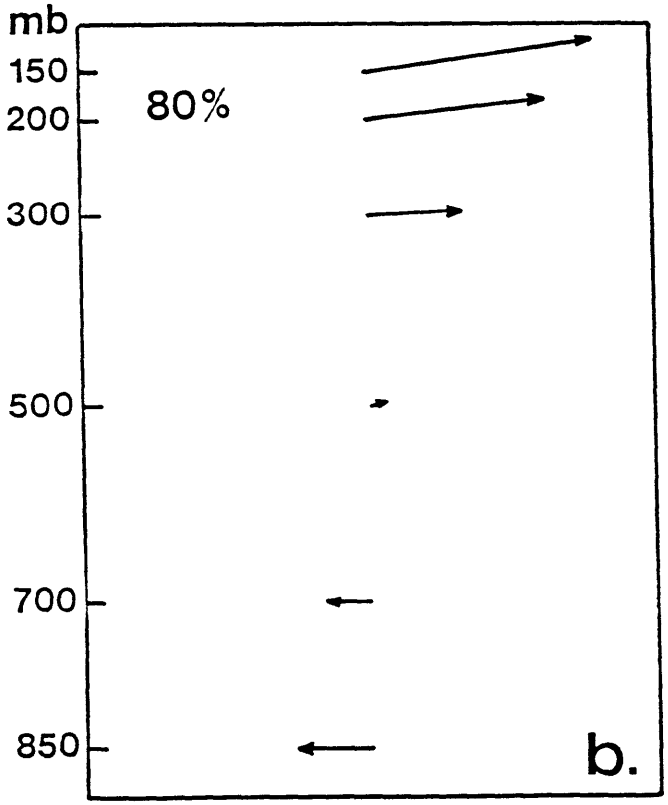


Figure 3.15 - Gravest mode of vertical EOF expansion of vector wind at Majuro.
(a) DJF season.



(b) JJA season.

surface winds was more severe in the meridional component, a result which probably is valid above the surface as well. The remainder of the thesis will focus on the zonal wind component, for which a clear inter-annual signal is present.

3.4 Horizontal structure of seasonal anomalies

In this section, the horizontal and vertical structure of inter-annual wind variability in the station data time series are described together, using both SOI - wind correlations (as in Selkirk, 1984), and a multi-station EOF analysis calculated independently of the SOI (as in Arkin, 1982). For a description of the three-dimensional structure of variability over the entire tropical region, correlations between the SOI and the seasonal wind anomalies are better suited to this data set than EOF calculations. This is because the EOF technique is sensitive to the spatial distribution of the data. If the data are unevenly spaced, as are these station data, then the selection of spatial modes may be biased by the data spacing. In the vertical dimension, the uneven spacing of the data points can be compensated by the mass-weighting scheme used here. Unfortunately, there is no obvious way to accomodate the sparse, uneven geographical distribution of stations. This is one great technical advantage offered by analysis products, where the data are available on an evenly spaced grid.

Therefore, part (a) of this Section will describe temporal correlations between the SOI and seasonal anomalies of wind at different levels for the entire tropical station network. The 1dEOF modes for individual stations derived in Section 3.3 are shown to provide a concise framework for describing the geographical distribution of the vertical structure

of wind anomalies associated with the SOI.

Then, in part (b), a two-dimensional EOF (2dEOF) analysis is used to describe the longitude-height structure of seasonal wind variability of the near-equatorial Walker Circulation over a subset of the station network where stations are spaced nearly uniformly, the Trivandrum-Atuona cross-section. The vertical structure of the 2dEOF analysis is compared with the 1dEOF calculations, and its horizontal structure is compared with the 200 mb calculations of Selkirk (1984) and Arkin (1982).

a. CORRELATIONS BETWEEN TROPICAL WINDS AND THE SOI

In Fig. 3.16, plots of the correlation between the zonal wind and the SOI at each level for the DJF season are shown. The statistical significance of these correlations is discussed in Section 1 of Appendix C. For most stations (those with more than 15 years of data), correlations of magnitude 0.4 to 0.5 can be considered significantly different from zero with 95% confidence. The calculated correlation coefficient is plotted at every station, with the ±0.4 contours delineated.

Large-scale, significant correlations at 850 mb are restricted to the southern Pacific Ocean. A third equatorial center, positively correlated with the SOI over South America, is stronger at 700 mb. Negative correlations over the Indian Ocean and the Caribbean regions become more prominent with height, and the regions of high correlations elongate zonally in the upper troposphere. The correlations at the centers over South America and the Pacific decrease in magnitude with height up to 500 mb. Between 500 mb and 300 mb, the signs of the correlations reverse near the equator. Above 300 mb, the magnitudes of the correlations then

increase with height again.

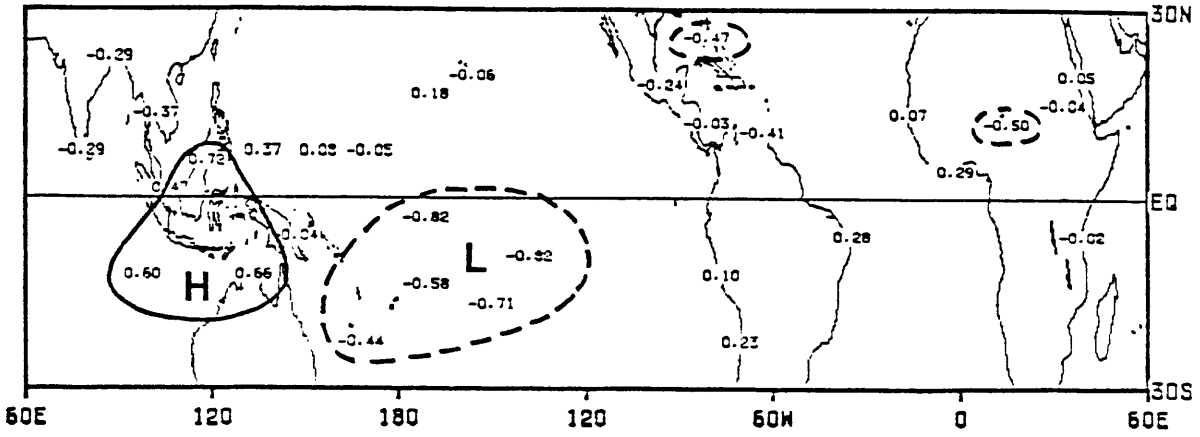
The 1dEOF modes described in Section 3.3 provide a concise, efficient depiction of the patterns observed in the plots of SOI - zonal wind correlations at individual pressure levels. The time series of principal components associated with baroclinic and equivalent-barotropic modes were correlated with the SOI at each station. For these calculations (and the corresponding statistics for other seasons shown subsequently), the second 1dEOF mode was examined as well as the first mode at most stations. This was possible because (1) the shape of the second mode corresponded visually to a baroclinic or equivalent-barotropic form at nearly every station (the second mode taking the shape not assumed by the gravest mode), and (2) the baroclinic and equivalent-barotropic structures are spatially near-orthogonal, allowing the EOF algorithm to separate them cleanly.

Fig. 3.17 shows the plots of the correlations thus obtained, with a blank plotted at locations for which the second mode was not readily associated with a baroclinic or equivalent-barotropic shape. The baroclinic modes are highly correlated with the SOI at stations within 12° of the equator from the eastern Indian Ocean eastward to South America. Even at Truk and Majuro, where the dominant mode of DJF interannual variability has an equivalent-barotropic vertical structure, it is the baroclinic mode which is strongly correlated with the SOI. The SOI is negative during a DJF season corresponding to a fully developed El Niño event, so that the correlation pattern in Fig. 3.17a is associated with upper tropospheric easterly anomalies across the equatorial Pacific flanked by upper tropospheric westerly anomalies over Indonesia and South America. Lower tropospheric anomalies have the opposite signs.

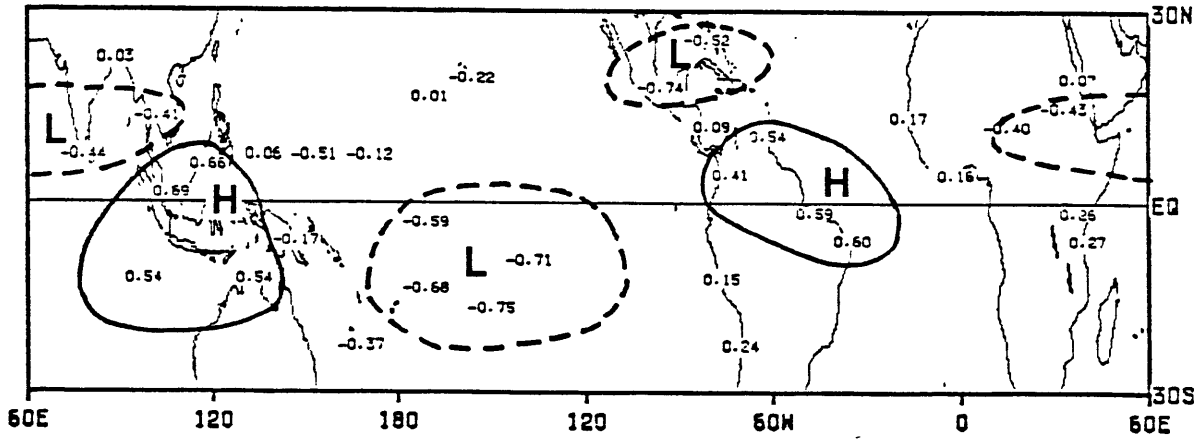
Figure 3.16 - Correlation coefficient between SOI and seasonal anomalies of zonal wind at each station for the DJF season.

(a) 850 mb level
(b) 700 mb level
(c) 500 mb level
(d) 300 mb level
(e) 200 mb level
(f) 150 mb level

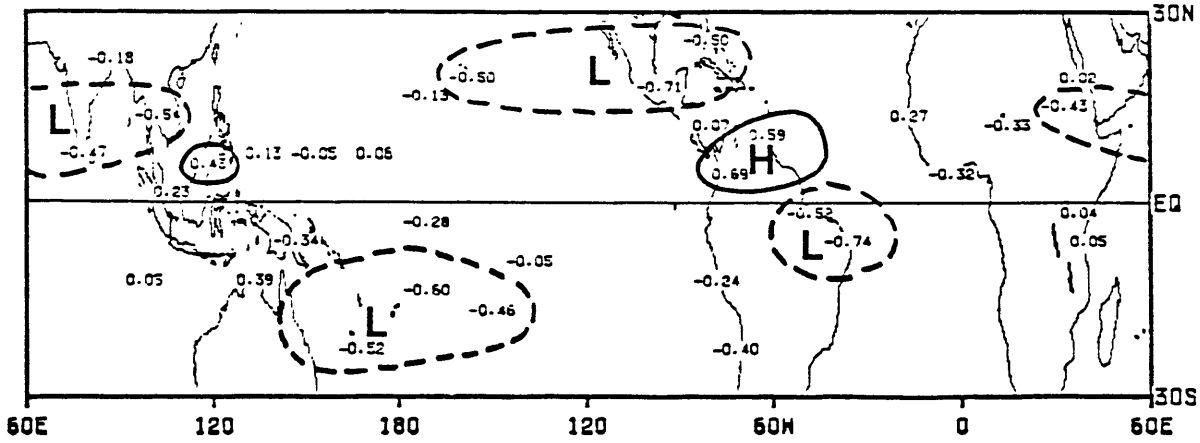
a. SOI - U850 - DJF



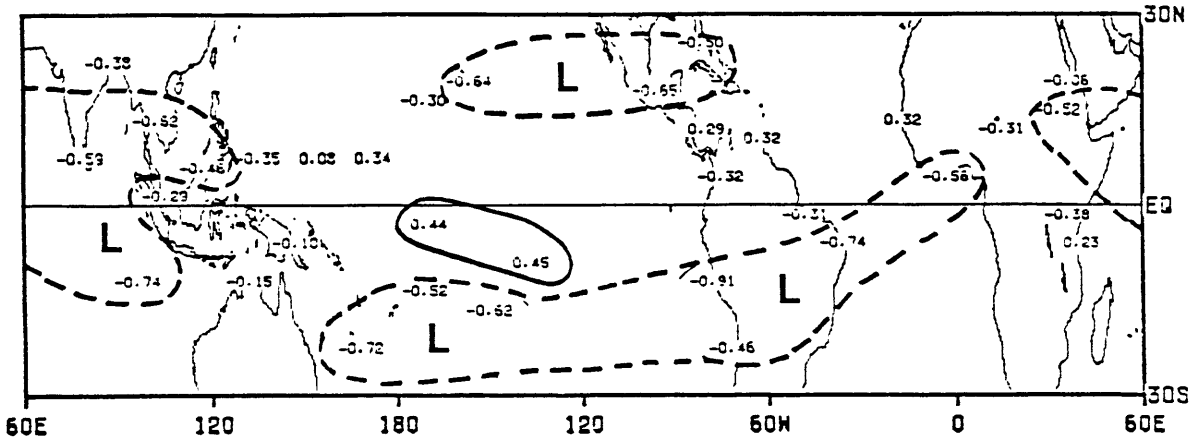
b. SOI - U700 - DJF



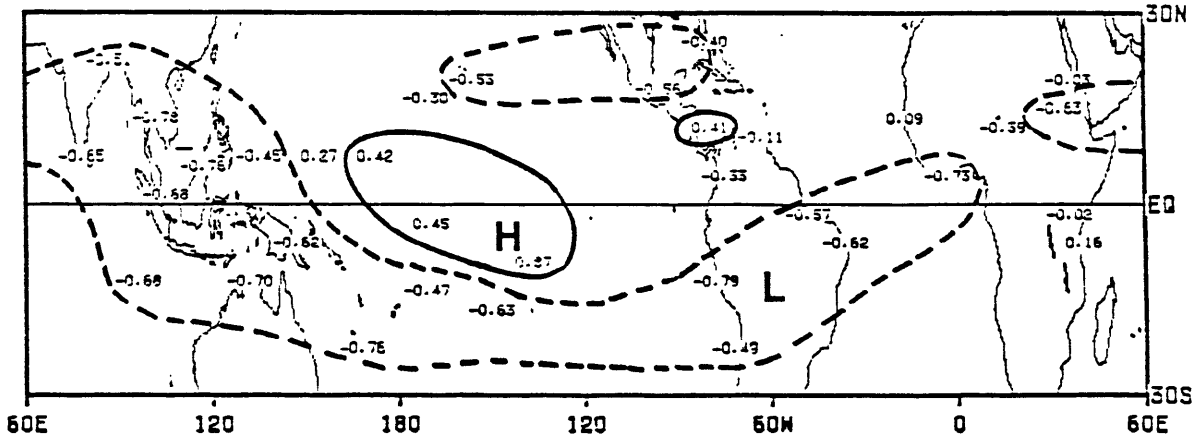
c. SOI - U500 - DJF



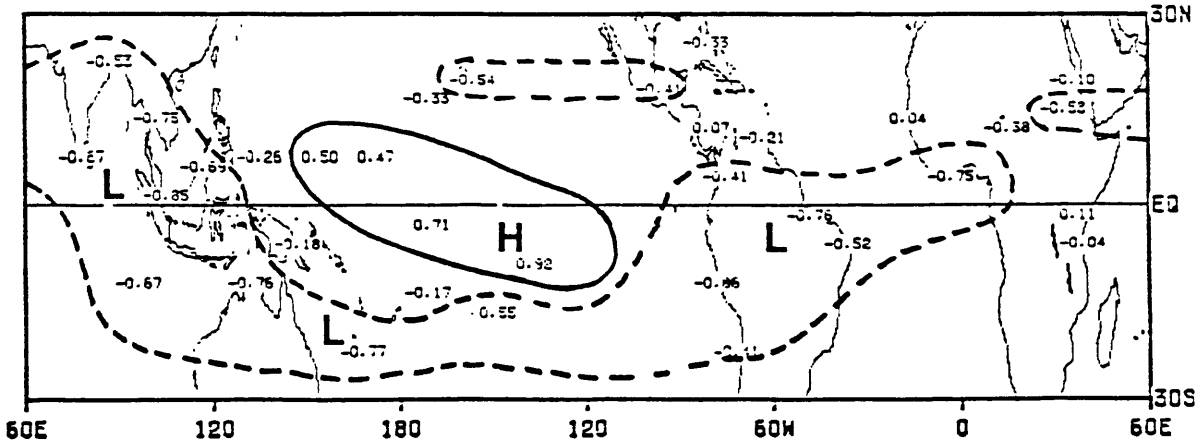
d. SOI - U300 - DJF



e. SOI - U200 - DJF



f. SOI - U150 - DJF



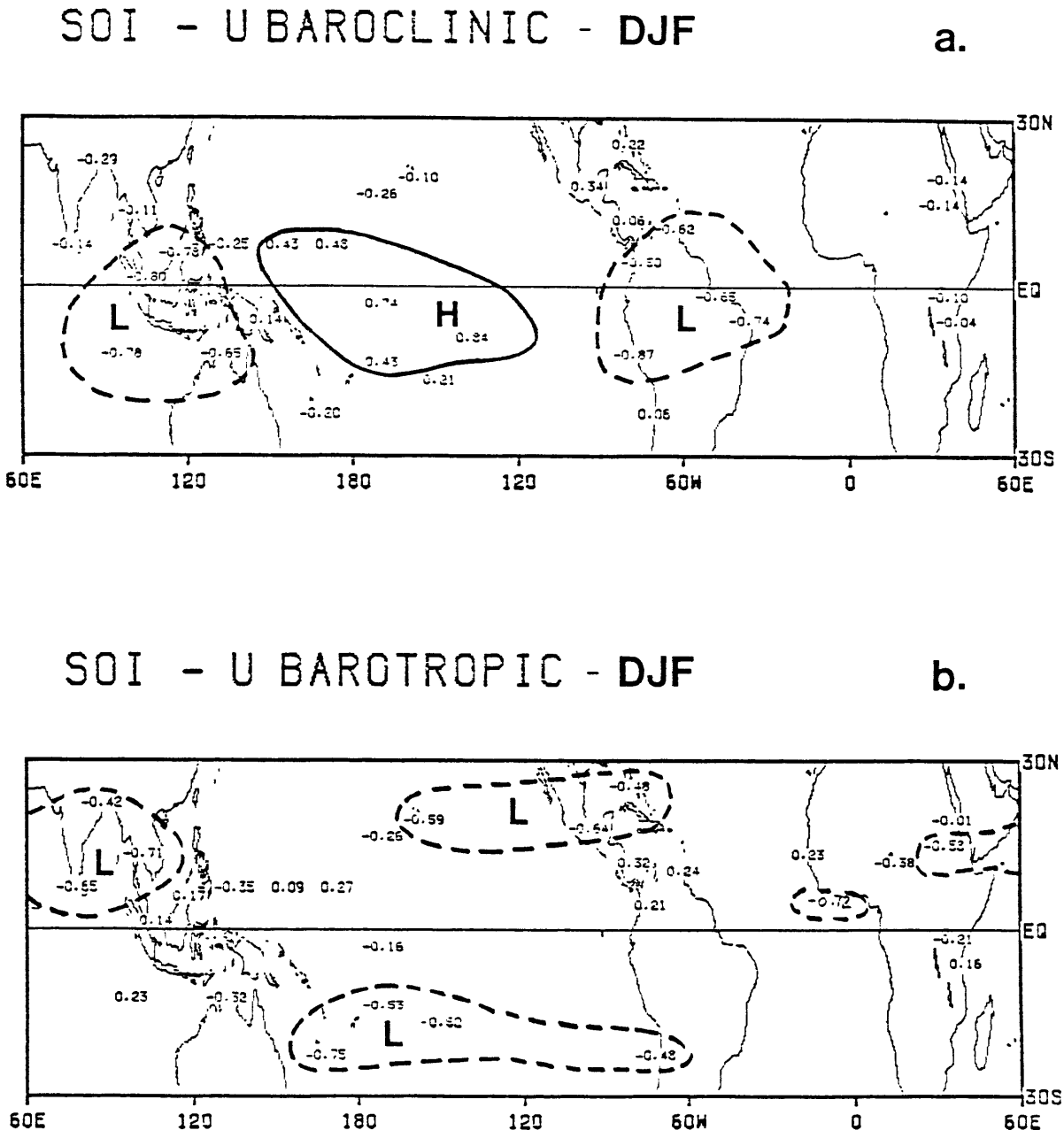


Figure 3.17 - (a) Correlation coefficient between SOI and principal components of the EOF mode with a baroclinic shape at each station for the DJF season. (b) As in (a), but for SOI correlated with principal components of the EOF mode with an equivalent-barotropic shape.

The near-equatorial upper tropospheric anomaly pattern is consistent with the patterns shown by Selkirk (1984, see Fig. 3.1b). Central Pacific surface westerlies during El Niño have been documented by Rasmusson and Carpenter (1982), and Pazan and Meyers (1982). The longitudinal position of the nodes of the pattern are consistent with low-level convergence near 120°W and divergence near 150°E during negative SOI seasons, corresponding to the eastward displacement of convection which occurs during El Niño (Bjerknes, 1969). The pattern also suggests lower tropospheric divergence over the Atlantic, an intriguing result because El Niño periods are associated with drought over northeastern Brazil (Caviedes, 1973).

The equivalent-barotropic modes are highly negatively correlated with the SOI over the Pacific at subtropical latitudes, over Southeast Asia, and over Africa. Correlations at the near-equatorial Pacific stations are small. If we consider that the SOI is a proxy index of tropical Pacific convective forcing, then the separation of the wind correlations into these vertical modes is consistent with the modeling result of Simmons (1982), who found that the local response to tropical heating had a vertical structure resembling that of the Gill (1980) model, whereas the far-field response had an equivalent-barotropic structure.

The vertical structure of the correlation between the SOI and interannual fluctuations of the DJF zonal wind field is further illustrated by considering two cross-sections. The first is the same Trivandrum-Atuona cross-section used to define the Walker Circulation (shown as Network A on the map in Fig. 3.18). The second cross-section, based on Network B in Fig. 3.18, has a southwest-northeast orientation extending from Noumea in the South Pacific across the equator to Miami.

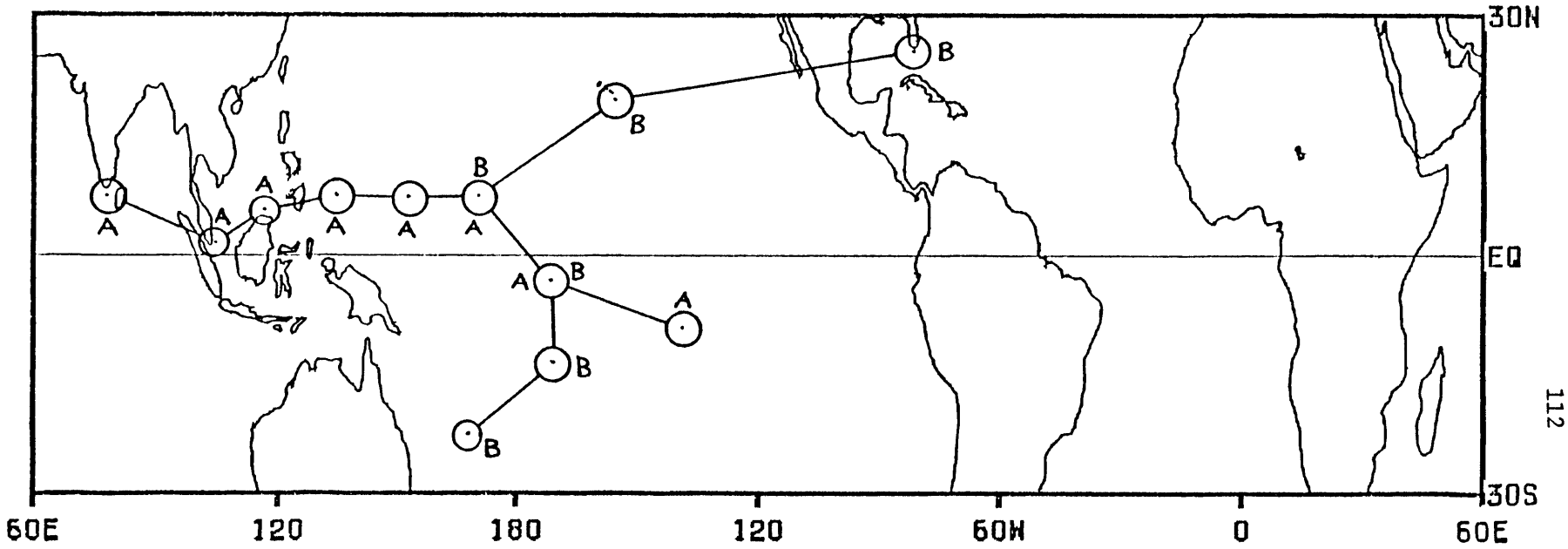


Figure 3.18 - Map showing locations of stations used in the cross sections plotted in Figs. 3.19 and 3.20.

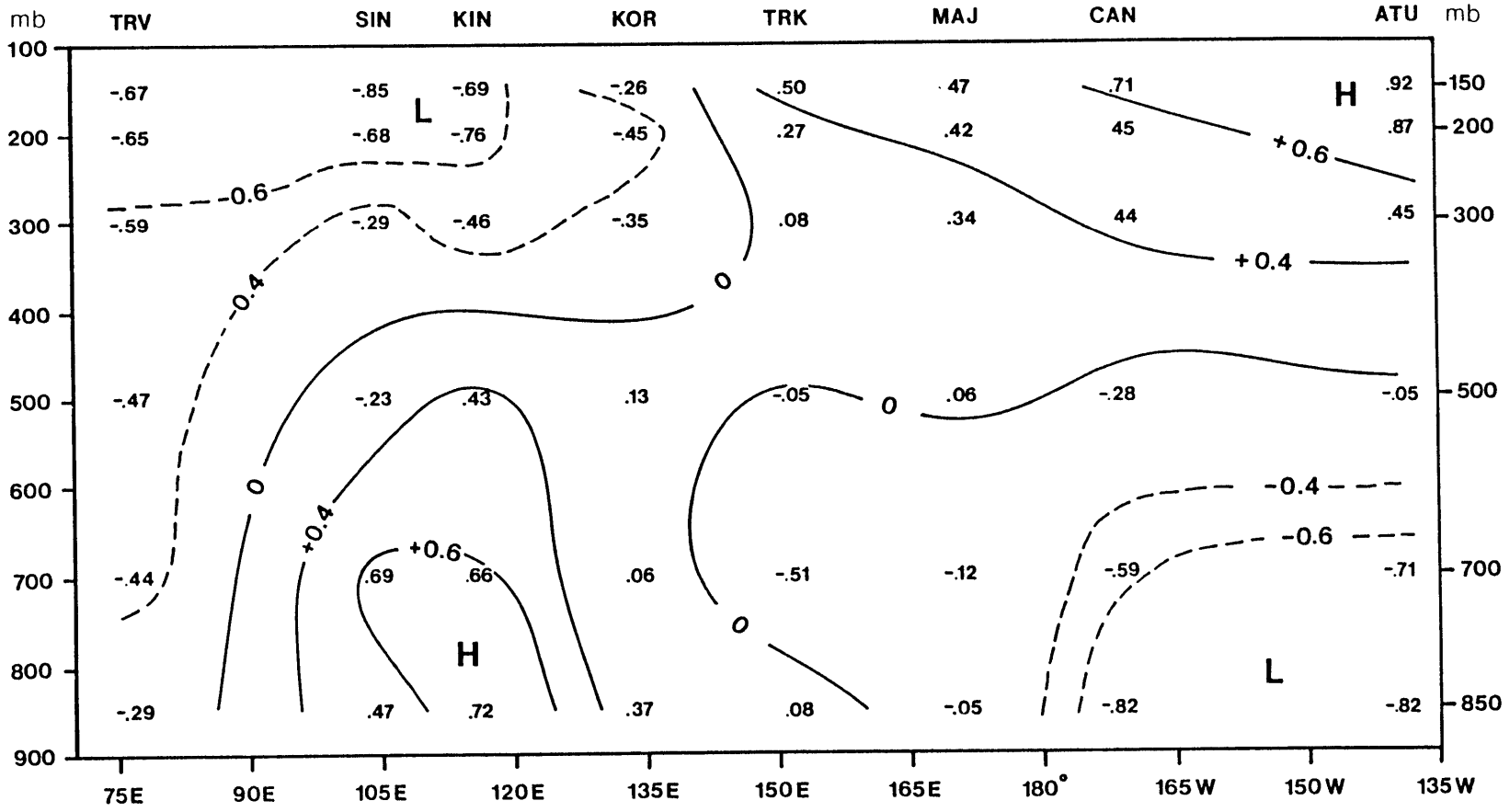


Figure 3.19 - Correlation coefficient between SOI and zonal wind anomalies at stations in cross section A, for the DJF season.

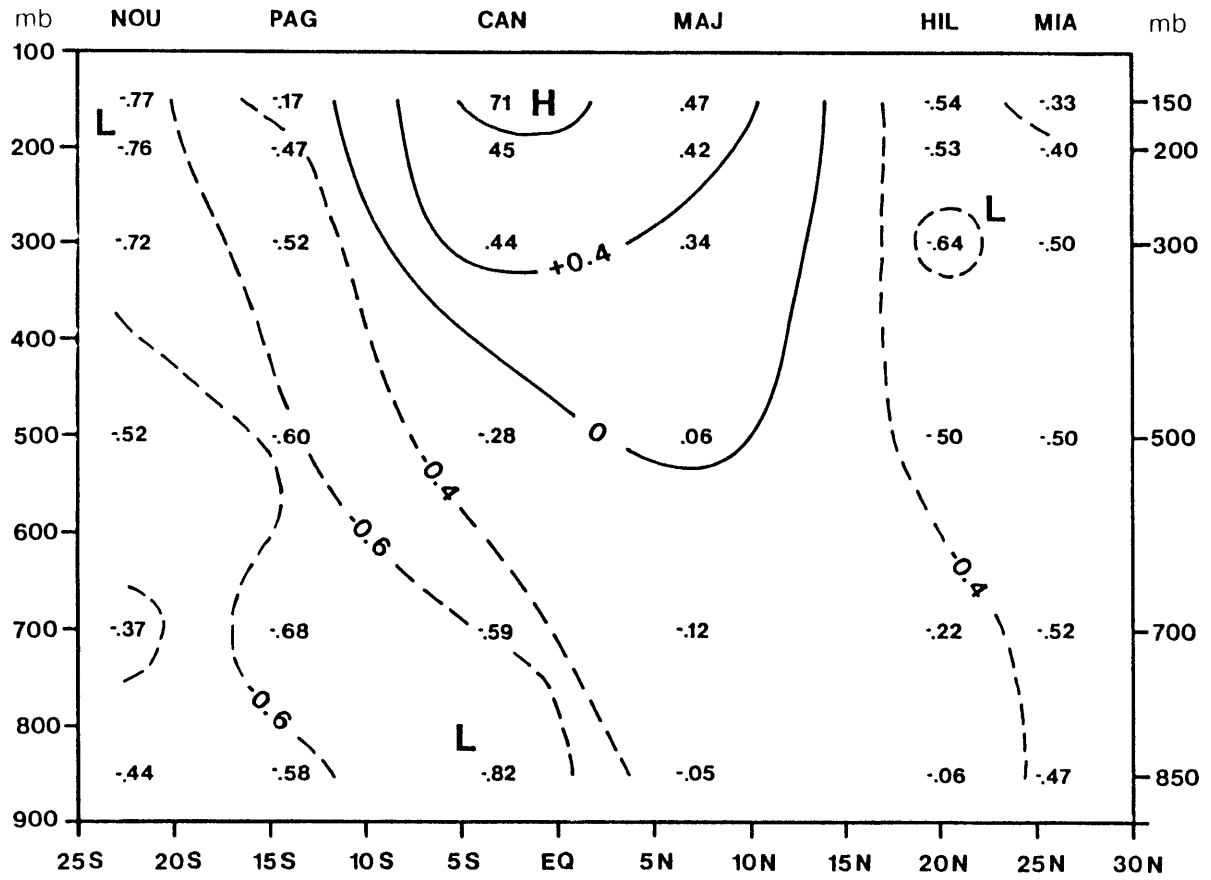


Figure 3.20 - As in Fig. 3.19, but for stations in cross section B.

The Network A cross-section (Fig. 3.19) shows that the correlations of largest magnitude along the equator have opposite signs at the highest and lowest levels (i.e. a baroclinic structure) with no indication of any east-west tilt, in contrast to the westward tilt with height of the DJF climatological Walker Circulation (Fig. 2.11a). Hence, the vertical structure of interannual variability is different from the vertical structure of climatology. At the western end of the cross-section (Trivandrum), the vertical structure becomes equivalent-barotropic, consistent with the shape of the dominant EOF mode there.

The Network B cross-section cuts meridionally through three vertical structure regimes, as defined by the dominant EOF modes. In the subtropics of both hemispheres, the dominant vertical structure is equivalent-barotropic, while near the equator the baroclinic structure is predominant. The Network B cross-section in Fig. 3.20 shows that the correlation field tilts from northeast to southwest with height.

Correlations between the SOI and EOF modes for other seasons are presented in Figs. 3.21-3.23. In the MAM season (Fig. 3.21), the baroclinic correlations are weaker over the maritime continent; otherwise the near-equatorial correlation pattern has about the same amplitude and phase as in DJF. The subtropical equivalent-barotropic pattern is substantially reduced compared to DJF, however. The band of negative correlation over the Northern Hemisphere subtropical East Pacific is located slightly equatorward of its DJF position, and the Southern Hemisphere correlations do not appear at all.

In JJA (Fig. 3.22), the western cell of the baroclinic pattern no longer appears, and the central cell (positively correlated with SOI) expands to fill the western Pacific. Hence, the correlation between the

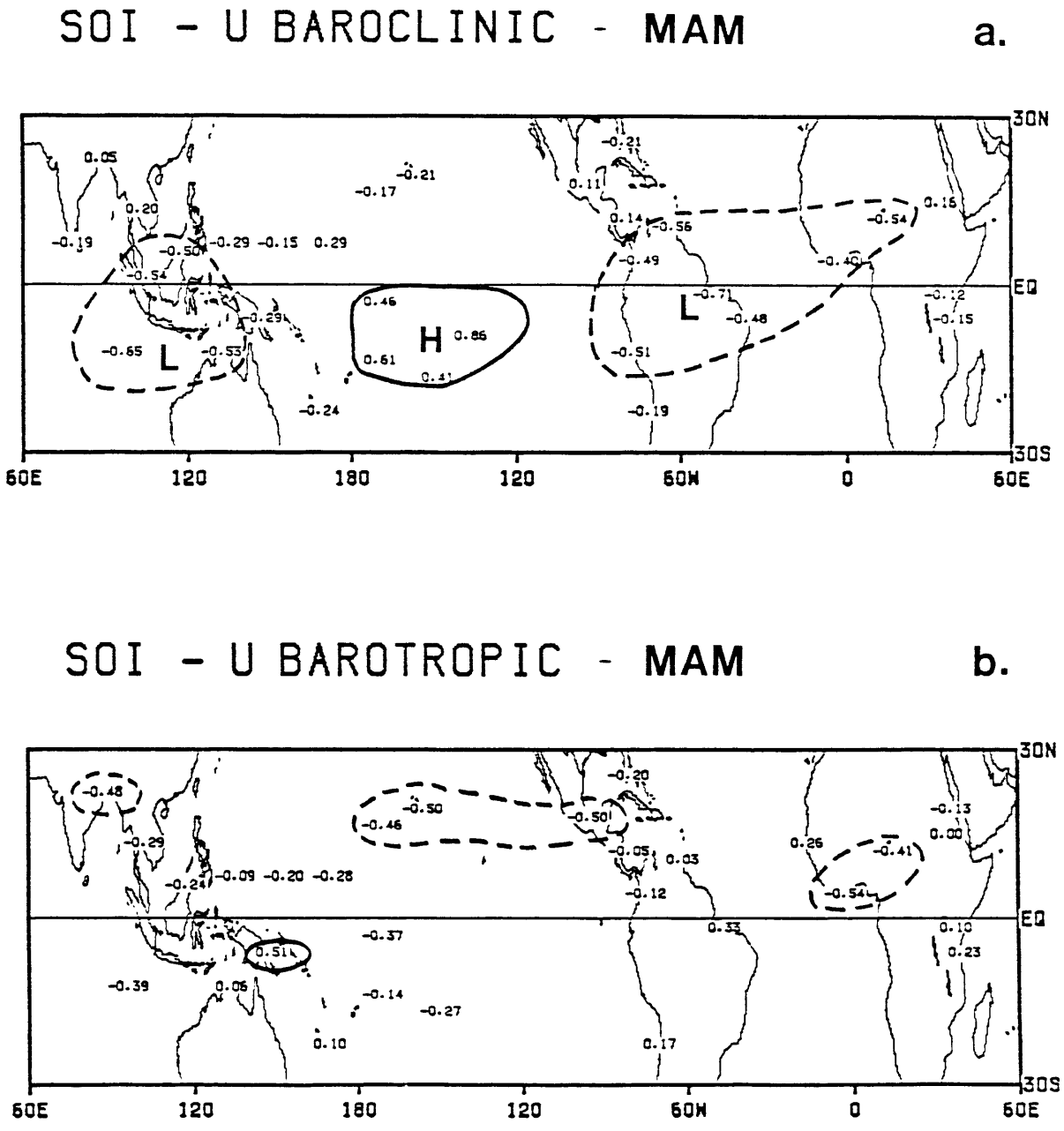
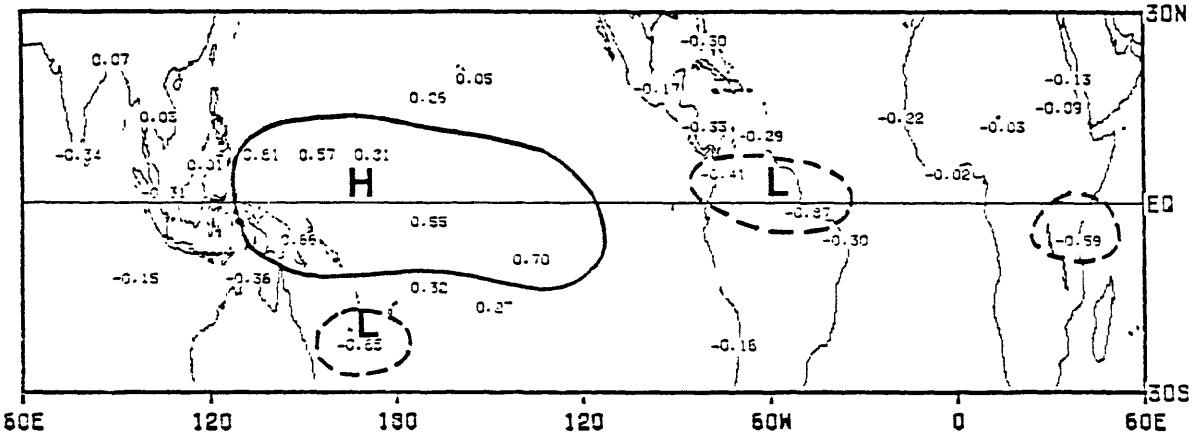


Figure 3.21 - As in Fig. 3.17, but for the MAM season.

SOI - U BAROCLINIC - JJA a.



SOI - U BAROTROPIC - JJA b.

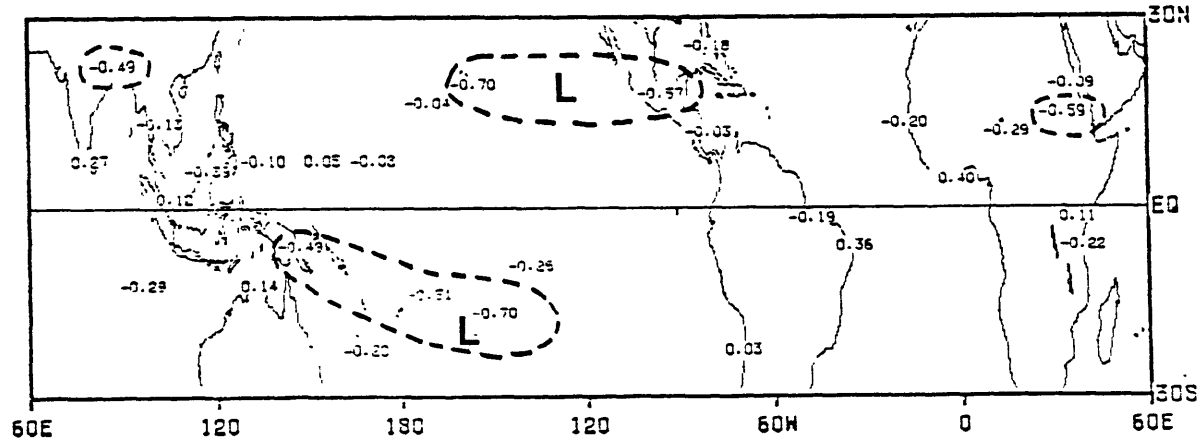
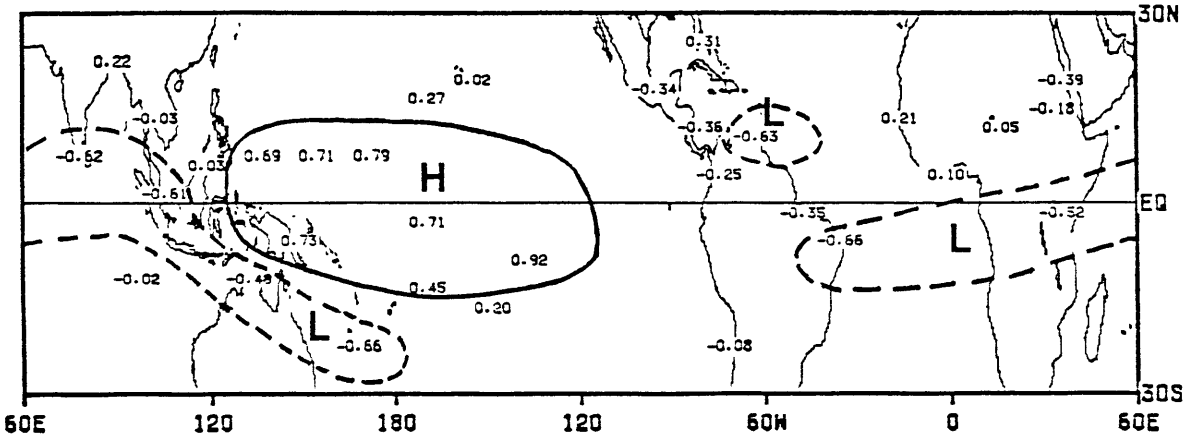


Figure 3.22 - As in Fig. 3.17, but for the JJA season.

SOI - U BAROCLINIC - SON a.



SOI - U BAROTROPIC - SON b.

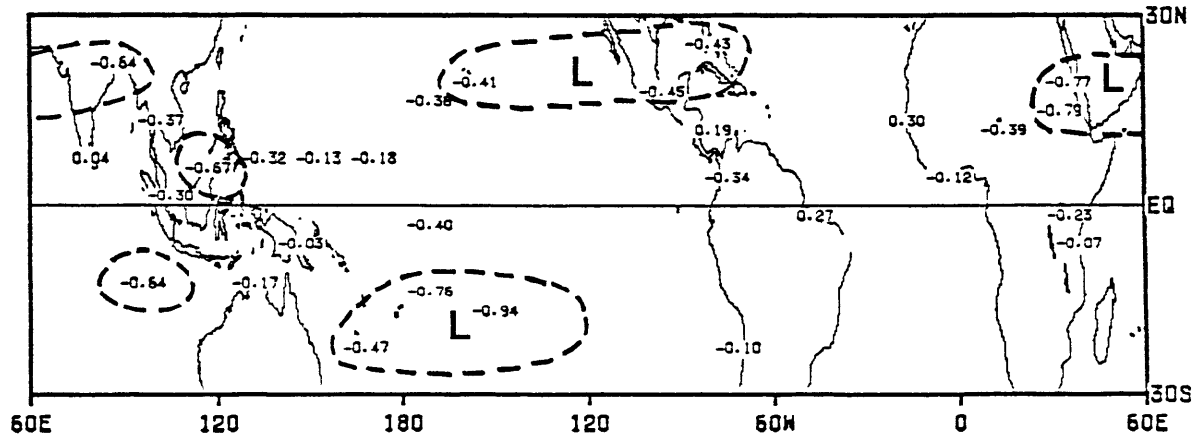


Figure 3.23 - As in Fig. 3.17, but for the SON season.

western Pacific and Indian monsoon regions is weakest during the season when the monsoon is strong. Extratropical correlations with an equivalent-barotropic vertical structure appear prominently during this season.

Finally, in SON (Fig. 3.23), the baroclinic equatorial pattern has a two-celled structure rather than the three-celled structure that was so clear in the DJF correlations. Subtropical correlations are strong around 20° latitude in both hemispheres.

The largest near-equatorial correlations move north and south with season, following the band of baroclinic mode predominance. The DJF baroclinic mode correlations are highest north of the equator, and the latitudinal position of the center of the cells moves into the Southern Hemisphere during the JJA season.

Bands of significant subtropical correlation in the Northern Hemisphere exist every season, not just during DJF. It has been conjectured that the presence of a zero-wind line in the seasonal zonal mean wind field prevents the meridional propagation of a tropical signal into the extratropics (e.g. Webster and Holton, 1982) for all seasons except Northern Hemisphere winter, but the subtropical equivalent-barotropic correlations in other seasons are significant at locations poleward of the zero-wind line in the upper troposphere during all seasons.

b. SPATIAL EOFS OVER THE EQUATORIAL INDIAN AND WESTERN PACIFIC OCEANS

The first and second 2dEOF modes for the DJF season are shown in Fig. 3.24. The gravest mode, explaining 44% of the total mass-weighted variance, represents a standing oscillation incorporating anomalies at 200 mb and 150 mb of the same sign at the four westernmost stations,

with smaller opposing anomalies at Truk and Majuro to the east. The same upper tropospheric anomaly structure is apparent in the DJF 200 mb correlation map derived by Selkirk (1984), shown in Fig. 3.1b. The correlation coefficient between the time series of principal components associated with this mode and the SOI is -0.83. The vertical structure of the zonal wind anomalies is equivalent-barotropic at Trivandrum, and baroclinic at the other five stations, with upper tropospheric anomalies larger than lower tropospheric anomalies. The reversal in sign of the anomalies at the five easternmost stations takes place at or slightly above 500 mb.

The second mode, which explains 31% of the variance, is dominated by anomalies with an equivalent-barotropic structure at Majuro and Truk, with smaller upper tropospheric anomalies of the same sign at stations to the west. The temporal fluctuations of this mode are nearly uncorrelated with the SOI (correlation coefficient 0.17).

The dominant vertical structures of DJF zonal wind anomalies calculated separately for each station were plotted in Fig. 3.11a. They are the same as the vertical structure of mode 1 of this analysis at Trivandrum, Singapore, Kota Kinabalu, and Koror. The equivalent-barotropic structure, which is the principal vertical mode of DJF interannual zonal wind variability at Majuro and Truk, is represented in mode 2. The amplitude of mode 1 is high in the western half of the network, and low in the eastern half, whereas the amplitude of mode 2 is high only at the eastern stations. In other words, the variance cannot be described by a single standing oscillation. Either the zonal wind anomalies at Truk and Majuro are nearly contemporaneously uncorrelated with the anomalies to the west and with the SOI, or else the variability

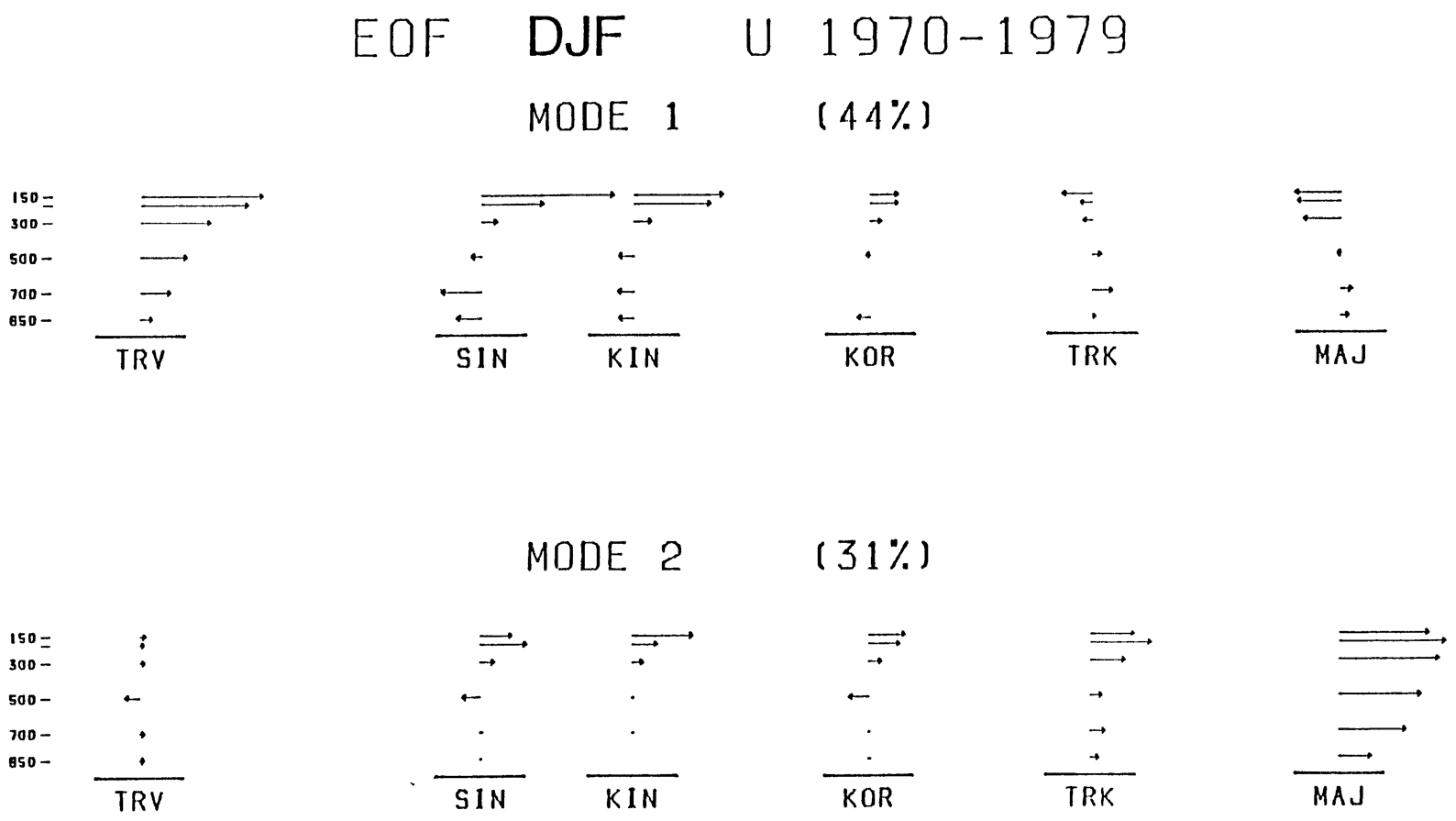


Figure 3.24 - First two modes of an EOF analysis of DJF seasonal anomalies of seasonal zonal wind anomalies, for the period 1970-1979, at six near-equatorial stations over the eastern Indian and western Pacific Oceans.

is more appropriately described as a propagating oscillation. The latter conjecture will be verified in Chapter 4, where the temporal evolution of wind anomalies is discussed.

The first and second modes for all seasons are shown in Fig. 3.25. The first mode, explaining 43% of the total variance, represents a standing oscillation with a node between 500 mb and 300 mb in the vertical direction, and a horizontal node near Kota Kinabalu. The contemporaneous (lag 0) correlation coefficient between the principal components associated with this mode and the SOI is -0.58 (see Table 3.1a). Therefore, negative SOI (an El Niño state, with warm equatorial sea surface temperatures) is associated with zonal wind anomalies directed in the same sense as the arrows in Fig. 3.25: easterly lower tropospheric anomalies at Trivandrum and Singapore, westerly upper tropospheric anomalies at Koror, Truk, and Majuro, and oppositely directed anomalies in the upper troposphere. The anomaly pattern indicates low level divergence and upper level convergence near Kota Kinabalu, consistent with the observation of decreased cloudiness over the maritime continent concurrent with El Niño events (Kidson, 1975; Murakami, 1975; Heddinghaus and Krueger, 1981). The opposite anomalies are implicitly associated with positive SOI.

The second mode represents 19% of the total variance. The lag 0 correlation coefficient between its principal components and the SOI is 0.43 (Table 3.1a). Hence, the anomalies associated with this mode during negative SOI seasons are the reverse of the arrows drawn in Fig. 3.25: easterly lower tropospheric anomalies at Singapore, Kota Kinabalu, and Koror, westerly lower tropospheric anomalies at Majuro, and westerly upper tropospheric anomalies from Truk westward.

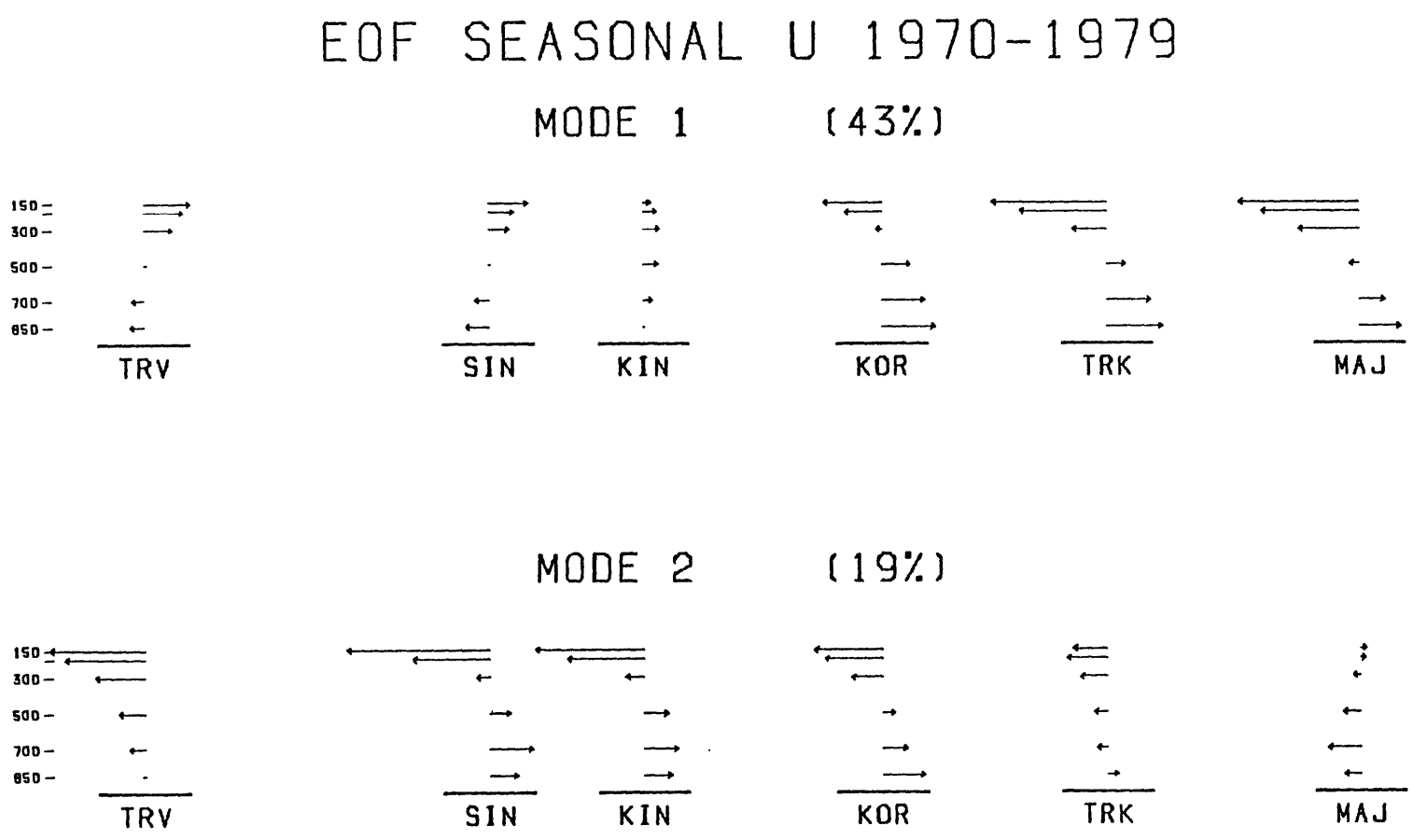


Figure 3.25 - As in Fig. 3.24, but for all seasons.

TABLE 3.1

(a) Lag correlation coefficients between SOI (see Fig. 3.1 a) and time series of principal components associated with first two modes (denoted A_1, A_2) of EOF analysis of seasonal zonal wind anomalies at six near-equatorial stations between 80°E and 170°E, for time lags up to three seasons.

	Lag (seasons; positive → SOI leads)						
	-3	-2	-1	0	1	2	3
A_1	0.20	0.01	-0.28	-0.58	-0.69	-0.57	-0.30
A_2	0.22	0.39	0.49	0.43	0.18	-0.01	0.00

(b) Lag correlation coefficients between A_1 and A_2 for various seasonal lags. The correlations are tabulated for the component in each row lagging the component in each column by the specified lag.

	leads by 0		leads by 1		leads by 2		leads by 3	
	A_1	A_2	A_1	A_2	A_1	A_2	A_1	A_2
A_1	1.00	0.00	0.58	-0.52	0.05	-0.46	-0.29	-0.32
A_2	0.00	1.00	0.31	0.09	0.10	-0.10	-0.09	0.08

Part (b) of Table 3.1 shows correlation coefficients between the principal components of the first two modes for lags up to three seasons. By construction, the correlation between the modes at lag 0 is identically 0.0. However, the table shows that the modes are highly correlated with each other at lag, as well as being autocorrelated. The fact that both of the first two modes are correlated with the SOI, and with each other at lag, suggests again that the wind variability over the equatorial Indian Ocean and western Pacific Ocean associated with the Southern Oscillation is not adequately described by a standing oscillation.

3.5 Discussion

Interannual wind fluctuations in the tropics do not have the same dominant vertical structure as the annual mean or annual variability in many locations. This is evident from the observation that the vertical structure of interannual fluctuations changes from season to season at some stations (Majuro and Darwin, for example). The vertical structure of the Indian summer monsoon provides another example. The annual mean and annual variability at Trivandrum both have a baroclinic vertical structure (clearly shown in Figs. 2.3, and 2.11), but interannual fluctuations about the summer mean have an equivalent-barotropic structure, however.

The vertical structure and meridional extent of the baroclinic modes are consistent with latent heat-forced circulations. The mode structures and vertical correlations presented here indicate that the level of overturning is between 500 and 300 mb, more closely resembling the calculated response to a Yanai et al. (1973) heating profile than the

response to an elevated heating profile. In addition, the interannual SOI correlations show no evidence of a tilt in the longitude-height plane. Since the interannual variability in latent heating primarily consists of longitudinal movement along the equator (Heddinghaus and Krueger, 1981), one would expect any tilt associated with anomalous forcing to appear in these statistics. The absence of a tilt in the equatorial cross-section in Fig. 3.19 argues against the elevated heating profile for the forcing of interannual variability near the equator.

The geographical extent of zonal wind - SOI correlations changes dramatically with height. At 850 mb, significant correlations are limited to the Pacific basin, and are strongest south of the equator. The surface pressure correlation pattern which defines the Southern Oscillation is also clearly asymmetric (Walker and Bliss, 1932), and van Loon (1984) has documented significant sea level pressure anomalies associated with El Niño as far south as 40°. In the upper troposphere, though, the zonal wind signature of the Southern Oscillation extends throughout the entire tropical region, and is nearly centered on the equator. The principal El Niño - associated anomalies of sea surface temperature (Rasmusson and Carpenter, 1982; Pan and Oort, 1983) and outgoing IR (Heddinghaus and Krueger, 1981) also occur along the equator.

The documentation of significant zonal wind variance in the tropics with an equivalent-barotropic vertical structure is a new result. The cause of such variability is uncertain. We have shown that the variability associated with the Southern Oscillation near the equator has a baroclinic vertical structure, yet for a few stations and seasons (e.g. Majuro and Truk in the DJF season), this vertical structure is not

the dominant mode of variability. Rossby waves propagating equatorward from the Northern Hemisphere are one possible explanation for variability with an equivalent-barotropic structure, but the climatological near-equatorial wind field over the western Pacific (Fig. 2.10a) should not allow such propagation. The climatological zonal wind is easterly at all levels, so that a zero-wind line exists to the northeast of Truk and Majuro during DJF which should prohibit transmission of equatorward-moving Rossby waves (Held, 1983). Furthermore, the upper tropospheric meridional winds are southerly, also inhibiting barotropic wave transmission (Schneider and Watterson, 1984). A zonal wind anomaly with an equivalent-barotropic vertical structure at the equator near the date line could be achieved by shifting the entire climatological wind field eastward, because $\partial\bar{u}/\partial(\text{longitude}) < 0$ at the date line in DJF at all levels (see Fig. 2.10a). However, such movement is not characteristic of anomalies correlated with the Southern Oscillation, which have opposite signs in the upper and lower troposphere. We will show in the next chapter that the baroclinic vertical anomaly structure is typical of El Niño - related anomalies as well.

Chapter 4

TEMPORAL EVOLUTION OF SEASONAL WIND ANOMALIES OVER THE WESTERN PACIFIC OCEAN

4.1 Introduction

As the results of the previous chapter demonstrated (consistent with earlier studies) the interannual variability of the tropical atmosphere is dominated by the El Niño - Southern Oscillation (ENSO) signal. In the past twenty years, ENSO has come to be recognized as an identifiable event involving a complex set of interactions between the atmosphere and ocean. Although tremendous observational and theoretical progress has been made on the ENSO problem, many questions remain. In this chapter, the evolution of tropospheric wind anomalies during ENSO events will be examined and interpreted in terms of results from previous studies and the two preceding chapters.

The oceanic component of ENSO consists of a dramatic increase in sea surface temperature (SST) along the equator in the eastern half of the Pacific Ocean, called El Niño. The warm SST anomaly persists for several seasons. This phenomenon was first noticed along the South American coast, where the warm water had extremely detrimental effects on the fishing industry. Upon further study, it was found that the patch of anomalously warm water typically appeared first at the South American coast in February or March, and then propagated westward along the equator as the magnitude of the anomaly amplified (Rasmusson and Carpenter, 1982, hereafter referred to as RC). However, several recent events (in 1963 and 1982) started with a warm patch that appeared first along the equator in the mid-Pacific (Philander, 1983).

The ENSO signal extends throughout the tropical atmosphere. Bjerknes (1969) first showed that large positive equatorial SST anomalies in the mid-Pacific are associated with negative sea level pressure (SLP) anomalies in the Southeast Pacific and positive SLP anomalies over the Indonesian region (this set of pressure anomalies was discovered by Walker (1924), who denoted it the Southern Oscillation). The trade winds collapse to the west of the SST anomaly during El Niño (Wyrtki, 1975). The Intertropical Convergence Zone (ITCZ) over the eastern Pacific is positioned close to the equator, well to the south of its climatological location (Trenberth, 1976; Pazan and Meyers, 1982). Rainfall over eastern Australia and the southwestern Pacific is below normal, while rainfall amounts over the equatorial mid-Pacific are above normal (Julian and Chervin, 1978; Horel, 1982a). In the upper troposphere, a distinct pattern of wind anomalies, extending far beyond the region of anomalously warm SST in the equatorial Pacific, is correlated with the Southern Oscillation (Arkin, 1982; Selkirk, 1984; see also Chapter 3).

Attempts to simulate the oceanic component of El Niño preceded modeling of the atmospheric component, but parallel methodologies were employed. Oceanographic studies were first concerned with the linear response of the mixed layer of an idealized equatorial basin to prescribed surface wind stress (McCreary, 1976). Later studies have included more model physics and/or more realistic winds (e.g. Harrison and Schopf, 1984; Busalacchi and Cane, 1985). Atmospheric studies focused on the linear, stationary response of the surface wind field to prescribed, idealized heating near the equator (Gill, 1980). These simple models reproduce many of the near-surface features associated with fully developed El Niño events.

More detailed studies of the genesis, evolution, and decay of El Niño episodes began with the seminal observational study of RC. After discussing the similar evolution of SST anomalies along cross-equatorial ship tracks during six El Niño episodes (1951, 1953, 1957, 1965, 1969, and 1972), RC devised a superposed epoch analysis of a composite El Niño event. The compositing scheme was fixed with respect to the calendar, reflecting the "phase-locked" characteristic of El Niño: i.e., the tendency of El Niño genesis and development to occur at fixed times of the year. The composite surface wind and convergence fields associated with each stage were calculated by averaging anomalies for the same three-month calendar period during each of the six events. This tendency to be phase-locked generated tremendous interest, because it seemed to imply that once the commencement of an El Niño was observed, its subsequent evolution (along with the attendant global-scale climate anomalies) might be predicted months in advance.

Five stages in the evolution of SST anomalies were identified by RC, beginning with antecedent conditions in the calendar year preceding ocean surface warming, and ending with a fully developed SST anomaly in the mid-Pacific a year after the appearance of warm water. The year in which the warm water appeared (the six years listed above) was denoted year (0) of the composite event, with the preceding and following years denoted year (-1) and year (+1), respectively. For example, composites of the Peak Phase, which RC define to be the period March(0) to May(0), were calculated by averaging 18 monthly anomalies: March, April, and May for the years 1951, 1953, 1957, 1965, 1969, and 1972.

The RC compositing scheme has since been widely adopted as a basis for studying the El Niño phenomenon. Arkin (1982) composited 200 mb

tropical wind anomalies in the NMC tropical analysis with respect to the RC event phases. Horel (1982a) composited 300 mb wind, temperature, and geopotential height anomalies from a global station network. Zebiak (1984) used the RC surface wind composites to judge the veracity of the simulated El Niño events produced by a coupled ocean-atmosphere model. Several general circulation model studies (e.g. Shukla and Wallace, 1983) have used the RC SST composite as a prescribed boundary condition.

In this chapter we will examine the vertical structure of seasonal wind anomalies in the Trivandrum-Atuona zonal cross-section during five El Niño episodes. In Section 4.2, a compositing methodology similar to the one developed by RC is applied to the vector winds and equatorial zonal mass flux over the western Pacific. The anomalies of zonal mass flux derived this way are compared to the annual mean and annual variability, which were discussed in Chapter 2.

One intriguing feature of the wind and zonal mass flux composites to be shown is the presence of an 'anti - El Niño' state over the far western Pacific preceding the appearance of warm SST in the eastern Pacific. A weak precursive pattern was noted near the dateline in the surface wind field by RC, and in the 300 mb wind field by Horel (1982a). The present analysis suggests that a more substantial precursive anomaly may originate even further west, and subsequently propagate slowly eastward during the El Niño event.

The 2dEOF analysis presented in Section 3.4 also suggested that the dominant signal of nonperiodic seasonal zonal wind variance over the Trivandrum-Atuona cross-section is a propagating feature correlated with the Southern Oscillation. In Section 4.3, a generalized complex EOF analysis, which can explicitly identify propagating as well as standing

oscillations, is used to elucidate the relationships across the basin.

There are obvious problems of statistical significance associated with a composite of only five events. The problem is exacerbated in the current study because not every station was reporting during some events. Rather than attempt to apply formal statistical tests to the composite, the question of significance will be treated in Section 4.4 by presenting the individual seasonal wind fields whose average is the composite. Similarities and differences between the various El Niño events are noted. A discussion in Section 4.5 concludes the chapter.

4.2 Spatial structure of composite El Niño event phases

The compositing scheme used in this section to describe the western Pacific wind field associated with El Niño events is similar to the scheme developed by RC. The period of record of our wind data includes the three most recent El Niño years considered by RC (1965, 1969, and 1972). In addition, we include the 1963 event (which was regarded as "atypical" by RC because the SST anomalies appeared later in the year compared with other El Niños), and the 1976 event, for a total of five events. Table 4.1 documents the data coverage for the composites. Trivandrum, Singapore, Koror, and Truk are represented in each event, and Majuro is missing only during the 1969 event. Canton stopped reporting in 1967, Kota Kinabalu is represented in the three most recent events, and Atuona reported only during the 1970s.

The selection of events for inclusion in the composites is a matter of some controversy. A NOAA committee (SCOR Working Group 55) was organized in 1982 for the purpose of creating a standard definition of an El Niño event. By their definition (a positive SST anomaly of

TABLE 4.1

Data coverage for the five El Niño events contributing to the composite anomalies shown in Figs. 4.1 and 4.2. An asterisk is entered when observations for all seasons from SON(-1) to DJF(+1) were taken at the station during an event. The table entry is blank when no observations were taken during the event. The footnotes explain cases where most but not all seasons are represented in the composite.

Abbreviation	Station name	1963	1965	1969	1972	1976
TRV	Trivandrum	a	*	*	*	b
SIN	Singapore	*	*	*	*	*
KIN	Kota Kinabalu			*	*	c
KOR	Koror	*	*	*	*	*
TRK	Truk	*	*	*	*	*
MAJ	Majuro	*	*		*	*
CAN	Canton	*	*			
ATU	Atuona			a	*	*

Footnotes: a) all seasons except SON(-1) and DJF(0)
b) all seasons except JJA(0)
c) all seasons except MAM(0)

magnitude one standard deviation persisting for four months simultaneously at three South American stations) the 1969 El Niño does not qualify as an "event", but the 1963 El Niño excluded by RC does qualify. Horel (1982a) included both 1963 and 1969 in his composites, as will the present study.

Composite fields are calculated for the four seasons of the El Niño years (denoted DJF(0), MAM(0), JJA(0), and SON(0)), for the SON season preceding each El Niño year, SON(-1), and for the DJF season following each El Niño year, DJF(+1). The seasonal composites presented here correspond closely to the RC compositing periods in the following way: SON(-1) with Antecedent Phase; DJF(0) with Onset Phase; MAM(0) with Peak Phase; SON(0) with Transition Phase; and DJF(+1) with Mature Phase. The seasonal sequence of composite vector wind anomalies for the near-equatorial stations in the Trivandrum-Atuona cross-section is shown in Fig. 4.1. The prominent features in the composites for each season are discussed in turn.

(a) SON(-1). A clear, coherent pattern of anomalies appears in the Antecedent composite. At 850 mb, westerly anomalies with magnitude about 2 m/s are observed at Trivandrum and Singapore, and easterly anomalies of similar magnitude occur to the east, between 120°E and 150°W. These are strong anomalies, since the standard deviation of zonal wind anomalies at these stations is between 1 and 2 m/s (Fig. 3.1). The anomalies reverse in the upper troposphere: easterly anomalies occur above 500 mb at Trivandrum and Singapore, and westerly anomalies occur above 700 mb at Majuro, Canton, and Atuona. The strongest upper level wind anomalies are found at Majuro and Canton (near the date line), where westerly anomalies exceed 5 m/s. These anomalies are also well in

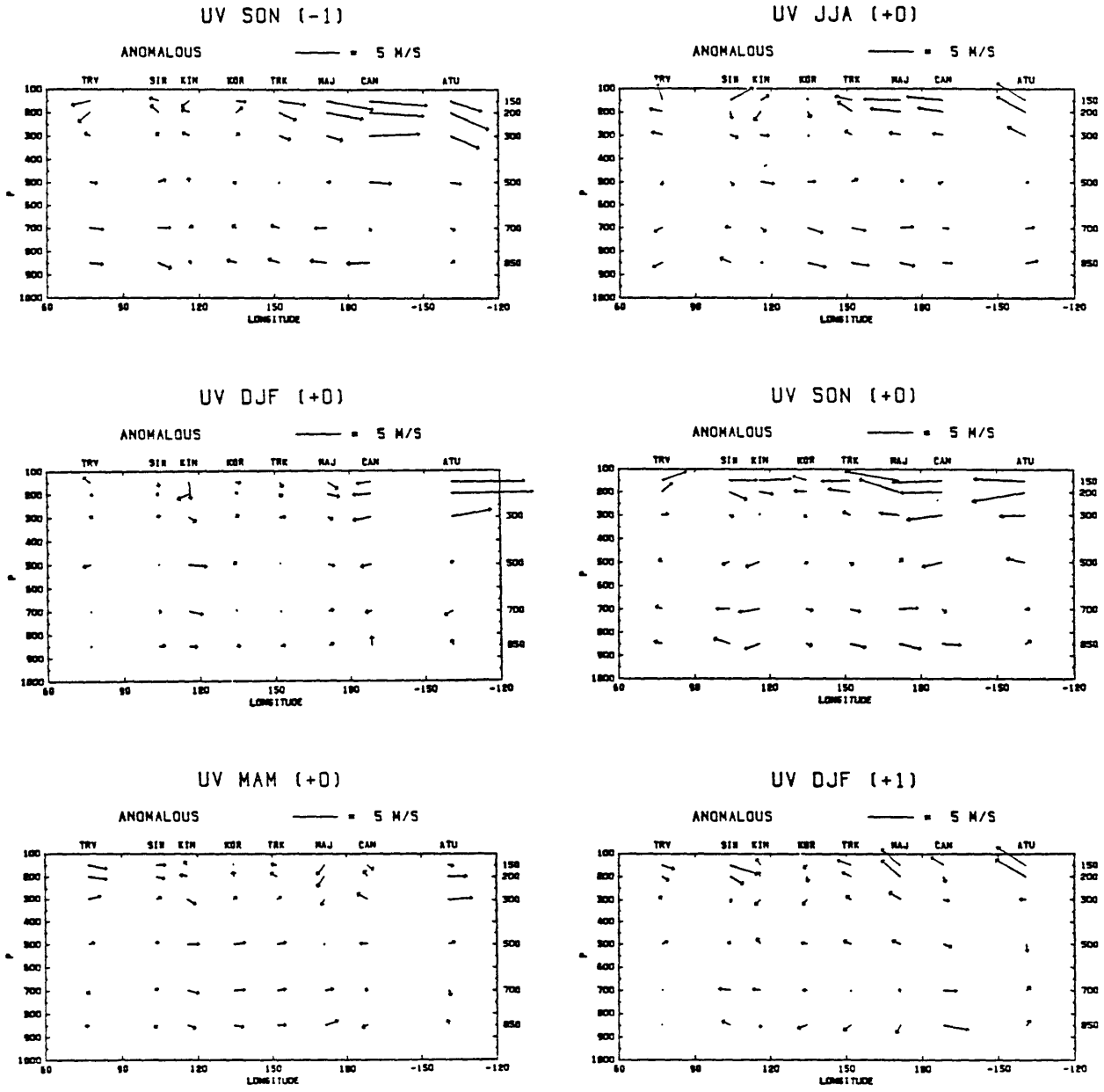


Figure 4.1 - Vector wind anomalies across the Trivandrum-Atuona cross-section for the composite El Nino event, based on events in 1963, 1965, 1969, 1972, and 1976.

excess of 1 standard deviation, which is 3 m/s at Majuro and Canton. The RC surface wind anomaly composite for this period contains a small, weak patch of easterlies located near the date line along the equator. The 850 mb anomalies near the date line are about twice the magnitude of the RC surface anomalies, consistent with the ratio of (850 mb)/(surface) zonal wind variability found by Harrison and Gutzler (1985).

(b) DJF(0). The composite shows no coherent, large-scale circulation patterns. The largest anomalies in the composite occur at Kota Kinabalu, Canton, and Atuona, which are the stations that are represented the fewest times in the composite (Table 4.1). The significance of these anomalies will be discussed further in Section 4.4. During this phase in the RC composites, sea surface temperatures along the Peru - Ecuador coast are near normal but rising rapidly. A second warm SST anomaly is located along the equator at the dateline, overlain by westerly surface wind anomalies with a magnitude of about 1 m/s. Precipitation is above normal near the equator west of the dateline, and below normal east of the dateline. 300 mb geopotential height is below normal throughout the tropics, with the largest anomalies over the western Pacific and India.

(c) MAM(0). Significant westerly anomalies, approximately 2 m/s in strength, occur throughout the lower troposphere between 120°E and the date line. The upper tropospheric anomaly field between 300 and 150 mb has changed dramatically from its state in SON(-1): over the equatorial Indian Ocean, the anomalies have shifted from easterly to westerly (with maximum strength greater than 2 m/s at Trivandrum), and between 150°E and 180° the anomalies have collapsed. The RC composite SST anomaly is now greatest along the Peru coast, with a magnitude of nearly 2°C. A warm SST anomaly of about 0.5°C extends westward along the equator to

160°E. The equatorial surface wind anomalies also have a westerly component between 160°E and 160°W, and between 140°W and 110°W.

(d) JJA(0). The lower tropospheric westerly anomalies have moved eastward relative to their position during MAM(0), and strengthened to 3 m/s between 130°E and 160°E. Anomalous lower tropospheric westerlies now extend eastward at least as far as Atuona. At 200 mb and above, easterly anomalies exceeding 4 m/s are present near the dateline. To the west of 100°E, lower tropospheric easterly anomalies exceeding 1 m/s are observed.

(e) SON(0). This season, corresponding to the Transition phase of RC, contains the largest anomalies of the sequence. 850 mb westerly anomalies exceed 3 m/s near the date line, an eastward shift from their position during JJA(0). At 200 mb, easterly anomalies greater than 6 m/s exist eastward of 170°E. The RC composites for this season show a positive SST anomaly exceeding 1°C extending along the equator from 170°W to the South American coast, and westerly surface wind anomalies near the equator between 140°E and 170°W. A clear anomaly signature is apparent in the present analysis far to the west, where lower tropospheric easterly anomalies exceeding 2 m/s occur between 90°E and 120°E. Upper level westerly anomalies with magnitude 3 m/s are present from 80°E to 120°E. The entire circulation pattern is nearly the reverse of the SON (-1) anomaly composite.

(f) DJF(+1). Easterly anomalies at 850 mb now extend eastward to 150°E; westerly anomalies are confined to Canton and Atuona. The same longitudinal distribution of surface wind anomalies along the equator was found by RC for this season. The easterly upper tropospheric anomalies to the east of 150°E have weakened to less than 5 m/s, and

southerly meridional anomalies of the same magnitude are observed at Majuro, Canton, and Atuona. The SOI reaches its most negative value during this phase of the event, so the meridional anomalies at 200 mb over the central Pacific are consistent with the negative SOI - 200 mb meridional wind correlations found by Selkirk (1984) at these locations for the DJF season (Fig. 3.1c).

The anomalous zonal mass flux, calculated from [2.2] by substituting the seasonal zonal wind anomalies u' from the composites in place of the climatological wind u, provides a concise depiction of the large-scale circulation anomalies in the zonal plane associated with each phase. The seasonal mean zonal mass fluxes for the same cross-section were shown in Fig. 2.11. The position, tilt, and intensity of the climatological Walker Circulation was found to change with season. In all seasons, however, the Walker Circulation includes westward transport of mass in the lower troposphere, i.e. $M_z > 0$ and $\partial M_z/\partial z > 0$ in the lower troposphere. Hence, closed isopleths of $M_z > 0$ (solid lines) derived from anomalous winds represent a circulation which strengthens the climatological Walker Circulation, and closed isopleths of $M_z < 0$ (dashed lines) represent anomalies opposing climatology.

Plots of the anomalous zonal mass flux derived from the zonal component of the composite El Niño wind anomalies are shown in Fig. 4.2. The anomalous circulations are weak compared with the seasonal means, but there is clear evidence of an anomalous circulation directed counter to the climatological Walker Circulation, which propagates from a position over the eastern Indian Ocean in SON(-1) eastward into the mid-Pacific during the evolution of the event. The circulation undergoes a longitudinal shift of approximately 25° per season. It is plainly

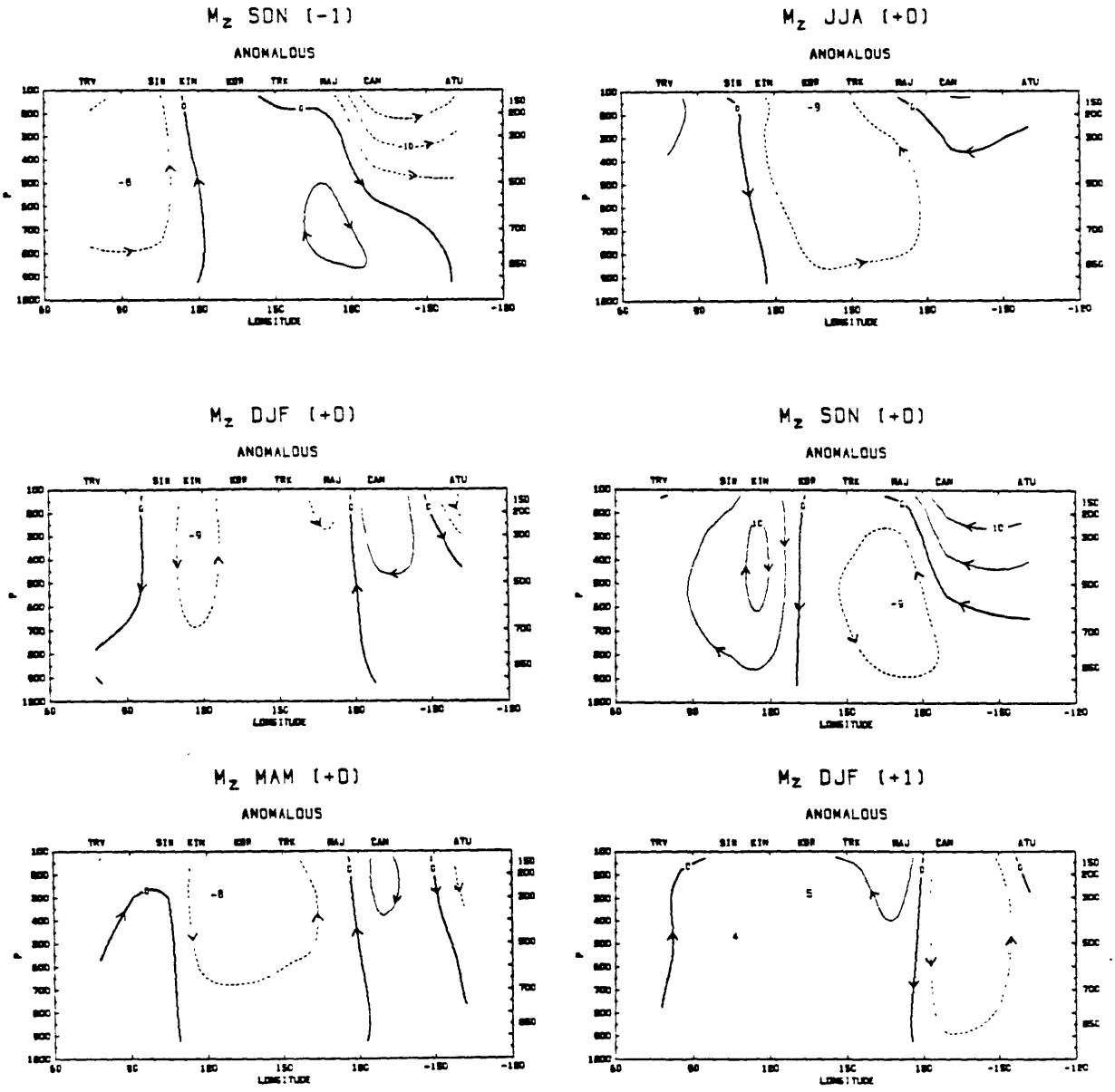


Figure 4.2 - Anomalous zonal mass flux across the Trivandrum-Atuona cross-section for the composite El Nino event, based on the zonal component of the wind fields shown in Fig. 4.1.

evident in the SON(-1) composite, a full season before a warm SST anomaly appears in the eastern Pacific.

The composites presented here show that a coherent, highly significant pattern of zonal wind anomalies, extending vertically throughout the troposphere, evolves along the equator over the eastern Indian and western Pacific Oceans in conjunction with El Niño events. The Pacific surface wind composites of RC, and the 200 mb wind composites of Arkin (1982), contain features qualitatively consistent with the major features of the present composites at stations in the eastern half of the Trivandrum-Atuona cross-section. However, the anomalies shown here are much larger in magnitude and statistical significance, and contain vertical structure information. The increased anomaly strength can be attributed to the use of station data here rather than the highly smoothed analysis product used by RC and Arkin, because the western and central Pacific is a data-sparse region. The composites in Figs. 4.1 and 4.2 demonstrate that the circulation anomalies associated with El Niño extend far to the west of the Pacific basin into the Indian Ocean.

4.3 Complex EOF analysis of zonal wind anomalies

In Chapter 3, the interannual variability of the tropical wind field was studied using 1dEOF and 2dEOF analyses to isolate the dominant modes of variability. The EOF procedure statistically separates individual orthogonal patterns with a variance-maximizing algorithm. The El Niño composites presented in the previous section are based on a different technique for defining the dominant modes of variability, namely averaging several fields with respect to a known, well-defined signal (in this case, sea surface temperature in the eastern Pacific Ocean).

Comparable results were obtained from the two different approaches. Time series of the principal components associated with the baroclinic 1dEOF mode of zonal wind at stations within 12° of the equator were highly correlated with the Southern Oscillation (Figs. 3.17, 3.21-23). Conversely, the composite El Niño anomalies over the western Pacific have a baroclinic vertical structure.

However, the propagating feature in the series of El Niño composites cannot be correctly described by the 2dEOF method applied to interannual variability in Section 3.4, which decomposes the wind variance in terms of standing oscillations only. A propagating disturbance would be partitioned by the 2dEOF algorithm into separate orthogonal modes of similar structure, but phase-shifted. The two gravest modes of the 2dEOF were in fact found to have similar spatial patterns that were phase-shifted (Fig. 3.25), and the associated time series of principal components were correlated at lags of one and two seasons (Table 3.1).

A generalization of the EOF analysis technique that can resolve both standing and propagating disturbances was introduced by Barnett (1983) and reviewed by Horel (1984). This procedure, referred to as complex empirical orthogonal function (or CEOF) analysis, is documented in Section 4 of Appendix B. It differs from the scalar 2dEOF procedure in that the eigenvectors are derived from the covariance matrix associated with complex time series $\mathbf{U}(t) = u(t) + i\hat{u}(t)$, where u is the zonal wind component for a particular station and pressure level, and $\hat{u}(t)$ is the Hilbert transform of u(t). The Hilbert transform preserves phase information, so that the CEOF eigenvectors describing the spatial variability are complex, with variable phase and amplitude (rather than the variable

sign and amplitude of scalar EOFs). Eigenvectors are calculated for the mass-weighted complex covariance matrix

$$\mathbf{C}_{rlsm} = \overline{\mathbf{U}_{rl}\mathbf{U}_{sm}}\,\sqrt{\Delta_l \Delta_m}$$

where complex quantites are shown in boldface, the overbar represents a time average, subscripts r and s represent stations, subscripts l and m represent pressure levels, and Δ is a mass-weighting factor (see Appendix B). The gravest CEOF $\mathbf{E}^1_{rl}$ explains the most variance of any single spatial mode. Associated with each CEOF is a time series of complex principal components (or CPCs). The CPCs $\mathbf{P}^k(t)$ are calculated from the formula

$$\mathbf{P}^k(t) = \sum_r \sum_l \mathbf{U}_{rl}\mathbf{E}^k_{rl}\,\Delta_l \qquad [4.1]$$

The (complex) time series of observations $\mathbf{U}_{rl}(t)$ can then be represented as the linear sum of contributions from the entire set of CPCs from

$$\mathbf{U}_{rl}(t) = \sum_k \mathbf{E}^{k*}_{rl}\,\mathbf{P}^k(t) \qquad [4.2]$$

where the asterisk denotes the complex conjugate. The actual wind anomaly $u_{rl}(t)$ is simply the real part of $\mathbf{U}_{rl}(t)$, and the wind anomaly associated with a single mode is the product of that mode alone with its CPC, without taking the sum over k in [4.2].

The CEOF procedure is applied here to the zonal wind field for the same set of six near-equatorial stations (Trivandrum, Singapore, Kota Kinabalu, Koror, Truk, and Majuro), for the same period of record (1970-1979), as for the scalar 2dEOF analysis in Section 3.4b. In three of the forty seasons during this decade, one station was missing data, in which case the anomalies were linearly interpolated from the preceding and succeeding seasonal anomalies at the same station and pressure level.

The structure of the gravest mode E^1 of this analysis is shown in Fig. 4.3. The element of the CEOF mode at each station and pressure level is plotted as an arrow, which depicts the amplitude and phase of each element relative to all the other elements. A CEOF mode representing a standing oscillation would contain arrows which are all parallel to each other (i.e. all elements fluctuating exactly in or out of phase). This structure is close to the vertical structure observed in mode 1. At each station, the element at 850 mb is directed nearly opposite the element at 150 mb. However, the horizontal structure is characteristic of a propagating oscillation: the elements at a particular level rotate clockwise moving eastward. This mode explains 52% of the total variance, a 9% increase from the gravest 2dEOF mode shown in Fig. 3.25.

The direction of propagation is determined by the time series of CPCs $P^1(t)$, shown in the lower half of Fig. 4.3. The amplitude of the zonal wind anomaly field associated with mode 1 for a particular season is proportional to the amplitude of the CPC for that season. A distinctive signal is observed in the time series of CPCs prior to and during the El Niño events of 1972 and 1976. One season before the appearance of warm water in the eastern Pacific, during the SON seasons of 1971 and 1975, the amplitude of the CPC increases, with a negative real part and positive imaginary part (i.e. the CPC vector points to ten o'clock). The CPCs subsequently rotate clockwise with time through the following seasons.

The projection of the CEOF mode onto the zonal wind anomaly field is the real part of the inner product of the CEOF mode and its CPC. The "ten o'clock" phase of the CPC represents upper tropospheric zonal wind

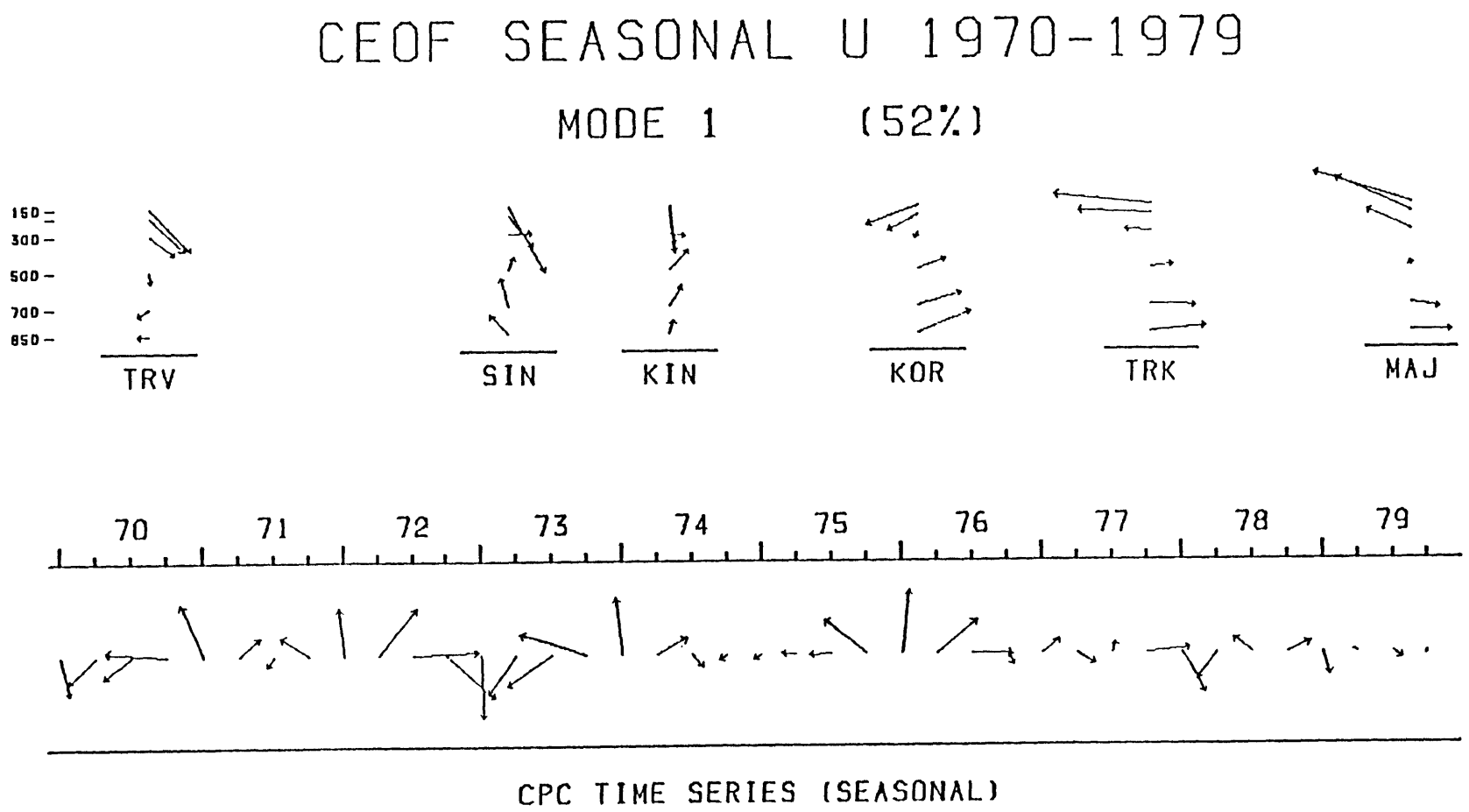


Figure 4.3 - Top: Structure of the gravest mode of a complex EOF analysis of seasonal anomalies of zonal wind (for the period 1970-1979) for six near-equatorial stations over the eastern Indian and western Pacific Oceans.
Bottom: Time series of complex principal components associated with the gravest mode.

anomalies which are negative at Trivandrum, negligible at Koror, and positive at Truk and Majuro. These are the same features shown on the SON(-1) composite in Fig. 4.1. The combination of clockwise rotation of the CEOF elements moving eastward from Trivandrum to Majuro, along with clockwise rotation of the CPCs with time, imply that the anomaly field associated with mode 1 propagates eastward with time during El Niño events, a feature which is also consistent with the El Niño composites in Figs. 4.1 and 4.2.

As examples of the relationship between the CEOF mode structure, the CPC vector, and the wind anomaly field, the reconstructed wind fields (calculated from [4.2] considering only mode 1) are compared to the observed anomalies for seasons SON(1975), DJF(1976), and JJA(1976) in Figs. 4.4 through 4.6. These seasons are shown as representative examples of the near-complete description of the zonal wind anomaly field provided by the single CEOF mode during El Niño events. Although the gravest mode explains 52% of the total non-periodic seasonal wind variance for the entire 1970-1979 decade, during the El Niño periods of SON(1971)-DJF(1973) and SON(1975)-DJF(1977) the gravest mode explains 73% of the variance.

The CEOF mode 1 reconstruction for SON(1975) (Fig. 4.4) contains easterly anomalies at 200 mb and 150 mb of approximately 4 m/s at Trivandrum and Singapore, westerly anomalies of 6-7 m/s at Truk and Majuro, and smaller anomalies of opposite sign at 700 mb and 850 mb at each station. The pattern of the mode 1 reconstruction agrees closely with the observed anomalies: the spatial correlation between the mode 1 estimated anomalies and the observed anomalies for this season is 0.94. The only notable discrepancies between the reconstruction and the

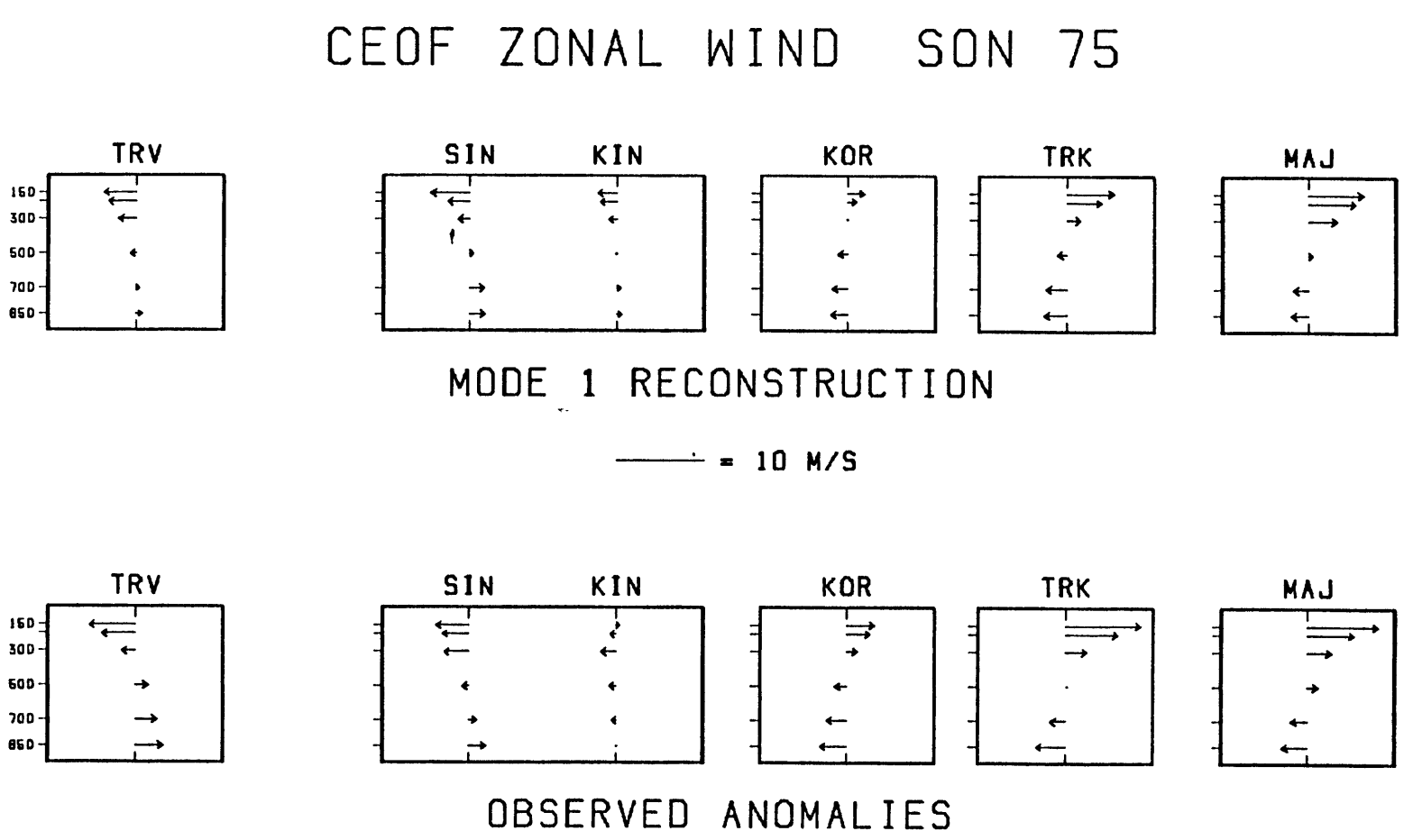


Figure 4.4 - Top: Reconstructed zonal wind anomaly field associated with CEOF mode 1 for SON(1975).

Bottom: Observed zonal wind anomaly field for SON(1975).

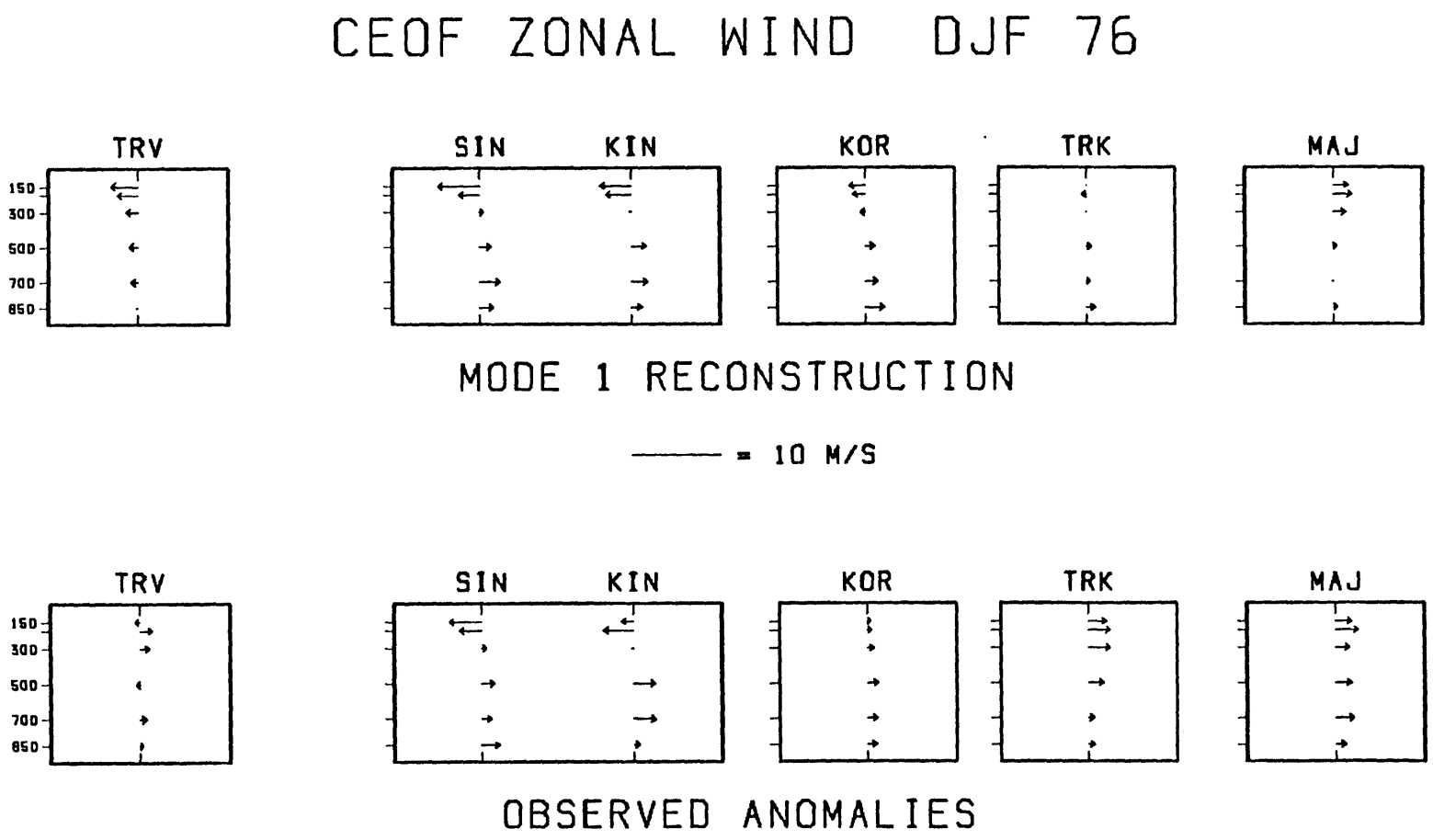


Figure 4.5 - As in Fig. 4.4, but for DJF(1976).

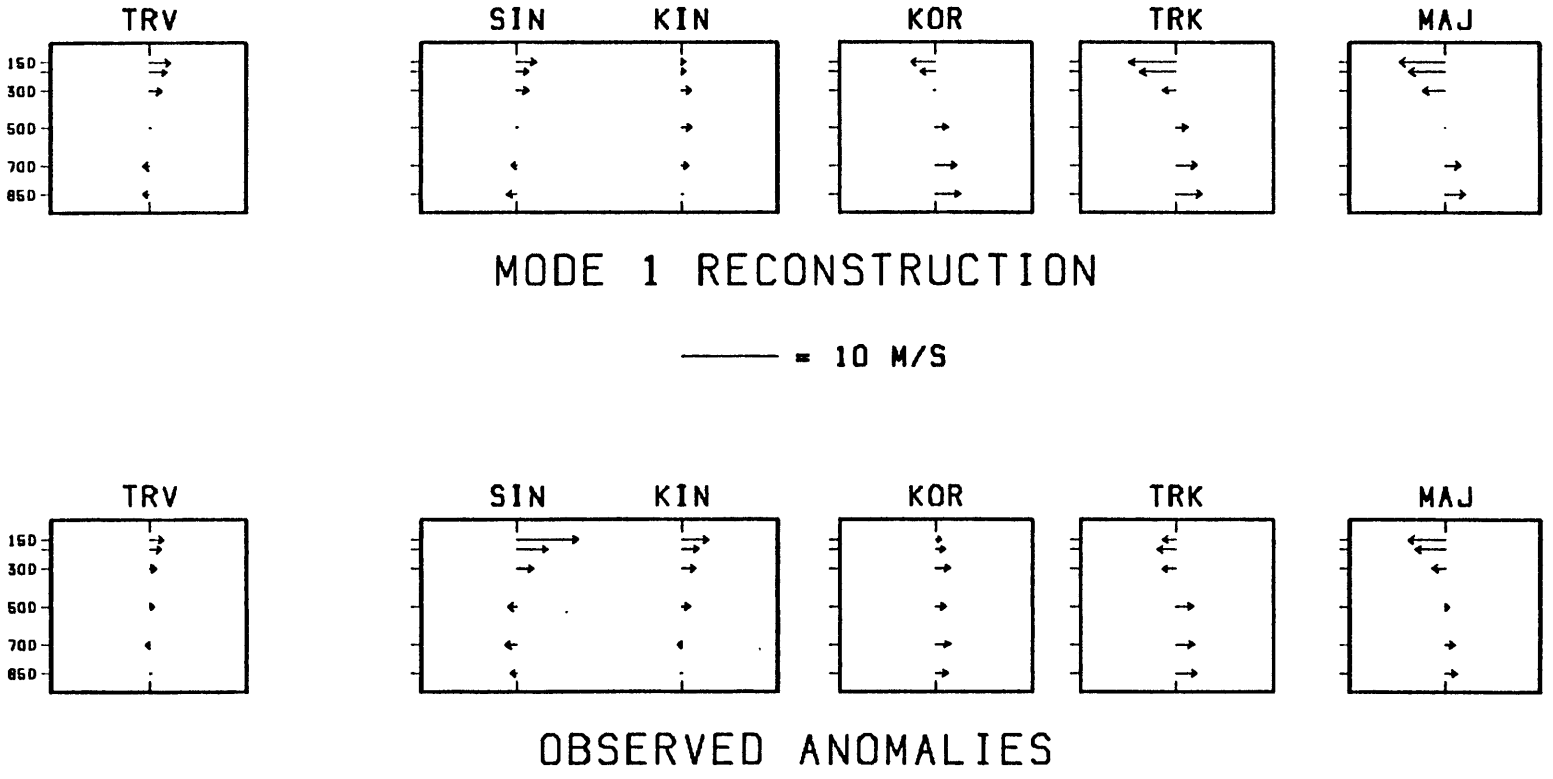


Figure 4.6 - As in Fig. 4.4, but for JJA(1976).

observations are the underestimates of the amplitude of the observed anomalies in the lower troposphere at Trivandrum and in the upper troposphere at Truk and Majuro.

During the Onset Phase in the following season, DJF(1976), the reconstructed field contains anomalies of greatly reduced amplitude at Truk and Majuro, and anomalies at Koror which are reversed in sign relative to the SON 1975 reconstruction (Fig. 4.5). The agreement with observations is particularly close in the lower troposphere, where the reconstruction successfully shows that the easterly anomalies which were present at the three western stations in SON 1975 have switched direction to westerly. The reconstruction fails to simulate the equivalent-barotropic vertical structure of anomalies at these stations, and incorrectly shows upper tropospheric easterly anomalies at Trivandrum, where the actual anomalies are near zero.

Two seasons later, the JJA(1976) anomalies (Fig. 4.6) are nearly the opposite of the Antecedent conditions. The eastward propagation of the anomaly field is indicated by the shift of the band of lower tropospheric westerly anomalies from Singapore, Kota Kinabalu, and Koror in DJF to Koror, Truk, and Majuro in JJA. The principal error in the reconstructed field is the longitudinal position of the node between opposing anomalies, which is located near Kota Kinabalu in the reconstruction but located farther east, between Kota Kinabalu and Koror, in the observations.

The rate of rotation of the CPC during these events is close to $\pi/4$ per season, so that the "period" of the oscillation is approximately two years. The amplitude of the CPC remains large through a complete cycle in 1972-73, but dies out after the JJA season in 1976, so that it would

be misleading to denote this fluctuation as a 'quasi-biennial oscillation'. Since Trivandrum and Majuro are separated by about 90° of longitude, the anomaly pattern projects onto zonal wavenumber 2 and the phase speed of the anomaly is approximately 0.3 m/s, or 25 km/day.

Time series of the real and imaginary parts of the CPC of mode 1 are shown in Fig. 4.7, with the sign of the imaginary part reversed. Plotted in this format, the rotation with time of the CPC vector is apparent as a time lag between the real and imaginary parts, with the imaginary part leading. Seasonal lag correlation coefficients between the real and imaginary parts of the gravest mode of the CEOF analysis and the SOI are documented in Table 4.2. Both the real and imaginary parts are highly correlated with the SOI, with the real part lagging and the imaginary part leading the SOI. The set of correlation coefficients in Table 4.2 are statistically indistinguishable from the SOI correlations associated with the first two scalar 2dEOFs presented in Table 3.1. The correlation between the principal component associated with scalar 2dEOF mode 1, and the real part of the CPC associated with CEOF mode 1, is 0.95. The correlation between scalar 2dEOF mode 2 and the imaginary part of CEOF mode 1 is 0.70. The first mode of the CEOF analysis, an eastward-propagating mode, effectively represents the first two modes, both standing oscillations, of the scalar 2dEOF analysis. Hence, seasonal zonal wind variability over the western Pacific is most properly treated as a propagating oscillation.

Two points are worth emphasizing. First, the beginning of the sequence of anomalies during the El Niño period occurs 4-6 months <u>before</u> the appearance of warm surface waters to the east. Second, the direction

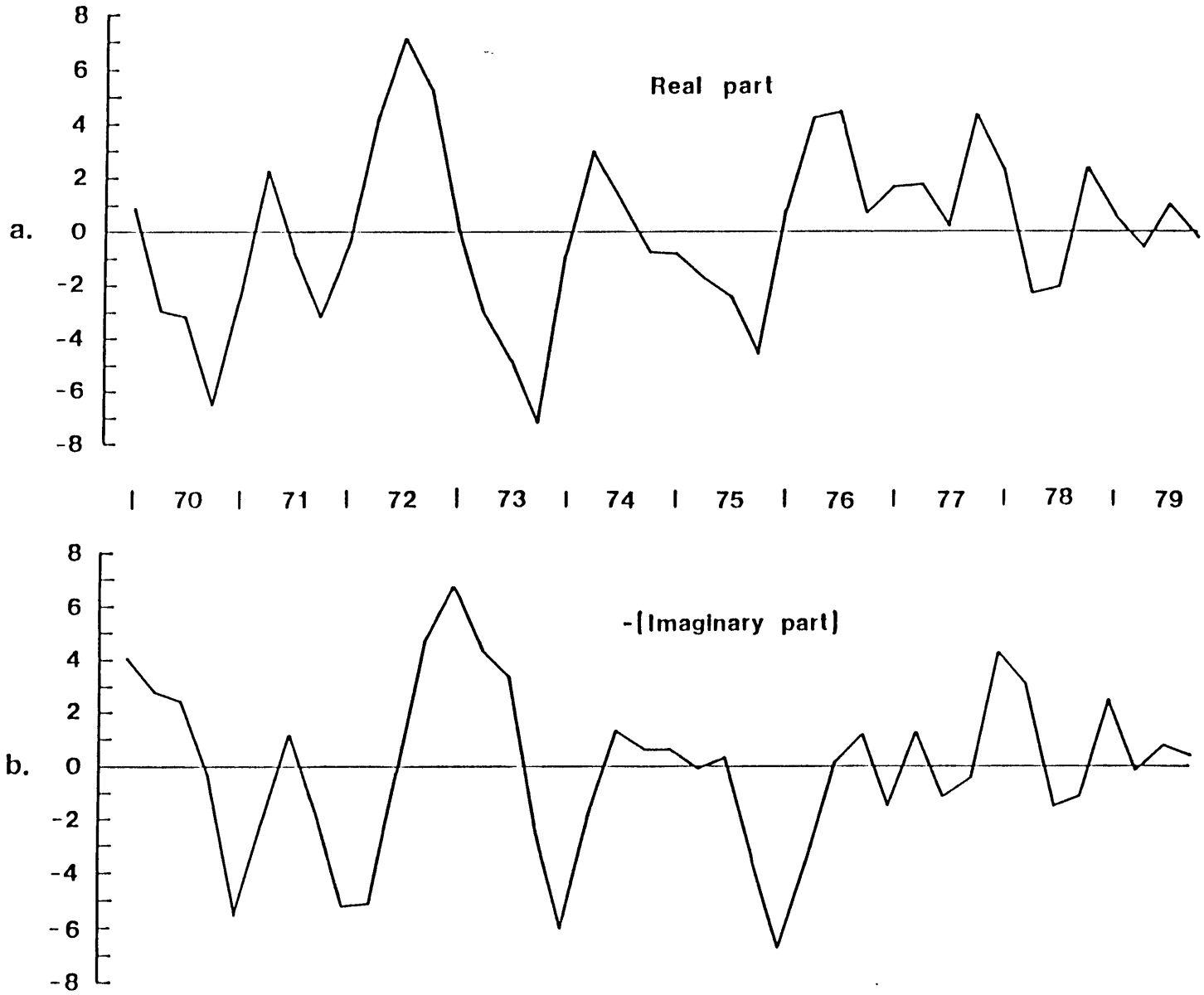


Figure 4.7 - Time series of (a) real part (b) -(imaginary part) of P^1.

TABLE 4.2

Lag correlation coefficients between SOI (see Fig. 3.1 a), and time series of the real and imaginary parts of the complex principal components associated with the first mode of the CEOF analysis of seasonal zonal wind anomalies at six near-equatorial stations between 80°E and 170°E, for time lags up to three seasons (compare with Table 3.1a).

	Lag (seasons; positive → SOI leads)						
	-3	-2	-1	0	1	2	3
Real part	0.35	0.17	-0.12	-0.47	-0.65	-0.56	-0.38
Imaginary part	0.34	0.52	0.62	0.49	0.16	-0.18	-0.33

of rotation of the CPC is always clockwise, implying eastward propagation of anomalies. No "back-and-forth" movement of anomalies is evident.

To test the dependence of these results on the use of seasonal anomalies, the CEOF analysis was repeated for the same set of stations using monthly anomalies of zonal wind rather than seasonal anomalies. The gravest mode of the monthly CEOF analysis, and the corresponding time series of CPCs, are shown in Fig. 4.8. The spatial pattern associated with the gravest mode is indistinguishable from the gravest mode based on seasonal anomalies, but the mode explains a smaller fraction of the total variance (38%) in the monthly time series. The CPCs display the same direction of rotation, and generally the same rotation rate, as in the seasonal analysis. The monthly time series is considerably noisier, however. Since considerable variance in the zonal wind field over the western Pacific is associated with a 40-50 day oscillation (Madden and Julian, 1971) which would be severely aliased in monthly mean data, it is not surprising that fluctuations in the monthly mean data show considerably less temporal continuity than the corresponding seasonal means. The analysis using the monthly means serves to demonstrate that the spatial structure and eastward propagation of the gravest mode of the seasonal mean CEOF analysis are not artifacts of seasonal averaging.

The data record for the decade of the 1960's, preceding the period used for the CEOF analysis, contained too many missing records to independently reproduce the analysis. However, it was possible to project the gravest spatial mode derived from the later period of time onto the wind anomalies for the earlier period, thus extending the time series of CPCs backward in time. First, the CEOF analysis based on the

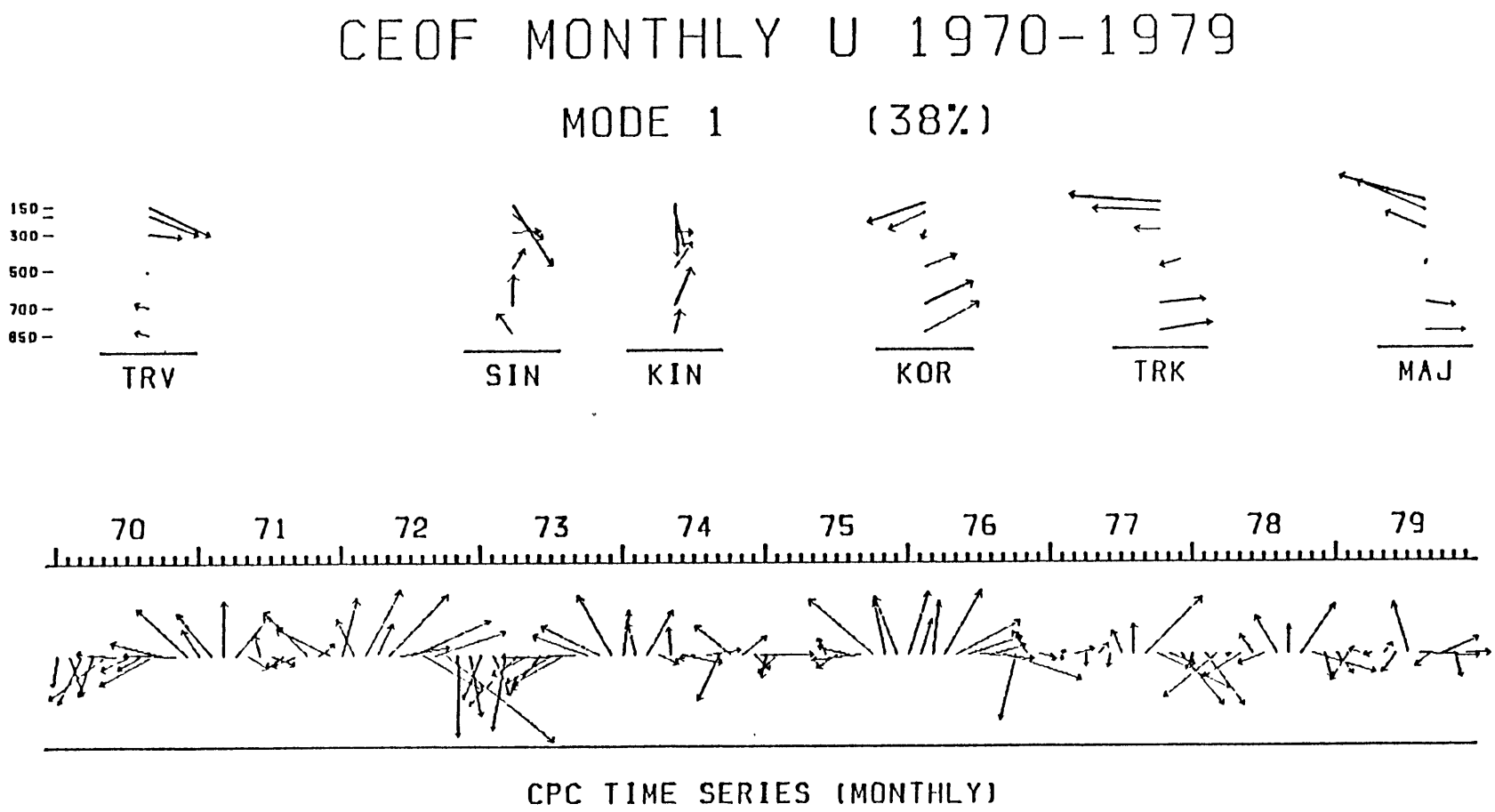


Figure 4.8 - As in Fig. 4.3, but based on monthly wind anomalies.

1970's data was repeated six times, deliberately removing a different station in turn from the network. These results (not shown) demonstrated that the shape of mode 1 was not sensitive to removal of any single station.

The extended CPC time series was then calculated by taking the inner product of $\mathbf{U}$ and $\mathbf{E}^{1}$ as in [4.1], but summing only over those stations reporting at each time t, and normalizing the partial sum to compensate for the missing stations, i.e.

$$\mathbf{P}^{1}(t) = \sum_{r} \left(\sum_{1} \mathbf{U}_{r1}(t)\, \mathbf{E}^{1}_{r1}\, \Delta_{1} \quad \frac{8.00}{\sum_{1} \mathbf{E}^{1}_{r1} \Delta_{1}} \right)$$

where here the sum over r is a partial sum, excluding any stations which are missing.

The extended CPC time series is shown in Fig. 4.9. The number of stations included in each season's CPC is indicated by the rows of numbers in the center of the plot; data for at least four stations are present in each season. It is immediately apparent that the amplitude of the CPCs (and therefore the amplitude of the associated zonal wind anomalies) is lower in the decade of the 1960's (as was the amplitude of the SOI - see Fig. 3.1a).

Still, there is some indication of the correspondence between this CEOF mode and El Niño events in the 1960's. Although the amplitude of the CPC early in the 1963 event (SON 1962 through JJA 1963) is small, the phase of the CPC is generally consistent with the corresponding seasons of the 1972 and 1976 events. Between JJA(1963) and DJF(1964), the amplitude of the CPC increases and its clockwise rotation is more regular.

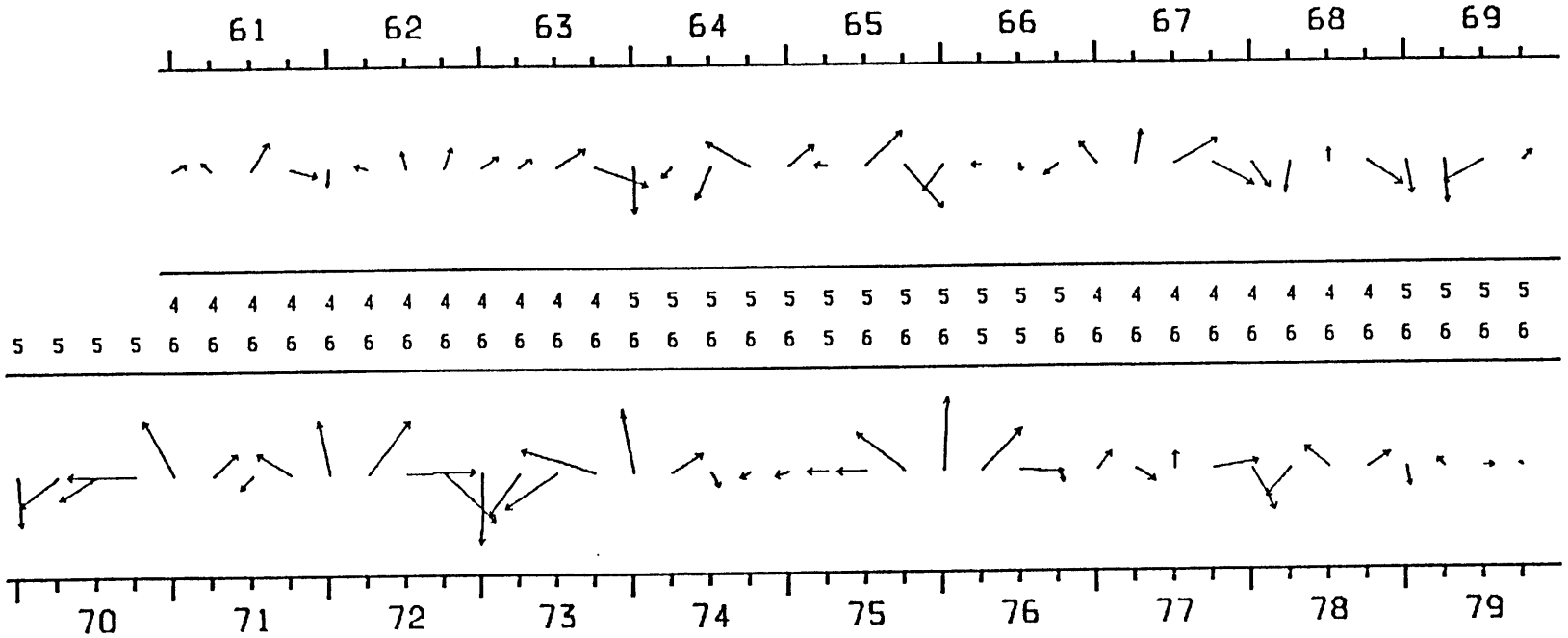


Figure 4.9 - Time series of complex principal components derived by projecting the complex EOF mode shown in Fig. 4.3 onto the observed anomaly field of available stations for the period 1961-1979. The number of stations available (out of a total of six) for each season's principal component is indicated along the abscissa.

The 1965 event is not clearly associated with coherent rotation of the CPC vectors, but the CPC vector for SON 1964 (immediately preceding the event) has nearly the same amplitude and phase as the vectors for SON(1971) and SON(1975), and the vectors during the Mature Phase (JJA and SON 1965) are also roughly consistent with the corresponding vectors for 1972 and 1976.

The 1969 period bears no resemblence whatsoever to other El Niño events in the CPC time series. Also, a period of clockwise rotation of the CPC vectors takes place during 1967, which does not correspond to an El Niño event.

In summary, the CEOF analysis has described a spatial pattern of near-equatorial tropospheric zonal wind anomalies which is closely associated with El Niño. The wind anomalies included in this pattern extend far to the west of the Pacific basin, at least as far as the southern tip of India. The vertical structure of these anomalies is the baroclinic structure described in Chapter 3. In 1962, 1964, 1971, and 1975, one particular phase of this pattern clearly preceded the appearance of warm water in the eastern Pacific, which up to now has defined the onset of an El Niño event. The anomaly pattern propagates eastward into the mid-Pacific with a period of two years; however, the anomalies typically do not remain large for an entire two-year cycle.

An attempt to reproduce the temporal characteristics of this mode for the decade of the 1960's proved inconclusive. Therefore, in the next section we examine in detail the similarities and differences between the evolution of wind anomalies during each of the individual El Niño events.

4.4 Comparison of individual El Niño events

The previous two sections documented the temporal evolution of wind anomalies over the equatorial eastern Indian and western Pacific Oceans associated with El Niño episodes. The composite wind anomalies presented in Section 4.2 showed a clear signal in the zonal wind component with a baroclinic vertical structure. The zonal mass flux composites indicated that an anomalous circulation cell, directed counter to the climatological Walker circulation, propagates eastward during the course of the event. The complex EOF analysis presented in Section 4.3 verified that an eastward-propagating signal with a baroclinic vertical structure was the dominant statistical mode of zonal wind variability during the 1970's over the equatorial region between 80°E and 140°W, and that the temporal fluctuations of this mode were highly correlated with the SOI.

However, the results of the extended CPC analysis (applied to data from the period 1961-1969) were not so clear-cut. Hints of systematic eastward propagation of anomalies were seen in the CPC time series during the 1960's, but the extended time series did not provide clear confirmation that the temporal evolution and spatial structure of wind anomalies during El Niño events derived from the later period of data were reproducible in independent data. Hence, closer inspection of the similarities and differences between individual El Niño events is called for.

In this section, seasonal wind anomaly fields and zonal mass flux anomalies are presented for individual events, i.e. the individual seasonal anomalies that were averaged together in Section 4.2 to form the composite event fields. Our aim is to see how closely the anomaly fields for each event resemble the composites; or, put another way, to

check the degree to which the composite anomalies reflect the structure of actual anomalies during individual events.

Fig. 4.10 contains plots of the anomalous vector wind for the five seasons contributing to the SON(-1) (Antecedent Phase) composite. The CEOF mode 1 CPC vector (P^1) is plotted next to the wind field for each season. Fig. 4.11 contains corresponding plots of the anomalous zonal mass flux for these five SON seasons. Four of the five fields (all except SON 1968) show features broadly resembling the SON (-1) composite (Figs. 4.1 and 4.2). These four anomaly fields each contain a pair of opposing circulation cells, with lower tropospheric convergence and upper tropospheric divergence over the far western Pacific. The center of convergence is located near 120^0E in 1964, 1971, and 1975, and near 150°E in 1962. Accordingly, the CPC vector for SON(1962) is rotated clockwise about 90° compared to 1964, 1971, and 1975. Strong westerly upper tropospheric anomalies occur over the central Pacific in each of these four seasons. Despite the evident similarity of these four anomaly fields, the differences between them, coupled with the presence of one season with a very different pattern (SON 1968), are sufficient to reduce the amplitude of the SON(-1) composite anomalies of wind and zonal mass flux considerably compared to any of the individual anomaly fields.

The anomalies associated with the following season, DJF(0) (Figs. 4.12 and 4.13), display much less consistency from event to event. The upper tropospheric anomalies at Truk and Majuro are easterly in 1963 and 1965, but westerly during subsequent events; the anomalies at Atuona in 1972 are opposite those in 1976; lower tropospheric zonal anomalies and upper tropospheric meridional anomalies at Canton in 1963 are directed

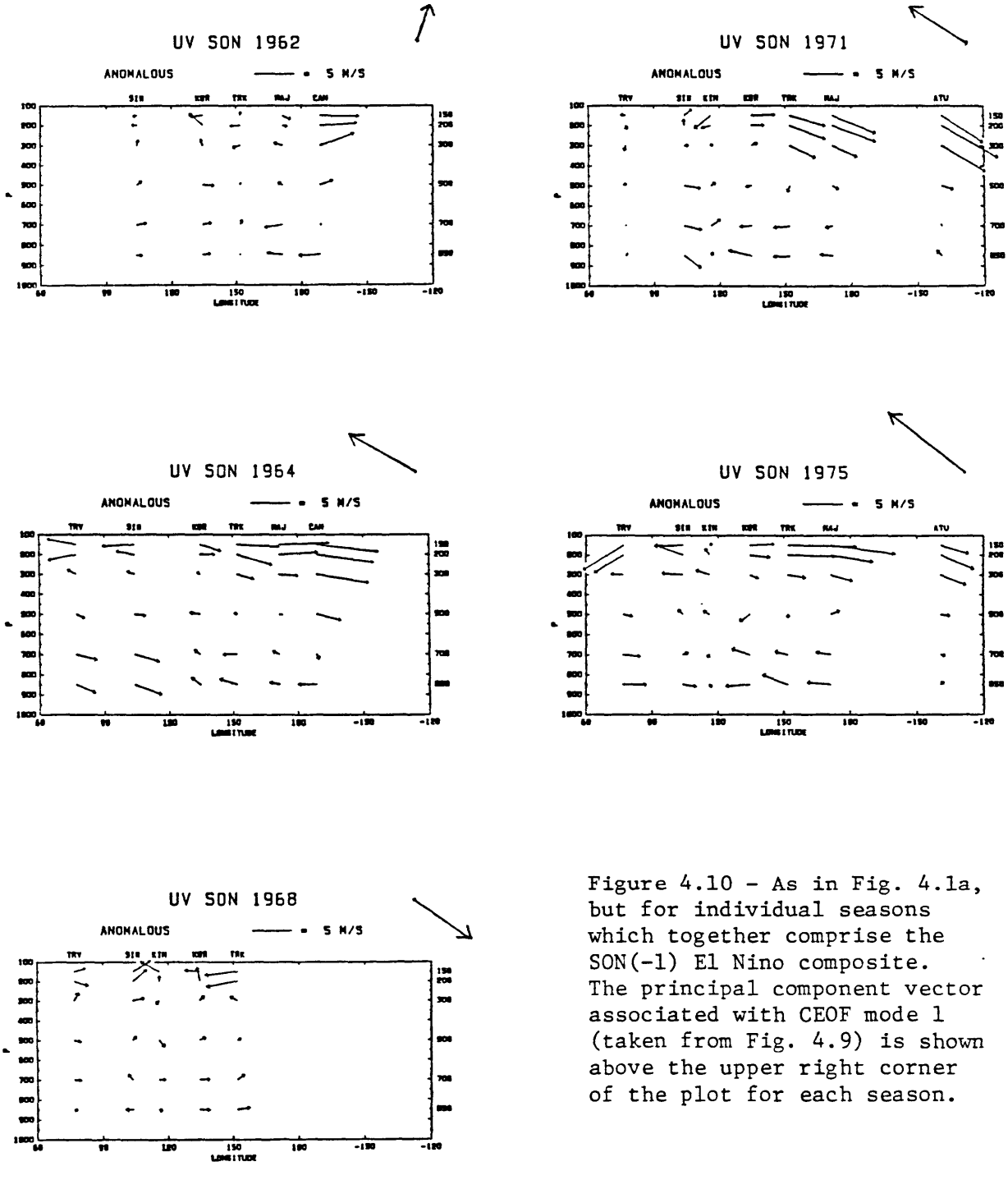
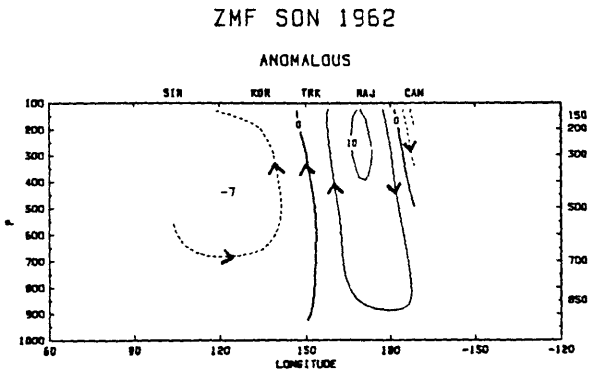
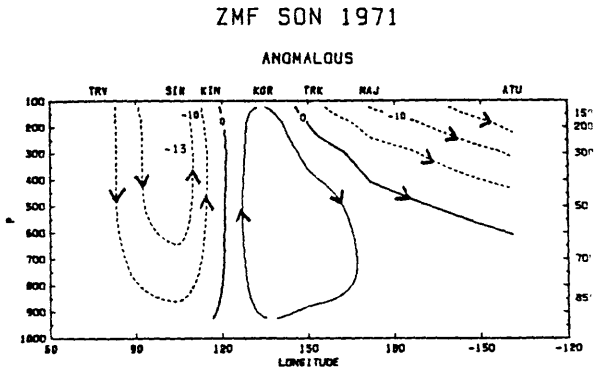
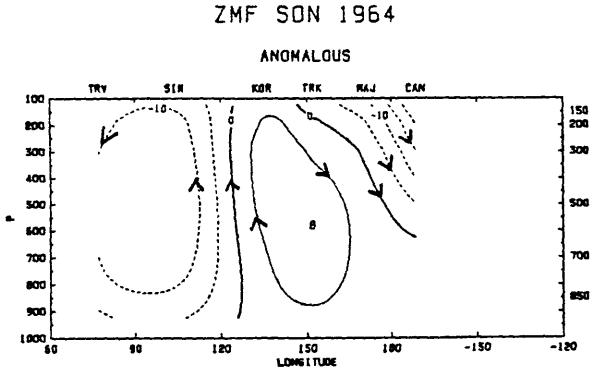
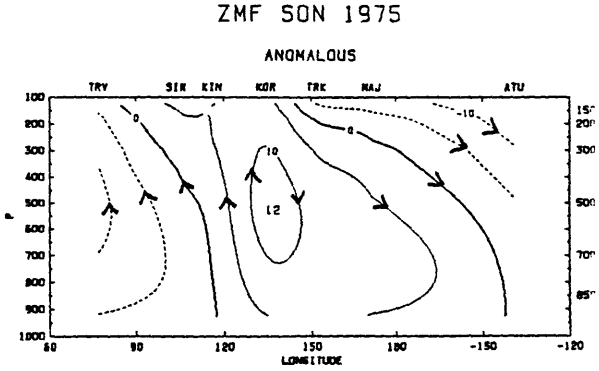


Figure 4.10 - As in Fig. 4.1a, but for individual seasons which together comprise the SON(-1) El Nino composite. The principal component vector associated with CEOF mode 1 (taken from Fig. 4.9) is shown above the upper right corner of the plot for each season.









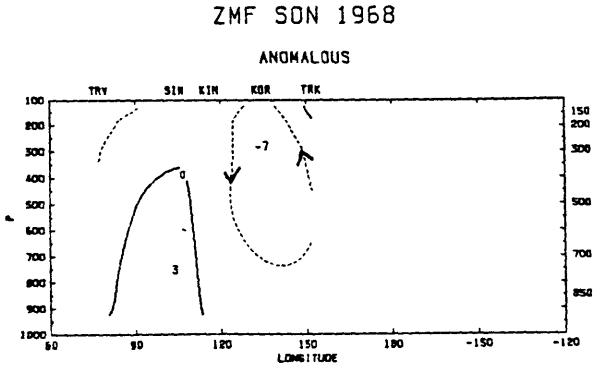


Figure 4.11 - As in Fig. 4.2a, but for individual seasons which together comprise the SON(-1) composite.

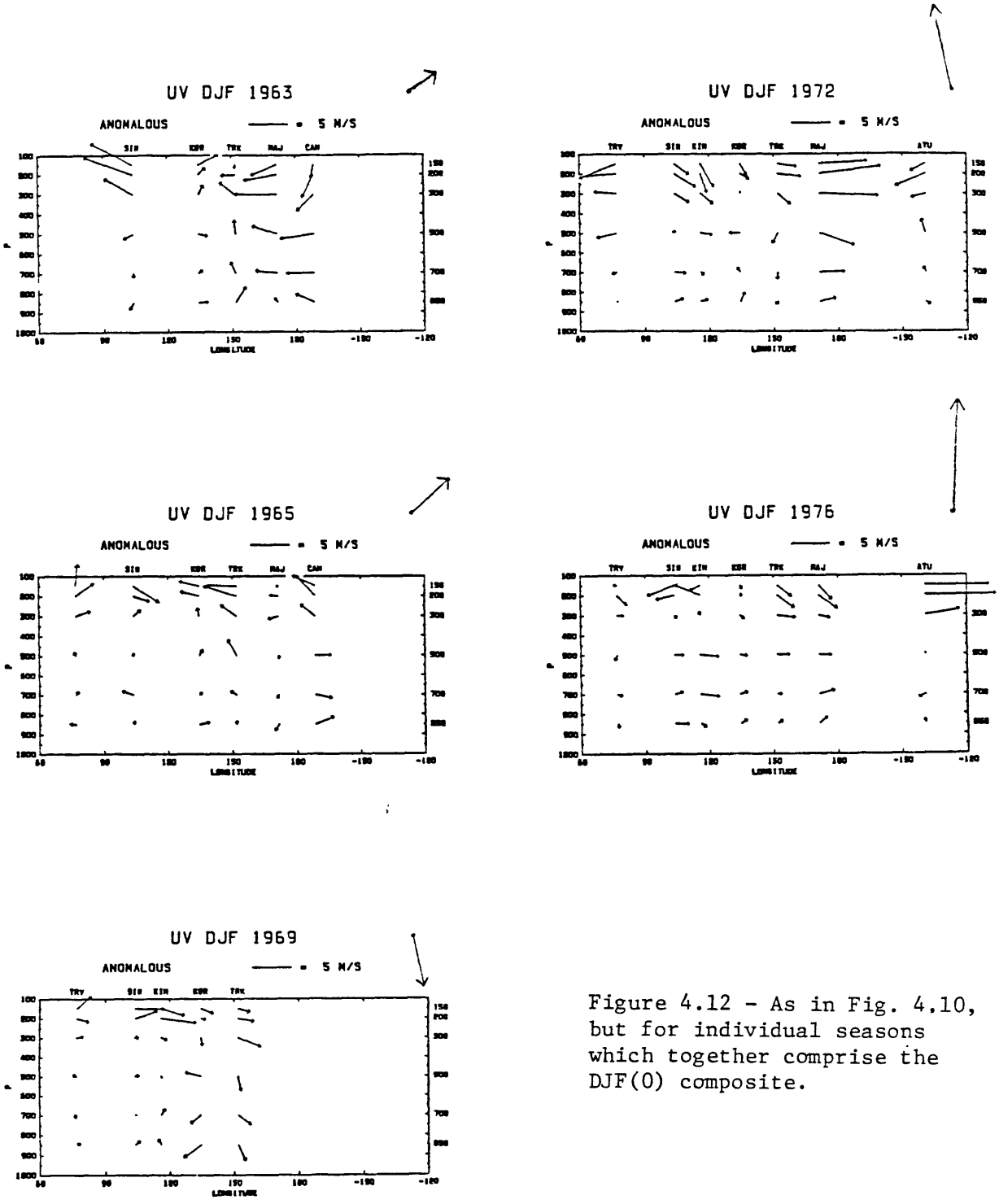


Figure 4.12 - As in Fig. 4.10, but for individual seasons which together comprise the DJF(0) composite.

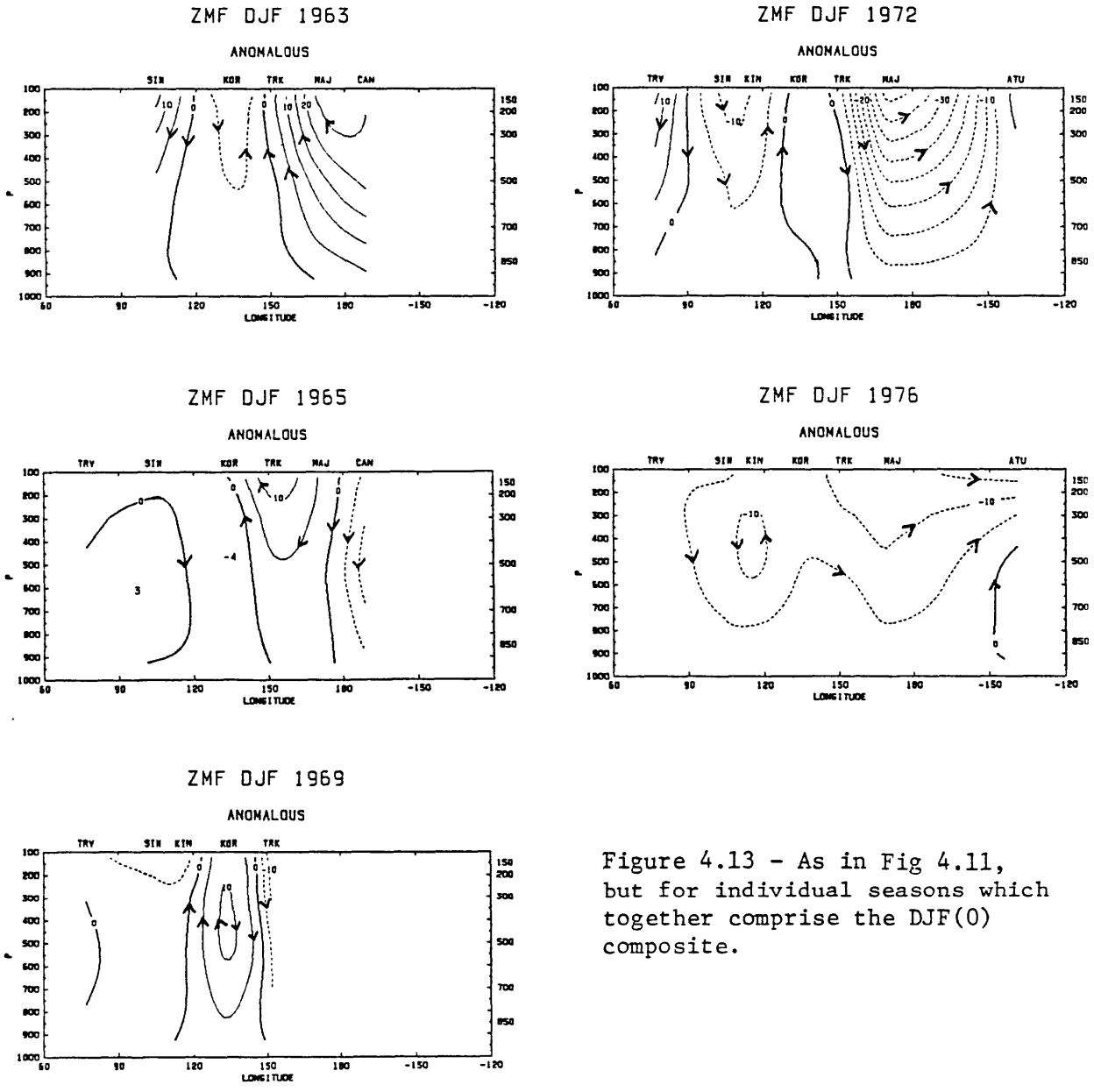
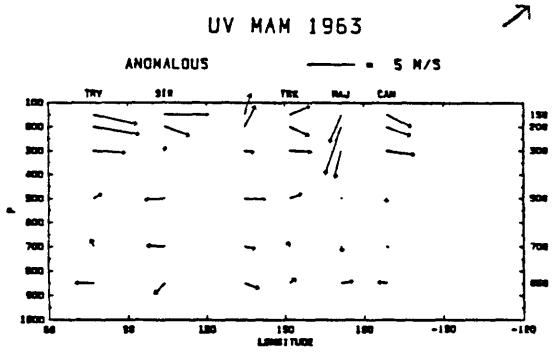
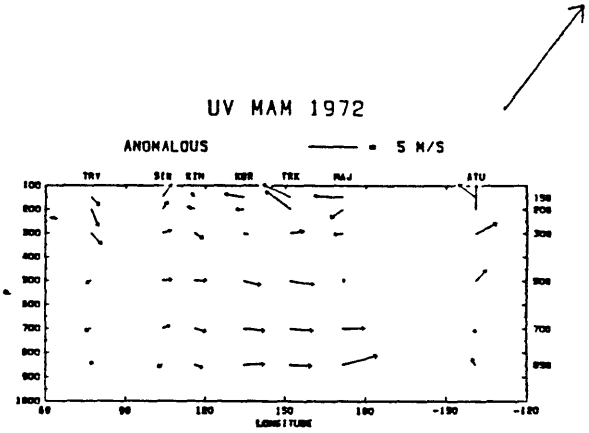
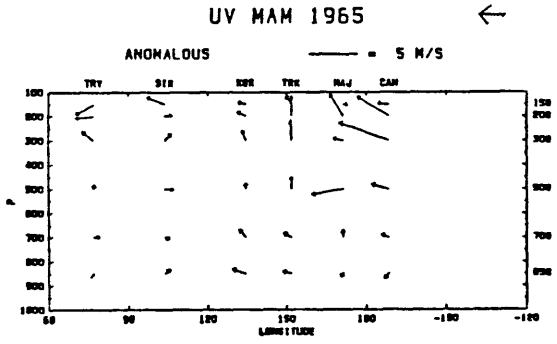
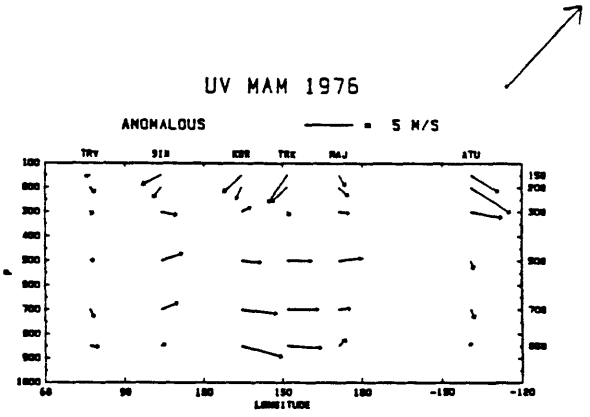


Figure 4.13 - As in Fig 4.11, but for individual seasons which together comprise the DJF(0) composite.









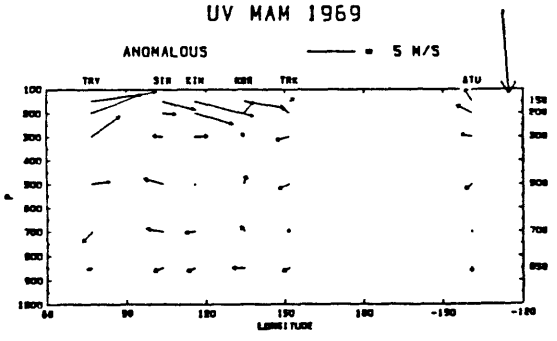


Figure 4.14 - As in Fig. 4.10, but for individual seasons which together comprise the MAM(0) composite.

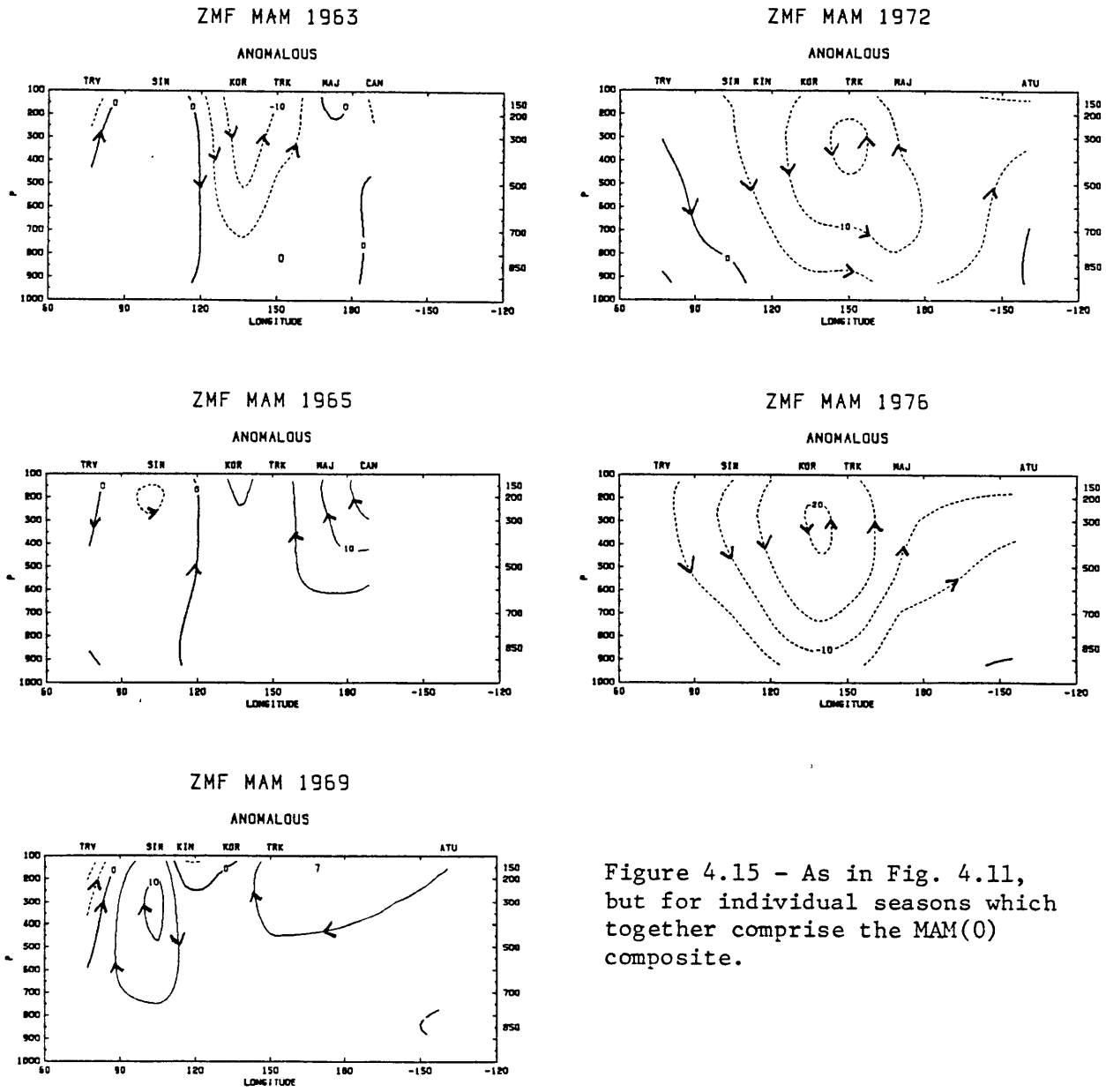


Figure 4.15 - As in Fig. 4.11, but for individual seasons which together comprise the MAM(0) composite.

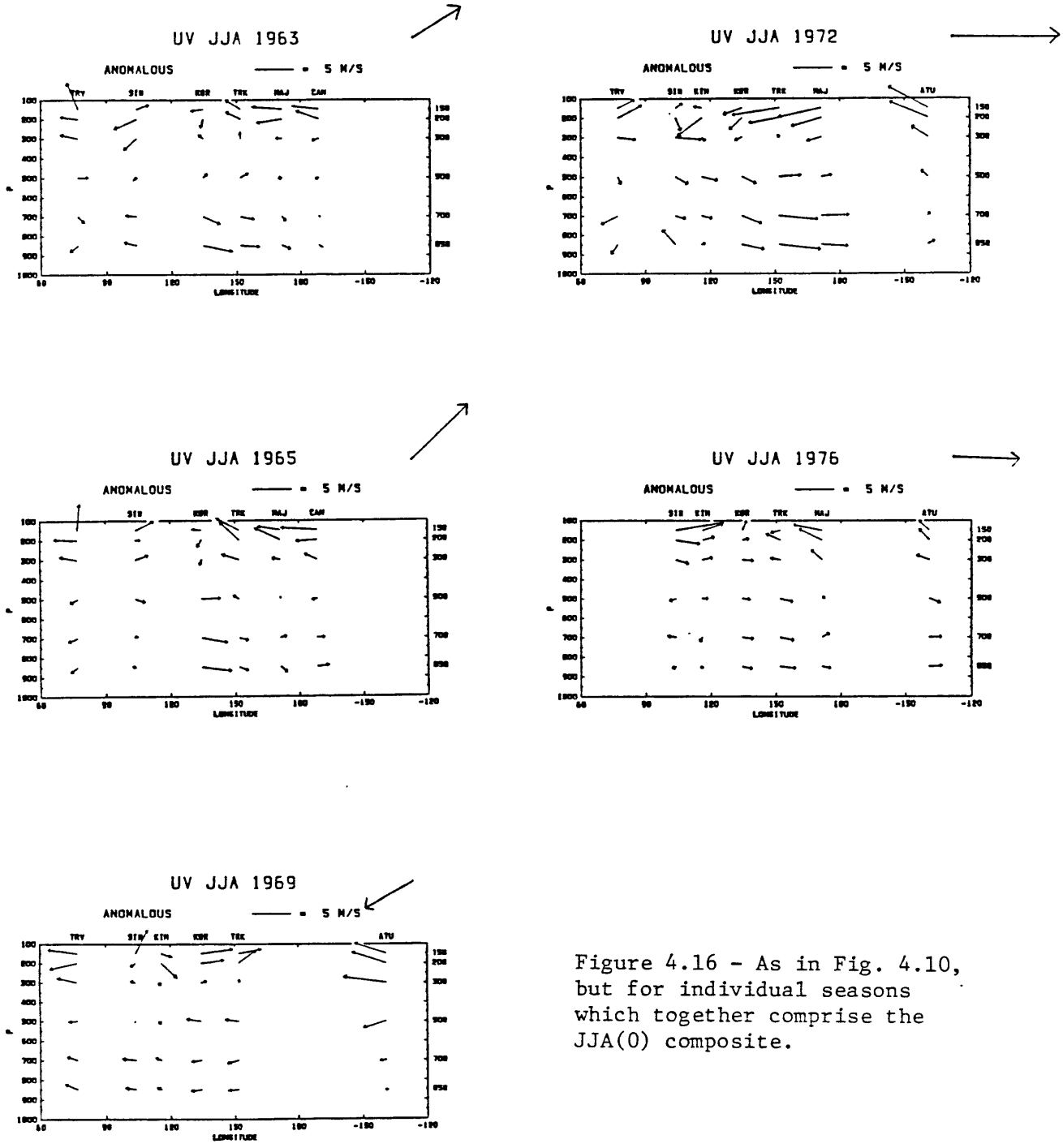
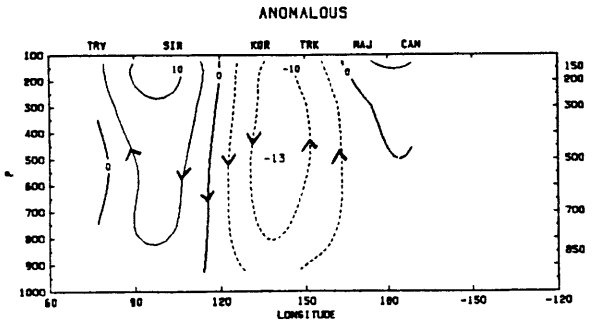
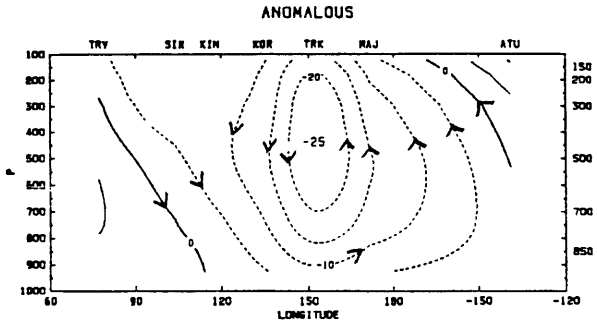


Figure 4.16 - As in Fig. 4.10, but for individual seasons which together comprise the JJA(0) composite.

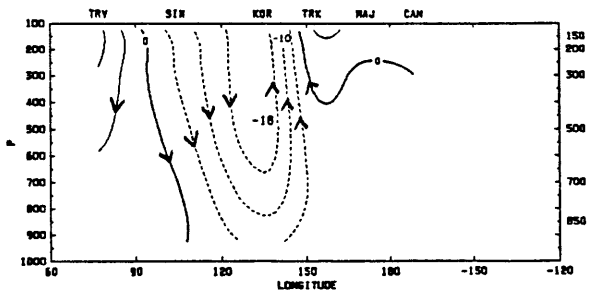
ZMF JJA 1963



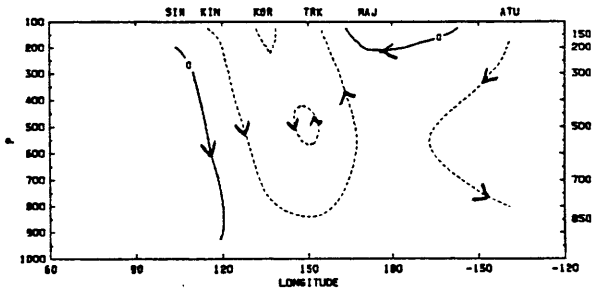
ZMF JJA 1972



ZMF JJA 1965



ZMF JJA 1976



ZMF JJA 1969

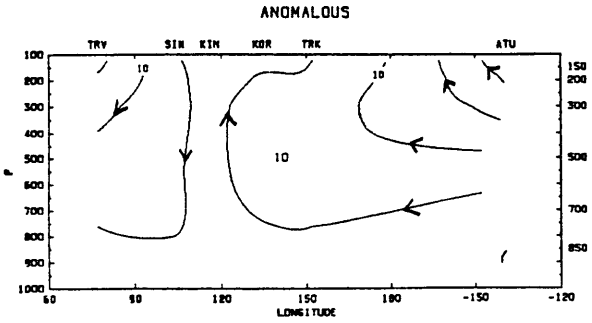
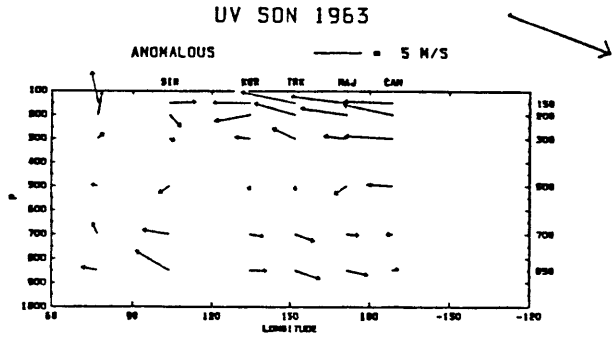
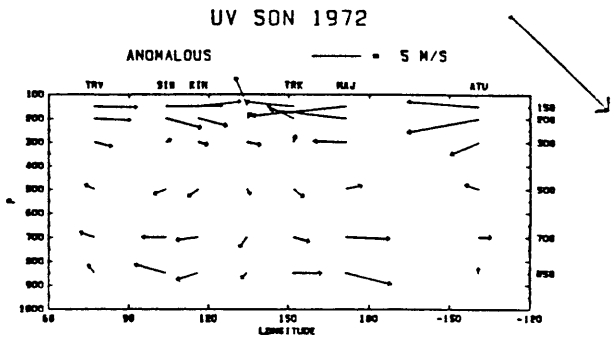
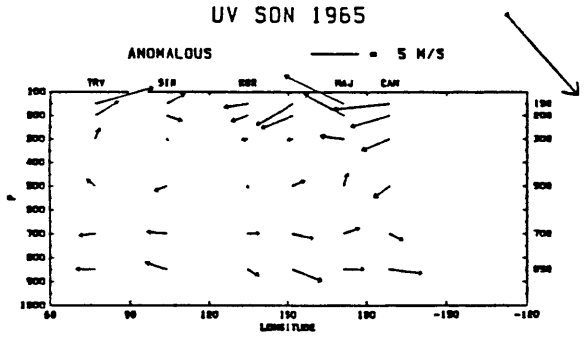
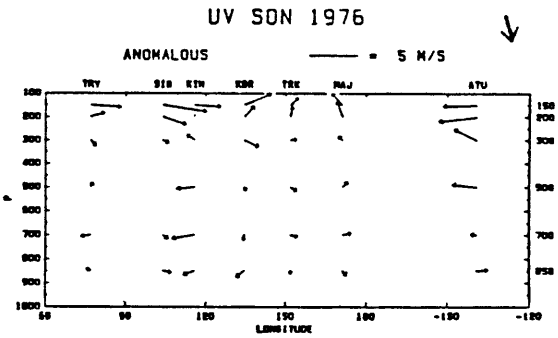


Figure 4.17 - As in Fig. 4.11, but for individual seasons which together comprise the JJA(0) composite.









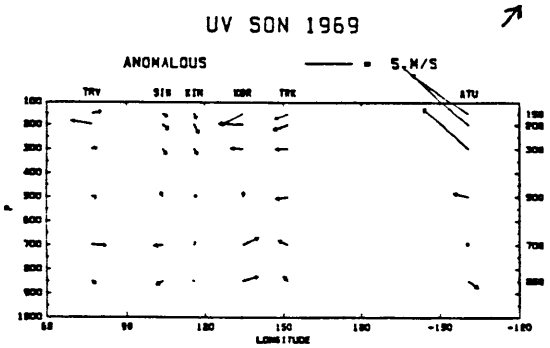


Figure 4.18 - As in Fig. 4.10, but for individual seasons which together comprise the SON(0) composite.

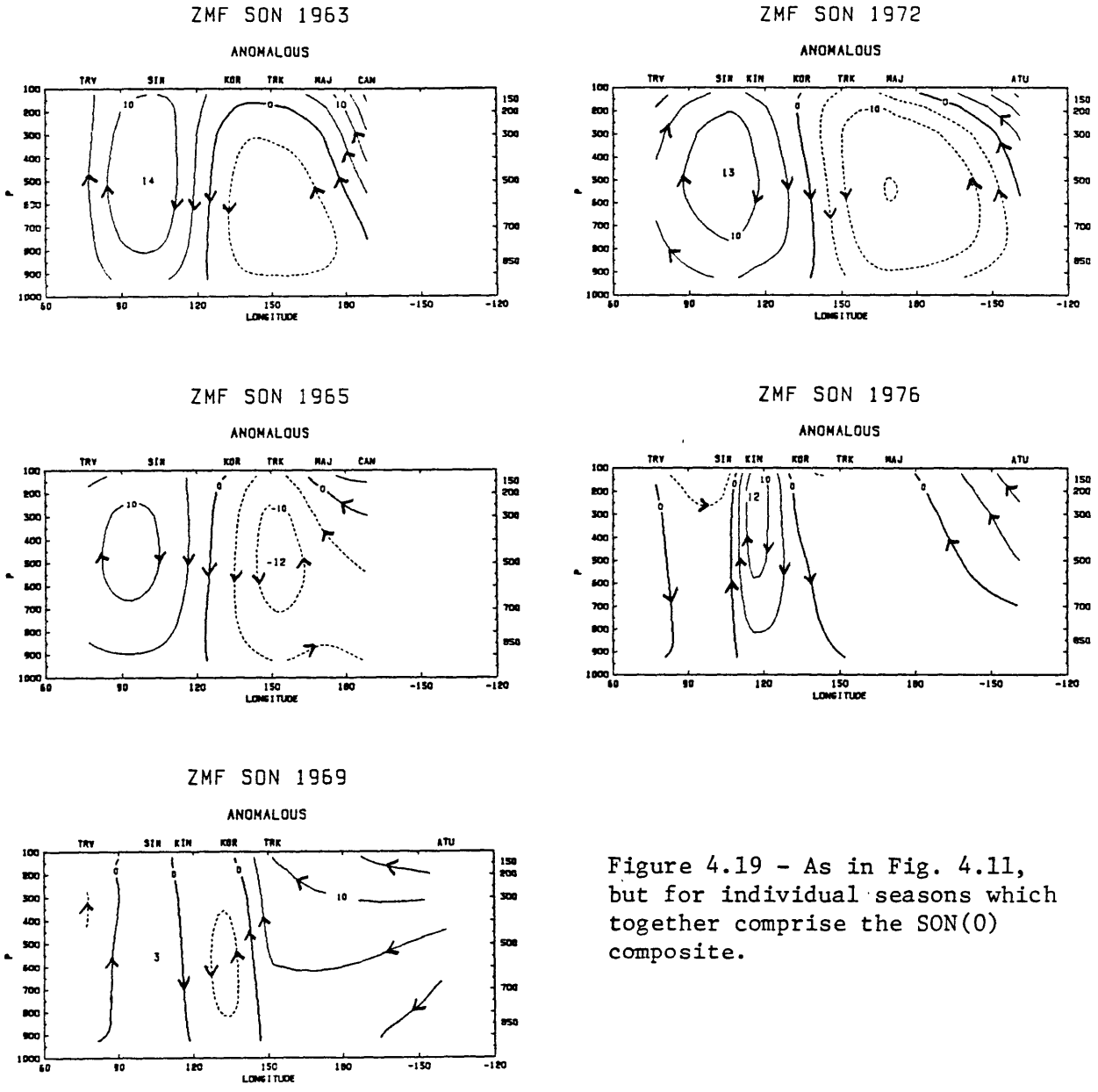
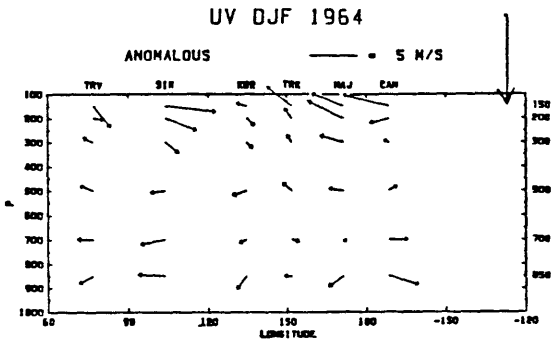
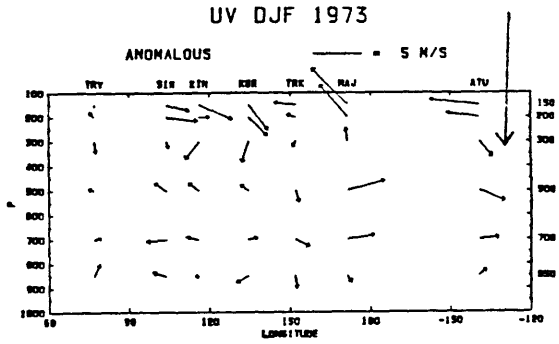
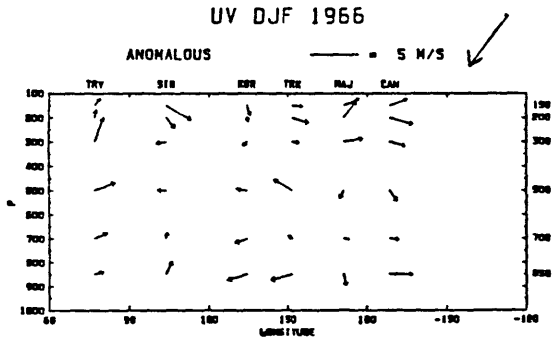
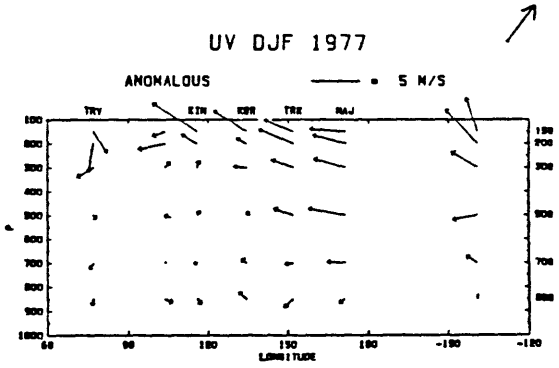


Figure 4.19 - As in Fig. 4.11, but for individual seasons which together comprise the SON(0) composite.









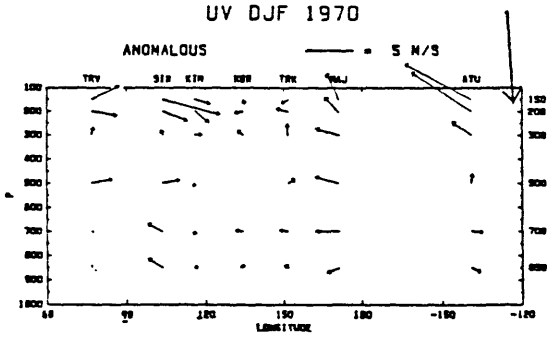


Figure 4.20 - As in Fig. 4.10, but for individual seasons which together comprise the DJF(+1) composite.

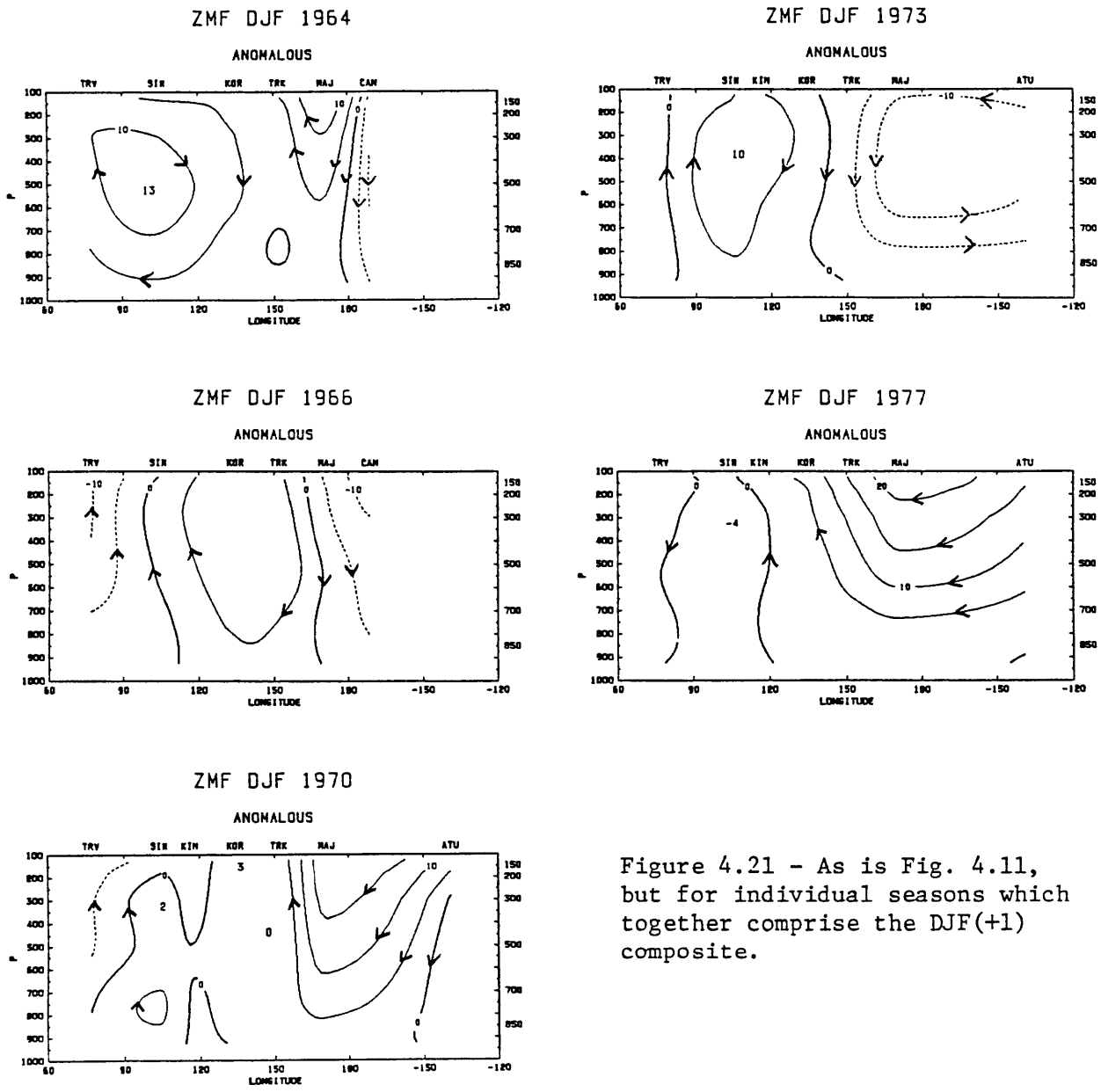


Figure 4.21 - As is Fig. 4.11, but for individual seasons which together comprise the DJF(+1) composite.

opposite those in 1965, 1969, and 1976. The composite DJF(0) anomalies in Figs. 4.1 and 4.2 are therefore a small residual of a set of widely-varying fields.

In MAM(0), the consistency between events improves once again (Figs. 4.14 and 4.15), although large differences between events are still observed. The anomaly patterns for 1972 and 1976 are large in amplitude and quite similar, and they determine the appearance of the composite. The small composite anomalies at Canton are the residual of two opposite anomaly fields in 1963 and 1965, and the individual seasonal anomalies at Majuro differ considerably from event to event. The 1965 easterly anomalies in the upper tropospheric at Trivandrum have the opposite sign of the anomalies for other events. Hence, the composite MAM(0) anomalies represent a very considerable underestimate of the amplitude of any particular seasonal anomaly.

Four of the five anomaly fields for JJA(0) (all events except 1969) contain the negative circulation cell observed in the composite over the western Pacific (Fig. 4.17). However, rather than the broad, weak M_z cell shown in the composite (Fig. 4.2), the individual anomalous M_z cells are stronger and narrower. In 1963 and 1965, the cell is centered at Koror (CPC vector pointing to "two-o'clock"), while in 1972 and 1976 the cell is centered farther east at Truk (CPC vector pointing to "three-o'clock"). The composite represents a broad dilution of the individual patterns.

The negative circulation cell moves eastward in all four events - again excluding 1969 - in the SON(0) season (Figs. 4.18 and 4.19), although it is quite weak in 1976. A positive circulation cell (i.e. easterly anomalies in the lower troposphere and westerly anomalies in

the upper troposphere, as in the climatological Walker Circulation) appears to the west over the equatorial eastern Indian Ocean in 1963, 1965, and 1972. These features are represented clearly on the composite.

The DJF(+1) anomaly fields are shown in Fig. 4.20 and 4.21. Consistent features are overshadowed by the differences between the fields. A positive circulation cell, with upper tropospheric easterly anomalies and lower tropospheric westerly anomalies, is present between 90°E and 150°E in all years except 1977. However, the magnitude and position of the anomalies differ considerably from event to event. Over the eastern half of the cross-section, upper tropospheric easterly anomalies occur during all years except 1966.

The discrepancies documented here between individual events and the El Niño composites have extremely important implications for the study of El Niño. If the composites for other fields presented by RC, Arkin (1982), and Horel (1982a) mask as much inter-event variability as the wind composites shown here, then such composites must be used with extreme caution as model/theory verification. Even in cases where the composites represent the sign or phase of the individual anomaly patterns faithfully, the present results demonstrate that the anomaly amplitudes are generally severe underestimates of the anomaly amplitudes for a particular event. For example, the composites are of no value in determining the magnitude of forcing required for a "realistic" response in a linear model.

Anomalies during the DJF season in particular are poorly represented by the compositing technique. The DJF(0) and DJF(+1) seasons display much more inter-event variability than the other seasons. The DJF(+1) season has been the focus of a tremendous amount of study regarding

tropical - extratropical interactions, and the lack of a single characteristic tropical circulation pattern during this El Niño phase has profound implications for these studies. Horel and Wallace (1981) presented evidence that El Niño events are associated with enhanced ridging during DJF(+1) over the west coast of North America. Critics were quick to note that the correspondence is far from perfect; as an example, it was pointed out that such ridging did not occur during the 1972 event, and in fact the winter of 1973 was characterized by planetary wave amplitudes smaller than normal (Wallace and Gutzler, 1981). However, Figs. 4.20 and 4.21 show clearly that the mid-Pacific anomaly pattern of DJF 1977 was quite different than the pattern of DJF 1973 even near the equator.

4.5 Discussion

This study is not the first to present evidence for atmospheric precursors of El Niño. Quinn and Burt (1972) pointed out that the SOI tends to be greater than zero (an anti-El Niño condition) the year before El Niño commences, which can be verified by inspection of Fig. 3.1a. Wyrtki (1975) showed that the trade winds over the central and eastern Pacific Ocean are typically stronger than normal prior to the SST warming along the coast. Newell et al. (1982) correlated surface wind and SST throughout the Pacific with the SOI, and found that anomalies of SST in the northwest subtropical Pacific led the SOI by two seasons. Horel (1982a) showed that composite geopotential heights and temperatures throughout the tropics are below normal for several seasons prior to the onset of El Niño. Luther et al. (1983) suggested that a break in the trade winds over the equatorial central Pacific, with a time scale of a few weeks,

occurred several months before the initiation of each El Niño since 1950 except the 1963 event. These precursive anomalies were each presented as possible "triggering" mechanisms. That is, the precursor was considered to be a separate phenomenon which somehow touched off a remote event, the El Niño. The SON(-1) precursive anomaly documented in this chapter is different in that it persists to become an integral part of the event.

Two recent studies have documented El Niño - related anomalies over the western Pacific which are probably be related to the circulation anomalies described here. Barnett (1983, 1984a) carried out a CEOF analysis of tropical surface winds over the Indian and Pacific Oceans. The gravest mode of his analysis propagated eastward and had a longitudinal structure similar to the 850 mb anomalies associated with CEOF mode 1 in our analysis. The phase speed of the pattern described by Barnett was considerably slower (period 3.3 years) than our results, so that the evolution of wind anomalies is completely different in his analysis. The phase propagation of the pattern derived by Barnett was nearly constant in time, so the different period in his analysis may reflect the average time interval between El Niño events rather than the phase speed of an anomaly during an event. The mode described by our analysis explains little variance between events, and the observation that its period is an integral number of years reflects the tendency for phase-locking during El Niño events, not the interval between events.

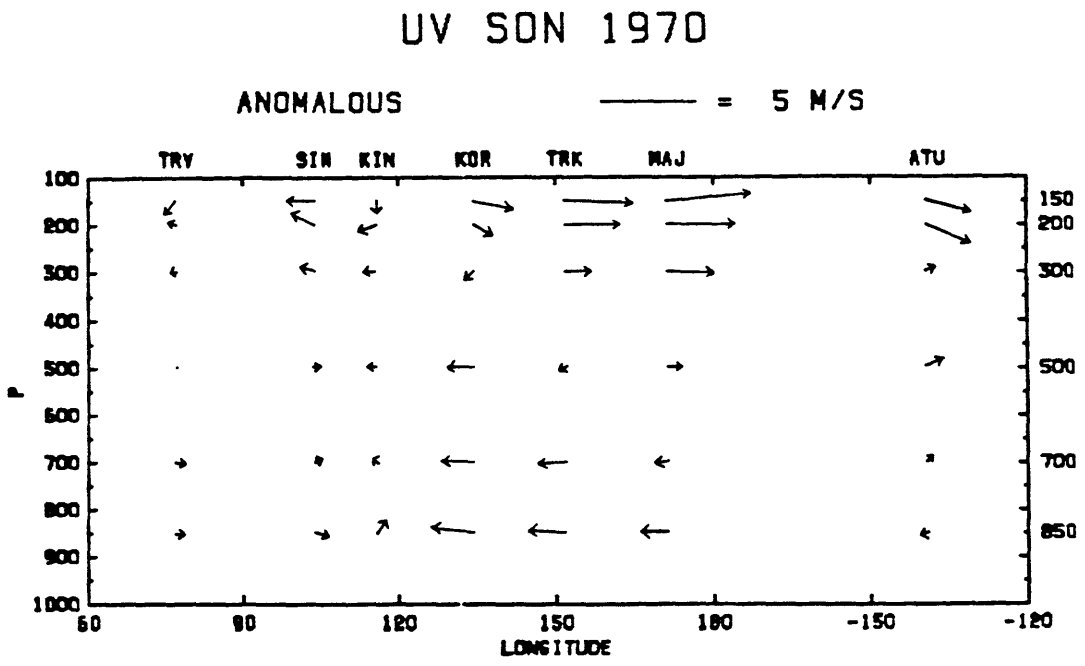
Nicholls (1984) composited SST anomalies off the northern coast of Australia (over the region 5-15°S, 120-160°E) for four El Niño periods and found a precursive positive anomaly of magnitude 0.3°C during the SON(-1) season. Although this is a small (but marginally significant)

anomaly, the presence of abnormally warm water in this longitude band is consistent with the location of anomalous low-level convergence in the SON(-1) wind anomaly pattern shown here (Figs. 4.1 and 4.11).

The presence of anomalous tropospheric circulation over the western Pacific preceding the appearance of warm SST anomalies in the eastern Pacific immediately suggests the possibility of predicting El Niño at least one season in advance. The precursive SON(-1) anomaly pattern shown in Figs. 4.10 and 4.11 is clearly apparent even before the 1963 event, when the evolution of SST anomalies differed markedly from the other events.

However, the precursive SON(-1) pattern was observed during two seasons which were not followed by El Niño events, so that the CEOF mode 1 pattern by itself is not a sufficient predictor (or cause) of El Niño. Fig. 4.22 shows the anomalous vector wind field over the Trivandrum-Atuona cross-section for the SON(1970) and SON(1973) seasons. In both of these seasons, lower tropospheric easterly anomalies of about 4 m/s and upper tropospheric westerly anomalies of 7-8 m/s are observed between 130°E and 170°E, and a weak counter-circulation exists over the eastern Indian Ocean. In both cases, the anomaly pattern propagated eastward during the subsequent DJF and MAM seasons, shown by the clockwise progression of CPC vectors in Fig. 4.3. No El Niño occurred in 1971 or 1974, however, and the magnitude of the CEOF mode 1 anomaly fell almost to zero in JJA(1970) and JJA(1974).

Several other potential SON(-1) wind indices were examined with an eye toward their predictive value for subsequent occurrence of El Niño. These indices included winds at 200 mb, winds at 850 mb, and the principal components of the vertical EOFs presented in Chapter 3, at



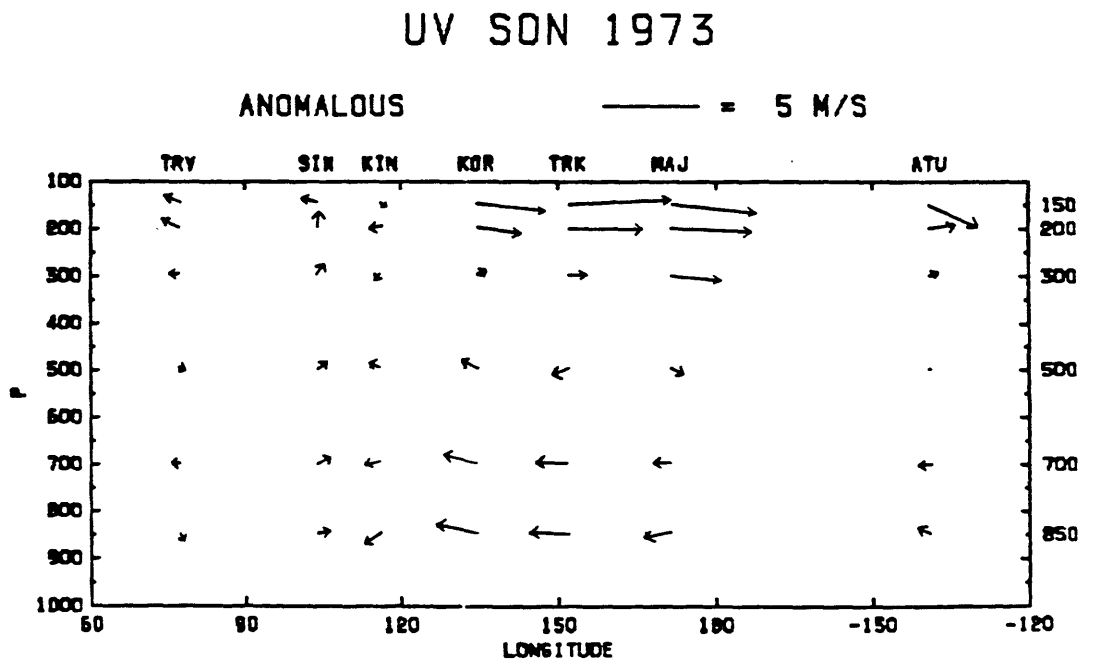


Figure 4.22 - Vector wind anomalies across the Trivandrum-Atuona cross-section for the SON(1970) and SON(1973) seasons.

Trivandrum, Singapore, and Truk. No criterion based solely on near-equatorial western Pacific circulation indices could be found which was both necessary and sufficient to predict El Niño.

However, this does not mean that atmospheric conditions over the equatorial eastern Indian and western Pacific Oceans are not crucial to the onset of El Niño. No necessary and sufficient precursors of any sort are known. Rather, it is likely that a complicated combination of oceanic and atmospheric conditions is necessary for an El Niño event to occur. This work has shown that a clear sequence of atmospheric anomalies extending through the entire troposphere evolves prior to and during the occurrence of the spectacular oceanic anomalies to the east. Because the atmospheric anomalies appear far to the west of, and prior to, the significant eastern Pacific SST anomalies, it is clear that the atmospheric anomalies documented here are <u>not</u> forced by El Niño.

It may be that the eastward-propagating anomaly described here is <u>initially</u> an independent phenomenon from the warming of eastern Pacific SST, and that <u>both</u> of these phenomena must occur and subsequently interact in order for a full-blown El Niño event to occur. This scenario is consistent with the occurrence of 'atypical' El Niños, such as the 1963 event, in which the eastern Pacific SST anomalies evolved differently from the RC composite, but the western Pacific atmospheric anomalies shown here were similar to other events.

The dynamics of the eastward-propagating anomaly remains to be determined. Its direction of propagation, near-equatorial latitudinal location, and zonal wind signature, are all consistent with Kelvin wave dynamics. However, the temporal and spatial scales of the anomaly are incompatible with theory. On an equatorial β-plane (Lindzen, 1967), a

free Kelvin wave has an equivalent depth of about 10 km and a period of about one day. Holton and Lindzen (1968) showed that a forced Kelvin wave satisfies the dispersion relation

$$\frac{\omega^2}{k^2} = \frac{\kappa g}{\lambda^2 H}$$

where ω and k are frequency and zonal wave number, $\kappa = 0.286$ for dry air, g is gravity, λ is the vertical wave number, and H is the scale height. Assuming values of $\lambda = (2\pi/15$ km) and $k = 2$, consistent with the structure of CEOF mode 1, then the period $(2\pi/\omega)$ is only 5.2 days. If we further assume the presence of a uniform mean flow of $u_o = -5$ m/s (roughly the annual mean zonal wind at 500 mb over the equatorial western Pacific - see Fig. 2.3a), then the period is increased to 5.8 days, still two orders of magnitude shorter than the observed period of two years. The theory also predicts that this Kelvin wave would rapidly propagate vertically.

The spatial structure of CEOF mode 1 is strikingly similar to the structure of the 40-50 day oscillation. Madden and Julian (1972) showed that zonal wind fluctuations within the 40-50 day period range are out of phase in the upper and lower troposphere, i.e. the 40-50 day wave has a baroclinic vertical structure. Furthermore, the amplitude of the fluctuation is strongest between the Indonesian region and the date line, and the zonal scale of the anomaly is approximately the same as the CEOF mode 1 anomaly. Hence, it is possible that the 40-50 day wave and the CEOF seasonal anomaly pattern are manifestations of a single, extremely broad-band phenomenon.

Any dynamical explanation of the seasonal anomaly sequence documented in this chapter must account for its strong phase-locked feature.

Although the season-by-season evolution of wind anomalies is properly described as a propagating fluctuation, the phase-locked nature of the signal accounts for the large correlation coefficients (representative of standing oscillations) in studies which considered interannual fluctuations stratified by season (e.g. Selkirk, 1984, and the 1dEOF calculations in Section 3.3).

Van Loon (1984) and van Loon and Shea (1985) have shown that surface pressure and surface wind anomalies over the South Pacific associated with El Niño are phase-locked as well. They interpret phase-locking as amplification/deamplification of the annual cycle. However, the annual varaibility of winds over the Trivandrum-Atuona cross-section was shown in Chapter 2 to be a complicated function of longitude and height. Hence, the phase propagation of the CEOF mode 1 circulation anomalies over this cross-section cannot be interpreted in terms of the annual cycle of the wind field.

The recent 1982-83 El Niño occurred while this work was in progress. This event was the most dramatic on record: unprecedented positive SST anomalies and negative values of the SOI were observed (Rasmusson and Wallace, 1983). The timing of this event was also quite unusual. The ocean surface warming over the eastern Pacific took place in JJA rather than the DJF season. While a complete analysis of the wind anomalies associated with this event is beyond the scope of this work, the preliminary data issued by the National Meteorological Center (based on their tropical analysis) offer some clues as to the applicability of the ideas presented in this chapter. Fig. 4.23 shows a longitude-time diagram of the 200 mb wind anomalies averaged over a latitudinal strip between the equator and 10°N (Arkin et al., 1983). The largest wind anomalies

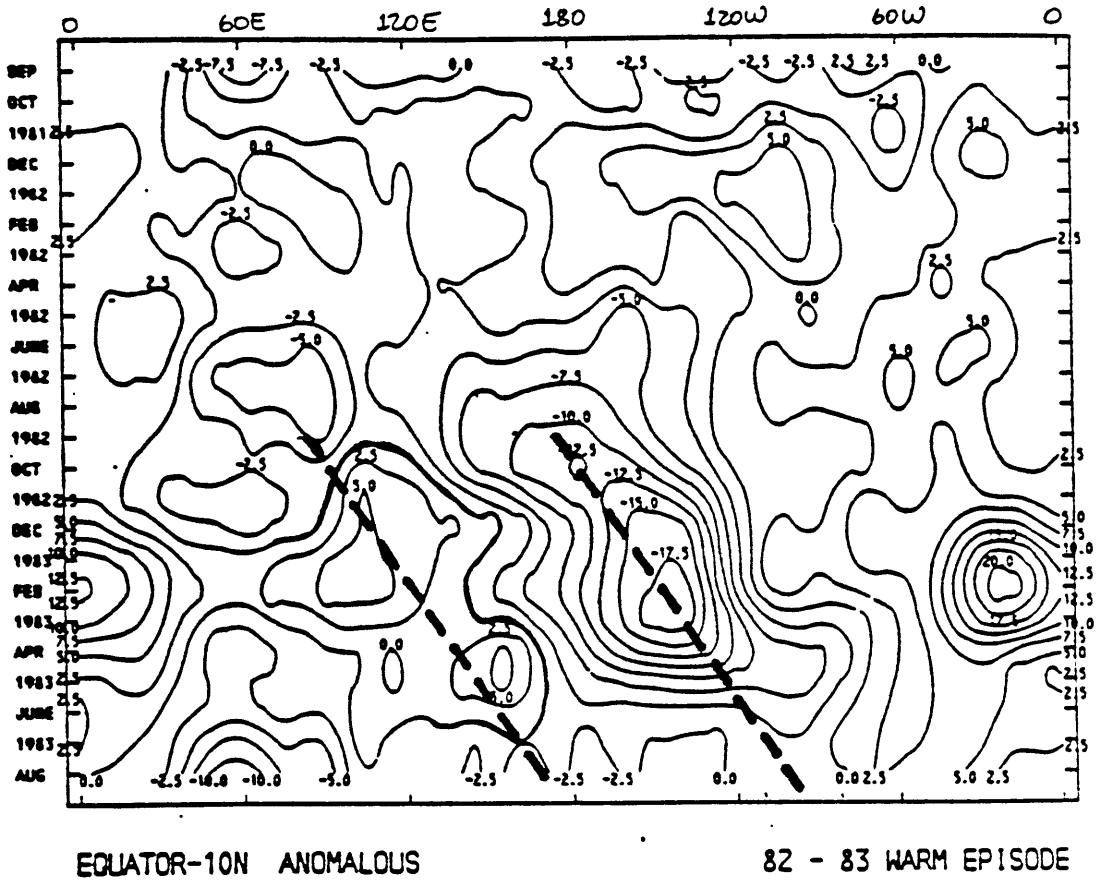


Figure 4.23 - Longitude-time plot of anomalous 200 mb zonal wind, averaged over a latitudinal strip between the equator and 10°N, for the period September 1981 - August 1983, taken from Arkin et al. (1983). Contour interval 2.5 m/s. Heavy dashed lines indicate longitude-time path corresponding to anomaly centers 90° apart, propagating eastward with period 2 years, starting in September 1982.

occurred during the DJF and MAM seasons in 1983. The heavy dashed lines in the figure indicate the longitudinal scale and phase speed of the CEOF mode 1 pattern: the lines are spaced 90° apart and propagate eastward at a rate of (1 cycle)/(2 years), starting in September 1982. The dashed lines match the eastward progression of the observed anomalies during the course of the event, suggesting that the near-equatorial atmospheric anomalies associated with El Niño are consistently phase-locked, even though the eastern Pacific oceanic component of El Niño is not. Independently, Donguy and Eldin (1985) reported that western Pacific anomalies of rainfall propagated eastward at the same rate, 0.3 m/s, during this El Niño event.

It has been known for some time that the region of heaviest convection over the western Pacific shifts eastward during the course of an El Niño event (Walker and Bliss, 1932; Bjerknes, 1969; Krueger and Gray, 1969; Kidson, 1975; Heddinghaus and Krueger, 1980; Horel, 1982a). We have demonstrated here that circulation anomalies implying enhanced convergence at 120°E near the equator exist during the SON(-1) season, before the onset of El Niño. Satellite-derived cloudiness statistics for El Niño events since 1965 show cloudiness anomalies consistent with the circulation anomalies.

Murakami (1975) presented monthly mean tropical cloudiness averages for the period February 1965 - July 1973, based on visual satellite imagery. Fig. 4.24 shows a time-longitude plot of cloudiness anomalies along the equator taken from his paper. Unfortunately, the data record starts after the commencement of the 1965 El Niño event. However, a prominent anomaly exists in February 1965 centered at 140°E, and the eastward propagation of this anomaly during the course of the event is

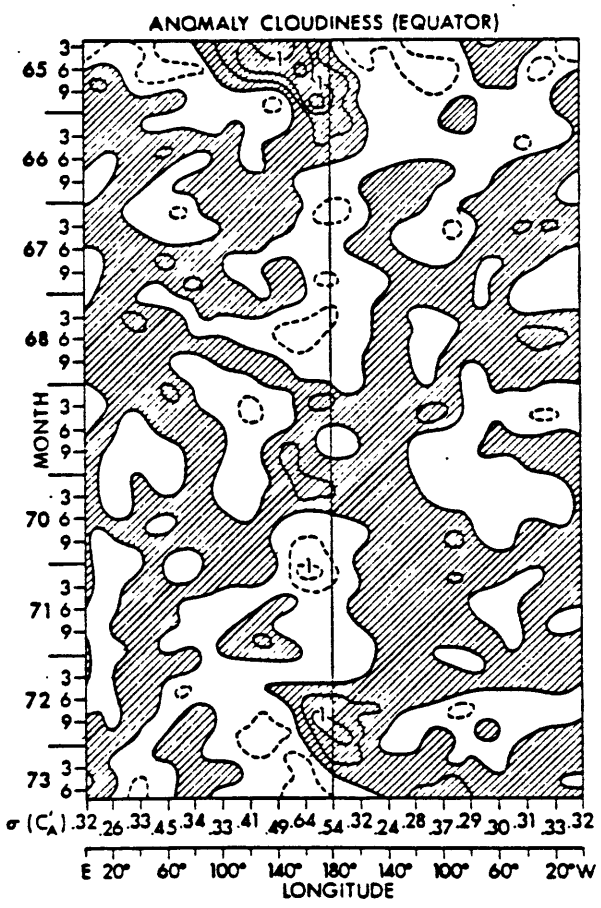


Figure 4.24 - Longitude-time plot of anomalous cloudiness along the equator for the period February 1965 - July 1973, taken from Murakami (1975). Contour interval 0.5 okta, with above normal cloudiness shaded. Standard deviation of anomalies is shown along the bottom.

obvious from the figure. By February of 1966, the anomaly is centered on the date line, having propagated eastward about 40° in one year. This propagation rate is slower than the CEOF mode 1 wind anomaly, but the the wind data suggest that the anomaly may have been centered near 120°E in the SON(1964) season (Fig. 4.10), which would improve the agreement.

The data record subsequently spans the 1972 El Niño (notice that the 1969 event is extremely weak in this cloudiness record, consistent with the lack of a signal in the wind data). In SON(1971), a positive anomaly exceeding 1 okta (greater than 2 standard deviations) is centered at 130°E. Although the anomaly disappears for two months in early 1972, a prominent eastward-propagating anomaly reappears in April 1972, and evolves so that the cloudiness anomaly in late 1972 between 100°E and 160°W is the reverse of the anomaly in late 1971.

Liebmann and Hartmann (1982) presented seasonal mean outgoing IR averages for the period JJA(1974) - DJF(1978), spanning the 1976 event. Fig. 4.25 shows the sequence of outgoing IR anomalies for four consecutive seasons for the period SON(1975) - JJA(1976). The top panel shows a pair of prominent anomalies near the equator in SON(1975): a negative anomaly (i.e. enhanced cloudiness, delineated by solid contours) over Indonesia, and a positive anomaly centered at 165°E. These anomalies are entirely consistent with the zonal convergence and divergence associated with CEOF mode 1 for this season (cf. Fig. 4.4). In DJF(1976), the negative IR anomaly is located over northern Australia, to the south and east of its position in SON(1975), and the center of the positive IR anomaly has spread eastward across the date line. By MAM(1976), Indonesia and the eastern Indian Ocean are covered by a positive IR anomaly, with weak negative IR anomalies now evident along 10°N between 150°E and

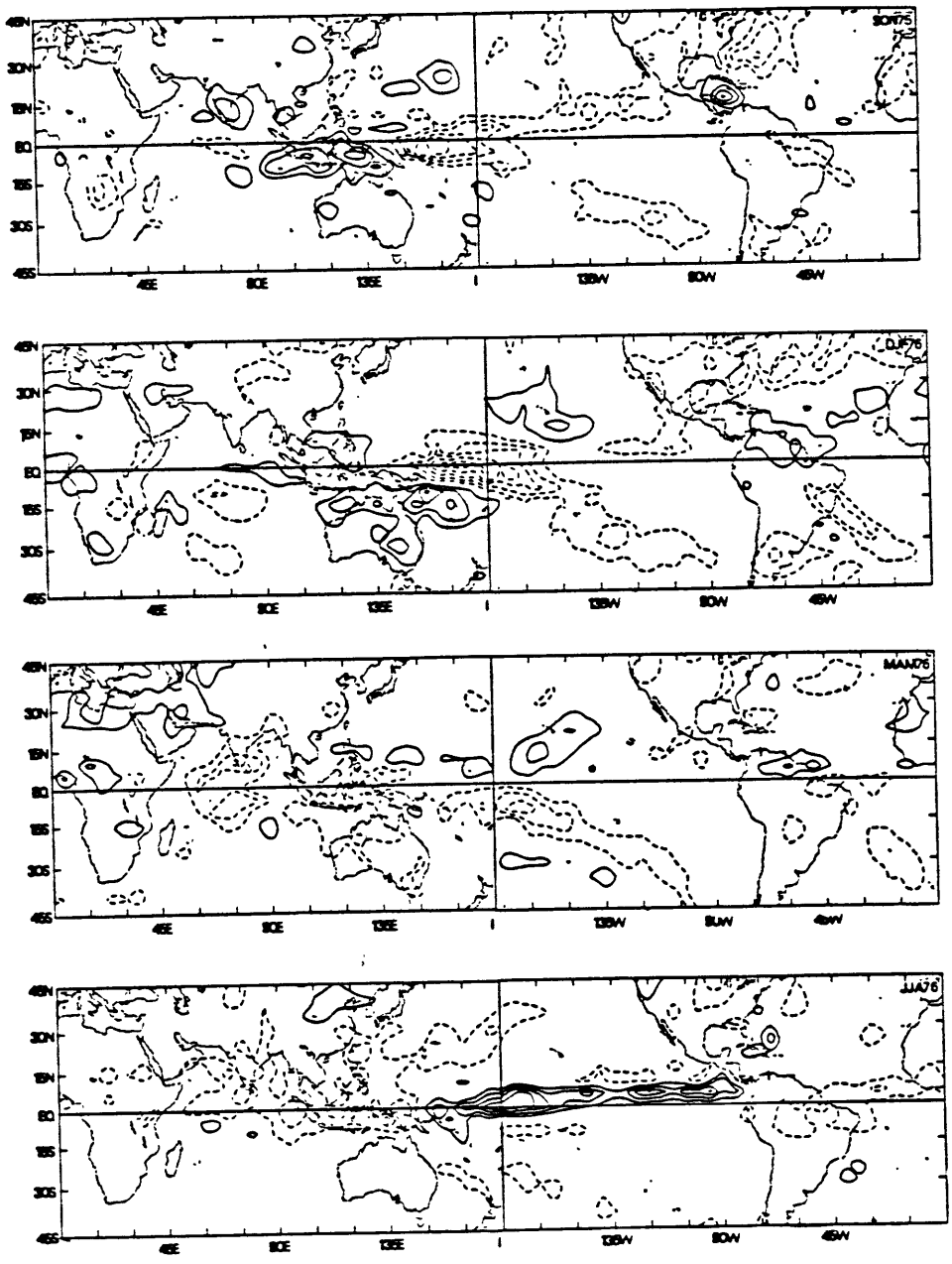


Figure 4.2 5 - Seasonal anomalies of outgoing IR, taken from Liebmann and Hartmann (1982). Contour interval 5 W/m^2, with positive anomalies dashed and negative anomalies solid.
(a) SON(1975) (b) DJF(1976) (c) MAM(1976) (d) JJA(1976)

the date line. In JJA(1976), the negative IR anomaly exceeds 20 W/m^2 along the date line in the vicinity of the equator. In summary, the SON(-1) precursive anomaly is quite clear in the outgoing IR data before the 1976 event. Subsequent eastward propagation of the anomaly pattern is also apparent, but is not as clear in the IR sequence as it is in the wind data.

These cloudiness statistics confirm that the spatial structure and temporal evolution of wind anomalies documented in this chapter are associated with equally prominent features in the convection patterns themselves. They underscore the fact that the principal tropospheric anomalies preceding El Niño events are located over the far western edge of the Pacific basin, not over the eastern Pacific. The convective anomalies associated with El Niño are not simply produced by the ocean surface warming off the South American coast; rather, the anomalous convection develops far to the west and propagates eastward to meet the oceanic SST anomalies several seasons later, during the fully-developed phase of the event.

Chapter 5

CONCLUSION

This thesis describes a study of the three-dimensional structure of wind variability in the tropical troposphere on seasonal time scales. The geographical and vertical structure of the annual mean, annual (periodic) variability, and interannual (nonperiodic) variability of the zonal and meridional wind components are documented in turn. In particular, the inclusion of the vertical structure of variability allows the direct interpretation of wind fluctuations in terms of diabatic heating and convection, which are of crucial importance in the tropics.

The annual mean and annual variability of the tropical wind field are examined in Chapter 2. The seasonal variability of the wind fields calculated from our data set agrees with previous calculations, confirming the significance of climatological seasonal differences. The vertical depth of zonal and meridional winds are distinctly different. The annual mean and variability of the zonal component are coherent through the depth of the troposphere, whereas the meridional wind is confined to rather thin layers in the upper and lower troposphere.

The annual mean and annual variability of the Walker Circulation, defined in this thesis as the zonal wind circulation in a zonal plane over the equator between the southern tip of India and the central Pacific Ocean, is examined in detail. The western (rising) branch of the Walker Circulation has a pronounced annual cycle, characteristic of the seasonal monsoon circulations of India and Southeast Asia. The annual variability of lower tropospheric winds is greater than the annual mean over this region. The eastern (sinking) branch is located in a tradewind

regime, where the annual mean easterly wind at low levels is greater in magnitude the annual variability. The zonal mass flux associated with the rising branch of the Walker Circulation has a pronounced westward tilt with height.

The structure of the interannual variability of the wind field, defined as the variance of time series of seasonally averaged departures from climatology, is examined in Chapter 3. Near the equator, the magnitude of interannual variance is greater than or equal to the variance contained in the annual and semiannual cycles. A transition in the vertical structure of zonal wind variability occurs at about 12° latitude in each hemisphere. Poleward of 12°, the standard deviation of seasonal anomalies increases rapidly with height, and anomalies are positively correlated in the vertical (i.e. an "equivalent-barotropic" structure). Equatorward of 12°, the vertical gradient of variability is much smaller, and anomalies in the upper and lower troposphere are negaively correlated, with a node in mid-troposphere (i.e. a "baroclinic" structure). The latitude of the transition is consistent with the theory of equatorial heat-forced circulations and with cloudiness fluctuation statistics, and suggests the dominance of convectively forced circulations near the equator.

The Southern Oscillation Index (SOI) is used as a proxy indicator of anomalous convective activity over the Pacific associated with El Niño events. We show that the SOI is the dominant interannual signal in these wind data. Interannual correlations between the zonal wind field in the Walker Circulation and the SOI contain no longitudinal tilt with height.

The temporal evolution of seasonal zonal wind anomalies within the Walker Circulation during El Niño events is documented in detail in

Chapter 4. A distinct anomaly pattern, extending through the depth of the troposphere with a "baroclinic" vertical structure, occurs over the entire Walker Circulation during the Northern Hemisphere autumn season, 4-6 months before the onset of ocean surface warming in the eastern Pacific. The pattern subsequently propagates eastward as the warm SST anomaly moves westward, and the fully developed phase of El Niño incorporates both anomalies over the central Pacific one year after the initial appearance of the atmospheric anomaly pattern. The space-time structure of the atmospheric anomaly is confirmed in satellite-derived cloudiness fluctuation statistics.

The results emphasize the primary role of latent heating for the forcing of low frequency tropical circulation fluctuations. The vertical structure of the wind response provides an indication of the profile of heating. We have shown here that the vertical structures of the mean wind field and the wind variability are different. The annual mean Walker Circulation has a pronounced westward tilt with height, which is also observed in each of the seasonally averaged cells. Interannual fluctuations show no indication of a tilt.

This result has important implications for the interpretation of simple models, which have been used to examine the stationary forced response to heating superimposed on a motionless basic state in order to explain the vertical structure of both the climatological wind field (e.g. Geisler, 1981; Hartmann et al., 1983) and time-averaged anomalies (e.g. Gill, 1980; Lim and Chang, 1983). The observed vertical structure of the equatorial zonal wind field cannot be used as evidence for any single vertical heating profile, because the vertical structures of the climatological winds and seasonal wind anomalies are different.

The Gill model, which assumes a broad vertical heating profile centered in mid-troposphere, provides a reasonable simulation to the vertical structure of near-equatorial interannual fluctuations. The observed anomalies have a "baroclinic" structure (with a node in mid-troposphere) within a Rossby radius of the equator, show no tilt with height, and the anomalies in the upper and lower troposphere are nearly equal in magnitude. The Gill model simulates all these features.

The agreement between the vertical structure of the Gill model and the observations is poorest in the Northern Hemisphere winter season, when the dominant vertical mode of variability near the date line has an equivalent-barotropic structure. This is also the season during which the agreement between CEOF mode 1 and the observations is poorest, and the near-equatorial seasonal anomalies for individual El Niño events are most disparate. One possible reason for the inconsistency of the DJF signal here is the latitudinal position of the station cross-section, which is north of the equator over the western Pacific. Both the surface wind regression of Pazan and Meyers (1982), and the DJF 1976 outgoing longwave radiation anomaly shown by Liebmann and Hartmann (1982, Fig. 4.25b), suggest that the strongest anomalies during this season exist south of the equator.

The Gill model also fails to explain the vertical structure of the wind anomaly pattern over regions remote from the Pacific basin. The dominant vertical structure of zonal wind fluctuations is "equivalent-barotropic" over the subtropics of both hemispheres, and over the near-equatorial regions of Africa and India. Simmons (1981) and Held (1983) suggested that a baroclinic mode would propagate vertically in the absence of a rigid lid at the top of the atmosphere (such a lid is

present in the Gill model), leaving an equivalent-barotropic (external) mode as the distant response. This explanation is consistent with the observations presented here. Nevertheless, the observed vertical structure of seasonal wind anomalies near the equator in the Pacific basin is consistent with the simplified Gill model.

A major result of this thesis is the documentation of the evolution of a pattern of highly significant wind anomalies, described by CEOF mode 1, over the western near-equatorial Pacific Ocean in conjunction with El Niño. The evolution of the anomaly pattern was shown to be very similar for four separate El Niño events (1963, 1965, 1972, and 1976). The anomaly pattern appears first during the SON (Northern Hemisphere autumn) season, more than a season before the onset of El Niño (defined as ocean surface warming along the South American coast). At this time, the western Pacific wind anomaly pattern describes lower tropospheric convergence and upper tropospheric divergence centered over the Indonesian region. This pattern propagates eastward during succeeding seasons and completes a half-cycle in one year, so that the wind anomaly pattern during the SON season following the onset of El Niño is the reverse of the pattern during the precursive SON season.

The spatial structure of CEOF mode 1 strongly resembles the response of simple models forced by near-equatorial latent heating. Furthermore, previous studies of equatorial cloudiness fluctuations (e.g. Murakami, 1975) suggest that the CEOF mode 1 wind anomalies documented here are associated with anomalous convection. In view of these results, as well as the inconsistency between the space-time structure of CEOF mode 1 and equatorial wave theory, we conclude that the evolution of CEOF mode 1

during El Niño events is not governed by dry atmospheric dynamics alone: the wind anomaly pattern does not represent a forced atmospheric Kelvin wave. If this is true, then the eastward propagation of the anomalies must be due to an air-sea interactive process.

Because the CEOF mode 1 anomaly pattern is linked to the onset of El Niño, further elucidation of its cause is of fundamental importance for the understanding and prediction of El Niño. Additional studies will be faced with the usual tropical problems of data paucity, in terms of both spatial and temporal coverage. With the CEOF mode 1 pattern having been established in this thesis on the basis of a few long time series, future studies can incorporate existing data records of shorter duration in order to provide more extensive spatial coverage. We hope that the results presented here will demonstrate the need for enhanced oceanic and atmospheric observations west of the date line, extending into the Indian Ocean.

Appendix A

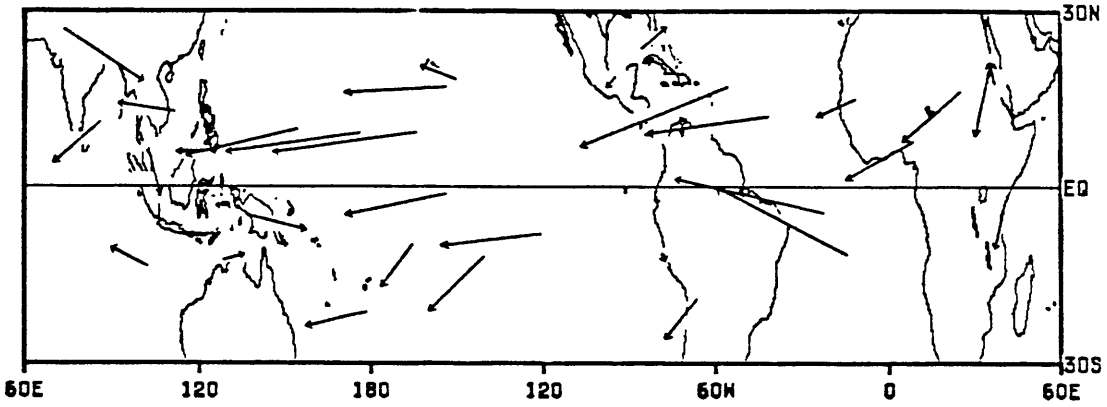
SEASONAL MEAN WIND PLOTS

Plots of the climatological vector winds for each season are presented in this appendix. These are the fields which are subtracted from each season's observed data in order to form the seasonal anomalies which are analyzed and discussed in Chapters 3 and 4. The plot headings refer to Northern Hemisphere seasons, so that "winter" is the December-January-February average, etc.

Seasonal mean wind plots similar to these were published by Newell et al. (1972), Gray et al. (1976), and Oort (1983). Despite differences in the the length and period of the data sets, the wind fields calculated here agree closely with the fields in these three atlases. Hence, the seasonal average wind in the tropics appears to be quite a robust average. It probably is important that each of the data sets spanned at least one El Niño event, in view of the large regions where interannual variability is greater than annual variability (see Figs. 3.5 and 3.6).

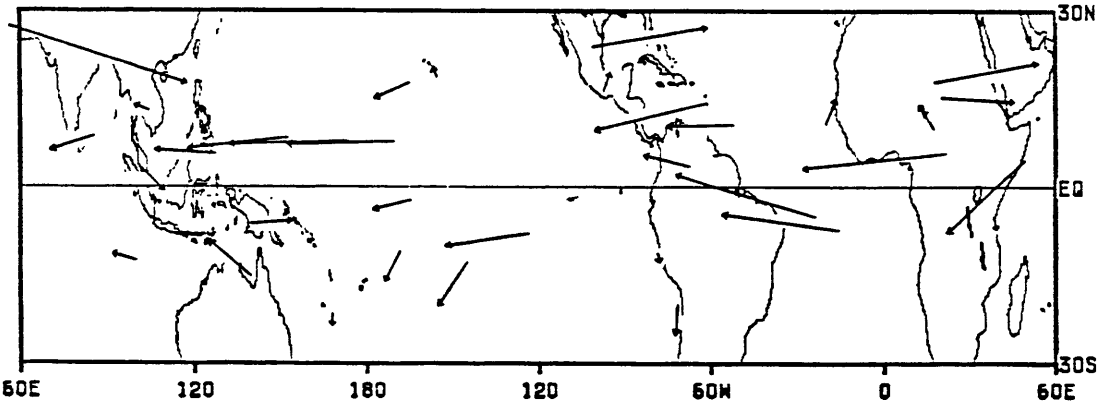
WINTER MEAN 850 MB

SCALE: —— = 5 M/S



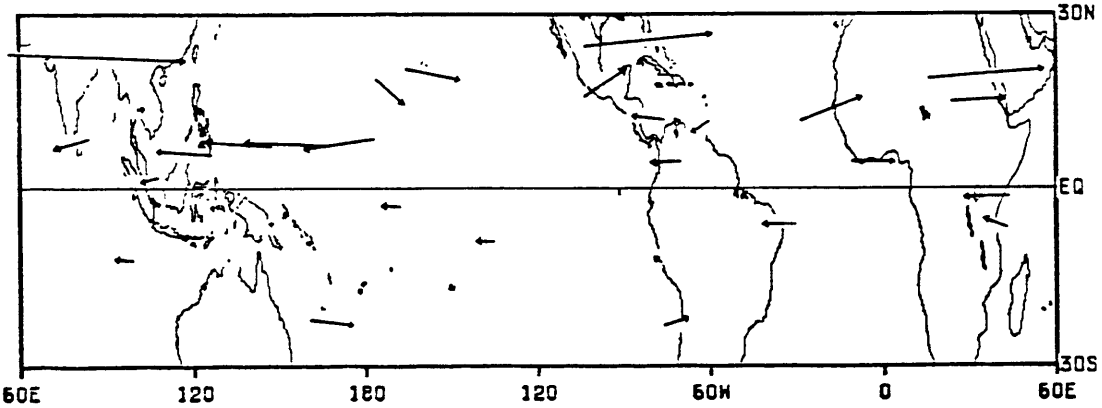
WINTER MEAN 700 MB

SCALE: —— = 5 M/S



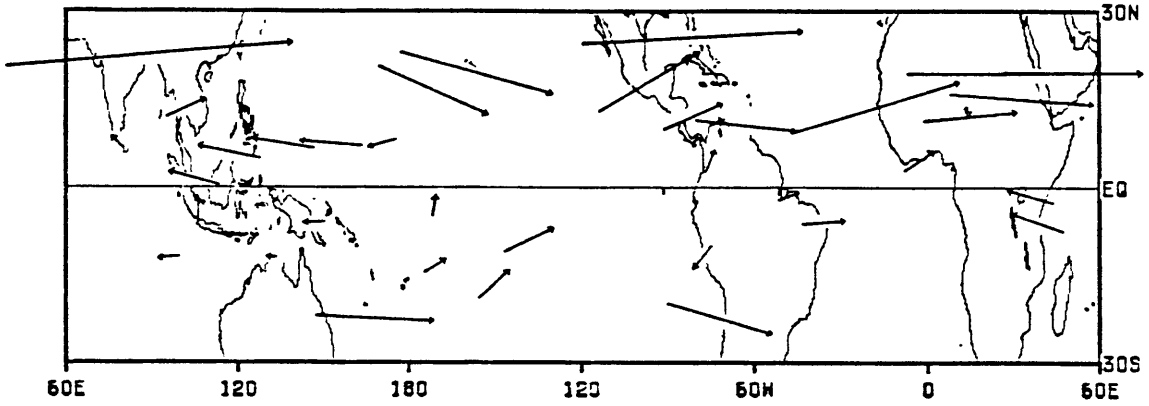
WINTER MEAN 500 MB

SCALE: —— = 10 M/S



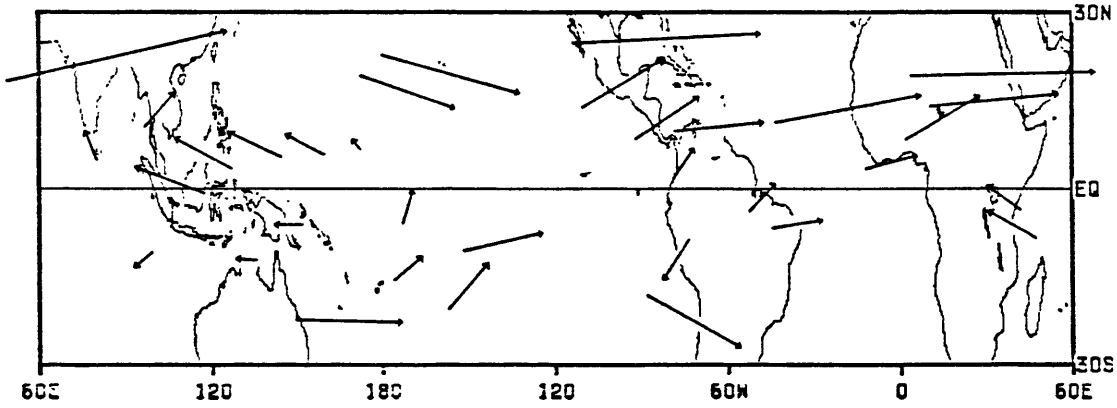
WINTER MEAN 300 MB

SCALE: ——— = 10 M/S



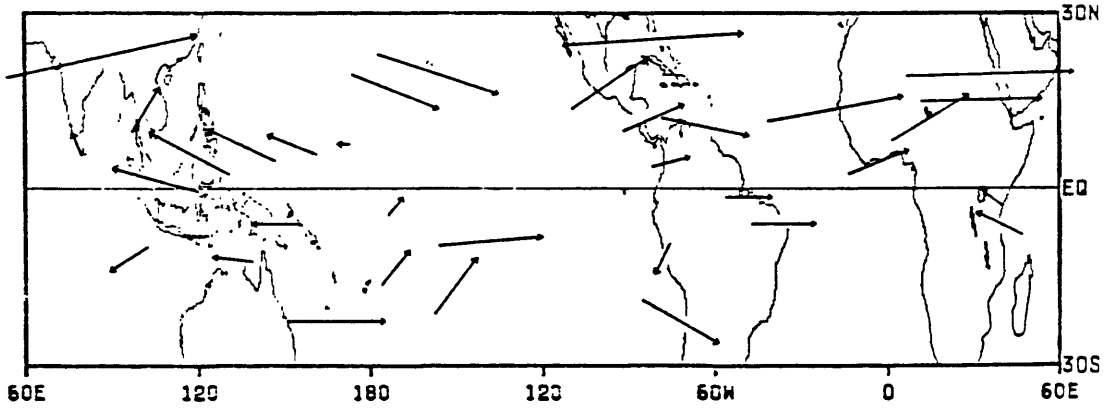
WINTER MEAN 200 MB

SCALE: ——— = 15 M/S



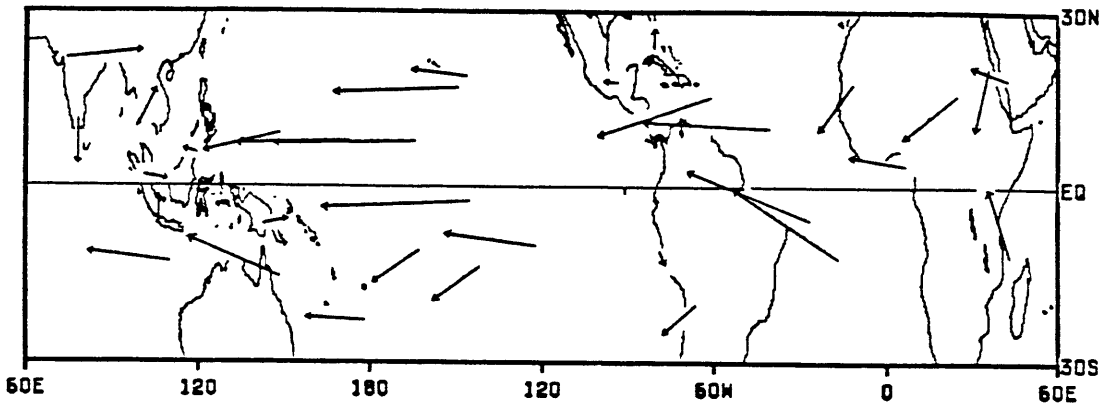
WINTER MEAN 150 MB

SCALE: ——— = 15 M/S



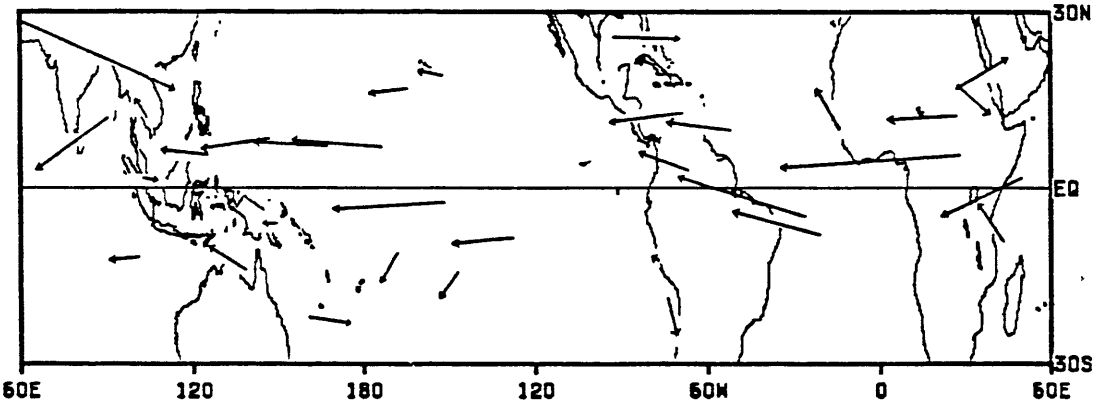
SPRING MEAN 850 MB

SCALE: ——— = 5 M/S



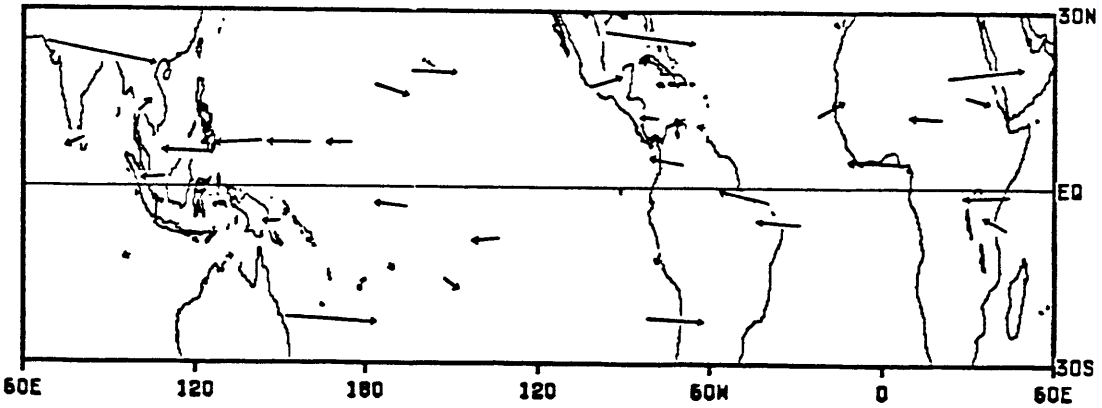
SPRING MEAN 700 MB

SCALE: ——— = 5 M/S



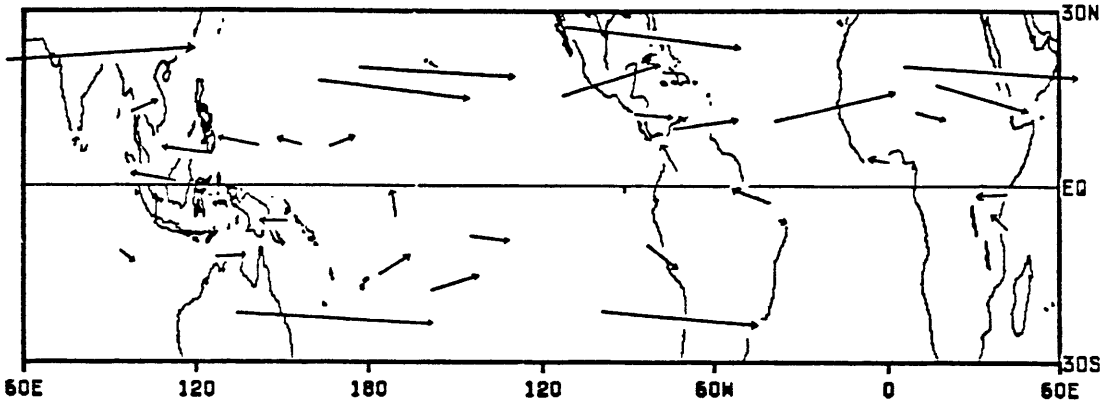
SPRING MEAN 500 MB

SCALE: ——— = 10 M/S



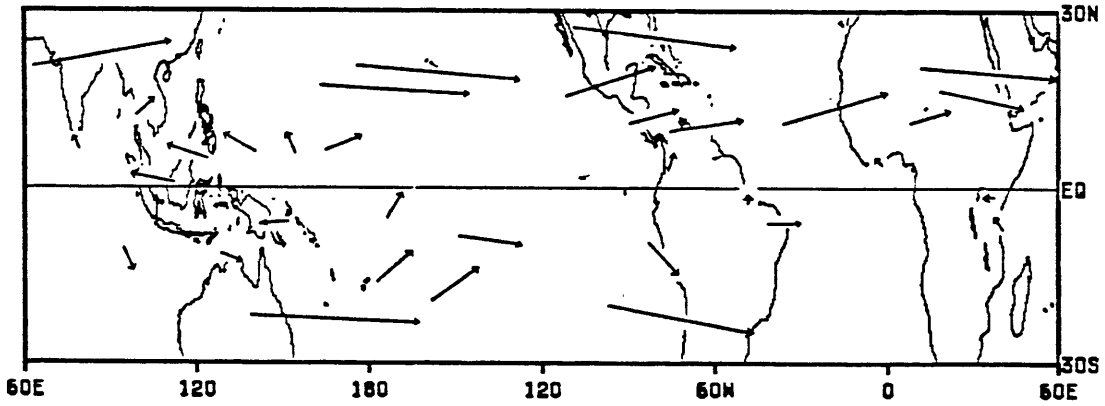
SPRING MEAN 300 MB

SCALE: ——— = 10 M/S



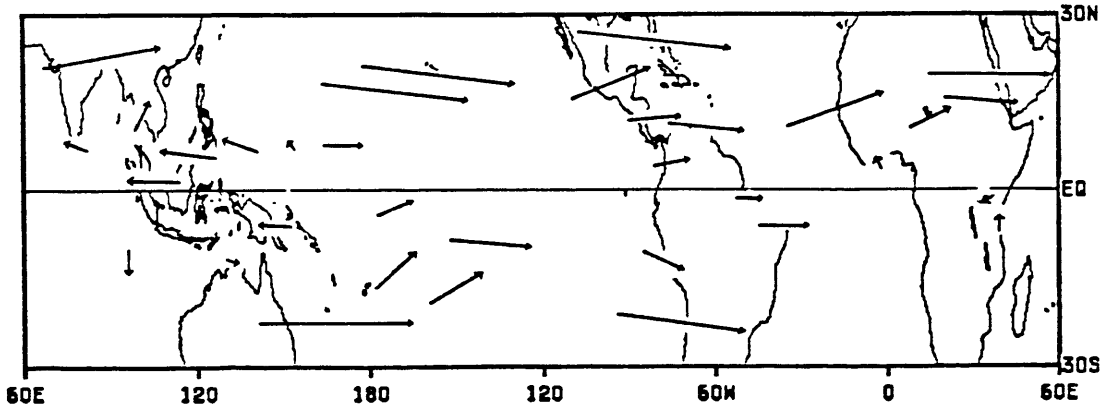
SPRING MEAN 200 MB

SCALE: ——— = 15 M/S



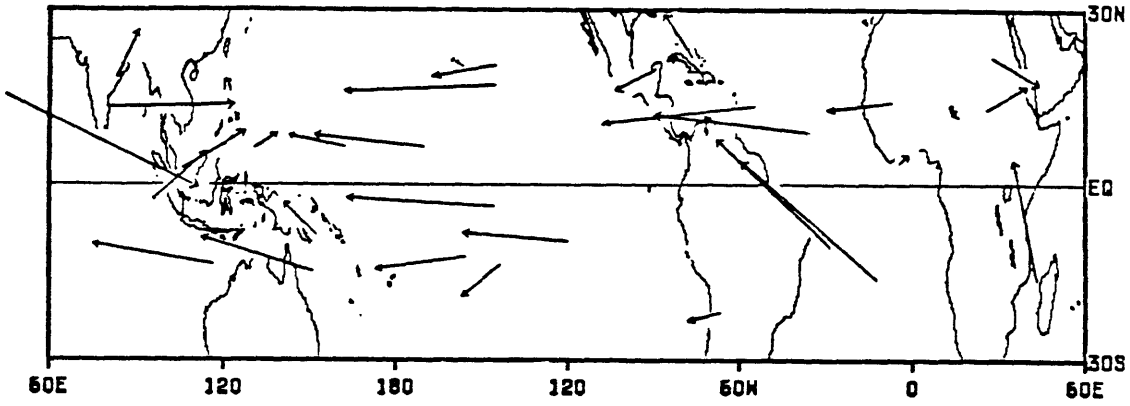
SPRING MEAN 150 MB

SCALE: ——— = 15 M/S



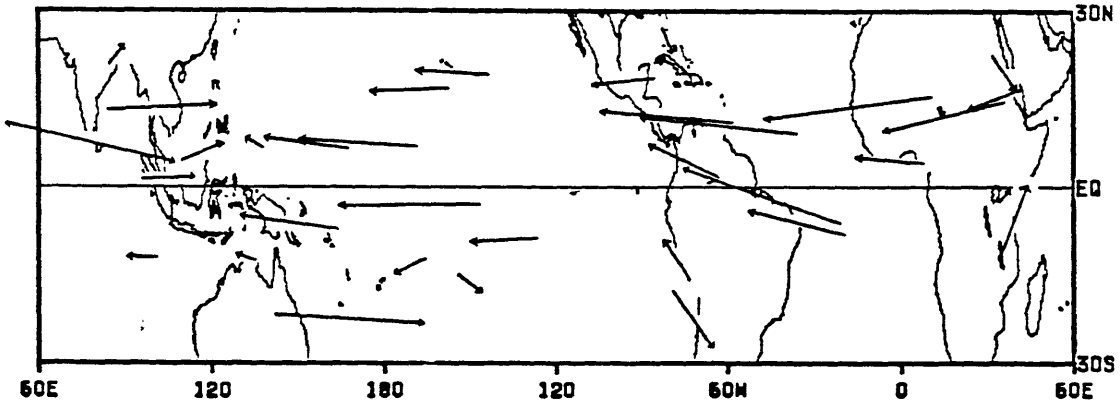
SUMMER MEAN 850 MB

SCALE: —— = 5 M/S



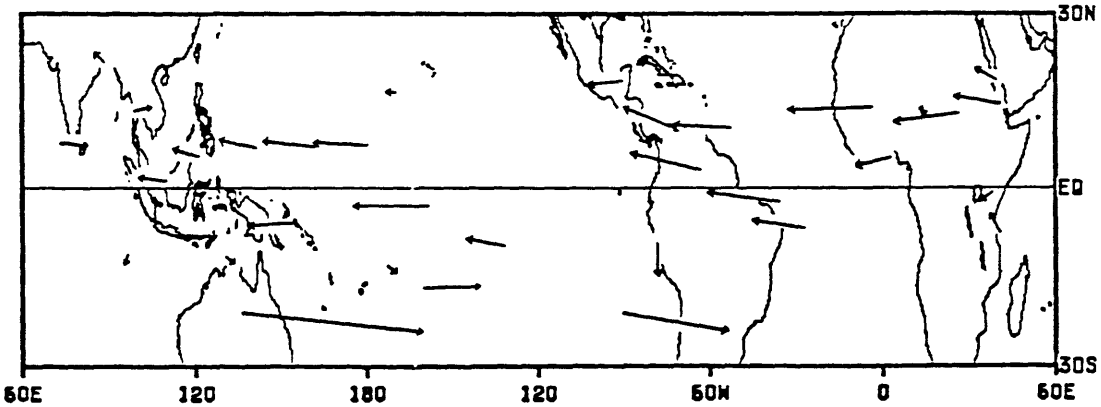
SUMMER MEAN 700 MB

SCALE: —— = 5 M/S



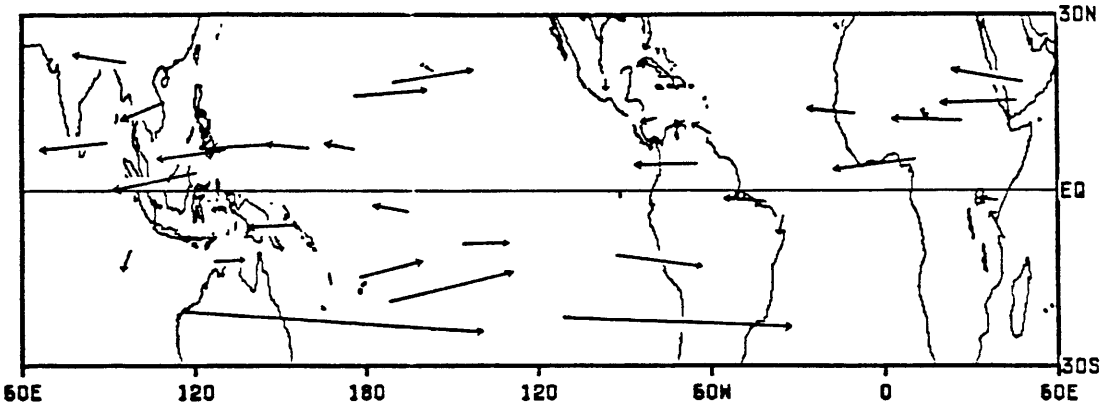
SUMMER MEAN 500 MB

SCALE: —— = 10 M/S



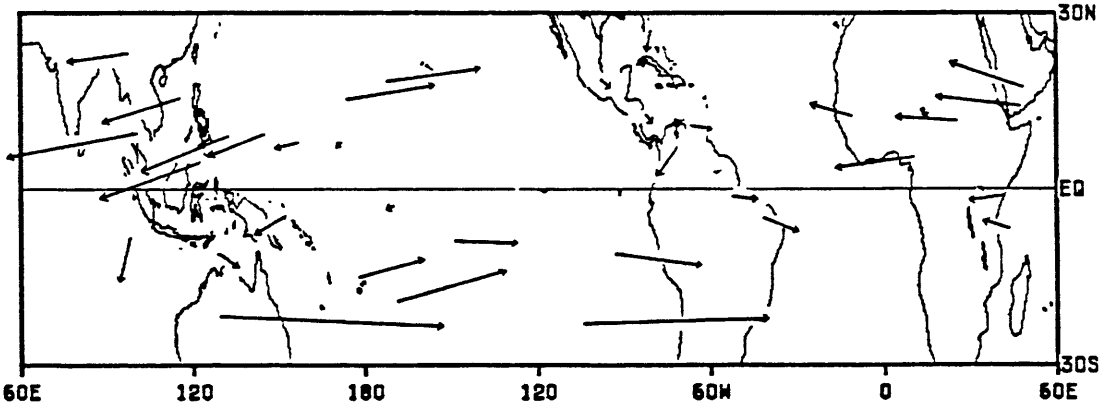
SUMMER MEAN 300 MB

SCALE: ——— = 10 M/S



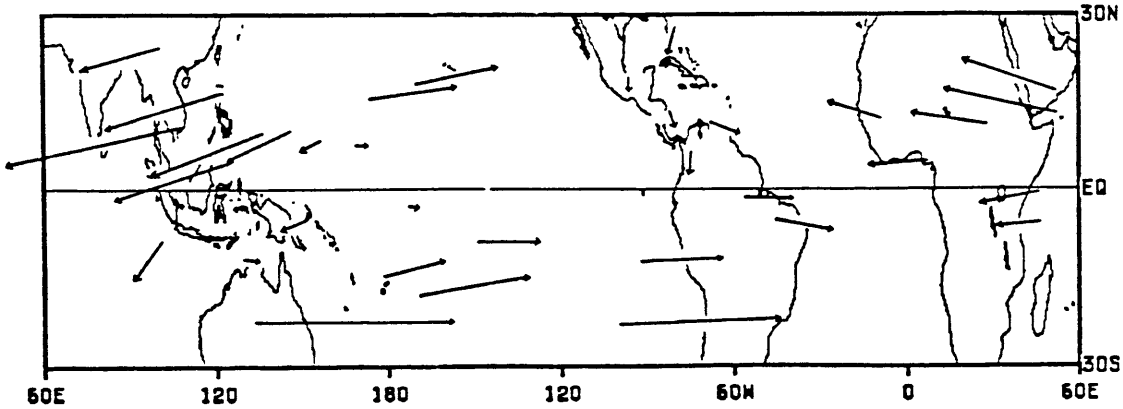
SUMMER MEAN 200 MB

SCALE: ——— = 15 M/S



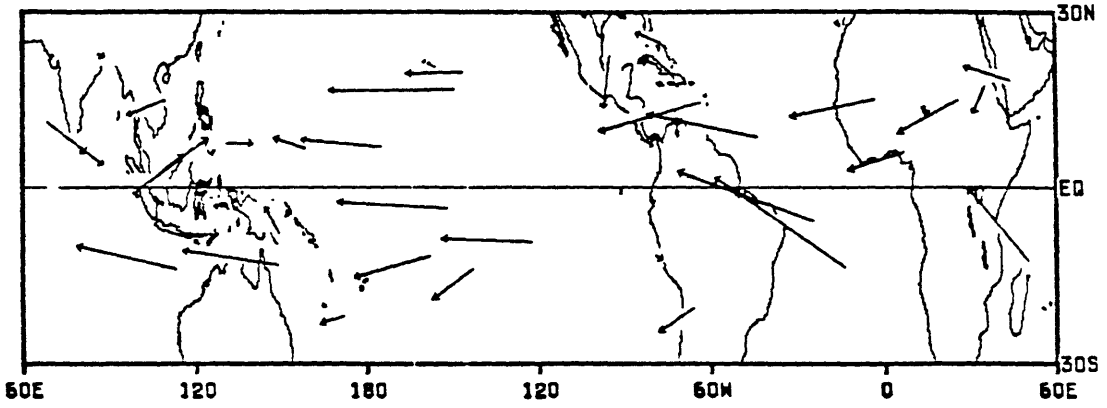
SUMMER MEAN 150 MB

SCALE: ——— = 15 M/S



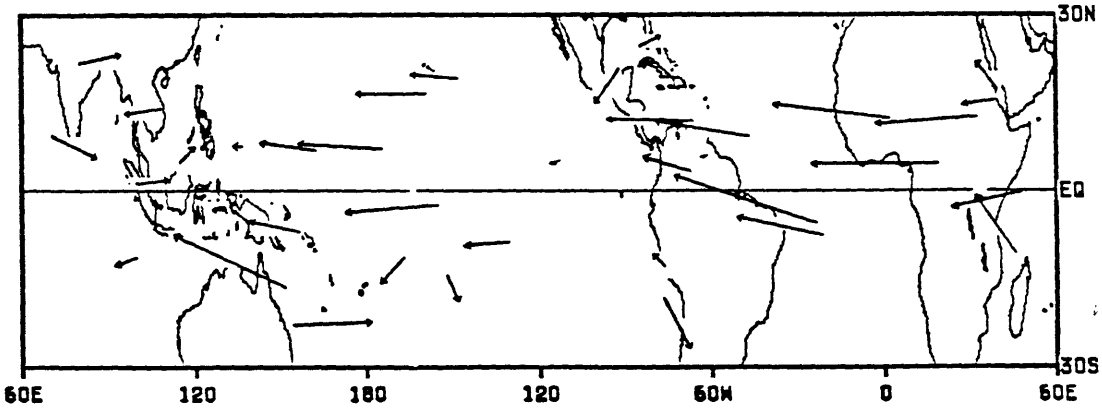
AUTUMN MEAN 850 MB

SCALE: —— = 5 M/S



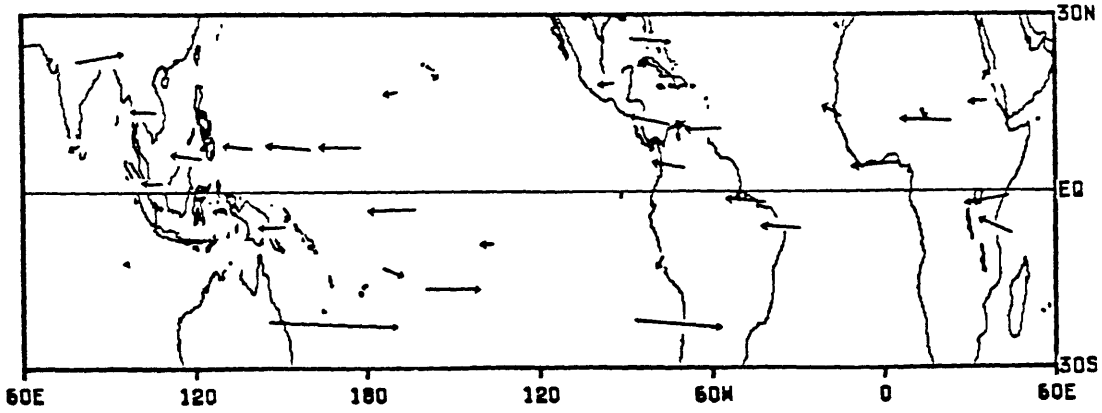
AUTUMN MEAN 700 MB

SCALE: —— = 5 M/S



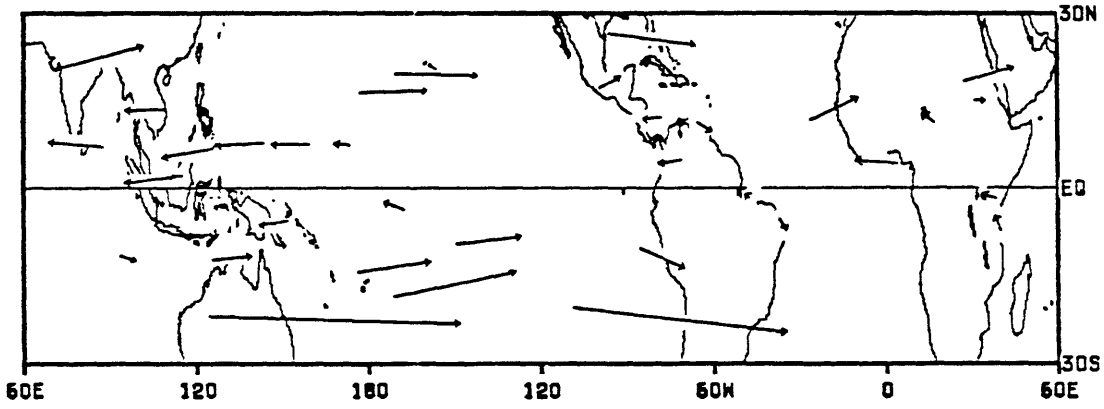
AUTUMN MEAN 500 MB

SCALE: —— = 10 M/S



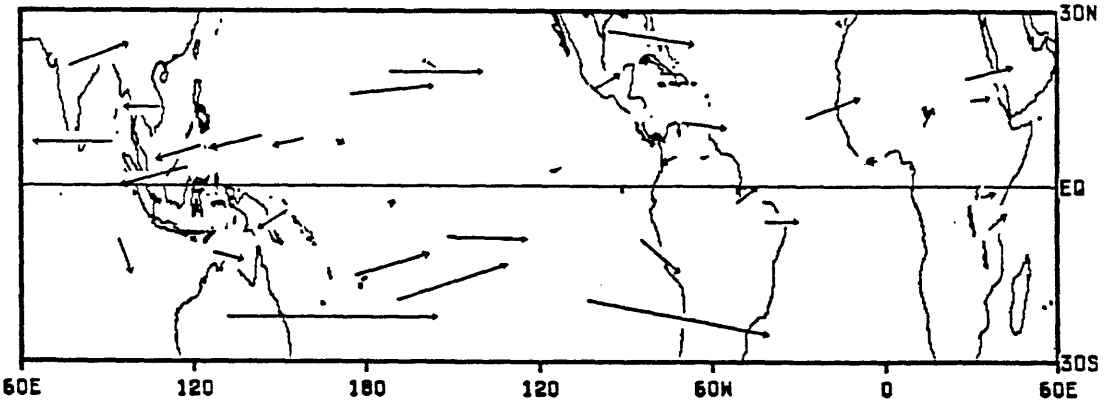
AUTUMN MEAN 300 MB

SCALE: —— = 10 M/S



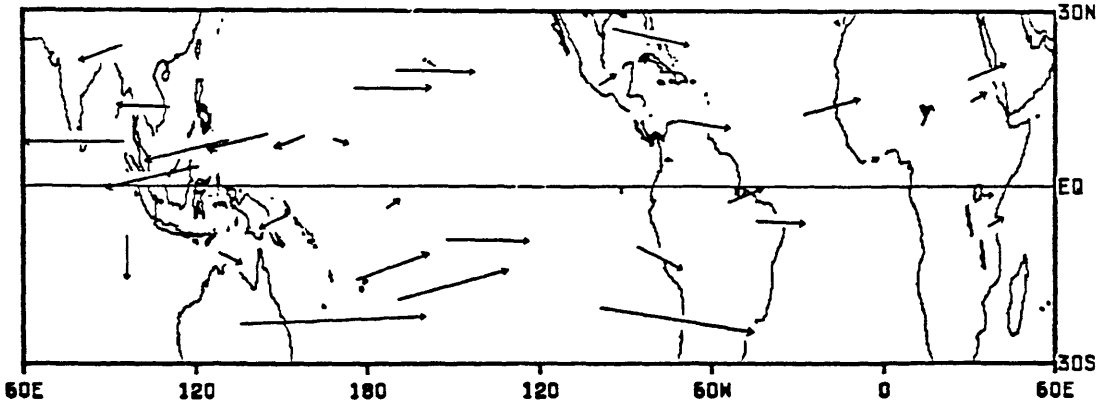
AUTUMN MEAN 200 MB

SCALE: —— = 15 M/S



AUTUMN MEAN 150 MB

SCALE: —— = 15 M/S



Appendix B

EMPIRICAL ORTHOGONAL FUNCTIONS

B.1 Introduction

Empirical orthogonal functions (EOFs) are used in this thesis to describe quantitatively the dominant spatial structures of wind variability. In this appendix, a summary of the properties and limitations of this analysis technique is given.

EOFs are employed here to represent wind observations at different pressure levels or stations in terms of one or two spatial modes. Thus, many time series are condensed into only one or two. The efficiency of the method depends on the spatial coherence of the variability. The spatial structures of the modes depend on the number and spatial distribution of the time series used.

Analyses are carried out using (1) scalar wind components, (2) vector wind components, and (3) Hilbert-transformed scalar wind components. (1) and (2) lead to EOFs describing standing oscillations, whereas (3) is a generalization to allow for the description of propagating oscillations. The mathematical procedure and interpretation of each variety of analysis are outlined in subsections B.2, B.3, and B.4 to follow. The EOFs for each of the analyses have the following common characteristics:

(a) The EOFs form a complete orthonormal basis set.

(b) The EOFs are ordered such that the gravest mode (EOF^1) explains more variability than any other possible single basis function. The next mode (EOF^2) which is orthonormal to EOF^1, explains more of the residual variance (not associated with EOF^1) than any other possible basis function, etc.

B.2 EOFs of scalar wind components

The most common application of EOFs in meteorological studies has been to time series of scalar quantities. EOFs were introduced into the meteorological literature by Lorenz (1956); a concise review of the properties of EOFs is given by Davis (1976). The procedure used to calculate EOFs in this thesis includes a mass-weighting scheme introduced by Blackmon et al. (1979). Consider a set of time series

$$u_{rln} \qquad \text{with} \quad \begin{array}{l} r = 1,2,\ldots,R \\ l = 1,2,\ldots,6 \\ n = 1,2,\ldots,N \end{array}$$

where u is a scalar wind component (either zonal or meridional) at station r, pressure level l, and time n. The EOFs describing the total variance of u for this set of stations are as the eigenvectors of the mass-weighted covariance matrix

$$C_{rlsm}w_{lm} \qquad \begin{array}{l} r,s = 1,2,\ldots,R \\ l,m = 1,2,\ldots,6 \end{array}$$

Here $C_{rlsm} = \overline{u_{rl}u_{sm}} - \bar{u}_{rl}\bar{u}_{sm}$, the overbar represents a time average

$$\overline{(\ )} = \frac{1}{N}\sum_{n=1}^{N}(\ )$$

and w_{lm} is a mass-weighting function. As in Blackmon et al. (1979), the weighting function is designed to compensate for the fact that the six pressure levels used in the analysis are unevenly spaced in the vertical. If we consider that the six levels are representative of the atmospheric column between 925 and 125 mb, we can express the mass of the column (in units of mb) represented by each level l as p_l (see Table B.1). The relative weight assigned to each level is $\Delta_l = 6p_l$ / 800 and the mass-weighting function is:

$$w_{lm} = \sqrt{\Delta_l \Delta_m}$$

TABLE B.1

Mass-weighting of the covariance matrix

l	1	2	3	4	5	6
pressure level (mb)	850	700	500	300	200	150
p_l (mb)	150	175	200	150	75	50
Δ_l	1.1250	1.3125	1.5000	1.1250	0.5625	0.3750

The eigenvectors are the solution of

$$E^k_{rl} C_{rlsm} w_{lm} = \lambda^k E^k_{rl} \qquad k = 1,2,\ldots,K=Rx6 \qquad [B.2.1]$$

The eigenvectors E^k_{rl} are real because C_{rlsm} is Hermitian. By convention, the eigenvectors E^k_{rl} and eigenvalues λ^k are ordered, so that $\lambda^1 > \lambda^2 > \cdots > \lambda^K$. The sum of the eigenvalues equals the trace of the mass-weighted covariance matrix:

$$\sum_{k=1}^{K} \lambda^k = \sum_{r=1}^{R} \sum_{l=1}^{6} C_{rlrl} w_{ll} \qquad [B.2.2]$$

Now the term on the right side is the total mass-weighted variance of the time series of u, since

$$C_{rlrl} w_{ll} = \overline{u^2_{rl}} \Delta_l \qquad [B.2.3]$$

Hence each eigenvalue λ^k represents the mass-weighted variance explained by eigenvector E^k, and the fraction of the total variance f^k explained by E^k is

$$f^k = \frac{\lambda^k}{\sum_{k=1}^{K} \lambda^k} \qquad [B.2.4]$$

Associated with each eigenvector is a time series of principal components P_n^k, which represent the projection of the observed field at time n (that is, u_{rln}) onto E_{rl}^k:

$$P_n^k = \sum_{r=1}^{R} \sum_{l=1}^{6} E_{rl}^k \, u_{rln} \, \Delta_l \qquad [B.2.5]$$

Then the observed field can be reconstructed in terms of the eigenvectors and principal components

$$u_{rln} = \sum_{k=1}^{K} E_{rl}^k \, P_n^k \qquad [B.2.6]$$

The observed field may be partially reconstructed by eliminating the summation in [B.2.6] and considering only the inner product associated with a single mode:

$$u_{rln}^k = E_{rl}^k \, P_n^k \qquad [B.2.7]$$

Scalar EOFs as developed here are used extensively in Chapter 3. Eigenvectors describing the vertical structure of zonal and meridional wind components separately at single stations (i.e. R=1) are discussed in Section 3.3 (these are denoted "1dEOFs" in the text of the thesis). In Section 3.4, EOFs are derived for a near-equatorial line of stations (R > 1) to describe the structure of variability in the longitude-height plane over the western Pacific. This analysis is denoted "2dEOF".

B.3 EOFs of vector winds

The extension of the analysis discussed in the previous section to vector quantities was developed by Hardy and Walton (1978). EOFs of vector winds are shown in Fig. 3.14. We consider complex time series of vector winds

$$\mathbf{V}_{rln} = u_{rln} + iv_{rln}$$

with the zonal wind expressed as the real component and the meridional wind expressed as the imaginary component of $\mathbf{V}$. Eigenvectors $\mathbf{E}^k$ and principal components $\mathbf{P}^k$ of the resultant mass-weighted covariance matrix $\mathbf{C}_{rlsm}$ are then found as for the scalar case, that is

$$\begin{aligned} \mathbf{C}_{rlsm} &= \overline{\mathbf{V}_{rl}\,\mathbf{V}_{sm}}\,w_{lm} \\ \mathbf{E}^k_{rl}\,\mathbf{C}_{rlsm} &= \lambda^k_{rl}\,\mathbf{E}^k_{rl} \\ \mathbf{P}^k_n &= \sum_{l=1}^{6}\sum_{r=1}^{R} u_{rln}\,\mathbf{E}^k_{rl}\,\Delta_l \end{aligned} \qquad \text{[B.3.1]}$$

Since $\mathbf{C}_{rlsm}$ is Hermitian, the eigenvalues λ^k are real and their interpretation is exactly the same as for the scalar case.

Whereas the sign of each scalar eigenvector E^k_{rl} defined by [B.2.1] was arbitrary, here the phase of each complex eigenvector $\mathbf{E}^k_{rl}$ from [B.3.1] is arbitrary. For purposes of physical interpretation, it is useful to shift the phase of each complex eigenvector so that the mean-square value of the imaginary component of u^k_n is minimized. This is done for each mode $\mathbf{E}^k$ by defining:

$$\tan \theta_k = \frac{\overline{Re(P_n^k)\ Im(P_n^k)}}{\overline{(Re(P_n^k))^2}} \qquad [B.3.2]$$

and using as EOFs the set of phase-shifted eigenvectors B^k, where

$$B^k = E^k e^{-i\theta_k}$$

After phase-shifting, the elements of B^k point in the direction of "preferred orientation", i.e. along the axis which accounts for most of the variance.

B.4 Generalization of EOFs for propagating waves

Empirical orthogonal functions developed in Sections B.2 and B.3 describe the observed variance in the wind field in terms of standing oscillations. Any variability associated with propagating waves is partitioned among several standing modes. A generalization of EOF analysis which provides a more efficient and physically meaningful basis set for use in describing variance associated with propagating anomalies was introduced by Barnett (1983) and described in detail by Horel (1984). This technique is denoted complex EOF (or CEOF) analysis.

First, each time series u_{rl} is decomposed into Fourier components. For time series of seasonal anomalies, the first and last year are tapered using a cosine bell to minimize end effects on the Fourier decomposition (Madden and Julian, 1971):

$$u_{rln} = A_n u_{rln} \quad \text{where } A_n = \begin{cases} \sin \pi n/5 & n=1,\ldots,4 \\ 1 & n=5,\ldots,N-4 \\ \cos \pi n/5 & n=N-3,\ldots,N \end{cases} \qquad [B.4.1]$$

After tapering the ends, the Fourier decomposition is performed by

summing over all frequencies ω:

$$u_{r1n} = \sum_{\omega=1}^{N/2} a_{r1\omega} \cos \omega_n + b_{r1\omega} \sin \omega_n$$

Then the Hilbert transform (or quadrature function) is obtained by shifting the phase of each Fourier component ahead by $\pi/2$:

$$\hat{u}_{r1n} = \sum_{\omega=1}^{N/2} b_{r1\omega} \cos \omega_n - a_{r1\omega} \sin \omega_n \qquad [B.4.2]$$

A complex wind field U_{r1n} is then formed, whose real and imaginary parts are the observed wind u_{r1n} and the Hilbert transform $\hat{u}_{r1n}$, respectively:

$$U_{r1n} = u_{r1n} + i\hat{u}_{r1n} = \sum_{\omega=1}^{N/2} c_{r1\omega} e^{-i\omega n} \qquad [B.4.3]$$

where $c_{r1\omega} = a_{r1\omega} + ib_{r1\omega}$. Then, complex EOFs are found by calculating the mass-weighted covariance matrix associated with the complex time series U_{r1n}. The eigenvectors E^k_{r1} and principal components P^k_n are complex, and the component of the reconstructed u_{r1n} field associated with each mode k (analogous to [B.2.7] for scalar EOFs) is the real part of the complex product between E^{k*}_{r1} and P^k_n, where the asterisk denotes the complex conjugate:

$$u^k_{r1n} = \mathrm{Re} \left\{ E^{k*}_{r1} P^k_n \right\} \qquad [B.4.4]$$

The reconstruction was performed only for points not tapered, where A_n=1 in [B.4.1].

Appendix C

SIGNIFICANCE TESTS

C.1 Correlation coefficients

The temporal correlation coefficient r(x,y) between time series of variables x_n and y_n is defined:

$$r(x,y) = \frac{\overline{xy} - \bar{x}\,\bar{y}}{\sigma_x\,\sigma_y} \qquad \text{with } \overline{(\ )} = \frac{1}{N}\sum_{n=1}^{N}(\ )$$

where the overbar represents a time average (here, an average over n), and σ represents the temporal standard deviation: $\sigma_x = \overline{x^2} - \bar{x}^2$. For finite sample sizes, the calculated correlation r(x,y) must be treated as a sample value approximating the "true" correlation $\rho(x,y)$ which would derive from an infinite population ($N \to \infty$). If x and y are normally distributed, then the t statistic

$$t = \frac{r(x,y)\sqrt{\nu}}{\sqrt{1 - r^2(x,y)}}$$

follows Student's distribution with ν degrees of freedom and can be used to test the hypothesis that $\rho \neq 0$ (Bulmer, 1967). If each value of x_n and y_n is independent, then $\nu = N-2$ since two degrees of freedom (the sample mean and variance) have been removed from each time series in the calculation of r.

Estimating ν can be extremely difficult in geophysical time series analysis. In this thesis, it is assumed that one degree of freedom per year is reasonable for seasonal wind anomalies, so that $\nu = M-2$, where M is the length of the time series in years. Table C.1 presents 95% and 99% confidence thresholds of r for the hypothesis $\rho \neq 0$ using a two-tailed test, for various values of M.

TABLE C.1

Confidence thresholds for correlation coefficients. Tabulated values are the minimum correlation magnitude necessary in order to satisfy the hypothesis that the true correlation ρ is different from zero (with 95% or 99% confidence), for time series of length M years.

M =	8	12	16	20	24
$\|r\|$ (95%) =	0.62	0.50	0.43	0.39	0.36
$\|r\|$ (99%) =	0.75	0.62	0.54	0.49	0.45

C.2 Empirical orthogonal functions

The EOFs calculated in Sections 3.3 and 4.3 to describe the vertical structure of interannual variability are subject to sampling uncertainties associated with the finite length of the time series used to generate them. These uncertainties can be estimated using the methodology developed by North et al. (1982).

We consider that the eigenvalues λ^k and eigenvectors E^k calculated from a time series of length N are estimates of the true eigenvalues χ^k and eigenvectors Φ^k which would derive from the infinite population of which our time series are a sample. We then create a perturbation expansion in a small parameter ε to describe the difference between the exact and sample eigenvalues and eigenvectors:

$$\lambda^k = \chi^k + \varepsilon\lambda'^k + \varepsilon^2\lambda''^k + \ldots$$

$$E^k = \Phi^k + \varepsilon E'^k + \varepsilon^2 E''^k + \ldots$$

To first order, the quantities $\varepsilon E'^k$ and $\varepsilon\lambda'^k$ represent the uncertainties $\delta\lambda^k$ and δE^k in the eigenvalues and eigenvectors. North et al. (1982) showed that these uncertainties could be approximated by

$$\delta\lambda^k \approx \varepsilon\lambda'^k \approx \lambda^k \sqrt{\frac{2}{\nu}} \qquad [C.2.1]$$

$$\delta E^k \approx \varepsilon E'^k \approx \frac{\varepsilon\lambda'^k}{\Delta\lambda^k} \Phi^k \qquad [C.2.2]$$

where ν is the number of degrees of freedom and $\Delta\lambda^k$ is the spacing between λ^k and its nearest neighbor (i.e. the lesser of the quantities $\lambda^k-\lambda^{k+1}$ and $\lambda^{k-1}-\lambda^k$). Here we are concerned primarily with the statistical significance of the gravest mode only. Assuming one degree of freedom per year yields the uncertainties shown in Table C.2 for time series of varying length. For convenience, the eigenvalues in the Table are expressed in terms of the percentage of explained variance f^k as defined in [B.2.4], that is

$$\delta f^1 = f^1 \sqrt{\frac{2}{M}} \qquad [C.2.3]$$

TABLE C.2

Uncertainty of eigenvalues for scalar wind calculations. Tabulated values are the uncertainties of the percentage of variance explained by the gravest mode, when the eigenvalue is based on a time series of length M years.

	M = 8	12	16	20	24
$f^1 = 0.5$	0.25	0.20	0.18	0.16	0.14
$f^1 = 0.6$	0.30	0.24	0.21	0.19	0.17
$f^1 = 0.7$	0.35	0.29	0.25	0.22	0.20
$f^1 = 0.8$	0.40	0.33	0.28	0.25	0.23
$f^1 = 0.9$	0.45	0.37	0.32	0.28	0.26

The uncertainty in the shape of the gravest eigenvector E^1 is a function of the uncertainty in λ^1 and the difference $(\lambda^1-\lambda^2)$. If λ^1 is distinct, i.e. if the uncertainty in λ^1 is less than the difference between λ^1 and λ^2, then the shape of E^1 is also distinct. If the uncertainty in λ^1 is comparable to the difference $(\lambda^1-\lambda^2)$, then E^1 and E^2 are 'effectively degenerate', and the gravest mode of the population Φ^1 is some unknown linear combination of E^1 and E^2. Hence, the ratio

$$\delta E^1 = (\delta\lambda'^1) / (\lambda^1-\lambda^2) = \delta f'^1 / (f^1-f^2) \qquad [C.2.4]$$

is a measure of the uncertainty in E^1.

To obtain a unique estimate of the uncertainty in E^1 for a particular value of λ^1, it is necessary to make some universal assumption about λ^2. To do this, we shall assume that the first two modes explain 95% of the total variance. This condition was nearly satisfied for the set of vertical modes described in Section 3.3, and in any case it is a conservative assumption since it nearly minimizes (f^1-f^2) and hence maximizes the uncertainty. Substituting $f^2 = 0.95 - f^1$ into [C.2.4] yields

$$\delta E^1 = \delta f'^1 / (2f^1 - 0.95) \qquad [C.2.5]$$

Values of δE^1 are given in Table C.3 as a function of f^1 and M. We have no confidence whatsoever in the shape of the gravest mode when the uncertainty in its eigenvalue is greater than the distance to the next eigenvalue, i.e. when $\delta E^1 \geq 1$. This uncertainty threshold is delineated in Table C.3 by a solid line. Not surprisingly, the uncertainty is larger than this threshold for $f^1 = 0.5$, for any length of time series up to M = 24 years. The spacing between f^2 (assumed equal to 0.45 for $f^1 = 0.5$) and f^1 is smaller than the uncertainty in f^1, and therefore the first two modes are effectively degenerate.

North et al. (1982) suggest that a more stringent test of reliability is to require $\delta E^k < 0.5$. This uncertainty threshold is delineated with a dashed line in Table C.3.

TABLE C.3

Uncertainty parameter δE^l for the gravest EOF mode E^l, using the uncertainties in eigenvalues tabulated in Table C.2. EOFs with $\delta E^l > 1$ (delineated with a solid line in the Table) are effectively degenerate, and no confidence in their shape is maintained. EOFs with $\delta E^l < 0.5$ (delineated with a dashed line) satisfy a more stringent confidence test.

	M = 8	12	16	20	24
$f^1 = 0.5$	5.0	4.0	3.6	3.2	2.8
$f^1 = 0.6$	1.2	0.96	0.84	0.76	0.68
$f^1 = 0.7$	0.78	0.64	0.56	0.49	0.44
$f^1 = 0.8$	0.62	0.51	0.43	0.38	0.35
$f^1 = 0.9$	0.53	0.44	0.38	0.33	0.31

Appendix D

LIST OF FIGURES

1.1 Map of station locations 13

1.2 Number of seasonal mean observations at each station . . . 16

2.1 Zonal mass flux along the equator for the DJF and JJA seasons, taken from Newell et al. (1974) . . 21

2.2 Annual mean vector wind at each level 25

2.3 Annual mean vector wind and zonal mass flux across the Trivandrum-Atuona cross-section . . . 30

2.4 Annual cycle of the zonal wind at each level 37

2.5 Annual cycle in the meridional wind at each level 42

2.6 Semiannual cycle of the zonal wind at each level 44

2.7 Semiannual cycle in the meridional wind at each level . . 46

2.8 Ratio of the amplitude of the annual cycle to the amplitude of the semiannual cycle for the zonal wind at 200 mb 48

2.9 Annual mean vector wind and annual variability across the Trivandrum-Atuona cross-section . . 51

2.10 Seasonal mean vector wind across the Trivandrum-Atuona cross-section . . 56

2.11 Seasonal mean zonal mass flux across the Trivandrum-Atuona cross-section . . . 58

3.1 a) Time series of Southern Oscillation Index (SOI) 66
b) Correlation coefficient between seasonal anomalies of 200 mb zonal wind and SOI for the DJF season, from Selkirk (1984)
c) As in (b), but for seasonal anomalies of meridional wind
d) Spatial variability associated with gravest mode of an EOF analysis of combined zonal and meridional 200 mb seasonal wind anomalies, from Arkin (1982)

3.2 Standard deviation of seasonal anomalies of zonal wind . . 74

3.3 Vertical profile of the standard deviation of seasonal anomalies of zonal wind at Truk and Johnston . . 77

3.4 As in Fig. 3.2, but for meridional wind 79

3.5 Ratio of interannual variance to periodic variance for zonal wind at 200 mb, 500 mb, and 750 mb . . . 80

3.6 As in Fig. 3.5, but for meridional wind 82

3.7 Examples of vertical 1dEOF modes from Holmström (1963), Blackmon et al. (1979), and Adams (1971) . 86

3.8 Gravest vertical 1dEOF mode of seasonal anomalies of zonal wind at Johnston, for DJF, JJA, and year-round data . 89

3.9 As in Fig. 3.8, but for Canton 90

3.10 As in Fig. 3.8, but for Majuro 92

3.11 As in Fig. 3.8, but for Darwin 93

3.12 Shape of the gravest vertical mode of seasonal zonal wind fluctuations at each station for each season . 94

3.13 Percentage of variance explained by the gravest vertical mode of zonal wind fluctuations at each station 100

3.14 As in Fig. 3.13, but for meridional wind fluctuations for DJF and JJA seasons . 102

3.15 Gravest mode of vertical EOF expansion of vector wind at Majuro for DJF and JJA seasons . 103

3.16 Correlation coefficient between SOI and seasonal anomalies of zonal wind at each level for the DJF season 107

3.17a) Correlation coefficient between SOI and the 1dEOF mode with a baroclinic shape at each station for the DJF season . 110

b) As in (a), but for the 1dEOF mode with an equivalent-barotropic shape.

3.18 Map showing locations of stations used in the cross-sections plotted in Figs. 3.19 and 3.20. . 112

3.19 Correlation coefficient between SOI and zonal wind anomalies at stations in cross-section A for DJF season . . 113

3.20 As in Fig. 3.19, but for stations in cross-section B . . 114

3.21 As in Fig. 3.17, but for the MAM season 116

3.22 As in Fig. 3.17, but for the JJA season 117

3.23 As in Fig. 3.17, but for the SON season 118

3.24 First two modes of 2dEOF analysis of DJF seasonal anomalies across the Trivandrum-Atuona cross-section . . . 121

3.25 As in Fig. 3.24, but for year-round data 123

4.1	Zonal and meridional wind anomalies across the Trivandrum-Atuona cross-section for the composite El Niño event	135
4.2	Anomalous zonal mass flux across the Trivandrum-Atuona cross-section for the composite El Niño event	139
4.3	Spatial and temporal structure of the gravest mode of a complex EOF analysis of seasonal anomalies of zonal wind across the eastern Indian and western Pacific Oceans	144
4.4	Zonal wind anomaly for SON(1975) associated with . . . CEOF mode 1	146
4.5	As in Fig. 4.4, but for DJF(1976)	147
4.6	As in Fig. 4.4, but for JJA(1976)	148
4.7	Real and imaginary parts of time series of the . . . . principal components of CEOF mode 1	151
4.8	As in Fig. 4.3, but based on monthly zonal wind anomalies	154
4.9	Time series of principal components derived by projecting CEOF mode 1 onto the observed anomaly field for available stations for the period 1961-1979.	156
4.10	Vector wind anomalies for individual seasons which . . together comprise the SON(-1) El Niño composite	160
4.11	Anomalous zonal mass flux for individual seasons . . . which together comprise the SON(-1) El Niño composite	161
4.12	As in Fig. 4.10, but for DJF(0) phase	162
4.13	As in Fig. 4.11, but for DJF(0) phase	163
4.14	As in Fig. 4.10, but for MAM(0) phase	164
4.15	As in Fig. 4.11, but for MAM(0) phase	165
4.16	As in Fig. 4.10, but for JJA(0) phase	166
4.17	As in Fig. 4.11, but for JJA(0) phase	167
4.18	As in Fig. 4.10, but for SON(0) phase	168
4.19	As in Fig. 4.11, but for SON(0) phase	169
4.20	As in Fig. 4.10, but for DJF(+1) phase	170
4.21	As in Fig. 4.11, but for DJF(+1) phase	171
4.22	Anomalous zonal mass flux for SON(1970) and SON(1973) .	177

4.23	Longitude-time plot of 200 mb wind anomalies along the equator during 1982-83 El Niño event, from Arkin et al. (1983)	181
4.24	Longitude-time plot of cloudiness fluctuations along the equator for period Feb(1965)-July(1973), from Murakami (1975)	183
4.25	Seasonal anomalies of outgoing IR for period SON(1975)-JJA(1976), from Liebmann and Hartmann (1982)	185
A.1	Seasonal mean vector wind plots for each level for the DJF (Northern Hemisphere winter) season	194
A.2	As in A.1, but for MAM (Northern Hemisphere spring)	196
A.3	As in A.1, but for JJA (Northern Hemisphere summer)	198
A.4	As in A.1, but for SON (Northern Hemisphere autumn)	200

REFERENCES

Adams, H.A., 1971: The application of empirical orthogonal functions to meteorological fields in the tropical western Pacific. M.S. Thesis, University of Washington, 86 pp.

Anderson, J.R., and R.D. Rosen, 1983: The latitude-height structure of 40-50 day variations in atmospheric angular momentum. J. Atmos. Sci., 40, 1584-1591.

Arkin, P.A., 1982: The relationship between interannual variability in the 200 mb tropical wind field and the Southern Oscillation. Mon. Wea. Rev., 110, 1393-1404.

-----, 1984: An examination of the Southern Oscillation in the upper tropospheric tropical and subtropical wind field. Ph.D. dissertation, University of Maryland, 240 pp.

-----, J.D. Kopman, and R.W. Reynolds, 1983: 1982-83 El Nino / Southern Oscillation Event Quick Look Atlas. NOAA/NWS/NMC/Climate Analysis Center, Washington D.C.

Barnett, T.P., 1983: Interaction of the monsoon and Pacific trade wind system at interannual time scales. Part I: The equatorial band. Mon. Wea. Rev., 111, 756-773.

-----, 1984a: Interaction of the monsoon and Pacific trade wind system at interannual time scales. Part II: The tropical band. Mon. Wea. Rev., 112, 2380-2387.

-----, 1984b: Interaction of the monsoon and Pacific trade wind system at interannual time scales. Part III: A partial anatomy of the Southern Oscillation. Mon. Wea. Rev., 112, 2388-2400.

Bjerknes, J., 1966: A possible response of the atmospheric Hadley circulation to equatorial anomalies of ocean temperature. Tellus, 18, 820-829.

-----, 1969: Atmospheric teleconnections from the equatorial Pacific. Mon. Wea. Rev., 97, 163-172.

Blackmon, M.L., R.A. Madden, J.M. Wallace, and D.S. Gutzler, 1979: Geographical variations in the vertical structure of geopotential height fluctuations. J. Atmos. Sci., 36, 2450-2466.

Bulmer, M.G., 1967: Principles of Statistics. Dover Publications, New York, 252 pp.

Busalacchi, A.J., and M.A. Cane, 1985: Hindcasts of sea level variations during the 1982-83 El Niño. J. Phys. Ocean., 15, 213-221.

Caveides, C.N., 1973: Secas and El Niño: Two simultaneous climatical hazards in South America. Proc. Assoc. Amer. Geograph., 5, 44-49.

Chen, W.Y., 1982: Assessment of Southern Oscillation sea-level pressure indices. Mon. Wea. Rev., 110, 800-807.

Davis, R.E., 1976: Predictability of sea surface temperature and sea level pressure anomalies over the North Pacific Ocean. J. Phys. Ocean., 6, 249-266.

Donguy, J.-R., and G. Eltin, 1985: Eastward propagation at the equator during the 1982-83 El Niño inferred from sea surface salinity. Trop. Ocean-Atmos. Newsletter, Number 32, 1-2.

Geisler, J.E., 1981: A linear model of the Walker Circulation. J. Atmos. Sci., 38, 1390-1400.

-----, and D.E. Stevens, 1982: On the vertical structure of damped steady circulation in the tropics. Quart. J. Roy. Meteor. Soc., 108, 87-93.

Gill, A.E., 1980: Some simple solutions for heat-induced tropical circulation. Quart. J. Roy. Meteor. Soc., 106, 447-462.

-----, and E.M. Rasmusson, 1983: The 1982-83 climate anomaly in the equatorial Pacific. Nature, 306, 229-234.

Gray, T.I., J.R. Irwin, A.F. Krueger, and M.S. Varnadore, 1976: Average Circulation in the Troposphere Over the Tropics. National Oceanic and Atmospheric Administration, Washington D.C.

Hantel, M., and H.-R. Baader, 1978: Diabatic heating climatology of the zonal atmosphere. J. Atmos. Sci., 35, 1180-1189.

Hardy, D.M., and J.J. Walton, 1978: Principal components analysis of vector wind measurements. J. Appl. Meteor., 17, 1153-1162.

Harrison, D.E., and P. Schopf, 1984: Kelvin-wave-induced anomalous advection and the onset of surface warming in El Niño events. Mon. Wea. Rev., 112, 923-933.

-----, and D.S. Gutzler, 1985: Variability of monthly-averaged surface and 850 mb winds at tropical Pacific islands. Mon. Wea. Rev., 113, accepted for publication.

Hartmann, D.L., H.H. Hendon, and R.A. Houze, 1984: Some implications of the mesoscale circulations in tropical cloud clusters for large-scale dynamics and climate. J. Atmos. Sci., 41, 113-121.

Hastenrath, S., and P. Lamb, 1978: Climatic Atlas of the Tropical Atlantic and Eastern Pacific Oceans. University of Wisconsin Press, 122 pp.

Heddinghaus, T.R., and A.F. Krueger, 1981: Annual and interannual variations in outgoing longwave radiation over the tropics. Mon. Wea. Rev., 109, 1208-1218.

Held, I., 1983: Stationary and quasi-stationary eddies in the extratropical atmosphere: Theory. Large-Scale Dynamical Processes in the Atmosphere, B.J. Hoskins and R.P. Pearce, eds., Academic Press, 127-168.

Holmström, I., 1963: On a method for parametric representation of the state of the atmosphere. Tellus, 15, 127-149.

Holton, J.R., and R.S. Lindzen, 1968: A note on 'Kelvin' waves in the atmosphere. Mon. Wea. Rev., 96, 386-386.

Horel, J.D., 1982a: On the annual and interannual variations of the tropical Pacific atmosphere and ocean. Ph.D. dissertation, University of Washington, 136 pp.

-----, 1982b: On the annual cycle of the tropical Pacific atmosphere and ocean. Mon. Wea. Rev., 110, 1863-1878.

-----, 1984: Complex principal component analysis: Theory and examples. J. Clim. Appl. Meteor., 23, 1660-1673.

-----, and J.M. Wallace, 1981: Planetary-scale circulations associated with the Southern Oscillation. Mon. Wea. Rev., 109, 813-829.

Hoskins, B.J., A.J. Simmons, and D.G. Andrews, 1977: Energy dispersion in a barotropic atmosphere. Quart. J. Roy. Meteor. Soc., 103, 553-557.

-----, and D.J. Karoly, 1981: The steady linear response of a spherical atmosphere to thermal and orographic forcing. J. Atmos. Sci., 38, 1179-1196.

Houze, R.A., 1982: Cloud clusters and large-scale vertical motions in the tropics. J. Meteor. Soc. Japan, 60, 396-410.

Janowiak, J.E., A.F. Krueger, P.A. Arkin, and A. Gruber, 1985: Atlas of outgoing longwave radiation derived from NOAA satellite data. NOAA Atlas No. 6, U.S. Dept. of Commerce, 44 pp.

Jenne, R.L., and H.L. Crutcher, 1976: Monthly Rawinsonde Data: Climat Reports. National Center for Atmospheric Research, 12 pp.

Julian, P.R., and R.M. Chervin, 1978: A study of the Southern Oscillation and Walker Circulation phenomena. Mon. Wea. Rev., 106, 1433-1451.

Kidson, J.W., 1975: Tropical eigenvector analysis and the Southern Oscillation. Mon. Wea. Rev., 103, 187-196.

Krishnamurti, T.N., 1971: Tropical east-west circulations during the Northern summer. J. Atmos. Sci., 28, 1342-1347.

Krishnamurti, T.N., M. Kanamitsu, W.S. Koss, and J.D. Lee, 1973: Tropical east-west circulations during the Northern winter. J. Atmos. Sci., 30, 780-787.

Krishnamurti, T.N., H.-L. Pan, R. Pasch, and D. Subrahmanyam, 1983: Interannual Variability of the Tropical Motion Field (Long-term Annual Cycle and Southern Oscillation). FSU Report No. 83-3, Department of Meteorology, Florida State University.

Krueger, A.F., and T.I. Gray, 1969: Longterm variations in equatorial circulation and rainfall. Mon. Wea. Rev., 97, 700-711.

Liebmann, B., and D.L. Hartmann, 1982: Interannual variations of outgoing IR associated with tropical circulation changes during 1974-78. J. Atmos. Sci., 39, 1153-1162.

Lim, H., and C.-P. Chang, 1983: Dynamics of teleconnections and Walker circulations forced by equatorial heating. J. Atmos. Sci., 40, 1897-1915.

Lindzen, R.S., 1967: Planetary waves on beta-planes. Mon. Wea. Rev., 95, 441-451.

Lorenz, E.N., 1956: Empirical orthogonal functions and statistical weather prediction. Sci. Rep. No. 1, Statistical Forecasting Project, MIT Dept. of Meteorology, 49 pp.

Luther, D.S., D.E. Harrison, and R.A. Knox, 1983: Zonal winds in the central equatorial Pacific and El Niño. Science, 222, 327-330.

-----, and D.E. Harrison, 1984: Observing long-period fluctuations of surface winds in the tropical Pacific: Initial results from island data. Mon. Wea. Rev., 112, 285-302.

Madden, R.A., 1985: The annual variation in the vertical structure of the 40-50 day tropical oscillation. Proc. Ninth Ann. Clim. Diag. Workshop, U.S. Dept. of Commerce, Washington DC.

-----, and P.R. Julian, 1971: Detection of a 40-50 day oscillation in the zonal wind in the tropical Pacific. J. Atmos. Sci., 28, 702-708.

-----, and -----, 1972: Description of global-scale circulation cells in the tropics with a 40-50 day period. J. Atmos. Sci., 29, 1109-1123.

Matsuno, T., 1966: Quasi-geostrophic motions in the equatorial area. J. Meteor. Soc. Japan, Ser. II, 44, 25-43.

McCreary, J.P., 1976: Eastern tropical ocean response to changing wind systems: with applications to El Niño. J. Phys. Ocean., 6, 632-645.

Murakami, T., 1975: Interannual cloudiness changes. Mon. Wea. Rev., 103, 996-1006.

Mysak, L.A., 1984: El Niño, Interannual Variability, and Fisheries in the Northeast Pacific Ocean. Technical Report 84-17, Institute of Applied Mathematics, University of British Columbia, 91 pp.

Newell, R.E., J.W. Kidson, D.G. Vincent, and G.J. Boer, 1972: The General Circulation of the Tropical Atmosphere and Interactions with Extratropical Latitudes, Vol. 1. The MIT Press, 258 pp.

-----, -----, -----, and -----, 1974: The General Circulation of the Tropical Atmosphere and Interactions with Extratropical Latitudes, Vol. 2. The MIT Press, 371 pp.

-----, R. Selkirk, and W. Ebisuzaki, 1982: The Southern Oscillation: Sea surface temperature and wind relationships in a 100-year data set. J. Clim., 2, 357-373.

Nicholls, N., 1984: The Southern Oscillation and Indonesian sea surface temperature. Mon. Wea. Rev., 112, 424-432.

North, G.R., T.L. Bell, R.F. Cahalan, and F.J. Moeng, 1982: Sampling errors in the estimation of empirical orthogonal functions. Mon. Wea. Rev., 110, 699-706.

Oort, A.H., 1983: Global Atmospheric Circulation Statistics, 1958-1973. NOAA Prof. Pap. 14, U.S. Dept. of Commerce, 180 pp.

Pan, Y.H., and A.H. Oort, 1983: Global climate variations connected with sea surface temperature anomalies in the eastern equatorial Pacific Ocean for the 1958-73 period. Mon. Wea. Rev., 111, 1244-1258.

Pazan, S.E., and G. Meyers, 1982: Interannual fluctuations of the tropical Pacific wind field and the Southern Oscillation. Mon. Wea. Rev., 110, 587-600.

Philander, S.G.H., 1983: El Niño Southern Oscillation phenomena. Nature, 302, 295-301.

Quinn, W.H., and W. Burt, 1972: Use of the Southern Oscillation in weather prediction. J. Appl. Meteor., 11, 616-628.

Ramage, C.S., 1968: Role of a tropical "maritime continent" in the atmospheric circulation. Mon. Wea. Rev., 96, 365-369.

-----, and A.M. Hori, 1981: Meteorological aspects of El Niño. Mon. Wea. Rev., 109, 1827-1835.

Rasmusson, E.M., and T.H. Carpenter, 1982: Variations in tropical sea surface temperature and surface wind fields associated with the Southern Oscillation/El Niño. Mon. Wea. Rev., 110, 354-384.

-----, and -----, 1983: The relationship between eastern equatorial Pacific sea surface temperatures and rainfall over India and Sri Lanka. Mon. Wea. Rev., 111, 517-528.

Rasmusson, E.M., and J.M. Wallace, 1983: Meteorological aspects of the 1982-83 El Niño - Southern Oscillation. Science, 222, 1195-1202.

Schneider, E.K., and R.S. Lindzen, 1977: Axially symmetric steady-state models of the basic state for instability and climate studies. Part I. Linearized calculations. J. Atmos. Sci., 34, 263-279.

-----, and I.G. Watterson, 1984: Stationary Rossby wave propagation through easterly layers. J. Atmos. Sci., 41, 2069-2083.

Selkirk, R., 1984: Seasonally stratified correlations of the 200 mb tropical wind field to the Southern Oscillation. J. Clim., 4, 365-382.

Shukla, J., 1984: Interannual variability of monsoons. Monsoons, J.S. Fein and P.L. Stephens, eds., Wiley and Sons, Chapter 5.3.

-----, and J.M. Wallace, 1983: Numerical simulation of the atmospheric response to equatorial Pacific sea surface temperature anomalies. J. Atmos. Sci., 40, 1613-1640.

Simmons, A.J., 1982: The forcing of stationary wave motion by tropical diabatic heating. Quart. J. Roy. Meteor. Soc., 108, 503-534.

Trenberth, K.E., 1976: Spatial and temporal variations of the Southern Oscillation. Quart. J. Roy. Meteor. Soc., 102, 639-653.

-----, and D.A. Paolino, 1980: The Northern Hemisphere sea-level pressure data set: Trends, errors and discontinuities. Mon. Wea. Rev., 108, 855-872.

Troup, A.J., 1961: Variations in 200 mb flow in the tropics. Meteor. Mag., 90, 162-167.

-----, 1967: Opposition of anomalies of upper tropospheric winds at Singapore and Canton. Australian Meteor. Mag., 15, 32-37.

Van Loon, H., 1984: The Southern Oscillation. Part III: Associations with the trades and with the trough in the westerlies of the South Pacific Ocean. Mon. Wea. Rev., 112, 947-954.

-----, and R.L. Jenne, 1969: The half-yearly oscillations in the tropics of the Southern Hemisphere. J. Atmos. Sci., 26, 218-232.

-----, and -----, 1970: On the half-yearly oscillations in the tropics. Tellus, 22, 391-398.

-----, and D.J. Shea, 1985: The Southern Oscillation. Part IV: The development of warm and cold events. Submitted to Mon. Wea. Rev.

Walker, G.W., 1924: Correlation in seasonal variations of weather IX: A further study of world weather. Mem. Indian Meteor. Dept., 24, 275-332.

Walker, G.W., and E.W. Bliss, 1932: World weather V. Mem. Roy. Meteor. Soc., 4, 53-84.

Wallace, J.M., 1971: Spectral studies of tropospheric wave disturbances in the tropical western Pacific. Rev. Geophys. Space Phys., 9, 557-612.

-----, and D.S. Gutzler, 1981: Teleconnections in the geopotential height field during the Northern Hemisphere winter. Mon. Wea. Rev., 109, 784-812.

Weare, B.C., A.R. Navato, and R.E. Newell, 1976: Empirical orthogonal analysis of Pacific sea surface temperatures. J. Phys. Ocean., 6, 671-678.

-----, P.T. Strub, and M.D. Samuel, 1980: Marine Climate Atlas of the Tropical Pacific Ocean. Department of Land, Air, and Water Resources, University of California, Davis, 147 pp.

Webster, P.J., 1972: Response of the tropical atmosphere to local, steady forcing. Mon. Wea. Rev., 100, 518-541.

-----, 1973: Remote forcing of the time-independent tropical atmosphere. Mon. Wea. Rev., 101, 58-68.

-----, and J.R. Holton, 1982: Cross-equatorial response to middle-latitude forcing in a zonally varying basic state. J. Atmos. Sci., 39, 722-733.

Weickmann, K.M., 1983: Intraseasonal circulation and outgoing longwave radiation modes during Northern Hemisphere winter. Mon. Wea. Rev., 111, 1838-1858.

Wyrtki, K., 1975: El Niño - The dynamical response of the equatorial Pacific Ocean to atmospheric forcing. J. Phys. Oceanogr., 5, 572-584.

Yanai, M., S. Esbensen, and J.-H. Chu, 1973: Determination of bulk properties of tropical cloud clusters from large-scale heat and moisture budgets. J. Atmos. Sci., 30, 611-627.

Zebiak, S.E., 1982: A simple atmospheric model of relevance to El Niño. J. Atmos. Sci., 39, 2017-2027.

-----, 1984: Tropical atmosphere-ocean interaction and the El Niño / Southern Oscillation phenomenon. Ph.D. dissertation, Massachusetts Institute of Technology, 261 pp.